Thermal cis → trans isomerization of azobenzenes studied by path sampling and QM/MM stochastic dynamics

Dissertation zur Erlangung des akademischen Grades

“Doctor rerum naturalium” (Dr. rer. nat.)

in der Wissenschaftsdisziplin Theoretische Chemie

vorgelegt von

Anja Muždalo

am

7. Juni 2017

an der

Mathematisch-Naturwissenschaftlichen Fakultät

der Universität Potsdam

The studies described in this dissertation were conducted from September 2013 until February 2017 at the Max Planck Institute of Colloids and Interfaces under the supervision of Dr Mark Santer and Prof Dr Peter Saalfrank.

1. Gutachter: Prof. Dr. Peter Saalfrank
2. Gutachter: Dr. Mark Santer
3. Gutachter: JProf. Dr. Bettina Keller

URN urn:nbn:de:kobv:517-opus4-405814
http://nbn-resolving.de/urn:nbn:de:kobv:517-opus4-405814

Contents

ABSTRACT

Thermal cis → trans isomerization of azobenzenes studied by path sampling and QM/MM stochastic dynamics

Anja Muždalo

Azobenzene-based molecular photoswitches have extensively been applied to biological systems, involving photo-control of peptides, lipids and nucleic acids. The isomerization between the stable trans and the metastable cis state of the azo moieties leads to pronounced changes in shape and other physico-chemical properties of the molecules into which they are incorporated. Fast switching can be induced via transitions to excited electronic states and fine-tuned by a large number of different substituents at the phenyl rings. But a rational design of tailor-made azo groups also requires control of their stability in the dark, the half-lifetime of the cis isomer. In computational chemistry, thermally activated barrier crossing on the ground state Born-Oppenheimer surface can efficiently be estimated with Eyring's transition state theory (TST) approach; the growing complexity of the azo moiety and a rather heterogeneous environment, however, may render some of the underlying simplifying assumptions problematic.

In this dissertation, a computational approach is established to remove two restrictions at once: the environment is modeled explicitly by employing a quantum mechanical/molecular mechanics (QM/MM) description; and the isomerization process is tracked by analyzing complete dynamical pathways between stable states. The suitability of this description is validated by using two test systems, pure azo benzene and a derivative with electron donating and electron withdrawing substituents ("push-pull" azobenzene). Each system is studied in the gas phase, in toluene and in polar DMSO solvent. The azo molecules are treated at the QM level using a very recent, semi-empirical approximation to density functional theory (density functional tight binding approximation). Reactive pathways are sampled by implementing a version of the so-called transition path sampling method (TPS), without introducing any bias into the system dynamics. By analyzing ensembles of reactive trajectories, the change in isomerization pathway from linear inversion to rotation in going from apolar to polar solvent, predicted by the TST approach, could be verified for the push-pull derivative. At the same time, the mere presence of explicit solvation is seen to broaden the distribution of isomerization pathways, an effect TST cannot account for.

Using likelihood maximization based on the TPS shooting history, an improved reaction coordinate was identified as a sine-cosine combination of the central bend angles and the rotation dihedral, $\mathrm{r}\ (\omega, \alpha, \alpha')$. The computational van't Hoff analysis for the activation entropies was performed to gain further insight into the differential role of solvent for the case of the unsubstituted and the push-pull azobenzene. In agreement with the experiment, it yielded positive activation entropies for azobenzene in the DMSO solvent while negative for the push-pull derivative, reflecting the induced ordering of solvent around the more dipolar transition state associated to the latter compound. Also, the dynamically corrected rate constants were evaluated using the reactive flux approach where an increase comparable to the experimental one was observed for a high polarity medium for both azobenzene derivatives.

(130 pages, 61 Figures, 17 Tables, 110 References, Original in English)

Keywords: transition path sampling, thermal isomerization of azobenzene, QM/MM stochastic dynamics, DFTB3, activation entropy, reactive flux rate constants, reaction mechanism, solvent effect

“Svakoga dana u svakom pogledu sve više napredujem.”

Dino, Sjećaš li se Dolly Bell

1 Introduction

Azobenzenes are organic compounds whose discovery dates back to the early 1800s when the photochemical cis → trans isomerization was observed for the first time [1]. Due to their chemical structure, consisting of a central double bond N=N with the two attached phenyl rings as residues, they can isomerize. In the cis conformation, the phenyl rings are placed at the same side of the double bond, while in the trans conformation they are at the opposite sides. The cis → trans isomerization thus proceeds spontaneously in dark due to a greater thermodynamical stability of the trans conformer, but can also proceed upon irradiation by light in both directions (Figure 1). Since their discovery azobenzenes have been applied extensively as pigments and dyes due to good light stability [2]. Their photoswitching properties have been applied in biology only recently [3] which we discuss in Section 1.1.

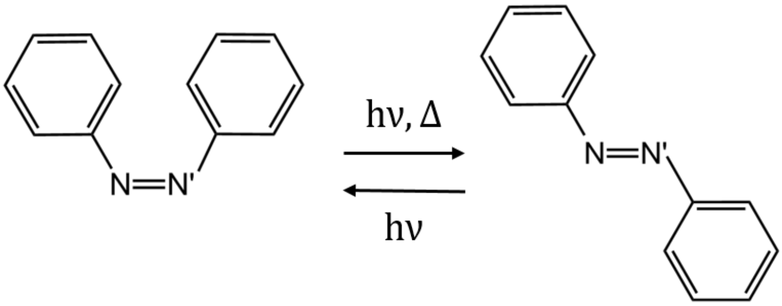

Figure 1. Molecular scheme for the cis ↔ trans interconversion of azobenzene. The reaction proceeds in both directions upon irradiation with UV light and thermally in the cis → trans direction.

For the optimal photoswitching behaviour it is favourable for the thermal relaxation to be slow so that the selective photoswitching in both cis ↔ trans directions can be achieved. Though many experimental studies regarding kinetics and reaction mechanisms for thermal relaxation of azobenzenes have been conducted, very few studies from the computational side exist [4]. We introduce relevant findings from the existing computational studies in Section 1.2. Within this work we also treat the effects of phenyl rings substitution with different functional groups and the effects of solvent polarity. Generally speaking, the (photo)chemical properties of azobenzenes can be fine-tuned by such substitutions. A double substitution with an electron accepting group (for example a nitro group NO_2) and an electron donor group (for example an amino group NH_2) constitutes a special class of azobenzenes, termed the push-pull azobenzenes. The transition structures of these derivatives have large dipole moments and as such are stabilized in polar solvents, allowing for a switch to a rotation mechanism. The push-pull azobenzenes and the effect of solvents is discussed in Section 1.2.1.

The cis → trans isomerization proceeds over a large energy barrier and as such is a rare event which cannot be adequately sampled with straightforward molecular dynamics. In addition, the transition structure for azobenzene is almost linear in the central sequence of N=N-C atoms [4] which requires the system to be described on a quantum level and not with a classical force field. This further increases the computational demand of sampling. In existing studies, the effect of solvent was included using polarizable continuum models. To improve on the drawbacks of the classical quantum theory treatment for this reaction, we employ an enhanced sampling technique for rare events, the transition path sampling within the QM/MM framework. Within this scheme, the azo-moiety is treated on a quantum level and the solvent molecules explicitly described with a force field. Using this approach we hope to improve on the model and representation of the system by sampling full dynamical trajectories within the QM/MM framework keeping the quantum level of theory for the accurate representation of the transition state as well as inclusion of solvent in an explicit manner with electronic embedding and polarization effects. Similar studies of transition path sampling applied to isomerization of (bio)organic molecules and the treatment of solvent therein is discussed in Section 1.3.

1.1 Azobenzene as a molecular photoswitch

Azobenzenes (AB) are bistabile photoswitchable molecules which undergo cis-trans isomerization upon irradiation by light. The cis isomer is thermodynamically unstable and as such cannot be isolated, but due to its absorption at shorter wavelengths than the trans isomer can be detected in a UV spectrum [2]. The photochemical properties are greatly altered upon substitution. For example, upon fluorination the cis isomer is greatly stabilized with a half-life of $\tau_{1/2} = 92\ \mathrm{h}$ measured for an F4-derivative (molecular structure in Appendix 5.6.) compared to the thermal half-life of $\tau_{1/2} = 4\ \mathrm{h}$ for unsubstituted azobenzene in the same conditions, as reported in [5]. The long lived cis isomers are stabilized by the electron withdrawing fluorine atoms in the ortho position. This improves the photochemical properties of azobenzenes as the selective switching can be better controlled solely by light. Fluorinated derivatives are promising for biological applications due to a shift in the absorption wavelengths form UV towards the non-damaging visible part of the spectrum.

There are several issues to consider with regards to the application of (photo)isomerization of ABs to biological systems [3]. Firstly, the azo-moiety has to be somehow linked to the biomolecule so as to not affect its function. Secondly, for the optimal photo-control of the $\mathrm{cis} \leftrightarrow \mathrm{trans}$ switching in in-vivo applications, it would be beneficial to use longer red-shifted wavelengths due to potential harmful effects of the higher energy UV light and also due to easier penetration of longer wavelength light into tissues and cells. Thirdly, the overlap of the absorption spectra for the cis and trans isoforms can be modified by phenyl rings substitution. Enhancing the rate for the thermal relaxation might be beneficial in some applications, for example in case of probing a fast biochemical process. The push-pull derivatives experience a red-shift in the absorption wavelengths because of the reduced $\mathrm{cis} \rightarrow \mathrm{trans}$ energy barriers due to a more dipolar transition state and thus exhibit a faster relaxation [6, 7, 8]. On the other hand, in case of probing a longer timescale biochemical process it would be beneficial to maintain the biomolecule in an on-off state during this time, instead of constantly irradiating it with light. For this purpose, long lived derivatives such as ortho substituted nitro-benzenes have been studied [9], as well as previously mentioned fluorinated azobenzenes. The optimal derivatives for biological applications would thus be spectrally tuned to absorb in the visible part of the spectrum and have either short-lived or long-lived cis isomers depending on the timescale of the biological processes being probed.

The azo-moiety experiences large structural changes upon $\mathrm{cis} \rightarrow \mathrm{trans}$ conversion which triggers the conformational change of the biomolecule to which the azo-moiety is attached to resulting with a change in function. The completeness of the (de)activation of the biomolecule is thus dependent upon the rigidity of the bound azo-moiety. Alkylation of the azo-substituents has been shown to be useful in the photo-control of peptides [10, 11]. Mastering the photo-control of peptides is highly valuable for studying the elementary steps in protein folding. In an exemplary study, an azobenzene amino acid was included as the turn element thus constituting a photo-switchable β-turn, where upon irradiation the cis → trans conversion accompanied by a large increase in the end-to-end distance induced the disordered state from an ordered β-hairpin [12]. In a similar study, the azo-photoswitch was incorporated as a side chain in a peptide sequence to control the helical content [13]. Since the conformational change was not induced by some specific interactions between the azo-switch and the peptide, and the timescale of the switching was unaffected, the linker could be applied to general studies of the widespread and extensively studied helical proteins. Going a step further, photoswitching was employed to induce structural changes in functional proteins. By cross-linking the surface exposed residues with azobenzene containing moieties, large conformational changes in biologically active proteins was induced upon cis ↔ trans photoswitching and thus their selective (de)activation was achieved [14]. This direct control of protein activity with photoswitching could be used for the synthesis of controllable biomolecules in complex environments and ultimately in *in-vivo* conditions. Another general approach in photo-controlling protein function was through azo-attached ligands, which depending on the conformational state of the azo-moiety would either bind to the protein active site or not. For example, by attaching a choline agonist via a photoisomerizable linker near the allosteric site of the ligand, photo-control of the acetylcholine receptor was achieved [15]. Upon irradiation by visible light characteristic for the trans state for the azo-linker, the receptor was activated. Furthermore, azo-based photoswitches have been applied to nucleic acids. In an interesting study, the transcription by the T7 RNA-polymerase was either activated or deactivated by selectively exciting the azo-linker intercalated within the promoter region [16, 17]. Upon irradiation, the cis → trans interconversion of the intercalated azo-moiety induced conformational changes in the DNA structure which in turn (de)facilitated the interaction and binding between the DNA and the RNA polymerase. The approach is promising in the context of creating synthetical biological systems in which gene expression can be controlled. Azobenzene photoswitches have also been employed in controlling the lipid membrane properties. For example, an increase in the membrane permeability was achieved for a certain concentration of azobenzene moieties included into the tails of an amphiphilic vesicular system by photo-inducing the trans → cis isomerization [18]. In another study, the morphological properties of synthetic amphiphiles containing azo-units could be modified by light, namely, budding towards the center as well as budding out of the liposome [19].

In conclusion, azobenzene photoswitches are particularly valuable in applications as photo-switches due do their extensively tuneable physical properties such as the range of excitation wavelengths and the excited states lifetimes, and in particular the thermal stabilities of the cis state. This makes them superior in their usage as switches compared to other similar compounds, for example stilbenes where the central bond is the C=C bond. The rigidity of the phenyl rings assures that the structural switch upon isomerization results in predictable distance changes, important for the further induction of conformational changes in bio-molecules the azo-moieties are attached to. Research is currently on the way to extend the current applicability by tuning the physical properties of azobenzenes [20], which can be achieved through substitution but also through the use of different solvents. It is in with this in mind thus relevant to gain further insight in the mechanistic aspects of thermal isomerization of azobenzenes and the associated rates, upon substitution and in variable solvent conditions especially with respect to polarity.

1.2 Thermal isomerization of azobenzene

The mechanism of the thermal $\mathrm{cis} \rightarrow \mathrm{trans}$ isomerization has long been debated, with many contradictive experimental and computational studies. Though in principle the isomerization can proceed through many pathways, the two main mechanisms were proposed: the pure rotation around the central double bond N=N where the double bond formally breaks, and an inversion with a linearization of the central bend angle N=N’-C and the change in the hybridization of the inverting nitrogen N’, from $\mathrm{sp}^2 \rightarrow \mathrm{sp}$. The geometry is thus changed from a triplanar to a collinear for the N=N-C sequence of atoms. In a seminal ab-initio study in which the photochemistry and the thermal relaxation of azobenzene was studied with a high level of quantum theory (CASSCF), the minimal energy transition structure associated to the ground state potential energy surface found was the perpendicular invertomer [21], shown in Figure 2. The other plausible transition structures, the rotamer and the planar invertomer associated to the ground state potential energy surface S_0 were both found to possess a higher electronic energy.

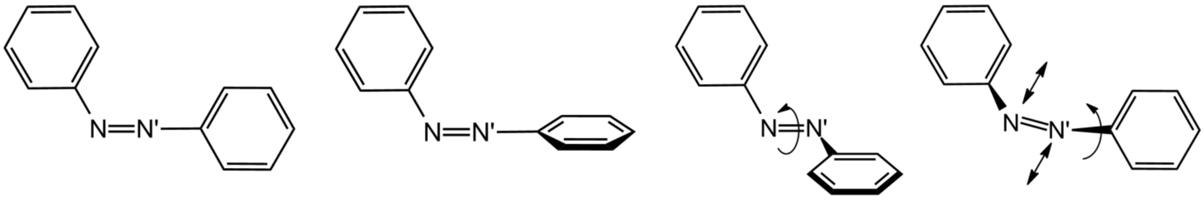

Figure 2. Scheme: possible transition structures for azobenzene, from right to left: a planar invertomer, a perpendicular invertomer, a rotamer with the annotated rotation direction along the double N=N bond. The directions of movement for a hula-twist is depicted in the molecular scheme on the rightmost. Adjusted from [21].

For the photo-induced isomerization via an excited electronic state, the transition was proposed to depend on the excitation pathways. For the $\pi \rightarrow \pi^*$ excitation [2, 21], the lowest energy transition structure associated to the excited state surface was identified as the rotamer, while for the formally symmetry forbidden $n \rightarrow \pi^*$ excitation as a perpendicular invertomer [2], the same as for the ground state surface S_0. The relative orientation of the phenyl rings in the transition state, which for the two extremal cases is either planar or perpendicular, seemed not to be important for photochemical reactivity due to a weak variation in energy along the phenyl twisting dihedral angle. For the thermal isomerization, the planar invertomer was found to be substantially higher in energy than the perpendicular, namely $\Delta \mathrm{E} = 37.2\ \mathrm{kJ\ mol^{-1}}$ for CASSCF/6-31G. The involvement of the phenyl ring twisting coordinate was recently considered in terms of the thermal relaxation after $\pi \rightarrow \pi^*$ and $n \rightarrow \pi^*$ photo-excitation [22] where the potential energy surface was calculated with respect to a hula-twisting coordinate. The hula-twisting involves a simultaneous rotation around N=N and twisting around an adjacent N-C bond, shown in Figure 2 in the rightmost scheme. It was experimentally found for the reaction rate not to depend on the viscosity indicative that the reaction was not likely to involve substantial movements of the phenyl rings, as would be the case in pure rotation around the N=N bond. This was indicative of in fact the hula-twisting mechanism being predominant, since it involves minimal change in the relative orientation of the phenyl rings. The invertomer was ruled out based on the geometry of the structures for the intermediates associated to the calculated PES. In the context of thermal isomerization associated to the ground state potential energy it is also plausible for the hula-twist component to contribute to the mechanism, especially in volume restrictive environments, for example in highly diffusive regimes of a crowded biological cell or in case of the azobenzene moiety attached to a biomolecule as a photo-switch.

The general finding of the few computational studies of the thermal isomerization for azobenzenes is that the transition structure associated to the ground state potential energy surface to be an invertomer, where some have found for the rotation dihedral associated to the invertomer midway between the cis and trans stable states [4, 23]. This would indicate that there is a concerted motion along both the bend angle and the rotation dihedral, and in fact the mechanism is the combination of both inversion and rotation. To corroborate this statement, the authors in [24] noted that inversion cannot operate alone since the opening of the bend angle has to be preceded by some degree of torsion in order to decouple the electronic conjugation across the two phenyl rings. In addition, the general finding concerning the relative orientation of the phenyl rings is that they are perpendicular, even for the range of substituted azobenzenes as found by [4]. In stable states, the rings are either planar in the trans or slightly tilted in the cis state due to steric clashes, which indicates some change in the relative orientation of the phenyl rings occurs within the transition. The weak energy dependence on the twisting dihedral coordinate identified in [21] revealed that this barrier is easily traversed thermally which makes this coordinate irrelevant for the thermal mechanism. With this in mind, the hula-twisting should be easily realized given the thermal energy provided by the surrounding heat bath and should be seriously considered as the contributing mechanism for the isomerization on the ground state PES.

The Arrhenius analysis for the variation of isomerization rates with temperature provides valuable insight into the mechanistic details of a reaction, in terms of activation parameters, the activation enthalpies and entropies. When compared to the computationally evaluated activation parameters calculated with the classical Eyring theory to experimentally measured ones, there is generally a good agreement between the activation enthalpies. Though experimental rates for the thermal isomerization were always measured in solution, in a recent experiment a quasi-vacuum conditions were achieved by integrating the azo-moiety into crystalline metal-organic frameworks [25]. The authors reported a remarkably good agreement between the obtained activation energies and the calculated ones by Dokić et al. [4], the two values being $1.09 \pm 0.09\ \mathrm{eV}$ and $1.1\ \mathrm{eV}$, respectively. Remarkably, though the authors did not discuss the activation entropies, from the Arrhenius plots reported in [25] we estimated them as negative. The obtained negative activation entropies from experiments in quasi-vacuum conditions are again in disagreement with the calculated ones from first principles of statistical mechanics which are always positive for a range of azobenzene derivatives [4]. This would imply that the flexibility and the associated entropy at the transition state is actually lower than at the cis state, a result not reproduced by the classical frequency analyses for the transition and the cis stable state. Furthermore, the $\mathrm{cis} \rightarrow \mathrm{trans}$ isomerization is an example of a reaction where there is significant charge rearrangement and an increase in the dipole moment for the transition state. Therefore, upon introduction of solvent, a great deal of solvent ordering is expected to occur around the more dipolar transition state compared to the cis stable state, and even more so for the low polarity solvents where this dipolar induction is more pronounced.

For the thermal isomerization of azobenzene(s) in organic solvents with increasing polarity it was found for the rate to also generally increase. As reported from the NMR spectroscopic measurements on an amino-AB derivative [26], the rate was increased twice going from the non-polar benzene to a highly polar DMSO (from $5.1 \cdot 10^{-5}\ \mathrm{s}^{-1}$ to $9.8 \cdot 10^{-5}\ \mathrm{s}^{-1}$ respectively, at temperature $\mathrm{T} = 298\ \mathrm{K}$).

In conclusion, the computational studies previously used to study the thermal $\mathrm{cis} \rightarrow \mathrm{trans}$ isomerization of azobenzenes were the electronic structure optimization with the high quantum levels of theory and the classical Eyring theory for rate calculation. Therein, it was found for the reaction to proceed via the so called perpendicular invertomer with a co-linear arrangement of N-N-C atoms (Figure 2) and the phenyl rings in perpendicular orientation. This would indicate for the mechanism to be a rotation assisted inversion with an additional twisting of the phenyl rings. The Arrhenius analysis for the rate dependence on temperature yielded good agreement for the activation enthalpies to the experimentally obtained ones, while it failed to reproduce the activation entropies predicting values false even in the sign. This might not be a surprise since the polarizable continuum models cannot account for the solvent ordering effects around the solute with a changing dipole moment going from the cis to the transition state, which should play a determining role for the entropy contribution.

1.2.1 The push-pull substitution of azobenzene: Solvent polarity effects.

Substitution of the phenyl rings with electron donating and accepting groups delocalizes the electrons of azobenzene chromophores and shifts the absorption wavelengths to the visible and infra-red part of the spectrum [8]. The corollary of this substitution is the reduction of the thermal barriers for this class of ABs, the so called push-pull ABs. The effect occurs due to a stabilization of the more dipolar transition state through resonance [4]. These effects have recently been decoupled by introducing substituents at all four ortho positions in addition to the original push-pull substituents at para positions of the phenyl rings, yielding red-shifted push-pull derivatives with slow thermal relaxation rates [27]. These compounds would be especially useful as photo-controlled drugs for in-vivo use, where the long lifetimes of the cis isomer would result in remarkable control in photo-switching.

Regarding the isomerization mechanism, the push-pull substituents increase the single bond character of the central N=N bond, making the rotation a more favourable route of interconversion. On the example of the DO3 push-pull derivative where the electron donating amino group NH_2 and the accepting nitro group NO_2 are attached at para positions of the opposing phenyl rings, the effect of solvent polarity on the geometries of optimized transition structures was studied in [4]. A non-linear transition structure was found in a high polarity continuum representing a solvent such as DMSO, with the energy barrier greatly reduced compared to the linear transition structure obtained in the gas-phase. In addition, the energetics and geometries of the transition structures were not affected in low-polarity continuum representation for the solvent. The conclusion was that a transition structure with the formally broken NN double bond and a ‘zwitterionic’ character which allows for the rotation mechanism was further stabilized in polar solvents. The associated activation entropy calculated by employing normal mode analysis at transition and the cis stable state changed sign from positive in the gas phase to increasingly negative in the highly polar solvent continuum.

The isomerization reaction is accompanied by a large change in the dipole moment when going from the cis to the transition state and it is thus expected for the ordering of the solvent molecules around the solutes to change as well. The ordering of solvent should be more pronounced at the transition state due to stronger dipole-dipole interactions, with the change in ordering more pronounced for the less polar solvents. This effect obviously cannot be accounted for with continuum solvent models.

On the experimental side, the solvent effect on the push-pull isomerization mechanism was studied by means of measuring the rate dependence on pressure. The rate of isomerization was increased with the increasing pressure in polar solvents, and not in low polarity solvents. This served as proof of change in mechanism, from inversion to rotation in polar solvents [28, 29, 30]. As an additional proof that the isomerization proceeded through a highly dipolar rotamer were the negative activation volumes obtained from the same pressure dependence of the isomerization rate, explained by the electrostriction of solvent during activation [31].

The rates of thermal isomerization of push-pull derivatives in organic solvents generally increase with increasing solvent polarity. The measured rate in low polarity toluene versus high polarity DMSO was increased 10000 times for a push-pull derivative DNAB [32], where $N(CH_3)_2$ and NO_2 groups are attached in para positions of the neighboring phenyl rings. As reported in [33], the increase was due to the lowering of the activation energy in the polar solvent while the Arrhenius prefactor was actually decreased. The stabilization of the rotamer transition state in highly polar solvents thus had a prevailing effect in the total reduction of the rate. The activation entropies evaluated from the experimental Arrhenius prefactors reported for the DNAB push-pull derivative at $\mathrm{T} = 298\ \mathrm{K}$, were $\Delta\mathrm{S}^{\#} = -73.5\ \mathrm{J\ mol^{-1}\ K^{-1}}$ in benzene [26] and $\Delta\mathrm{S}^{\#} = -81.7\ \mathrm{J\ mol^{-1}\ K^{-1}}$ in DMSO [33]. The experimental findings thus suggested that the reaction for a push-pull derivative was entropically disfavoured in both low and high polarity solvents. This again was argued to occur due to electrostriction of solvent around the highly dipolar rotamer transition state, as would the negative activation volumes measured for push-pulls in DMSO suggest [31].

The $\mathrm{cis} \rightarrow \mathrm{trans}$ isomerization of push-pull derivatives was thus explained with two competing mechanisms, the inversion and rotation, where rotation becomes predominant in case of solvent stabilization of the more dipolar rotamer transition state. This in turn results with lowering of the activation entropy due to electrostriction of solvent but in a total multifold increase in rate due to enthalpic stabilization.

1.3 Transition Path Sampling isomerization studies. Solvent effect

To the best of our knowledge, there were no enhanced path sampling studies we employ within this work applied to the thermal $\mathrm{cis} \rightarrow \mathrm{trans}$ isomerization of azobenzenes. There are many examples in the literature though, where transition path sampling was employed to study general reactions and isomerization in solutions [34, 35]. In a study for the simplest case of dissociation of the $\mathrm{Na^{+}..Cl^{-}}$ ionic system in aqueous solution [36, 37] a much more complex reaction mechanism was revealed where it was shown for the solvent degrees of freedom to play an important role. This was made clear by identifying a set of highly diverse ensemble of transition states associated to the reaction. In addition, as the transition pathways provide a time resolved picture the dynamical effect of solvent could be investigated. It was shown for the spontaneous fluctuations in electric fields produced through thermal motion of water molecules around the ions triggered the reaction of (di)association. These effects are expected to be relevant for all charge rearrangement reactions that is for the $\mathrm{cis} \rightarrow \mathrm{trans}$ isomerization of azobenzenes as well. In addition, the polar solvent is expected to enthalpically and/or entropically favour either of the reactant or transition states based on the strength of the solute-solvent dipolar interactions [35]. Also, a dynamic effect of solvent acting as a heat bath to induce or reduce the frequency (re)crossings of the transition region is accounted for by sampling the true dynamical paths in solution.

In the study of $\mathrm{trans} - \mathrm{gauche}$ isomerization in n –butane, the reaction rates obtained from the transition path ensemble showed good agreement with the rates obtained from straightforward molecular dynamics [38]. Though computationally costly, this method of rate calculation is superior due to the fact that no reaction coordinate has to be predefined, an advantage for complex systems that are reactions in solution. The analysis of the transition state ensemble identified other coordinates additional to the assumed torsion coordinate as reactive. The same effect was observed in a similar study for the isomerization of alanine dipeptide [39, 40]. The analysis of the transition state ensemble revealed additional torsional coordinate that contributed to the reaction coordinate. Therein, the solvent effect was addressed; the quality of the reaction coordinate as defined in the committor analysis, was reduced going from vacuum to a solvent. It was argued that the solvent motion occurred at the same time scale as the transition. The solvent degrees of freedom other than coordination numbers around solutes or a number of hydrogen bonds were assumed to be determinative for the reaction. In a more recent study for the conformational change for a prototypical disaccharide [41], the transition path sampling approach was explicitly compared to the potential of mean force approach. Reaction coordinates were defined as torsions around glycosidic bonds of the model molecule. Based on sampling many transitions between states defined for the torsional free energy surface, an additional reactive channel between the stable states was identified. This demonstrated that an important transition region was overlooked due to it not being a minimum of the underlying free energy surface.

In conclusion, in a series of studies transition path sampling performed in a superior fashion compared to both, straightforward molecular dynamics and the potential of mean force approaches. In transition path sampling, reactive events are sampled to yield a statistically representative transition path ensemble, from which the associated transition states can be extracted. In turn, the transition state ensemble configurations capture the relevant reactive coordinates which provide further insight into the reaction mechanism. Both the dynamic and static effect of solvent arising due to specific solute-solvent interactions and solvent rearrangements are included.

1.4 The goals and research questions

Our goal is to extend the classical transition state theory in the form of ‘transition path formalism’ to study the thermal relaxation of azobenzene AB and a push-pull derivative, 4NO_2-6'NH_2-AB both in vacuum and in presence of a high polarity (DMSO) and a low polarity (toluene) solvent. Our hope is to calculate the ‘true dynamical’ transition rates within the reactive flux formalism to improve on the classical Eyring transition state theory treatment. Therein, the reaction rates are calculated from first principles in statistical mechanical using partition functions for translational, rotational and vibrational degrees of freedom for a molecule. Given the partition functions, the thermodynamic activation parameters are calculated using standard formulas of statistical mechanics [42]. The classical approach works well for gas phase, but is problematic in solution due to non-ideal behaviour and the breakdown of approximations used to derive the partition functions. The activation entropies for azobenzene isomerization were typically evaluated to be slightly positive in the gas phase. This would imply a more flexible transition structure compared to the cis stable state. The experimentally measured values for the activation entropies of azobenzenes in low polarity solvents were found to be negative, indicative of ordering of the solvent at the transition state. It is thus not surprising the computational model treating the solvent as a polarizable continuum did not prove to yield the experimentally found result. In the current work where we explicitly sample the solute and solvent degrees of freedom, including the dipolar interactions, the effect of solvent ordering should be captured and the activation entropies more accurately evaluated. For this, we perform the computational van’t Hoff analysis, where from the free energy variations with temperature the activation entropies are obtainable from straight line fits [43].

In the following, we state the research questions and offer testable hypotheses.

Q1: In how far does the mechanism of thermal isomerization and the nature of the transition state change upon solvation?

H1: Upon solvation with polar solvent the mechanism assumes a more rotation-like character with the transition state best described as a rotamer and not the invertomer, found to be the optimal transition structure with classical quantum optimization in gas phase and low polarity polarizable continuums.

H2: The effect is most pronounced for the push-pull derivative due to the higher polarity of the push-pull substituted transition state which has a ‘zwitterionic’ character

Q2: Does the explicit representation of the polarizing solvent result with markedly different reaction dynamics and how do the resulting dynamically corrected isomerization rates compare to the result obtained by classical transition state theory and experiments?

H1: The solvent effect is assumed to include more than the pure static effect which arises due to both specific solute-solvent interactions and non-specific polarization effects of the azo-moiety due to presence of solvent. We expect for the dynamical effect of path recrossings affected by explicit solvent to play a role.

Q3: Can the computational van’t Hoff type of analysis for activation parameters that deconstructs the enthalpic and entropic contributions to the free energy provide further insight into the mechanism for this system?

H1: The $\mathrm{cis} \rightarrow \mathrm{trans}$ isomerization of azobenzene(s) is a reaction involving an increase in the dipole moment in the transition state. For this category of reactions, the ordering of the solute molecules in the vicinity of the interconverting solvent plays a crucial role, and thus the configurational entropy of solvent is crucial for determining the enthalpic-entropic partitioning for the overall free energy. These mechanistic insights can be obtained from the van’t Hoff type of analysis, with the direct sampling of solvent degrees of freedom with molecular dynamics.

2 Methods

2.1 Electronic Structure Calculation

Under the Born-Oppenheimer approximation it is assumed that nuclear and electronic motions are decoupled due to nuclei being much heavier than electrons [44, 45]. This reduces the problem of solving the time independent Schrödinger equation

$$\mathbf{H}_{\mathrm{tot}}\mathbf{\Psi}_{\mathrm{tot}}(\mathbf{R},\mathbf{r}) = \mathrm{E}_{\mathrm{tot}}\mathbf{\Psi}_{\mathrm{tot}}(\mathbf{R},\mathbf{r}) \tag{1}$$

for the total wave function $\mathbf{\Psi}_{\mathrm{tot}}(\mathbf{R},\mathbf{r})$ dependent on both electronic $\mathbf{r}$ and nuclear $\mathbf{R}$ coordinates, to solving only the electronic wave function $\boldsymbol{\psi}_{\mathrm{e}}(\mathbf{r};\mathbf{R})$ which depends on the nuclear coordinates parametrically. The so called electronic Schrödinger equation is the central equation in computational chemistry, where the electronic Hamiltonian $\mathbf{H}_{\mathrm{e}}$ acts on the electronic wavefunction $\mathbf{\Psi}_{\mathrm{e}}$ to yield the electronic energy E_{e}

$$\mathbf{H}_{\mathrm{e}}\mathbf{\Psi}_{\mathrm{e}}(\mathbf{r}) = \mathrm{E}_{\mathrm{e}}\mathbf{\Psi}_{\mathrm{e}}(\mathbf{r};\mathbf{R}). \tag{2}$$

The molecular Hamiltonian represents the electronic energy constituted of kinetic energy of all electrons and the Coulomb interaction energies of the charged particles, the electron-electron, electron-nuclear energy and the constant term representing the nuclear repulsive energy for a fixed nuclear geometry $\mathbf{R}$. The electronic wave function and its associated electronic energy E_{e} are calculated for many nuclear configurations and as such represents a potential energy surface upon which the nuclei move. The electronic wave function for a fixed set of nuclear coordinates is expressed by a Slater determinant of one-electron molecular orbitals, $\boldsymbol{\phi}_{\mathrm{i}}(\mathbf{x})$, each a product of a spatial orbital $\boldsymbol{\phi}_{\mathrm{i}}(\mathbf{r})$ and a spin function $\sigma(\mathrm{s}) = \alpha(\mathrm{s})$ or $\sigma(\mathrm{s}) = \beta(\mathrm{s})$, so that the anti-symmetry of the total wave function is ensured. The ground state wavefunction $\mathbf{\Psi}_0$ can be thus expressed as

$$\mathbf{\Psi}_0 \approx \mathbf{\Psi}_{\mathrm{HF}} = \frac{1}{\sqrt{\mathrm{N}!}}\begin{vmatrix} \boldsymbol{\phi}_1(\mathbf{x}_1) & \dots & \boldsymbol{\phi}_1(\mathbf{x}_{\mathrm{N}}) \\ \dots & \dots & \dots \\ \boldsymbol{\phi}_{\mathrm{N}}(\mathbf{x}_1) & \dots & \boldsymbol{\phi}_{\mathrm{N}}(\mathbf{x}_{\mathrm{N}}) \end{vmatrix}. \tag{3}$$

The one-electron molecular orbitals are mutually orthonormal, $\int \boldsymbol{\phi}_{\mathrm{i}}^*(\mathbf{r})\boldsymbol{\phi}_{\mathrm{j}}(\mathbf{r})\,\mathrm{d}\mathbf{r} = \delta_{\mathrm{ij}}$, that is orthogonal in space since $\delta_{\mathrm{ij}} = 0$ for $\mathrm{i} \neq \mathrm{j}$, and normalized, since $\delta_{\mathrm{ij}} = 1$ for $\mathrm{i} = \mathrm{j}$ holds. In turn, the molecular orbitals are expressed as a sum of atom-centered basis functions, $\boldsymbol{\chi}_\alpha$, where the indices denote the $\alpha - \mathrm{th}$ basis function in the expansion of the $\mathrm{i} - \mathrm{th}$ one-electron molecular orbital,

$$\boldsymbol{\phi}_{\mathrm{i}} = \sum_\alpha \mathrm{c}_{\alpha\mathrm{i}}\,\boldsymbol{\chi}_\alpha. \tag{4}$$

This formalism is also referred to as the linear combination of atomic orbitals (LCAO). Within the Hartree-Fock approach by employing the variational principle, the energy is minimized with respect to the expansion coefficients $\mathrm{c}_{\alpha\mathrm{i}}$ to obtain the wavefunction where the expansion coefficients are optimized and the resulting energy the upper-bound for the total energy. By employing the variational principle and the orthonormality constraint, a system of differential linear equations can be derived, written in matrix form as

$$\mathbf{FC} = \mathbf{SC}\varepsilon \tag{5}$$

The Hartee-Fock equations are defined for the i-th one-electron molecular orbital as $\hat{\mathbf{f}}\boldsymbol{\phi}_\mathrm{i} = \epsilon_\mathrm{i}\boldsymbol{\phi}_\mathrm{i},\ \mathrm{i} = 1, \dots, \mathrm{N}$, for N molecular orbitals $\boldsymbol{\phi}_\mathrm{i}$ and orbital energies ϵ_i, with the one-electron Fock operator as elements of the Fock matrix $\mathbf{F}$,

$$\hat{\mathbf{f}} = -\frac{1}{2}\boldsymbol{\nabla}_\mathrm{i}^2 - \sum_\mathrm{A} \frac{\mathrm{Z_A}}{\mathbf{r_{iA}}} + \mathrm{V_{HF}}(\mathrm{i}). \tag{6}$$

The terms are the kinetic energy and the potential energy due to nuclear attraction for the i-th electron, with $\mathrm{V_{HF}}$ the Hartee-Fock potential or the average repulsion potential due to interaction with the rest of the $(\mathrm{N} - 1)$ electrons. The Hartree-Fock potential can be expressed as

$$\mathrm{V_{HF}}(\mathbf{x_1}) = \sum_\mathrm{j}^\mathrm{N}(\hat{\mathbf{J}}_\mathbf{j}(\mathbf{x_1}) - \widehat{\mathbf{K}}_\mathrm{j}(\mathbf{x_1})), \tag{7}$$

with $\hat{\mathbf{J}}$ and $\widehat{\mathbf{K}}$ the Coulomb and the exchange operator, respectively. They are also referred to as two-electron integrals, since they represent the interaction between two electrons and are expressed as integrals over the respective orbitals.

$$\mathbf{J}_\mathrm{ij} = \int\int \boldsymbol{\phi}_\mathrm{i}\,(\mathbf{x_1})\,\boldsymbol{\phi}_\mathrm{i}^*(\mathbf{x_1})\frac{1}{\mathbf{r}_{12}}\boldsymbol{\phi}_\mathrm{j}^*(\mathbf{x_2})\boldsymbol{\phi}_\mathrm{j}(\mathbf{x_2})\mathrm{d}\mathbf{x_1}\mathrm{d}\mathbf{x_2} \tag{8}$$

$$\mathbf{K}_\mathrm{ij} = \int\int \boldsymbol{\phi}_\mathrm{i}\,(\mathbf{x_1})\,\boldsymbol{\phi}_\mathrm{j}^*(\mathbf{x_1})\frac{1}{\mathbf{r}_{12}}\boldsymbol{\phi}_\mathrm{i}(\mathbf{x_2})\boldsymbol{\phi}_\mathrm{j}^*(\mathbf{x_2})\mathrm{d}\mathbf{x_1}\mathrm{d}\mathbf{x_2}$$

The Coulomb integral $\mathbf{J}_\mathrm{ij}$ represents the average repulsion potential experienced by the i-th electron at position $\mathbf{x}_1$ due to interaction with the charge distributions of the remaining $(\mathrm{N} - 1)$ electrons in spin orbitals $\boldsymbol{\phi}_\mathrm{j}$. The exchange integral $\mathbf{K}_\mathrm{ij}$ has no classical counterpart and is related to spin, a quantum mechanical property.

Further terms in the Hartree-Fock equation, Equation 5, are the coefficient matrix $\mathbf{C}$, containing the orbital expansion coefficients $\mathrm{c}_{\alpha\mathrm{i}}$, the overlap matrix $\mathbf{S}$, containing the overlap elements over the basis functions,

$$\mathrm{S}_{\mu\nu} = \int \boldsymbol{\chi}_\mu(\mathbf{r})\,\boldsymbol{\chi}_\nu(\mathbf{r})\,\mathrm{d}\mathbf{r}, \tag{9}$$

and the diagonal matrix $\boldsymbol{\varepsilon}$ containing the single-electron orbital energies. Since the Fock operator depends on the wavefunctions of all the electrons due to the $\mathrm{V_{HF}}$ term, the Hartree-Fock equation is solved self-consistently with the initial guess for the expansion coefficients in form of the coefficient matrix $\mathbf{C}$. The Fock matrix $\mathbf{F}$ is then calculated and diagonalized which is the most computationally consuming step since it involves the calculation of two-electron integrals. Since these are integrated over four basis functions, the computational demand increases as the number of basis functions to the fourth power $\sim \mathrm{N}^4$. After diagonalization of the Fock matrix, the new coefficients are used to update the density matrix until convergence of quantities such as the total energy or the density matrix elements themselves is achieved.

The convergence criteria that were used throughout this work were $10^{-6}\,\mathrm{Hartree}$ or $2.6 \cdot 10^{-3}\,\mathrm{kJ\,mol^{-1}}$ for the total energy and 10^{-8} for the root-mean-square value of density matrix elements, as implemented in the Gaussian03 [46].

A downside of the Hartree-Fock method is that it is a mean-field approach regarding the treatment of electron-electron interactions. A single electron is represented as interacting with the smeared out distribution of all other electrons and electron correlation is not accounted for: electrons are correlated in motion and move in a more correlated fashion at smaller distances due to strong Coulombic repulsion, than at larger distances. Also, a single Slater determinant is used to describe the electronic distribution. In cases of bond breaking and forming this representation is inaccurate, as there are other electronically excited configurations contributing to these molecular states. There are therefore many chemical phenomena that are poorly described by Hartree-Fock approach. In the case of azobenzene isomerization a general finding is that the electronic energies are overestimated by the Hartree-Fock method, compared to the energies calculated with density functional theory which treats the correlation effects more accurately. The correlation energy generally accounts for $\sim 1\%$ of the total electronic energy, comparable to typical binding energies [47].

In practice, any type of function centered at a nucleus can be used as a basis function. Exponential functions of the form $\chi \sim \exp(-\alpha r)$ would be the most convenient as they represent the exact solution of the electronic Schrödinger equation for the hydrogen and, generally, one-electron atoms. In practice, one uses functions computationally easier to handle, especially since the calculations include many integrals over two or four basis functions. Gaussian functions of the form $\chi \sim \exp(-\alpha r^2)$ are easily integrated and still represent a good description for the underlying physics. A number of primitive Gaussian functions are used to represent a single orbital, while for split-valence basis set more of the basis functions are used to build valence orbitals which are more important for molecular bonding than the core orbitals.

In this work, we used the Pople's 6-31G* basis set with polarization functions added to heavy atoms, that is all except hydrogen and helium, represented in notation by an asterisk. It is a split valence set insofar different basis functions are used to build core and valence orbitals. The core orbitals are comprised from 6 primitive Gaussians, while the valence orbitals from two basis functions, each formed as a linear combination of 3 primitive Gaussian functions that is as a single primitive Gaussian.

2.1.1 Density Functional Theory

Density Functional Theory is a widely used method in electronic structure calculation and is considered an improvement of the Hartree-Fock approach because of a more accurate treatment of the electron correlation effects [48]. It can be proved that the ground state energy $E_0\,[\rho(\mathbf{r})]$ is completely determined by the electronic density $\rho(\mathbf{r})$ which in turn is dependent only on three spatial coordinates. The exact ground state energy can be expressed in a usual manner as a sum of contributions, namely the electron kinetic energy, the electron-nucleus attraction energy, the electron-electron repulsion energy and the exchange-correlation energy,

$$\mathrm{E}\,[\rho] = \mathrm{E_K} + \mathrm{E_{ne}} + \mathrm{E_{ee}} + \mathrm{E_{XC}}\,[\rho]. \tag{10}$$

The total energy can thus be expressed as a function of the electronic density, which consecutively can be expressed as an integral over the squared wavefunction,

$$\rho(\mathbf{r}) = \sum_{\mathrm{i}} |\boldsymbol{\phi}_{\mathrm{i}}(\mathbf{r})|^2. \tag{11}$$

Constructing the electronic density out of the molecular orbitals is useful for the accurate description of the kinetic energy and makes this wave-function based approach, called the Kohn-Sham approach, computationally very similar to the Hartree-Fock approach. The associated Kohn-Sham orbitals are not physical orbitals insofar they represent the exact molecular orbitals for the system of non-interacting electrons. By applying the variational principle to the electron energy and using the constraint $\int \rho(\mathbf{r})\mathrm{d}\mathbf{r} = \mathrm{N}$, where N is the total number of electrons, the total energy can be expressed as

$$\mathrm{E}\,[\rho] = -\frac{1}{2}\sum_{\mathrm{i}} \int \boldsymbol{\phi}_{\mathrm{i}}(\mathbf{r})\nabla_{\mathrm{i}}^2\boldsymbol{\phi}_{\mathrm{i}}(\mathbf{r})\,\mathrm{d}\mathbf{r} - \sum_{\mathrm{i}}\int\sum_{\mathrm{A}}\frac{\mathrm{Z_A}}{\mathbf{r}_{1\mathrm{A}}}|\boldsymbol{\phi}_{\mathrm{i}}(\mathbf{r_1})|^2\,\mathrm{d}\mathbf{r_1} + \\ \frac{1}{2}\sum_{\mathrm{i}}\sum_{\mathrm{j}}\int |\boldsymbol{\phi}_{\mathrm{i}}(\mathbf{r_1})|^2\frac{1}{\mathbf{r}_{12}}|\boldsymbol{\phi}_{\mathrm{i}}(\mathbf{r_2})|^2\,\mathrm{d}\mathbf{r_1}\mathrm{d}\mathbf{r_2} + \mathrm{E_{XC}}\,[\rho], \tag{12}$$

with the terms arranged in the same order as in Equation 10. Electronic and nuclear Coulomb interaction terms are given as integrals over squared orbitals that run over i, j electrons that is A nuclei, as this is equivalent to integrating the electronic density.

The functional form for the dependence of the exchange-correlation energy $\mathrm{E_{XC}}\,[\rho]$ on the electronic density defines the DFT method at hand. Within the local density approximation (LDA) which is the simplest approximation, it is assumed that the density is uniform. The exchange-correlation energy can be expressed as

$$\mathrm{E_{XC}}\,[\rho] = \int \rho\,(\mathbf{r})\,\mathrm{E_{XC}}\,[\rho(\mathbf{r})]\,\mathrm{d}\mathbf{r}, \tag{13}$$

where $\mathrm{E_{XC}}\,[\rho(\mathbf{r})]$ is the exchange-correlation energy per particle of an uniform electron gas, weighted by the probability to find an electron at this position, the density $\rho(\mathbf{r})$.

Further improvements of the LDA is to include the energy dependence on the electronic density gradients $\nabla\rho\,(\mathbf{r})$ as well. This generalized gradient approximation (GGA) describes the non-homogeneity of the actual electronic distribution more accurately. The exchange-correlation energy is expressed as a function of α- and β- spin densities, ρ_α and ρ_β respectively with the total density given by the sum $\rho = \rho_\alpha + \rho_\beta$, as

$$\mathrm{E_{XC}^{GGA}}[\rho_\alpha, \rho_\beta] = \int \mathrm{f}\left(\rho_\alpha, \rho_\beta, \nabla\rho_\alpha, \nabla\rho_\beta\right)\mathrm{d}\mathbf{r}. \tag{14}$$

The so-called hybrid functionals are constructed as a linear combination of the Hartree-Fock exchange $\mathrm{E_X^{KS}}$, defined through two-electron exchange integrals over the exact Kohn-Sham wavefunction, and an additional appropriate form for the exchange-correlation functional $\mathrm{E_{XC}^{GGA}}$

$$\mathrm{E_{XC}^{hyb}} = \lambda\mathrm{E_X^{KS}} + (1-\lambda)\mathrm{E_{XC}^{GGA}}, \tag{15}$$

with λ the fitting parameter. The use of the generalized gradient and hybrid approximations greatly reduces the LDA error though these methods are still inadequate in describing highly correlated systems where density is not a slowly varying function.

An example of very successful hybrid functional is B3LYP which uses the Becke three-parameter hybrid functional [49] and additional non-local correlation functionals (LYP and VWN III), and is the usual method of choice in studies of azobenzene isomerization [4]. Another noteworthy functional is the pure PBE functional of Perdwe, Burke and Ernzerhof [50], made into a hybrid functional [51] which uses 25 % exact exchange and 75 % density functional exchange.

As part of the benchmarking for various level of quantum theory in this work we used the hybrid B3LYP and PBE functionals, in order to compare the result of various semi-empirical methods that will be introduced later in Methods Section 2.1.2.

The Kohn-Sham approach to the density functional theory just described can also be expressed in the linear combination of atomic orbitals (LCAO) formalism. The Kohn-Sham orbitals are expanded as the sum of basis functions as in Equation 4 and one can write in the matrix notation

$$\mathbf{F}^{\mathbf{KS}}\mathbf{C} = \mathbf{SC}\varepsilon. \tag{16}$$

This is equivalent to the Hartree-Focks Equation 5, except for the Fock matrix elements where the Kohn-Sham one-electron Fock operators $\hat{\mathrm{f}}^{\mathrm{KS}}$ for the i-th electron are expressed as

$$\hat{\mathbf{f}}^{\mathrm{KS}} = -\frac{1}{2}\boldsymbol{\nabla}^2 + [\sum_{\mathrm{j}} \int \frac{\left|\boldsymbol{\phi}_{\mathrm{j}}(\mathbf{r}_2)\right|^2}{\mathbf{r}_{12}} \mathrm{d}\mathbf{r}_2 + \mathrm{V}_{\mathrm{XC}}(\mathbf{r}_1) - \sum_{\mathrm{A}} \frac{\mathrm{Z}_{\mathrm{A}}}{\mathbf{r}_{1\mathrm{A}}}], \tag{17}$$

contain the exchange-correlation potential operator V_{XC} along with the usual kinetic energy, Coulomb electron repulsion and nuclear attraction terms. The exchange-correlation potential operator is defined as the derivative of the exchange-correlation energy with respect to the electronic density $\mathrm{V}_{\mathrm{XC}}\,[\rho] = \delta\mathrm{E}_{\mathrm{XC}}\,[\rho]\,/\,\delta\rho$. The functional form for the exchange-correlation energy varies among the DFT methods used as defined in Equations 13, 14, 15.

2.1.2 Semi-empirical methods: DFTB, DFTB3

The computational demand of approximate quantum methods in general is reduced by neglecting all three- and four- centre two-electron integrals of the form of Equation 8. This is a consequence of the zero differential overlap (ZDO) approximation under which the integrals involving same electron coordinates centered on different atoms are ignored [44]. Furthermore, only valence electrons are considered for the electronic parameters calculation and a minimal basis set of Slater type in the form of exponential functions is usually used. The minimal basis set is a set that accommodates the electrons in a neutral atom, $\mathrm{s} -$ and $\mathrm{p} -$ orbitals for atoms in third and fourth row of the periodic table.

To compensate for these approximations, parameters are introduced which in the case of DFTB are obtained from DFT calculations. DFTB is computationally comparable to other semi-empirical methods, for example PM3 [52], and 100-1000 faster than the HF or DFT ab-initio methods [53].

Density functional tight binding (DFTB) is an approximate method based on the expansion of the total Kohn-Sham energy with respect to the charge density fluctuations up to the second order [54] or up to the third order [55]. The extended self-consistent charge methodology increases the accuracy of the method, which is comparable to the generalized-gradient DFT in case of molecular geometries, but is less accurate for reaction energies and vibrational frequencies [53]. The reference charge density ρ_0 is calculated as a superposition of neutral atomic charge densities, ρ_a^0. The total energy expanded up to the second $E^{SCC-DFTB}$ that is the third order $E^{SCC-DFTB3}$ around the reference electronic density, can be written as a sum of contributions

$$E^{SCC-DFTB} = E^{HO} + E^{\gamma} + E^{rep}, \tag{18}$$

$$E^{SCC-DFTB} = E^{HO} + E^{\gamma} + E^{\Gamma} + E^{rep}.$$

The energy contribution from an atomic orbital Hamiltonian depending only on the reference density, E^{HO}, $E^{HO} = \sum_{a,b} \sum_{\mu \in a} \sum_{\nu \in b} n_i c_{\mu i} c_{\nu i} H_{\mu\nu}^0$, with n_i the occupation number of the i-th molecular orbital and $H_{\mu\nu}^0$ the Hamilton matrix with precomputed and tabulated matrix elements. The repulsive energy contribution E^{rep} approximated as short-ranged two-center potentials V_{ab}^{rep} dependent on the reference densities ρ_a^0, ρ_b^0 and the distances r_{ab} for atom-pairs a and b, $E^{rep} = 1/2 \sum_{ab} V_{ab}^{rep}[\rho_a^0, \rho_b^0, r_{ab}]$. The energy contribution from the second order expansion term $E^{\gamma} = 1/2 \sum_{ab} \Delta q_a \Delta q_b \gamma_{ab}$ with Δq_a the atomic partial charge for atom a, or $\Delta q_a = q_a - q_a^0$ and γ_{ab} the integral over a product of two normalized Slater-type spherical charge densities. It describes the Coulomb interaction between the two partial charges $\Delta q_a, \Delta q_a$ and reduces to $1/r_{ab}$ for large distances. For a $=$ b, it describes the self-repulsion and equals the Hubbard parameter U_a or the chemical hardness, $\gamma_{aa} = U_a$, affecting the electron-electron interaction within one atom and the size of atoms when estimating the two-center terms γ_{ab}. The third order energy contribution can be approximated with $E^{\Gamma} = \frac{1}{3} \sum_{ab} \Delta q_a^2 \Delta q_b \Gamma_{ab}$, where $\Gamma_{ab}, \Gamma_{ba}, \Gamma_{aa}$ are functions reflecting the dependence of the γ function with respect to charge, $\delta\gamma/\delta q$, and implies the change of the chemical hardness or the Hubbard parameter with charge. This introduces the desired chemical behaviour for the charged system.

The DFT functionals used were PBE for the calculation of one-center Hamiltonian matrix elements and hybrid functional B3LYP when fitting the two-centre repulsive potential V_{ab}^{rep}. The actual parameters organized into the so called Slater-Koster files [57], were thus the on-site Kohn-sham eigenenergies for the angular momenta d, p and s for a given atom, the Hubbard values for the given angular momenta and the occupation numbers in the ground state. The precomputed integral table contains the DFTB(3) Hamiltonian and the overlap matrix elements for the two-center interactions between the atomic orbitals. The two-center repulsive energy parameters are given in the form of the polynomial coefficients c_i and the cut-off radius r_{cut} of the repulsive interaction, where the repulsive polynomial is calculated as, $\sum_{i=2}^{8} c_i (r_{cut} - r)^i$.

In geometry optimization of the cis and trans stable states and the transition state optimization the method used was DFTBA as implemented in Gaussian 03 [46], a version that uses analytic expressions for the matrix elements, instead of the tabulated ones developed originally by Elstner et al. [55,56]. For the dynamical simulations we used the DFTB3 method and the 3OB parameter set, as implemented in Gromacs package 5.0 [58, 59].

2.1.3 Semi-empirical methods: Parametric Method number 3, PM3

Parametric Method number 3 (PM3) is a parametrization of the neglect of diatomic overlap approximation (NNDO) method, in which all three- and four-centered two-electron integrals are neglected and the overlap matrix $\mathbf{S}$ is reduced to a unit matrix [44, 52]. This markedly reduces the quality of the wavefunction which makes it necessary to include the rest of the integrals in form of parameters and assign their values based on experimental data or calculate them from the atomic orbitals for which the minimal sp basis set is used. Only valence electrons are assigned to the Slater-type exponential basis functions, while the core electrons are included through the reduction of nuclear charges and the modification of the core-core repulsion. The specific functional form for PM3 is modified by additional Gaussian functions the number of which varies between atoms. PM3 is a parametrization of the more general NNDO method and in terms of only atomic variables that is in reference to the single atoms only. The one electron one center integrals correspond to the energy of a single electron due to nuclear charge and the charges of the rest of the nuclei. The two-center two-electron integrals within an sp- basis correspond to the G-type parameters or Coulomb integrals and H parameter or the exchange integral for different types of orbitals, s and p, and there are 5 of them, $\mathrm{G_{ss,}G_{sp,}H_{sp,}G_{pp,}G_{p2}}$. For example, the $\mathrm{G_{p2}}$ integral involves two different types of p functions, $\mathrm{p_x, p_y}$ or $\mathrm{p_z}$.

For the PM3 method, an automatized optimization technique was derived for these two-electron parameters as well as all the repulsion potential parameters with a significantly larger training set of experimental data in form of the atomic spectra used [52]. The known drawbacks of the PM3 methods are the reduction of rotational energy barriers around bonds with double bond character, as well as “incorrect” charges for nitrogen atoms and wrong geometries predicted for $_2$HN=NH$_2$ compound, all relevant to the azobenzene molecules treated within this study. Also, the weak non-bonded interactions are poorly predicted including van der Waals interactions and hydrogen bonds.

2.1.4 Solvent Treatment: Polarizable Continuum Model (PCM)

The Polarizable Continuum Model (PCM) is a reaction-field solvation model where the solvent is treated as a uniform polarizable continuum with a dielectric constant ε and the solute is placed in the hole in the medium [60, 61, 62]. With the solute described on a quantum level, the associated wavefunction is polarized by the electric medium but the calculated electric moments also induce charges back to the medium, which then influences the wavefunction again changing the electric moments. This back-polarization of the quantum system by the medium has to be calculated in a self-consistent way, the so called Self-consistent Reaction Field (SCRF). The stabilizing solvation free energy $\Delta\mathrm{G_{elec}}(\mu)$ due to the interaction of the molecular dipole μ with the reaction field can be expressed as

$$\Delta\mathrm{G_{elec}}(\mu) = -\frac{\varepsilon - 1}{2\varepsilon + 1}\frac{\mu^2}{\mathrm{a}^3}\left[1 - \frac{\varepsilon - 1}{2\varepsilon + 1}\frac{2\alpha}{\mathrm{a}^3}\right]^{-1} \tag{19}$$

with a the radius of the cavity and the back-polarization by the medium described with the molecular polarizability α, the first order change of the dipole moment in an electric field. Another contribution to the free energy of solvation is the one arising due to the short-range solute-solvent interactions and is proportional to the solvent accessible surface area (SASA). This area is calculated as the area of the surface obtained by rolling a sphere of a given radius representing the solvent, over the van der Waals molecular surface. Within the PCM model the solute cavity is constructed from the overlaid van der Waals radii of the constituting atoms. That is, the solute cavity is formed from interlocking spheres centered on nuclei and their surfaces subsequently smoothed out following the GEPOL procedure [63]. Furthermore, the molecular shaped surface is divided into smaller surface elements, the so-called tesserae or tiles, over which the surface charges and associated potentials are numerically integrated and included in the molecular Hamiltonian. At the Hartree-Fock level of theory, the additional solute-solvent interaction potential enters the Hamiltonian, with the Fock operator $\hat{\mathrm{f}}$ in the Equation 6 and the PCM corrected Fock matrix elements with the term proportional to the dipole moment $\boldsymbol{\mu}$ of the form

$$\mathrm{F}_{\mu\nu} = \int \boldsymbol{\chi}_{\mu} \hat{\mathrm{f}}\, \boldsymbol{\chi}_{\nu}^{*}\, \mathrm{d}\boldsymbol{\tau} - \mathrm{g}\boldsymbol{\mu} \int \boldsymbol{\chi}_{\mu} \mathbf{r}\, \boldsymbol{\chi}_{\nu}^{*}\, \mathrm{d}\boldsymbol{\tau}\,. \tag{20}$$

Here, g is the proportionality constant $\mathrm{g} = 2(\varepsilon - 1)/(2\varepsilon + 1)\mathrm{a}^3$ and $\mathbf{r}$ is the dipole moment operator or simply the position vector, with $\int \dots \mathrm{d}\boldsymbol{\tau}$ representing integration over the whole volume. What is treated by reaction field models in general are only the long range polarization effects which lead to screening of charge interactions. To include the short-range effects such as specific hydrogen- or van der Waals binding, or solvent-solute dynamics and hydrophobic entropy effects an explicit description for the solvent molecules and direct sampling of the phase space are necessary.

The classical quantum optimization used for benchmarking and presented in the Results Section 3.1, the stationary points on the potential energy surface, the stable cis, trans states and the transition structures for azobenzene(s) were calculated using the PCM field to represent solvents. The DMSO solvent was represented with the dielectric constants $\varepsilon = 46.7$ and the solvent radius of 2.82 Å, while the toluene solvent with the dielectric constant $\varepsilon = 2.38$ and the solvent radius 2.46 Å. The Simple United Atom Topological Model (UA0) for the atomic radii and the construction of the cavity was employed with the tesserae of the average area of 0.2 Å^2, the default for the SCRF=PCM option in Gaussian 03.

2.2 Transition State Theory

Within the semi-classical transition state theory framework a chemical reaction can be viewed as nuclei moving on a potential energy surface (PES) between the minima which represent the stable states [44]. Since under the Born-Oppenheimer approximation the nuclear and electronic motions are separated, the potential energy itself is the actual electronic energy calculated for different set of molecular coordinates $\mathbf{R}$ that is for different molecular geometries, as defined with the electronic Schrödinger equation in Equation 2. The reaction thus proceeds from reactants through a transition state to products over a potential energy barrier. This multidimensional problem is depicted schematically in Figure 3, where the reaction coordinate represents the direction along which the energy reaches its maximum and the transition state (TS) a configuration at which the energy is maximal in the direction of the reaction coordinate.

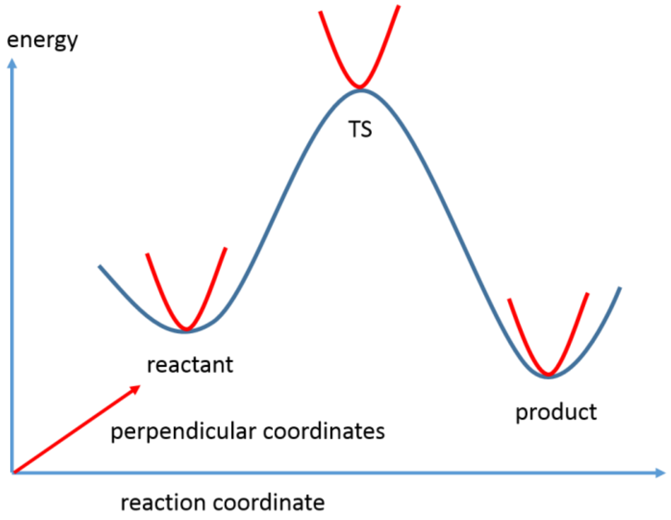

Figure 3. Scheme: Transition state theory. The energy profile for the path on the multidimensional surface. The transition state (TS) is a first order saddle point, minimum in all perpendicular directions, but a maximum in the direction of the reaction coordinate.

In what follows, the mathematical approach of locating the stable states and transition structures is described and the original Eyring theory [64] represented by the scheme in Figure 3 is introduced.

2.2.1 Optimization – Stable states and Transition Structures

In mathematical terms, the problem of locating the reactant, product and transition states can be set up as the optimization of the underlying potential energy surface (PES). The minima represent the stable states and the first order saddle points via which the stable states are connected represent the transition structures. Given the energy as the function of nuclear coordinates $\mathrm{E_e}(\mathbf{R})$ the aim is to perform steps given by the energy gradients until a minimum or a first order saddle point is reached. In the Newton-Rhapson (NR) method the gradient or the first derivative of the energy function with respect to all variables, a vector $\mathbf{g} = \delta \mathrm{E_e}(\mathbf{R})/\delta \mathbf{R}$**,** and the Hessian matrix with elements the second derivative of the energy function, $\mathbf{H}_{\mathrm{ij}} = \delta^2 \mathrm{E_e}/\delta \mathbf{R}_\mathrm{i} \delta \mathbf{R}_\mathrm{j}$ are used. In matrix form the step can be written

$$(\mathbf{R} - \mathbf{R}_0) = -\mathbf{H}^{-1}\mathbf{g}. \qquad (21)$$

After the diagonalization of the Hessian matrix, a linearly transformed coordinate system contains eigenvectors of the unitary transformation matrix $\mathbf{U}$ and the elements of $\mathbf{H}$ matrix in the diagonal form (ε), the eigenvalues. The unitary transformation of the Hessian in the matrix form can be expressed as $\varepsilon = \mathbf{UHU}^{-1}$. This is a linear transformation since the eigenvectors are linear combinations of the original coordinates. The NR step in the new coordinate system $\mathbf{R}'$ can be expressed as $\Delta\mathbf{R}' = (\Delta\mathbf{R}'_1, \Delta\mathbf{R}'_2, \Delta\mathbf{R}'_2, \dots, \Delta\mathbf{R}'_\mathrm{N})^\mathrm{T}$ for N nuclear coordinates. The i-th step defined as the negative projection of the gradient along the i-th eigenvector $\mathbf{f}_\mathrm{i}$ scaled by its associated eigenvalue ε_i is

$$\Delta\mathbf{R}'_\mathrm{i} = -\frac{\mathbf{f}_\mathrm{i}}{\varepsilon_\mathrm{i}}. \tag{22}$$

All Hessian eigenvalues are positive near a minimum and the step direction is opposite the gradient which moves the system in the right direction decreasing the energy function value. Both the step size and the step direction can be controlled. In case of stepping down the gradient or towards the minima, the denominator should be positive which can be ensured by introducing the shift parameter λ and setting it to the lowest Hessian eigenvalue $\Delta\mathbf{R}'_\mathrm{i} = -\mathbf{f}_\mathrm{i} / (\varepsilon_\mathrm{i} - \lambda)$. This ensures that the stepping is down the gradient even when not all Hessian eigenvalues are positive.

One of the methods often used, in fact set as default in Gaussian 03, is the Eigenvector Following in which the step is effectively directed to lie along one of the eigenvectors by evaluating the suitable shift parameter λ [65]. The optimization is performed in internal coordinates constituted from a set of bond lengths, angles and dihedral angles which makes the interpretation of resulting geometries more straightforward compared to their representation in Cartesian coordinates for the nuclei. Instead of $3\mathrm{N}_\mathrm{atom}$ Cartesian coordinates, the molecule is represented with $\mathrm{N}_\mathrm{atom} - 1$ distances, $\mathrm{N}_\mathrm{atom} - 2$ angles and $\mathrm{N}_\mathrm{atom} - 3$ dihedrals, making in total $3\mathrm{N}_\mathrm{atom} - 6$ internal variables, collected in the so called Z matrix representation.

The transition structure optimization entails locating the first order saddle points, which for a multidimensional energy surface are minimum in all directions, the eigenvectors, except for in one eigenvector for which they reach a maximum, as schematically depicted in Figure 3. A stable state is a minimum in all directions and has all Hessian eigenvalues positive. In case of a transition structure which is a first-order saddle point, the Hessian has a single negative eigenvalue with the associated eigenvector representing the “internal reaction coordinate”. The reaction coordinate is thus simply expressed as a linear combination of the Cartesian coordinates.

The local methods for locating the transition structure depend strongly on the initial geometries provided, which should be sufficiently close to the first order saddle point for the optimization NR algorithm to converge. This means that ideally, the Hessian matrix of the initial structure has a single negative eigenvalue with the associated TS eigenvector in the right direction. For the present case of azobenzene transition states, we had a good idea about the geometry of transition states from previous studies [4] which made the local method of augmented Hessian Newton-Rhapson approach appropriate.

For the optimization of stable states for the azobenzene(s) considered in this study we used the Berny algorithm that uses the forces on atoms and the Hessian matrix to move the system to energetically more favourable regions. Only the initial Hessian is explicitly calculated. The subsequent Hessians are approximated using the values for the energy change between optimization steps and the energy gradients. We used the local NR augmented Hessian method for the optimization of transition structures with the explicit calculation of the initial Hessian and the eigenvector following switched off. Since more than one negative eigenvalues sometimes appeared in the initial Hessian, the eigenvector following in the form of checking the eigenvalues was turned off not to enforce following the eigenvector with the most negative eigenvalue.

This corresponded the optimization settings opt = (ts, calcfc, noeigen) in the input file for Gaussian 03. The convergence criteria for the root-mean-square of the force on all atoms used was $0.0003\ \mathrm{Hartree/Bohr}$. Once the transition structure was located it had to be confirmed that it actually connects the two stable states. The Internal reaction coordinate following is performed by stepping along the transition eigenvector, which is the internal reaction coordinate, down the electronic energy gradient in both positive and negative directions. This steepest descent along the transition eigenvector is performed by taking steps of fixed size followed by a search for the minimum energy structure which is then the new point on the IRC path. We performed the IRC following with the step size $0.1\ \mathrm{Bohr} \equiv 0.053\ \mathrm{Å}$ in 40 steps for both forward and backward direction.

2.2.2 The Eyring Theory: Rate Constants

The transition state or the activated complex as defined by the Eyring theory is different from the transition structure, a single configuration associated to the first order saddle point on the underlying potential energy surface. The transition state(s) represent a set of configurations near the saddle point from which either of the stable states can be reached with an equal probability. The transition structure can be thought of as an ordinary molecule with one less vibrational degree of freedom, but with an additional fourth translational degree of freedom, along which it approaches the maximum of the barrier and crosses it [64, 66]. This ideal or the minimum energy reaction path is depicted as a cross-section along the reaction coordinate in Figure 3. The rate of crossing the barrier can be expressed as

$$\mathrm{k^{TST}} = \kappa \frac{\mathrm{k_B T}}{\mathrm{h}} \exp - \frac{\Delta \mathrm{G}^{\#}}{\mathrm{RT}}, \tag{23.a}$$

$$\Delta \mathrm{G}^{\#} = \Delta \mathrm{G^{TS}} - \Delta \mathrm{G^{reactant}}, \tag{23.b}$$

with the activation Gibbs free energy $\Delta \mathrm{G}^{\#}$as the difference in free energies of the transition state and the reactant state and $\mathrm{k_B}$ the Boltzmann constant. The transmission coefficient κ is a dynamical property that accounts for recrossings of the barrier and can be less than unity. As given by the original Eyring's derivation where classical statistical mechanics was used [54], the factor $\mathrm{k_B T/h}$ was the result of calculating the averaged velocity associated to the translational mode of transition or the reaction coordinate when passing the free energy barrier. The expression for the rate can be rewritten in terms of the equilibrium constant defined between the activated complex and the reactant state or the ratio of the associated partition functions $\mathrm{K}^* = \mathrm{q^{TS}/q^{reactant}}$ and the average velocity of passing the barrier $\sqrt{\mathrm{k_B T/2\pi m}}$,

$$\mathrm{k^{TST}} = \kappa\, \mathrm{K}^* \frac{\sqrt{2\pi \mathrm{m k_B T}}}{\mathrm{h}} \sqrt{\frac{\mathrm{k_B T}}{2\pi \mathrm{m}}} \tag{24}$$

$$\mathrm{k^{TST}} = \kappa\, \mathrm{K}^* \frac{\mathrm{k_B T}}{\mathrm{h}}$$

The $\sqrt{2\pi m k_B T}/h$ factor comes out as a result of integration of the classical translational partition functions over the phase space, $q_{classical} \sim \int\int \dots \int \exp -(\mathbf{H}(\mathbf{p},\mathbf{q})/k_B T) d\mathbf{p}\, d\mathbf{q}$. The classical energy Hamiltonian $\mathbf{H}(\mathbf{p},\mathbf{q})$ is expressed in terms of the configuration $\mathbf{q}$ and momenta $\mathbf{p}$ for the particles in the system. The partition functions for the other degrees of freedom, the vibrational, rotational and electronic are included in the equilibrium constant.

2.2.3 Statistical Mechanics and the Approximations. Thermochemistry.

The concept of the partition function was already briefly introduced in Section 2.2.1. The partition function q is a central quantity in statistical mechanics from which all properties can be calculated, similar to the wavefunction in quantum mechanics. In the discrete form it can be written as a sum over all quantum energy states E_i,

$$q = \sum_i \exp -\frac{E_i}{k_B T}. \tag{25}$$

In case of closely spaced energy levels the quantum effects can be neglected and the sum in the classical partition function replaced by an integral over the phase space, that is all coordinates $\mathbf{q}$ and momenta $\mathbf{p}$, $q_{classical} = \int\int \dots \int \exp -(\mathbf{H}(\mathbf{p},\mathbf{q})/k_B T) d\mathbf{p}\, d\mathbf{q}$, with $\mathbf{H}(\mathbf{p},\mathbf{q})$ the classical Hamiltonian. The partition function represents the sum of the probability weights of all energy states and can be thought of as a normalization factor of the Boltzmann distribution, where a probability of a microstate with the energy E_i is expressed as $P(E_i) = q^{-1} \exp -(E_i/k_B T)$.

The total molecular partition function sums all states in a molecule $q_{tot} = q_{trans} q_{rot} q_{vib} q_{elec}$, and can be written as a product of partition functions for individual contributions, that is the translational, rotational, vibrational and electronic degrees of freedom for a molecule. This is equivalent to expressing the total energy as a sum of said contributions, $E_{tot} = E_{trans} + E_{rot} + E_{vib} + E_{elec}$, due to the logarithmic relationship, $E \sim \ln q$. The individual partition functions are evaluated by summing over all quantum states as in Equation 25 with the appropriate expression for the energy of a quantum state, E_i. For that certain approximations are enforced [67]; the translational energy is derived from the "particle-in-a-box" model, the rotational energy by treating the molecule as a rigid rotor and vibrational energy for the harmonic oscillator of decoupled normal modes. The electronic partition function is just the sum over all electronic quantum states, where the energies are given as the solution to the electronic Schrödinger equation, given in the Equation 2.

The total molecular partition function q_{tot} is defined for a single molecule, whereas all the thermodynamic properties are defined for an ensemble or a large number of molecules. Since they are identical particles and indistinguishable, the ensemble partition function Q can be written as a product of N molecular partition functions, $Q = q_{tot}^N/N!$, corrected by $N!$ for over-counting the states. It is important to note that the molecular ensemble here is treated as an ideal gas, a set of non-interacting particles.

The ensemble partition function is valuable because all other thermodynamic functions, such as the internal energy U, enthalpy H, entropy S and Gibbs free energy G, can be calculated from it. The central result is the logarithmic dependence of the internal energy U and the Helmholtz free energy A, at constant volume V, on the ensemble partition function Q

$$U = k_B T^2 \left(\frac{\partial \ln Q}{\partial T}\right)_V ; \; A = -k_B T \ln Q \tag{26}$$

Through the use of thermodynamic relations the enthalpic and entropic contributions to the free energy can be expressed as functions of the ensemble partition function as well, with p the pressure and V the volume.

$$H = U + pV, \; TS = U - A, G = H - TS. \tag{27}$$

The calculation of the activation free energy $\Delta G^{\#}$ or the difference in free energies of the transition structure and the reactant cis state in Gaussian 03 is implemented in the following way. After the optimized structures are obtained for the reactant cis and the transition state, the associated Gibbs free energies G^{state} are evaluated as the sum

$$G^{state} = E_{el} + E_{ZPE} + \Delta E_{vib}(T) + 4RT - TS. \tag{28}$$

Here, E_{el} is the electronic energy of the optimized structure, $E_{ZPE} + \Delta E_{vib}(T)$ is the vibrational contribution to the internal energy with the zero-point energy E_{ZPE} included. The rotational and translational contributions are included following the equipartition theorem as $U_{rot} = U_{trans} = (3/2)RT$ and the $pV = RT$ factor for the ideal gas as well. Entropy is calculated using the ensemble partition function and the derivation described above as

$$S = R \left(\ln(q_{trans} q_{rot} q_{vib} q_{elec}) + T \left(\frac{\partial \ln Q}{\partial T}\right)_V \right). \tag{29}$$

The weak temperature dependence of entropy is neglected, $S = S\,(T_0)$ with T_0 the reference temperature. In our case the reference temperature used was $T_0 = 298.15$ K. The main contribution to the entropy is the vibrational contribution defined with the vibrational partition function q_{vib} written as the product over $3N - 6$ vibrational partition functions for the normal modes of the stable states, or $3N - 7$ normal modes of the transition structure

$$q_{vib} = \prod_{i=1}^{3N-6(7)} \frac{e^{-h\nu_i/2k_BT}}{1 - e^{-h\nu_i/2k_BT}} \tag{30}$$

or $3N - 7$ normal modes of the transition structure because the transition mode is treated as a translational mode and not accounted for in the sum. The difference in Gibbs free energies for the transition state and the cis reactant state gives the Gibbs activation energy $\Delta G^{\#} = G^{TS} - G^{reactant}$.

One can also calculate the heat capacity at constant volume as $C_V = (\partial U / \partial T)_V$ with the temperature dependence also neglected $C_V = C_V(T_0)$. The thermal contribution to the internal energy, the $\Delta E_{vib}(T)$ term, can then simply be evaluated as $U(T) = U(0) + C_V(T_0)T$, with $U(0) = E_{el} + E_{ZPE}$ the energy at $T = 0$.

2.3 Ab-initio Stochastic/Molecular Dynamics

In molecular dynamics simulations the initial configurations and momenta of atoms are propagated in time by solving the Newton equations of motions. Written in differential form for the i-th nucleus with mass $\mathrm{m_I}$ at position $\mathbf{R}_\mathrm{I}$ and V the potential energy,

$$-\frac{\mathrm{dV}}{\mathrm{d}\mathbf{R}_\mathrm{I}} = \mathrm{m_I}\frac{\mathrm{d}^2\mathbf{R}_\mathrm{I}}{\mathrm{dt}^2}, \tag{31}$$

it is numerically integrated for a finite number of time steps $\Delta\mathrm{t}$. The common leap-frog integrator updates the positions and velocities using the forces as the potential energy gradients, $\mathbf{F} = -\,\mathrm{dV}/\mathrm{d}\mathbf{R}_\mathrm{I}$, according to these relations [68]:

$$\mathbf{v}\left(\mathrm{t}+\frac{1}{2}\Delta\mathrm{t}\right) = \mathbf{v}\left(\mathrm{t}-\frac{1}{2}\Delta\mathrm{t}\right) + \frac{\Delta\mathrm{t}}{\mathrm{m}}\mathbf{F}(\mathrm{t}) \tag{32}$$

$$\mathbf{R}(\mathrm{t}+\Delta\mathrm{t}) = \mathbf{R}(\mathrm{t}) + \Delta\mathrm{t}\,\mathbf{v}(\mathrm{t}+\frac{1}{2}\Delta\mathrm{t})$$

In general, the objective of molecular dynamics is to evaluate a thermodynamic observable dependent on both position and momenta, $\mathrm{O}\,(\mathbf{R},\mathbf{p})$ as an average over a long time trajectory, the temporal average

$$\langle\mathrm{O}\rangle = \lim_{\mathrm{T}\to\infty}\frac{1}{\mathrm{T}}\int \mathrm{O}(\mathbf{R}(\mathrm{t}),\mathbf{p}(\mathrm{t})\,\mathrm{dt}. \tag{33}$$

The ergodicity principle states that in the case of sufficient sampling the temporal average approaches the ensemble average, calculated as the expectation value over the Boltzmann distribution with the associated operator for the observable $\mathrm{O}(\mathbf{R},\mathbf{p})$

$$\langle\mathrm{O}\rangle = \frac{\int \mathrm{O}(\mathbf{R},\mathbf{p})\exp-\frac{\mathrm{E}(\mathbf{R},\mathbf{p})}{\mathrm{k_B T}}\mathrm{d}\mathbf{R}\mathrm{d}\mathbf{p}}{\int \exp-\frac{\mathrm{E}(\mathbf{R},\mathbf{p})}{\mathrm{k_B T}}\mathrm{d}\mathbf{R}\mathrm{d}\mathbf{p}}. \tag{34}$$

The energy function is written as the sum of the nuclear kinetic energy and the potential energy $\mathrm{E}(\mathbf{R},\mathbf{p}) = \sum_\mathrm{I}\mathbf{p}_\mathrm{i}^2/2\mathrm{m_I} + \mathrm{V}(\mathbf{R})$. If the system is described on the quantum level, the potential energy function is just the electronic energy $\mathrm{E_e}$, obtained by solving the electronic Schrödinger equation, as given in Equation 2. The forces are then evaluated “on-the-fly” as electronic energy gradients by electronic structure calculation at each time step [68, 69]

$$\mathbf{F}_\mathrm{I} = -\boldsymbol{\nabla}_{\mathbf{R}_\mathrm{I}}\mathrm{V}(\mathbf{R}) \tag{35}$$

by electronic structure calculation at each time step and subsequently used to propagate the positions of the nuclei for the next time step. The symbol nabla is a compact way of writing the derivative with respect to the three Cartesian coordinates for the I-th nucleus, as $\boldsymbol{\nabla}_{\mathbf{R}_\mathrm{I}} = \{\partial/\,\partial\mathbf{R}_{\mathrm{x,I}},\partial/\,\partial\mathbf{R}_{\mathrm{y,I}},\partial/\,\partial\mathbf{R}_{\mathrm{z,I}}\}$.

The effect of the solvent molecules representing the environment can be included by means of adding noise and friction to the Newton dynamics in form of an additional random force and friction force components. The stochastic dynamics is described by the Langevin equation

$$\mathrm{m_I}\frac{\mathrm{d}^2\mathbf{R}_\mathrm{I}}{\mathrm{dt}^2} = -\mathrm{m_I}\gamma_\mathrm{i}\frac{\mathrm{d}\mathbf{R}_\mathrm{I}}{\mathrm{dt}} + \mathbf{F}_\mathrm{I}(\mathrm{R}) + \mathbf{r}_\mathrm{I}^0. \tag{36}$$

The friction constant γ_i is the inverse relaxation time for the velocity autocorrelation function τ_frict, $\langle \mathrm{v}(0)\mathrm{v}(\mathrm{t})\rangle \sim \exp(-\mathrm{t}/\tau_\mathrm{frict})$, or the time in which the particle velocity is randomized and its memory lost. For very weak friction the relaxation time is large and Langevin dynamics can be used as a thermostat, as the canonical constant temperature NVT ensemble is naturally sampled with this description for the dynamics. The other terms are the force due to the underlying potential $\mathbf{F}_\mathrm{I}(\mathrm{R})$ and the random force with properties: its expectation value is zero, $\langle \mathbf{r}^0(\mathrm{t})\rangle = 0$ and its variance proportional to the friction constant $\langle \mathbf{r}^0(0)\, \mathbf{r}^0(\mathrm{t})\rangle = 2\mathrm{k_B}\mathrm{T}\gamma\delta(\mathrm{t})$.

In Gromacs, a stochastic integrator is implemented with random components added to the velocities and friction in an impulse fashion. First the velocity $\mathbf{v}'$ is updated without friction and noise as in Equation 31 for the regular molecular dynamics, and then the $\Delta\mathbf{v}$ factor added to obtain the full velocity at $\mathrm{t} + \Delta\mathrm{t}$ step,

$$\Delta\mathbf{v} = -\alpha\mathbf{v}'\left(\mathrm{t} + \tfrac{1}{2}\Delta\mathrm{t}\right) + \sqrt{\frac{\mathrm{k_B T}}{\mathrm{m}}(1-\alpha^2)}\,\mathbf{r}_\mathrm{i}^\mathrm{G};\ \alpha = 1 - \mathrm{e}^{-\gamma\Delta\mathrm{t}}. \tag{37}$$

The Gaussian distributed noise $\mathbf{r}_\mathrm{i}^\mathrm{G}$ has the mean $\mu = 0$ and the unit variance $\sigma = 1$. The position $\mathbf{R}(\mathrm{t} + \Delta\mathrm{t})$ is then updated with this randomized velocity, $\mathbf{v}\,(\mathrm{t} + 1/2\,\Delta\mathrm{t}) = \mathbf{v}' + \Delta\mathbf{v}$.

2.3.1 Hybrid QM/MM dynamics: Electronic embedding

The main objective when considering the effect of solvent on the isomerization mechanism or the nature of the transition state for azobenzene is having a good description for the solvent that goes beyond treating only the long-range polarization effects with the continuum solvent models, described in Section 2.1.4. The static effects arising due to the specific solvent-solute interactions can be accounted for only by including the solvent molecules explicitly. In addition, by explicitly sampling all solvent degrees of freedom the dynamical and the entropic solvent effects are also included. To achieve this improved treatment we use the QM/MM hybrid potential for the azobenzene/solvent system and molecular dynamics sampling.

Within the QM/MM framework [71, 72, 73], the system is partitioned into the quantum region for which the electron distribution is calculated, QM: azobenzene, and the classical molecular mechanics region described by a classical force field, MM: solvent, schematically depicted in Figure 4.

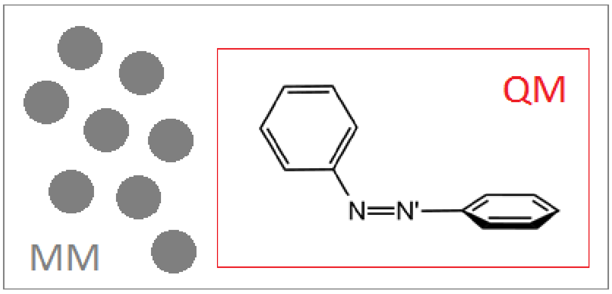

Figure 4. Partitioning of the azobenzene/solvent system within the QM/MM framework. Solvent molecules are treated on the MM level and are depicted as grey spheres. The azo-moiety depicted schematically in its perpendicular invertomer transition state is treated on a QM level of theory.

The total potential V_{tot} can be divided into three contributions, namely the quantum potential, V_{QM}, molecular mechanics potential, V_{MM}, and the interaction potential $V_{QM/MM}$

$$V_{tot} = V_{QM} + V_{MM} + V_{QM/MM}. \tag{38}$$

The quantum potential is calculated independently as the electronic energy for a given nuclear configuration $\mathbf{R}$ and for those atoms treated with QM, the azo-moiety. The molecular mechanics potential is given by the classical force field for bonded and non-bonded interactions,

$$\begin{aligned} V_{MM} = \sum_{i}^{N_{bonds}} V_i^{bond} + \sum_{j}^{N_{angles}} V_j^{angle} + \sum_{l}^{N_{torsions}} V_l^{torsion} \\ + \sum_{i}^{N_{MM}} \sum_{j>i}^{N_{MM}} V_{ij}^{Coul} + \sum_{i}^{N_{MM}} \sum_{j>i}^{N_{MM}} V_{ij}^{LJ}. \end{aligned} \tag{39}$$

Normally, harmonic functions are used for bonds and angles, V_i^{bond}, V_j^{angle} and periodic functions for torsions, $V_l^{torsion}$. The non-bonded interactions are summed over all pairs of atoms described on the MM level, N_{MM}. The van der Waals interactions are modelled with the Lennard-Jones potential,

$$V_{ij}^{LJ} = 4\epsilon_{ij}\left[\left(\frac{\sigma_{ij}}{R_{ij}}\right)^{12} - \left(\frac{\sigma_{ij}}{R_{ij}}\right)^{6}\right], \tag{40}$$

Where the $(1/R_{ij})^{12}$ term accounts for short-range repulsion and the $(1/R_{ij})^{6}$ term for the long-range dispersion attraction. The well depth ϵ_{ij} and the distance σ_{ij} where the LJ potential is zero are the LJ parameters defined for pairs of atom types i and j. The electrostatic interactions are modelled as the Coulomb interactions between atoms with partial charges Q_i and Q_j at a distance R_{ij}

$$V_{ij}^{Coul} = \frac{Q_i Q_j}{R_{ij}}, \tag{41}$$

written in atomic units $e^2/4\pi\varepsilon_0$ where e is the elementary charge and ε_0 the vacuum dielectric constant.

The treatment of the interaction term $V_{QM/MM}$ is what defines the hybrid QM/MM scheme in use. In this work the interaction between the QM and MM regions is treated using the electronic embedding scheme. Therein, the electron distribution of the QM region is polarized by the MM charges Q_J of those atoms within the non-bonded interaction cut-off. This is achieved by modifying the QM Hamiltonian, or the one-electron operator, see the Fock operator defined in Equation 6, which now includes the electron-nuclei interactions with the MM nuclei as well,

$$\hat{\mathbf{h}}_{\mathrm{i}}^{\mathrm{QM/MM}} = \hat{\mathbf{h}}_{\mathrm{i}}^{\mathrm{QM}} - \sum_{\mathrm{J}}^{\mathrm{M}} \frac{\mathrm{Q_J}}{|\mathbf{r}_{\mathrm{i}} - \mathbf{R}_{\mathrm{J}}|}. \tag{42}$$

The operator is given in atomic units with $|\mathrm{r_i} - \mathrm{R_J}|$ the distance between the i-th electron and the J-th nucleus and the sum running over M nuclei of the MM region that are within some cut-off value for the electrostatic interaction. The electrostatic interactions between the QM and MM regions are thus treated on the quantum level, but within the framework we used the back-polarization of the electron distribution is not accounted for. Also, the QM atoms are assigned Lennard-Jones parameters and included in the classical force field. In this way they are mechanically embedded in the MM system. The interaction potential $\mathrm{V_{QM/MM}}$ can be thus written as the sum of the MM-nuclei-electron attraction and MM-nuclei-QM-nuclei repulsion that enter the QM Hamiltonian, where the nuclear charges of QM atoms are denoted with $\mathrm{Q_K}$ and the nuclear charges of MM atoms within a cut-off with $\mathrm{Q_J}$,

$$\begin{aligned}\mathrm{V_{QM/MM}} = -\sum_{\mathrm{i}}^{\mathrm{N}}\sum_{\mathrm{J}}^{\mathrm{M}} \frac{\mathrm{Q_J}}{|\mathrm{r_i} - \mathrm{R_J}|} + \sum_{\mathrm{J}}^{\mathrm{M}}\sum_{\mathrm{K}}^{\mathrm{L}} \frac{\mathrm{Q_J Q_K}}{|\mathrm{R_K} - \mathrm{R_J}|} \\ + \sum_{\mathrm{J}}^{\mathrm{M}}\sum_{\mathrm{K}}^{\mathrm{L}} 4\epsilon_{\mathrm{JK}}\left[\left(\frac{\sigma_{\mathrm{JK}}}{\mathrm{R_{JK}}}\right)^{12} - \left(\frac{\sigma_{\mathrm{JK}}}{\mathrm{R_{JK}}}\right)^{6}\right].\end{aligned} \tag{43}$$

and the Lennard-Jones interaction of the QM atoms and the MM atoms that are within the cut-off, $\mathrm{V_{QM/MM}^{LJ}}$ as the third term of the sum. The summations run over N electrons, L QM atoms and M MM atoms that are within the interaction cut-off. To point out, the sums for the Lennard-Jones interaction in the force field term of Equation 40 the MM atoms only are counted.

In the current implementation of Gromacs and the DFTB3 method for QM/MM hybrid simulations [74], the electrostatic interactions are treated with the Particle Mesh Ewald [75, 76]. Within the Ewald treatment, there is an electrostatic potential in each QM atom induced by all MM atoms and their periodic images. The total electrostatic potential can be broken down to the long range and short range potentials, and the "exclusion" potentials not to overcount the pairwise and self-interactions of QM atoms, already included in the long range interaction term. The long range interaction potential on the QM atom a, $\varphi_{\mathrm{a}}^{\mathrm{lr}}$ is calculated between all atoms, the MM and QM atoms with the partial charges denoted Ω_{i}, in the first summation,

$$\varphi_{\mathrm{a}}^{\mathrm{lr}} = \frac{4\pi}{\mathrm{V}} \sum_{\mathrm{i}}^{\mathrm{QM+MM}} \Omega_{\mathrm{i}} \sum_{\vec{\mathrm{k}}\neq\vec{\mathrm{o}}} \frac{1}{|\vec{\mathrm{k}}|^2} \exp\left(-\frac{|\vec{\mathrm{k}}|^2}{4\beta^2}\right) \cdot \exp(-\mathrm{i}\cdot\vec{\mathrm{k}}\cdot(\vec{\mathrm{r}}_{\mathrm{i}} - \vec{\mathrm{r}}_{\mathrm{a}})). \tag{44}$$

The second summation spans the reciprocal vector $\vec{\mathrm{k}}$, the parameter β controls the spatial extension of the charge densities and V is the box volume. The short range interaction potential $\varphi_{\mathrm{a}}^{\mathrm{sr}}$ is evaluated for the MM atoms within a cut-off distance from the QM atom a and is calculated in real space as

$$\varphi_a^{sr} = \sum_J \frac{Q_J}{|\mathbf{R}_J - \mathbf{R}_a|} \cdot \mathrm{erfc}(\beta \cdot |\mathbf{R}_J - \mathbf{R}_a|). \quad (45)$$

The erfc is the error function, which arises due to the original separation of a diverging summation with two converging ones, the one in the reciprocal Fourier space and the other in real space. The Particle Mesh Ewald improves the computation performance of the reciprocal summation by assigning the charges to a grid using interpolation.

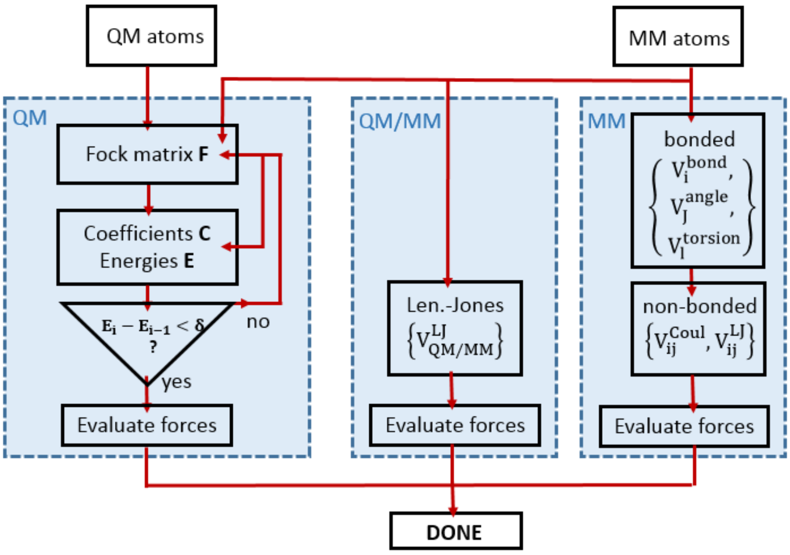

Figure 5. Flow scheme of the energy calculation for the electrostatic embedding QM/MM scheme. Adapted from [73].

Because the electronic embedding requires the modification of the QM Hamiltonian, the quantum chemistry software needs to be modified as well. As the MD engine, Gromacs can be interfaced with all of the major quantum chemistry software. Gaussian 03 and ORCA [77] have been tested for the purpose of this study. On the example of the ORCA-Gromacs interface, Gromacs modifies the input for the QM program as to include the list of MM partial charges as well as the Lennard-Jones parameters for the MM atoms within the non-bonded interaction cut-off. The single point energy evaluation is then performed by the QM program, and the resulting QM energies and forces read by the MD engine and the positions of all atoms updated according to the underlying dynamical equation (Equations 31, 35, 36).

We performed the ab-initio simulations in vacuum with the azobenzene moiety treated with the semiempirical functional DFTB3, recently implemented within Gromacs [74]. For the simulations in explicit solvent, we used the General Amber Force Field parameters [78] for both the azo-moiety and the solvent. However, the partial charges for the solvent molecules were re-parametrized charges with the Restrained Electrostatic Potential (RESP) method [79] with a two-stage Amber fitting procedure to better reproduce the intermolecular interactions. The charges were derived to reproduce the charge interactions in solution but based on the geometry optimization in the gas phase using B3LYP/6-31G* level of theory. The quantum mechanical electrostatic potential was evaluated for a set of points lying outside the van der Waals surface of the molecule and the least square procedure was used to fit the partial charges at the atomic centres of the molecule. A restraint was introduced in the form of a penalty function in the fitting procedure, which made the calculated charges more transferable between functional groups and less conformationally dependent.

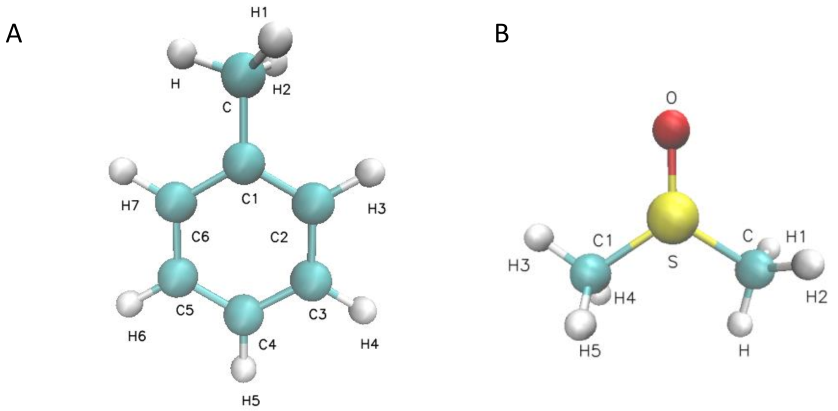

Figure 6. Molecular schemes for toluene (A) and DMSO (B) with atom labels.

The force field parameters with the RESP fitted charges used for DMSO and toluene are listed in Table 1. The molecular schemes with atom labels are depicted in the Figure 4. The difference in Lennard-Jones parameters for toluene were present only for the aromatic carbons (C1, C2, C3, C4, C5) and the methyl carbon (C), as well as for the aromatic (H3, H4, H5, H6, H7) and methyl (H, H1, H2) hydrogens.

The Lennard-Jones parameters used for the QM atoms for the two azo-compounds treated in this study are listed in Table 2. Those were General Amber Force Field (GAFF) parameters [78], where we used GAFF parameters for the pre-equilibration where the whole system was treated on the MM level. See the next Section 2.3.2 for the equilibration protocols. The atom types for the azo-moieties are the aromatic carbon and hydrogen (CA and HA), amino hydrogen (HN), nitrogen (N) and oxygen (O), the atom labels for which can be read from Figure 7.

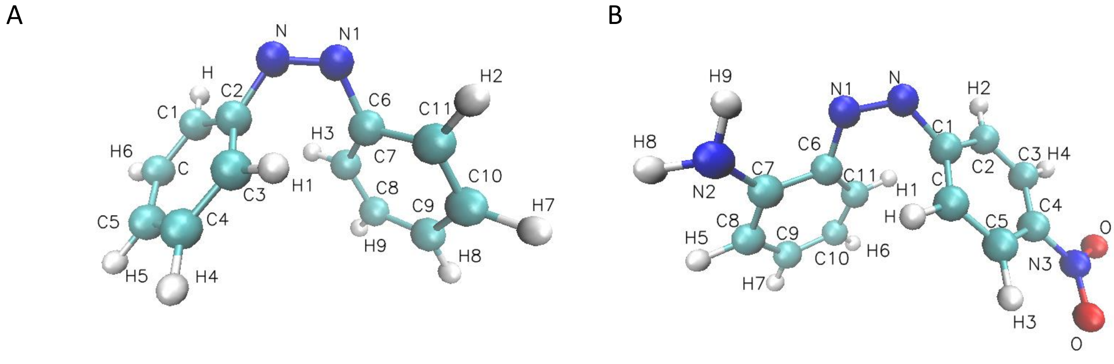

Figure 7. Molecular schemes for azobenzene (A) and the push-pull 4NO$_2$-6’NH$_2$ AB (B) with atom labels.

Table 1. Force Field parameters for solvents, DMSO (right) and toluene (left): RESP fitted charges in atomic units, Q_K, and Lennard-Jones parameters, σ [nm], ϵ [kJmol^{-1}]. The Lennard Jones parameters for i, j pairs of atoms were evaluated as $\epsilon_{ij} = \sqrt{\epsilon_{ii}\epsilon_{jj}}$ and $\sigma_{ij} = (\sigma_{ii} + \sigma_{jj})/2$.

atom	Q_K	σ	ϵ
C	-0.383925	0.34	0.458
H, H1, H2	0.106283	0.265	0.0657
C1	0.287509	0.34	0.36
C2	-0. 278596	0.34	0.36
C3,C5	-0.105781	0.34	0.36
C4	-0.178865	0.34	0.36
C6	-0.278596	0.34	0.36
H3, H7	0.156958	0.260	0.0628
H4, H6	0.135671	0.260	0.0628
H5	0.139928	0.260	0.0628

atom	Q_K	σ	ϵ
S	0.26972	0.356	1.046
O	-0.54168	0.296	0.879
C, C1	-0.24118	0.34	0.458
H – H5	0.12572	0.247	0.0657

Table 2. Lennard-Jones parameters for the QM atoms of the azo-moiety (AB and ppAB). CA and HA denote the aromatic carbon and hydrogen atom types, while HN is the amino hydrogen type.

atom	σ	ϵ
CA	0.34	0.36
HA	0.26	0.0628
HN	0.107	0.0657
N	0.325	0.711
O	0.296	0.879

2.3.2 Equilibration protocols in vacuum and in solvents

Within this study two azobenzene compounds were investigated, namely the unsubstituted AB and the push-pull ppAB, $4NO_2$-6'NH_2 AB (Figure 7). The starting structures were built in Molden (35) the cis state and optimized at the DFTBA level of theory. The system was first equilibrated with both the azobenzene moiety and the solvent treated on the MM level. The azobenzene moiety was first solvated in a quadratic box, 3x3x3 nm in size, by random insertion of solvent particles. The AB compound was solvated with a total of 458 DMSO that is 308 toluene molecules. The ppAB compound was solvated with a total of 455 DMSO that is 309 toluene molecules. A steepest descent minimization was performed, followed by 1 ns of NPT equilibration: constant pressure of $1\ \mathrm{bar}$ with and a constant temperature of $333\ \mathrm{K}$ a time constant of $1\ \mathrm{ps}$ were maintained using the Berendsen barostat with stochastic dynamics. What followed was a QM-MM equilibration run with the same conditions and a time step of 1 fs for a total run time of 200 ps. The non-bonded interactions were treated with a cut-off 1.4 nm, for both van-der Waals and the electrostatic interactions. The electrostatic interactions were handled by Particle Mesh Ewald with the grid spacing of 0.12 nm, while van der Waals interactions with a simple cut-off scheme. Neighbour lists were updated every 5 time steps ($0.5\ \mathrm{ps}$), that is the list of pairs of atoms within a cut-off for the non-bonded interaction. We used the stochastic dynamics integrator with the time constant of $1\ \mathrm{ps}$, essentially a stochastic thermostat at a temperature $333\ \mathrm{K}$, which produced the correct canonical NVT ensemble.

2.4 Potential of Mean Force: Enhanced Sampling

A reaction can be described as crossing the free energy barrier between the two stable states. For isomerization of azobenzene this barrier is large compared to thermal energy, $\sim 40\ \mathrm{k_B T}$, which makes the direct sampling of the reactive event unfeasible. With enhanced sampling the system is pushed to sample higher energy regions. With umbrella sampling a set of harmonic potentials are set up along a plausible direction for the reaction, the reaction coordinate, and the resulting free energy profile obtained through reweighting of the restrained ensembles. Metadynamics is more flexible with respect to choosing multiple collective variables along which to deposit Gaussian like potentials, the so called hills, but results in less accurate free energies which are in turn calculated as the negative sum of the deposited hills during the total biasing run. The value of direct sampling of both the reactive azo-moiety and the surrounding solvent is that the obtained free energy profile contains the entropic factor, importantly since the transition states are defined on the level of the free energy and not the bare potential.

The potential of mean force refers to any method that maps out the energy with respect to a coordinate, with all other degrees of freedom integrated out, and is usually used interchangeably with the "free energy function". Strictly speaking though, the potential of mean force is obtained with evaluation of average forces $\langle \mathbf{F}_\xi \rangle_\xi$ for restrained values of a coordinate ξ. The associated energy barrier $\Delta\mathrm{E}_{\mathrm{A}\to\mathrm{B}}$ for crossing between the two states A, B along the coordinate ξ is given by the gradient, $\langle \mathbf{F}_\xi \rangle_\xi = -\,\partial(\Delta\mathrm{E}_{\mathrm{A}\to\mathrm{B}})/\,\partial\xi$.

First, we introduce the reaction coordinate as the sine-cosine transform of the variables most relevant for the isomerization, namely the central dihedral and the bend angle that linearizes in the transition state, ω and α, respectively, as depicted in Figure 8 with labels. The coordinate X is

$$\mathrm{X} = \sin\alpha\cos\omega \tag{46}$$

$$\mathrm{Y} = \sin\alpha\sin\omega$$

As an orthogonal coordinate to X we defined Y an independent variable useful to measure decorrelation times when the system is restrained with respect to the coordinate X.

2.4.1 Meta-dynamics in the (ω, α) space

Metadynamics [80, 81] is an enhanced sampling technique along the selected collective variables, $\vec{\mathrm{s}}_\mathrm{i}(\mathrm{q})$ expressed as a function of q coordinates. A history dependent potential acting on the selected variables is added to the total Hamiltonian. The dynamics in the selected variables is essentially a steepest descent, where the system evolves along the collective variable $\sim\ \partial\vec{\mathrm{F}}_{\mathrm{s_i}}/\,\partial\mathrm{s_i}$. In the course of the biased dynamics the free energy wells are gradually filled by the Gaussian potentials and the system is pushed away from the previously visited regions of phase space by the force component coming from the Gaussian, $\vec{\mathrm{F}}_{\mathrm{s_i}}$. Eventually the sum of the Gaussian hills will almost exactly compensate for the underlying free energy surface, and at this point the system moves barrier-free among different states, see Figure 8. The free energy is thus given as the negative sum of the accumulated hills at the time point when the system is freely sampling the full phase space.

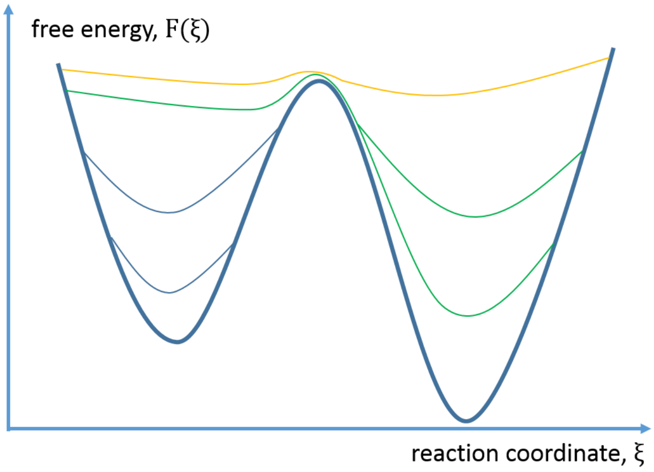

Figure 8. Scheme: Metadynamics. Filling the potential well as hills (the bias potentials) are deposited, starting from the left well. The system escapes into the right well (the change in colour from blue to green) and ends up freely diffusing between the wells (orange curve).

To map out the free energy in the central dihedral and angle (ω, α) space, well-tempered metadynamics was applied. A history dependent bias potential in the space of the selected collective variables $\vec{s}_i(q)$ is of the form

$$V(\vec{s},t) = \sum_{k\tau<t} W(k\tau)\exp\left(-\sum_{i=1}^{d}\frac{(s_i - s_i(q(k\tau))^2}{2\sigma_i^2}\right), \tag{47}$$

was deposited with the stride $\tau = 0.5$ ps, the height of the Gaussian potential $W(k\tau) = 2.0\ \mathrm{kJ\ mol^{-1}}$, for both collective variables ω, α, and the width of the Gaussian $\sigma_i^2 = 11.5°$ and $\sigma_i^2 = 5.7°$ for the dihedral ω and angle α, respectively. In well-tempered metadynamics, the height of the Gaussian potential is decreased with simulation time through the temperature parameter $\Delta T = 6.0$, as given by $W(k\tau) = W_0 \exp(-V(\vec{s}(q(k\tau)),\ k\tau)/k_B\Delta T)$ where W_0 is the initial height of the Gaussian. The total simulation time comprised 10 ns, where convergence was monitored with respect to the dihedral variable ω and the simulation ran until there was no considerable change in the free energy $F(\omega)$. The resulting 2D free energy map was calculated as the negative sum of the Gaussian hills added to the quantum potential during the biasing metadynamics run.

2.4.2 Umbrella Sampling for the coordinate $X\ (\omega, \alpha)$

In umbrella sampling a series of overlapping biasing potentials are set up along a reaction coordinate to enhance sampling of the energetically unfavourable regions [82, 83, 84], schematically depicted in Figure 9.

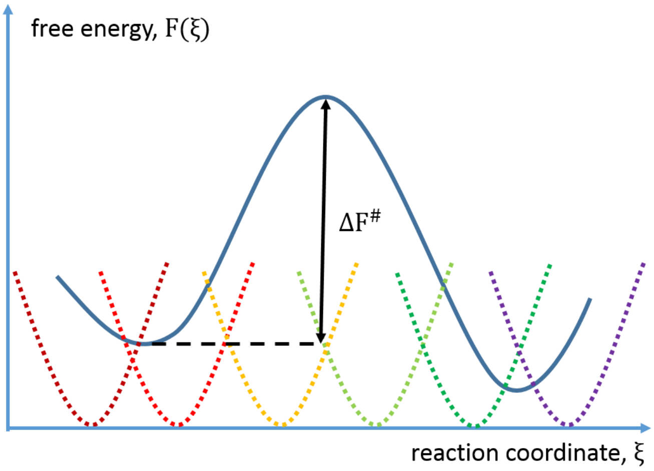

Figure 9. Scheme: Umbrella sampling. The free energy profile (thick line) and the biased potentials of the overlapping umbrella windows (dashed lines) with the free energy barrier $\Delta F^{\#}$ denoted as well.

The underlying objective is to reconstruct an approximate probability distribution $P(\xi)$ and with it the free energy $F = -k_B T \ln P(\xi)$ along a reaction coordinate ξ that by definition discriminates between the two states. Consequently, the free energy barrier $\Delta F^{\#}$ between the states is easily obtainable. The full unbiased probability distribution along the reaction coordinate is obtained in post-processing by combining the umbrella windows. We used the Weighted Histogram Analysis Method [85], specifically the software developed by Grossfield [86], to reweight the probabilities from different umbrella windows.

In the following we describe the procedure for the reaction coordinate $\xi \equiv X$ defined in Equation 46 for umbrella sampling of both compounds, pure azobenzene AB and the push-pull derivative ppAB. The reaction coordinate X was pulled by the biasing potential of the form

$$W_i = \frac{1}{2} k (X - X_{0,i})^2, \tag{48}$$

and restrained to a value $X_{0,i}$ the position for the i-th window center with the spring constants $k = 1100 \text{ kJ mol}^{-1}$ for AB and $k = 901 \text{ kJ mol}^{-1}$ for ppAB. The force constants were fine-tuned in order to ensure the optimal overlap of probability distributions between the neighboring windows. This was achieved by making the standard deviation in the coordinate X for a given strength of the harmonic restraint k approximately match the umbrella window size $\Delta X = 0.06$. The windows along the X coordinate were set up in the range $X_{min} = -0.90$ and $X_{max} = 0.84$ making for 29 windows in total. The restrained production runs per each window were 5 ns long, which proved to be sufficient for the resulting free energy not to change substantially. The WHAM equations iteratively solved for the probability distribution in X, $P(X)$, and its associated free energy, $F(X)$.

The free energy associated to the i-th umbrella window can be expressed

$$f_i = -k_B T \ln \left[\int dX \, p(X) \exp\left(-\frac{W_i(X)}{k_B T} \right) \right], \tag{49}$$

with $\mathrm{W_i(X)}$ the bias potential for the i-th window defined in Equation 48. The total probability distribution $\mathrm{P(X)}$ is then given by

$$\mathrm{P(X)} = \frac{\sum_\mathrm{i} \mathrm{n_i(X)}}{\sum_\mathrm{i} \mathrm{N_i} \exp(\mathrm{f_i} - \mathrm{W_i(X)/k_B T})}, \tag{50}$$

where $\mathrm{n_i(X)}$ is the number of counts in histogram bin associated with value X, and $\mathrm{N_i}$ the total number of counts for the i-th window. The two Equations 49 and 50 were solved iteratively until self-consistent convergence with tolerance of 0.001. The error in free energy associated to each window 'i' was evaluated by Monte Carlo bootstrap error analysis. The free energy was re-evaluated by re-sampling the values that were decorrelation number of steps apart in 100 trials. This decorrelation time was evaluated with respect to a coordinate orthogonal to X, the coordinate Y, $\mathrm{Y} = \sin\alpha \sin\omega$. The potential of mean force or the Helmholtz free energy for the NVT ensemble as the function of the coordinate X, was then obtained from the re-weighted probability distribution $\mathrm{P(X)}$ as $\mathrm{F(X)} = -\mathrm{k_B T} \ln \mathrm{P(X)}$.

2.4.3 Steered molecular dynamics

In steered molecular dynamics the system is pulled along a coordinate by applying force or adding a time dependent potential to the total Hamiltonian. It can be used as a potential of mean approach to map out the free energy between the two states along a coordinate through the use of the Jarzynski equality [87, 88, 89]. For our purposes it was used to produce the initial reactive trajectory for the TPS sampling and to prepare configurations across the umbrella windows in the coordinate X. The steered dynamics along the coordinate X was applied to produce the initial reactive trajectory connecting the cis $\mathrm{X_{cis}} = 0.85$, and trans $\mathrm{X_{trans}} = -0.85$, stable states. A time dependent harmonic restraint was added on the X coordinate, with the force constant $\mathrm{k\ (t)} = 1000\ \mathrm{kJ\ mol^{-1}}$, in the total of 500 or 1000 steps in vacuum or solvent, respectively. The harmonic restraint of the form

$$\mathrm{V(X,t)} = \frac{1}{2}\ \mathrm{k(t)}\ (\mathrm{X} - \mathrm{X_0(t)})^2 \tag{51}$$

was applied, where the values for $\mathrm{X_0(t)}$ at a specific time step linearly interpolated between the initial and final value, $\mathrm{X_{cis}} = 0.85$ and $\mathrm{X_{trans}} = -0.85$, respectively.

2.5 Transition Path Sampling

Transition path sampling is a Monte Carlo based sampling of reactive trajectories connecting the two predefined stable states [91, 92]. The predefinition of a reaction coordinate is not needed unlike in the potential of mean force approaches. This is crucial for complex systems like reactions in solution, where it is not obvious in what way the solvent degrees of freedom contribute to the reaction coordinate. By performing a random walk in the trajectory space and applying the Monte Carlo acceptance rules, a properly weighted ensemble of reactive paths is sampled, termed the transition path ensemble (TSE). Since the TP ensemble represent true dynamical trajectories, the transition rate constants can be calculated.

The TPS method is based on the statistical mechanics of trajectories. A trajectory can be represented by an ordered sequence of states, $x\,(T) = \{\, x_0, x_{\Delta t}, \ldots, x_{j\Delta t}, \ldots, x_T \,\}$, consisting of $L = T/\Delta t - 1$ states or time slices. A distribution functional for dynamical pathways, $P\,[x(T)]$, can be expressed for a trajectory of length T, $x\,(T)$,

$$P\,[x(T)] = \rho(x_0) \prod_{i=0}^{\frac{T}{\Delta t}-1} p\big(x_{i\Delta t} \rightarrow x_{(i+1)\Delta t}\big), \tag{52}$$

where $\rho(x_0)$ is the distribution of states x_0 as starting points for the trajectories and $p\big(x_{i\Delta t} \rightarrow x_{(i+1)\Delta t}\big)$ the probability for a state x_t to evolve into a state $x_{t+\Delta t}$ over the time Δt. Since it is the aim to sample only reactive trajectories connecting the stable states A and B, the starting and the ending point of trajectories have to be restricted, yielding a probability functional for the reactive trajectories

$$P_{AB}\,[x(T)] = \frac{h_A(x_0)\;P\,[x(T)]\;h_B(x_T)}{Z_{AB}(T)}. \tag{53}$$

By employing the so called characteristic functions for the stable states A and B, $h_A(x)$ and $h_B(x)$ respectively, the starting state x_0 is restricted to be in A and the ending state x_T in B. The characteristic functions are modelled as step functions for which $h_A(x) = 1$ if $x \in A$ and $h_A(x) = 0$ if $x \notin A$ and analogously for $h_B(x)$. The functional $P_{AB}\,[x(T)]$ for a reactive trajectory is its weight in the ensemble of transition paths with length T connecting the states A and B. The normalization factor is the path partition function $Z_{AB}(T) = \int Dx(T)\, h_A(x_0)\; P\,[x(T)]\; h_B(x_T)$, where $\int Dx(T)$ is the integral over paths.

To construct the transition path ensemble with representative weights for its members, an appropriated distribution of initial conditions has to be used along with short time transition probabilities [92]. The initial conditions might be distributed according to the canonical ensemble, $\rho(x_0) \sim \exp\,[-\beta H(x)]$ with $H(x)$ the Hamiltonian of the system. The transition probabilities are given by the underlying dynamical equation, either deterministic or stochastic. Here we employ a stochastic dynamics integrator where the states propagator contains a systematic component ∂x_S, completely determined by the position at x_t,

$$x_{t+\partial t} = x_t + \partial x_S + \partial x_R, \tag{54}$$

and a random component ∂x_R drawn from a Gaussian distribution, see Equations 36, 37.

Generally, a biased random walk through a state space is performed by generating a trial state out of a current state by modifying it in some way and accepting it with a probability proportional to its actual weight in the ensemble. If the current state is rejected, the original is retained and reused as current, with its weight increased by one. The same is true for sampling trajectories: given an initial reactive trajectory, a trial move is used to generate a new reactive trajectory, which is accepted in proportion to its weight in the ensemble P_{AB}. To ensure proper sampling, appropriate acceptance rules have to be derived. Those are based on the detailed balance of moves in the trajectory space: the frequency of the accepted moves from the old path to a new path $o \rightarrow n$, has to be exactly balanced by the reverse move, $n \rightarrow o$. The resulting acceptance probability follows

$$\frac{\mathrm{acc}(o \rightarrow n)}{\mathrm{acc}(n \rightarrow o)} = \frac{P(o)\, \alpha\, (o \rightarrow n)}{P(n)\, \alpha\, (n \rightarrow o)} = \frac{P(o)}{P(n)} \tag{55}$$

where $\mathrm{acc}(o \rightarrow n)$ is the probability of accepting a new path n from the old one o and vice versa, $P(o)$ and $P(n)$ are their associated weights in the path ensemble, Equation 53, and α-s are the probabilities to generate the new paths from the old one or vice versa, and are equal $\alpha\,(o \rightarrow n) = \alpha\,(n \rightarrow o)$. The condition in Equation 55 can be satisfied by employing the Metropolis rule

$$\mathrm{acc}(o \rightarrow n) = \min\left[1, \frac{P(n)}{P(o)}\right]. \tag{56}$$

The acceptance probability of this form is realized when a new pathway is accepted unconditionally when $P(n)/P(o) > 1$, and with a probability $P(n)/P(o)$ if the ratio $P(n)/P(o) < 1$. We see that a new pathway is always accepted if its weight is greater than the weight of the old path, but it is still accepted with a finite probability in case the opposite holds. This is implemented by drawing a random number ζ from a uniform distribution in the interval $[0,1]$ and accepting if it is $\zeta < P(n)/P(o)$. The scheme for the Metropolis algorithm for TPS is given in Figure 10.

(1) Generate a new pathway, n out of a current one, o

(2) Accept or reject according to the Metropolis rule: with a probability proportional to the weight in the path ensemble $P_{AB}\,[x(T)]$ for the old path $P(o)$

(3) If the new path is accepted it becomes the current one. If not the old one is retained as the current one

(4) Repeat from (1)

Figure 10. Metropolis algorithm for Transition Path Sampling

2.5.1 Shooting moves for Stochastic Dynamics

The shooting algorithm is an efficient algorithm for performing transition path sampling. It consists of randomly selecting a time slice along a current reactive trajectory, $x_{t'}^{(o)}$, modifying the configuration or the momentum component in some way, $x_{t'}^{(o)} \rightarrow x_{t'}^{(n)}$, and growing the new trajectory forward and backward in time with the underlying dynamical propagator. In practice, the backward propagation is performed by inverting the momenta at the selected time slice t' and propagating forward in time. In stochastic dynamics, the propagator itself generates a random position at the first time step, as given in the Equation 54, so no modification of the trial time slice is necessary, that is, $x_{t'}^{(n)} = x_{t'}^{(o)}$. The shooting procedure is illustrated in Figure 11.

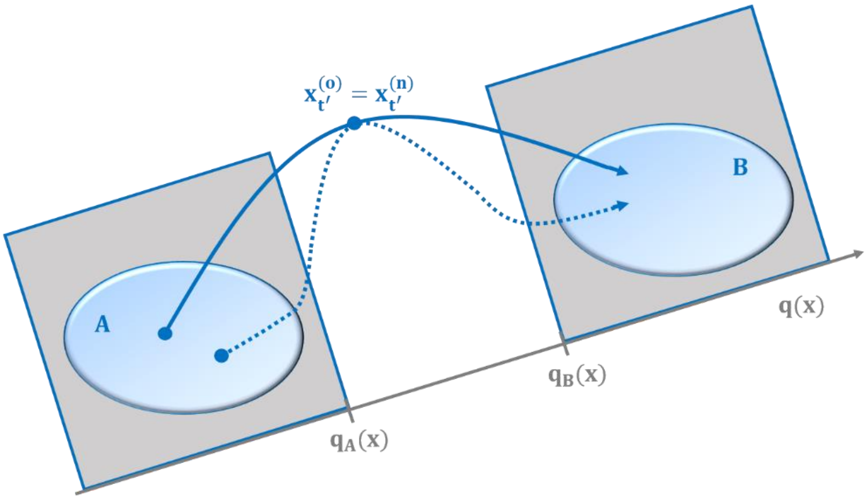

Figure 11. Scheme: Shooting algorithm for stochastic dynamics from an unchanged shooting point, $x_{t'}^{(o)} = x_{t'}^{(n)}$. The order parameter $q(x)$ separates the stable states A and B. With biased shooting, the shooting points are chosen from the interface only, from the interval $[q_A(x), q_B(x)]$.

The newly generated path is accepted with a probability $\mathrm{acc}(o \rightarrow n)$, which can be expressed as

$$\mathrm{acc}(o \rightarrow n) = h_A\left(x_0^{(n)}\right) h_B\left(x_T^{(n)}\right). \tag{57}$$

The only condition that needs to be fulfilled is for the new path to be reactive that is that its initial point $x_0^{(n)}$ lies in A and the final point $x_T^{(n)}$ in the state B. The probability of accepting a path can be increased by selecting shooting points near the barrier, or in the interface of the two stable states. In our implementation of the TPS algorithm we bias the shooting towards the interface. In case that the newly generated path is rejected, the current one is retained and the shooting re-iterated. The shooting algorithm for stochastic dynamics is summarized in Figure 12.

(1) Randomly select a time slice $x_{t'}^{(o)}$ on an existing path $x^{(o)}(T)$, $x_{t'}^{(o)} = x_{t'}^{(n)}$

(2) Compute a new stochastic trajectory segment from $x_{t'}^{(n)}$ to $x_{T}^{(n)}$

(3) Reject if the last state is not in B, $h_B\left(x_T^{(n)}\right) = 0$. Otherwise proceed with (4)

(4) Invert the momenta at $x_{t'}^{(n)}$

(5) Compute a stochastic trajectory 'back in time' to $x_0^{(n)}$, $t = 0$

(6) Invert the momenta along the whole segment so that the trajectory evolves forward in time

(7) Accept the new trajectory if the initial state is in A, $h_A\left(x_0^{(n)}\right) = 1$ and store as the current one. If not, use the old path to shoot from, or repeat from (1).

Figure 12. Shooting algorithm for stochastic dynamics.

2.5.2 Defining the stable states.

As previously stated, the main advantage of the TPS method is that it only requires a definition of low-dimensional order parameters, $q(x)$, that separate between the two stable states A and B. This is implemented by requiring the stable states to lie within some limits in $q(x)$. The order parameter need not actually represent the reaction coordinate which describes the transition through a dynamical bottleneck. An important requirement for the order parameter(s) and their stable states' boundaries, $q_A(x)$ and $q_B(x)$, is that there is no overlap between the two basins of attraction, A and B. A good definition of stable states must also accommodate equilibrium fluctuations with respect to the order parameter, since otherwise important transition pathways might be ignored

.

2.5.3 Transition Path Sampling – Protocol

In this work we employed a two-way shooting move algorithm with stochastic dynamics and biased shooting towards the interface. The TPS sampling was performed for both compounds AB and ppAB in the gas phase and solvents, DMSO and toluene, with the constant path lengths, namely 0.25 ps in vacuum and 0.5 ps in solvents. The stable states were defined with respect to the reaction coordinate $X\ (\omega, \alpha)$, as defined in Equation 46. As a consequence, the stable states were also defined with respect to the main reactive parameters for the cis $\rightarrow$ trans transition as well, namely the central dihedral and the bend angle, ω, α. Their corresponding values in stable states as defined for the TPS sampling as well as those extracted as border values from the equilibrium runs in cis and trans stable states, α_{ss}, ω_{ss}, are listed in Table 3.

Table 3. Definition of cis and trans stable states for the TPS simulations. Values for α, ω are for ppAB in gas phase and are extracted a posteriori from the TPS ensembles. The stable states are still defined solely with respect to X as stated in the text. Also given are the border values for α_{ss}, ω_{ss} for the stable states extracted from equilibrium runs.

stable state	**X**	$\boldsymbol{\alpha}$ [°]	$\boldsymbol{\omega}$ [°]	$\boldsymbol{\alpha_{ss}}$ [°]	$\boldsymbol{\omega_{ss}}$ [°]
cis	$\mathrm{X} > 0.5$	$\alpha < 150$	$\omega < 30$	$\alpha_{ss} < 150$	$\omega_{ss} < 45$
trans	$\mathrm{X} < -0.5$	$\alpha < 150$	$\omega > 140$	$\alpha_{ss} < 140$	$\omega_{ss} > 150$

The steered dynamics along the coordinate X was applied to produce the initial reactive trajectory connecting the cis, $\mathrm{X_{cis}} = 0.85$, and trans, $\mathrm{X_{trans}} = -0.85$, stable states. An initial configuration for the steered molecular dynamics were the equilibrated cis states for AB and ppAB across conditions, that is in vacuum and in solvents, as described Section 2.3.2. The TPS sampling was performed in the NVT ensemble at the temperature $\mathrm{T} = 333\ \mathrm{K}$. The force constant for the time dependent harmonic restraint along X was $\kappa\,(\mathrm{t}) = 1000\ \mathrm{kJ\ mol^{-1}}$ with the total of $\mathrm{L} = 500$ or $\mathrm{L} = 1000$ steps, in vacuum or solvent respectively, and with the time step $\Delta\mathrm{t} = 0.5$ fs.

The main means of analysing the collected TPS paths was in terms of configuration and path density plots, with respect to some order parameter(s). The configuration densities were simply calculated as 2D count-histograms and were not normalized, with 100 bins with varying range, readable from the actual plots. The path density plots show the fraction of pathways in the TPS ensemble that pass through the given values of the order parameters at least once [93, 94]. These plots were prepared as follows. Each pathway in the ensemble was smoothed by taking a running average with a window of 100 ps. Next, by discretizing each of the order parameter intervals in about 30–40 bins, we constructed for each trajectory in the ensemble a binary matrix, in which 1 means that the path visits the bin at least once and 0 means no visitations at all. These matrices were subsequently ensemble-averaged.

2.5.4 Transition State Ensemble – the Committor

A transition state is a configuration from which both stable states are equally accessible. The probability of relaxing from a transition state to either of the stable states is equal, and if we assume only two stable states, equal to $50\ \%$. Transition states defined in such a way do not necessarily correspond to the saddle-points of the potential energy. For complex systems the transition states are highly influenced by entropy. The stationary points of the potential surface do not coincide with stationary points on the free energy surface, a surface for which in fact the transition states are defined. A set of such configurations termed the transition state ensemble (TSE) forms a “separatrix” which is a high-dimensional surface separating the two stable states. For a reaction coordinate that adequately describes the reaction progress the transition states are configurations with the value of the reaction coordinate for which the free energy is maximal that is at the energy barrier. In this case of an ideal reaction coordinate, the separatrix containing the transition state configurations can be placed exactly at its energy barrier. On the other hand, the transition paths samples with TPS are reactive paths that must cross the separatrix at least once and thereby sample a transition state. The transition state ensemble should be thus obtainable from both approaches, by sampling the configurations at the energy barrier of an ideal reaction coordinate and screening the transition paths. These concepts are summarized in Figure 13.

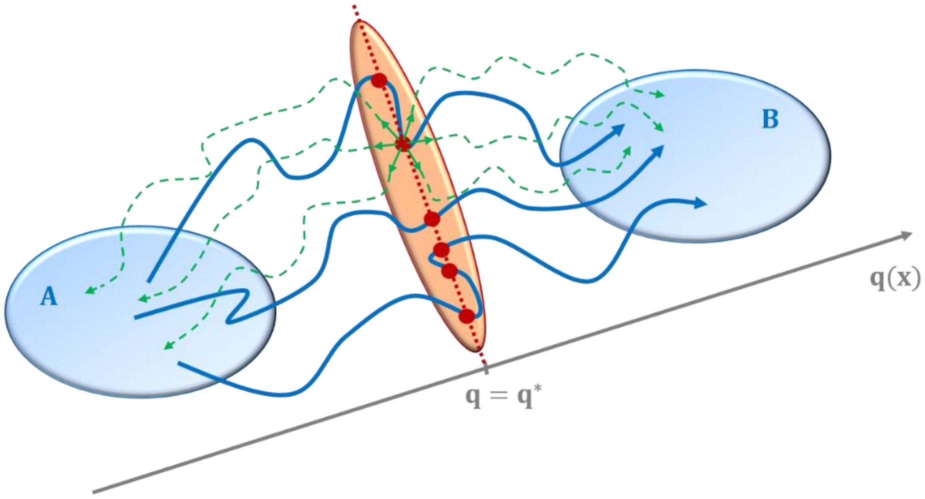

Figure 13. Scheme: Separatrix and the committor analysis Transition state ensemble as a set of configurations (red dots) forming the separatrix (dashed red line): a hypersurface separating the two stable states A, B. Transition paths (solid blue) must pass the separatrix at least once or they even re-cross it. For an ideal reaction coordinate configurations placed at its energy barrier top $\mathrm{q} = \mathrm{q}^*$are at the same time placed at the separatrix. Committor values for transition states, calculated by initializing trajectories with random momenta and counting outcomes of where they end up (in green) is $\sim 50\ \%$ to either of the stable states A, B.

Also depicted in Figure 13, in green, is the representation of the calculation of a committor probability for a configuration. The committor probability $p_B(x)$ is defined as the probability that trajectories initiated with random momenta from a configuration x reach the state B. In practice, the committor for a particular configuration is calculated by starting a number N fleeting trajectories $x^{(i)}(t)$ from that configuration,

$$p_B^N(x) \approx \frac{1}{N}\sum_{i=1}^{N} h_B(x_{t_s}^i) \tag{58}$$

initialized with momenta drawn from a Maxwell-Boltzmann distribution at a given temperature. The characteristic function $h_B(x_{t_s}^i)$ counts the occurrences of reaching the state B at the end of a fleeting trajectory. According to the central limit theorem, for large N the committor is a random Gaussian variable with fluctuations of size, averaged $\langle \dots \rangle$ over many independent calculations of p_B^N

$$\sigma = \sqrt{\langle (p_B^N - p_B)^2 \rangle} = \sqrt{\frac{p_B(1-p_B)}{N}}. \tag{59}$$

This is the error for the estimate of p_B based on a finite number of fleeting trajectories N, which have to be adjusted given a desired level of statistical accuracy. As a rule of thumb, for the error of 5 %, approximately ~ 100 fleeting trajectories have to be used to compute the committor. The configuration is then identified as the transition state, if the value 0.5 is in its committor confidence interval, $[p_B^N - \alpha\sigma,\ p_B^N + \alpha\sigma]$. For the value $\alpha = 2$ the confidence of the estimate is 95 %.

Distribution of committors are a valuable diagnostic of how good a coordinate $q \equiv q(x)$ approximates the true reaction coordinate. The separatrix is placed orthogonal to the ideal one-dimensional reaction coordinate at the value where its free energy $F(q)$ is maximal that is at the free energy barrier, $q = q^*$. Configurations x placed at this hypersurface have the committor probability $p_B(x \in \mathrm{TSE}) \sim 0.5$ and make up the transition state ensemble. For the ideal reaction coordinate, the ensemble of configurations, $q = q^*$ will coincide with the separatrix and the committor distribution for this ensemble $P(p_B)$ will be sharply peaked at 0.5.

$$P(p_B) = \langle \delta[p_B - p_B(x)] \rangle_{q(x)=q^*} \tag{60}$$

The average $\langle \dots \rangle_{q(x)=q^*}$ denotes the equilibrium average of the system restricted to $q(x) = q^*$.

In case that the committor distribution $P\left(p_B(x)\right)$ for the restrained ensemble $q(x) = q^*$ is not unimodal, different scenarios might be in play. Other coordinates might play a role as reactive coordinates that is there might be additional barriers in orthogonal directions, which would cause “leakage” to either of the stable states and result in spreading of the committor distribution. In case that the additional barrier is a symmetric double well in the q' direction, the trajectories split equally between the stable states and the committor distribution is bimodal for committor values $p_B \sim 0{,}1$. Another possibility is that the dynamics is diffusive in orthogonal directions q' which would result in completely randomized outcomes for the trajectories initiated at $q = q^*$, and a uniform committor distribution [91, 92]. Moreover, the quality of a reaction coordinate q can be diagnosed more specifically given the shape of the committor distribution for configurations restrained to its maximum $q = q^*$. Different scenarios for the features of the free energy $F(q, s)$, where s is the orthogonal coordinate, and the associated committor distributions is plotted in Figure 14. The orthogonal coordinate dominates, if the committor distribution is skewed to one extreme. If it is bimodal, that is has two maxima for committor values of $p_B \sim 0$ and $p_B \sim 1$, it is indicative that there is a barrier along the orthogonal coordinate. For a uniform committor, the dynamics along orthogonal coordinates is diffusive, which randomizes the outcome of trajectories shot from the true transition region. This does not necessarily signify that the reaction coordinate is a poor one.

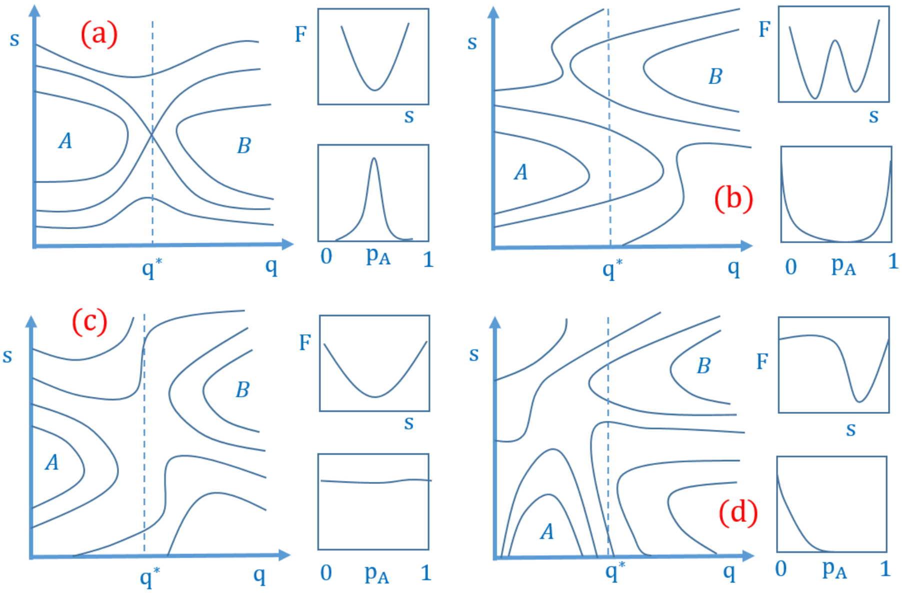

Figure 14. Scheme for the different free energy surfaces $F(q,s)$ and the associated committor distributions, $P(p_A)$ for configurations restrained at $q = q^*$, where q is the order parameter serving as a reaction coordinate and s are orthogonal coordinates for 4 different scenarios: (a) q is the ideal reaction coordinate. $P(p_A)$ is a Gaussian centered around $p_A = 0.5$. (b) There is an additional barrier in the orthogonal coordinate s. $P(p_A)$ is bimodal. (c) The dynamics is diffusive in the orthogonal coordinate s. $P(p_A)$ is uniform. (d) The orthogonal coordinate dominates. $P(p_A)$ is skewed to one side. Adapted from [91].

Comparing configurations with different committor values can give valuable insight into the reaction mechanism. Coordinates correlated with the transition are not necessarily a part of the reaction coordinate. The reaction coordinate completely describes the progress of the reaction as it passes through a dynamical bottleneck.

The identification of order parameters correlated with the transition was performed by comparing the transition state ensemble (TSE) for which $p_B \sim 0.5$ and stable states' configurations for which $p_B \sim 0{,}1$ with respect to angles, dihedrals etc. Then, those were tested as candidates for the reaction coordinate in the committor distribution analysis and especially considered in the maximum likelihood optimization methods, which we described in the Methods Section 2.6.

We employed two independent procedures to evaluate the committor values. In the first approach, configurations restrained to the free energy barrier $X = X^*$ in the coordinate X were screened. Starting from a configuration with $X = X^*$ 200 independent short stochastic dynamics runs in conditions of high friction where performed. The time coupling constant to the heat bath used was very small, $\tau = 0.01$ ps, to ensure decorrelation with respect to the initial state. Then 200 single configurations for which $\mathrm{X} = \mathrm{X}^*$ were chosen as last configurations across the 200 independent runs. For the exact value of X^* in different conditions see Table 6 in Results Section 3.2. The committor value for the chosen configurations was calculated. The committor value $\mathrm{p_B}\ (\mathrm{X} = \mathrm{X}^*)$ for a given configuration was calculated as a fraction of trajectories that reached the trans state after initiating 100 fleeting trajectories with the momenta sampled from a Maxwell-Boltzmann distribution at a temperature $\mathrm{T} = 333\ \mathrm{K}$. The resulting committor values were binned with a bin size $\Delta \mathrm{p_B} = 0.1$ and normalized to produce the committor distributions $\mathrm{P}\ (\mathrm{p_B})$.

The same procedure for calculating the committors, $\mathrm{p_B}(\mathrm{X})$, was employed in the second approach where we screened the configurations belonging to the interface of the sampled TPS paths. The configurations were chosen randomly across the transition path ensemble with the condition they laid in the interface, their value in the coordinate $\mathrm{X} = \{-0.5 < \mathrm{X} < 0.5\}$.

2.6 Reaction Coordinate Analysis

Since the committor function $\mathrm{p_B}(\mathrm{x})$ completely predicts the outcome of a process started from a given configuration x, it is the ideal reaction coordinate. Unfortunately its computation is highly demanding and requires simulating ~ 100 trajectories per configuration. It is thus beneficial to represent a reaction with a more intuitive low dimensional coordinate, which could be represented as a combination of distances, angles, dihedrals relevant for the transition. This reaction coordinate $\mathrm{r}(\mathrm{x})$ actually parametrizes the committor, $\mathrm{p_B}(\mathrm{r}) = \mathrm{p_B}[\mathrm{r}(\mathrm{x})]$, in the sense that there exists a one-to-one mapping between $\mathrm{p_B}(\mathrm{x})$ and $\mathrm{r}(\mathrm{x})$. That is to say, a given value of a good reaction coordinate at a configuration x, $\mathrm{r}(\mathrm{x})$, has to determine the value of the committor at that configuration, $\mathrm{p_B}[\mathrm{r}(\mathrm{x})]$.

In what follows, we describe two approaches for evaluation of reaction coordinates employed in this work which are both based on TPS sampling. The Best-Hummer analysis quantifies the quality of a reaction coordinate in terms of its distribution in transition path ensembles [95, 96], while the Likelihood Maximization extracts a combination of order parameters that best describe a reaction coordinate based on the shooting history in the TPS simulation [97, 98].

2.6.1 Best-Hummer approach: reaction coordinates from transition paths

The Best-Hummer approach is a general approach of inferring a reaction mechanism from transition paths and transition state ensembles. It uses a Bayesian formula between the equilibrium and transition path ensembles to assign a measure for the quality of a reaction coordinate r. The conditional probability for being on a transition path, given a value for the reaction coordinate $\mathrm{p}\ (\mathrm{TP} \mid \mathrm{r})$ can thus be expressed as

$$\mathrm{p}\ (\mathrm{TP} \mid \mathrm{r}) = \frac{\mathrm{p}\ (\mathrm{r} \mid \mathrm{TP})}{\mathrm{p_{eq}}(\mathrm{r})}\ \mathrm{p}\ (\mathrm{TP}), \tag{61}$$

a ratio of probability distributions for r in the transition path ensemble, $\mathrm{p}\ (\mathrm{r} \mid \mathrm{TP})$, and the equilibrium probability, $\mathrm{p_{eq}}(\mathrm{r})$. The ratio is normalized by the fraction of time spent in transition pathways for a long equilibrium trajectory $\mathrm{p}\ (\mathrm{TP})$. For a good reaction coordinate, the conditional probability $\mathrm{p}\ (\mathrm{TP} \mid \mathrm{r})$ peaks at the transition region since trajectories passing through those values of r are the most likely to be on a transition path. Also, since the spread in $\mathrm{p}\ (\mathrm{TP} \mid \mathrm{r})$ around some value $\mathrm{r} \equiv \mathrm{r}^*$

for the transition region indicates to what extent the transition region can be collapsed to a single value of $\mathrm{r} \equiv \mathrm{r}^*$ and thus quantifies the quality of the reaction coordinate r.

Using this approach, we tested the quality of putative reaction coordinate $\mathrm{r} \equiv \mathrm{X}$ given the sampled TPS ensemble to examine the features for the conditional probability $\mathrm{p}\ (\mathrm{TP} \mid \mathrm{r} \equiv \mathrm{X})$, the position of its maximum and the spread. We obtained the equilibrium probability distribution $\mathrm{p_{eq}}(\mathrm{r} \equiv \mathrm{X})$ from the free energy profiles calculated with umbrella sampling and WHAM reweighting. The conditional probability factor $\mathrm{p}\ (\mathrm{r} \equiv \mathrm{X} \mid \mathrm{TP})$ was calculated from the TPS ensemble of paths, and the $\mathrm{p}\ (\mathrm{TP})$ factor was calculated as the normalization factor for the resulting $\mathrm{p}\ (\mathrm{TP} \mid \mathrm{r})$ distribution. The conditions considered were the two compounds AB and ppAB in the gas phase and in DMSO.

The reaction rate can also be estimated employing the Best-Hummer analysis of transition paths. The number of transitions per unit time can be expressed as a fraction of time spent in transitions $\mathrm{p}\ (\mathrm{TP})$, divided by the average duration of a transition, $\langle \mathrm{t_{TP}} \rangle$.

For a two state model $\mathrm{A} \underset{\mathrm{k_2}}{\overset{\mathrm{k_1}}{\rightleftarrows}} \mathrm{B}$, with $\mathrm{k_1}$ and $\mathrm{k_2}$ the forward and the backward rate coefficients, respectively, the expression for the rate coefficients can be formulated

$$\frac{2}{\mathrm{k_1^{-1}} + \mathrm{k_2^{-1}}} = 2\mathrm{c_A}\mathrm{k_1} = 2\mathrm{c_B}\mathrm{k_2} \approx \frac{\mathrm{p(TP)}}{\langle \mathrm{t_{TP}} \rangle}. \tag{62}$$

The molar fractions for the states A and B, $\mathrm{c_A}$ and $\mathrm{c_B}$ respectively, were estimated using the probability distributions $\mathrm{P(X)}$ in the coordinate X obtained from the WHAM reweighted ensembles. The molar fraction in the state A, the cis isomer, was thus calculated as the integral $\mathrm{c_A} = \int_{\mathrm{X}=\mathrm{X}^*}^{1} \mathrm{P(X)dX}$. The integral boundaries in X used were from the position for the free energy maximum $\mathrm{X} = \mathrm{X}^*$ to the upper boundary for the cis state. The average duration for a transition path $\langle \mathrm{t_{TP}} \rangle$ was calculated as the time spent in the interface $\mathrm{X} = \langle -0.5, 0.5 \rangle$ averaged over the TPS ensemble. The fraction of time spent in transitions $\mathrm{p(TP)}$ was just the normalization factor for the conditional path probability $\mathrm{p}\ (\mathrm{TP} \mid \mathrm{r})$ as given in Equation 61.

2.6.2 Likelihood optimization based on the TPS shooting history

In approaches for identification of reaction coordinates previously considered, namely the committor based and the Best-Hummer approach, one needed to predefine a reaction coordinate. In the committor based approach, the ensemble restrained at the barrier top associated to the reaction coordinate was then tested as the presumable transition state ensemble. For the Best-Hummer approach, the probability distribution of a good reaction coordinate in the ensemble of transition paths would be sharply peaked around some value at the transition region. The Likelihood Maximization method is different insofar configurations are sampled independent of the reaction coordinate and then different forms for the reaction coordinate tested given the sample configurations.

As introduced by Peters et al. [97, 98], a valid input for the optimization process are shooting points of a TPS simulation, $\mathrm{x_{sp}}$ and their outcomes. The trajectories initiated from a shooting point might end in state A, $\mathrm{x_{sp}} \rightarrow \mathrm{A}$, or in state B, $\mathrm{x_{sp}} \rightarrow \mathrm{B}$. In case of a two-way shooting algorithm which we employ in this work, only forward or backward trajectory segments must be considered since the outcomes of forward and backward shootings from a configuration are correlated for non-diffusive dynamics. In this scheme, the committor function $\mathrm{p_B(x)}$ is modelled as a sigmoid function of the reaction coordinate, $\mathrm{r(x)}$,

$$\mathrm{p_B(r) = 0.5 + 0.5\tanh(r)}, \tag{63}$$

where the reaction coordinate is expressed as a linear combination of order parameters $\mathrm{q(x)}$, that is $\mathrm{r\,[q(x)]}$

$$\mathrm{r\,[q(x)]} = \sum_{\mathrm{i=1}}^{\mathrm{n}} \mathrm{a_i q_i(x) + a_0}. \tag{64}$$

The constant $\mathrm{a_0}$ is an adjustable parameter to ensure that the optimized reaction coordinate be centered at $\mathrm{r\,[q(x)] = 0}$ in the transition state region.

The committor probability $\mathrm{p_B(r\,[q(x)])}$ can be approximated by maximizing the likelihood

$$\mathrm{L} = \prod_{\mathrm{x_{sp\to B}}} \mathrm{p_B(r(x_{sp}))} \prod_{\mathrm{x_{sp\to A}}} \left(1 - \mathrm{p_B}\left(\mathrm{r(x_{sp})}\right)\right). \tag{65}$$

The notation indicates the product over all shooting points $\mathrm{x_{sp}}$ that end in $\mathrm{B}, \mathrm{x_{sp\to B}}$ in forward time and are accepted or end in $\mathrm{A}, \mathrm{x_{sp\to A}}$ in forward time and are rejected. According to the Bayes information criterion (BIC), if upon addition of another parameter the likelihood increases by $0.5 \ln \mathrm{M}$, with M the number of realizations in the likelihood function, there is a significant improvement in the optimization. In the present context of reaction coordinate optimization, M is just the number of shooting points used as input. Many combinations of structural order parameters for AB and ppAB across conditions were screened as putative reaction coordinates, the exact numbers of which are stated in the Result Section 3.4.4.

An aimless shooting algorithm was employed in the original scheme introduced in [97] to ensure the decorrelation of the shooting outcomes that serve as input for the maximization process. In aimless shooting, random momenta are assigned to shooting points which in turn are chosen to lie close to the transition region. In this was configurations relevant for the transition are used as input for the likelihood maximization. We also considered aimless shooting fates from the interface in coordinate X $\{-0.5 < \mathrm{X} < 0.5\}$, as well as from a tighter interface around the presumable transition region, $\mathrm{X}\,\{-0.15 < \mathrm{X} < 0.15\}$, as the input for the LM maximization which is presented in the Results Section 3.4.4.

2.7 Computation of rate constant

The computation of rate constants requires for them to be expressed in terms of the microscopic properties [99]. For the isomerization between the cis and trans conformers one can set up a two state model

$$A \underset{k_2}{\overset{k_1}{\rightleftarrows}} B$$

and a coordinate x by which the progress of a reaction is followed and with respect to which the states A, B are defined. The rate constant would then simply be calculated by counting the transitions between states. A generic double well potential as a model for the two-state isomerization of the form $U(x) = Q\,(1 - x^2)^2$ where Q is the barrier height, is depicted in Figure 15.

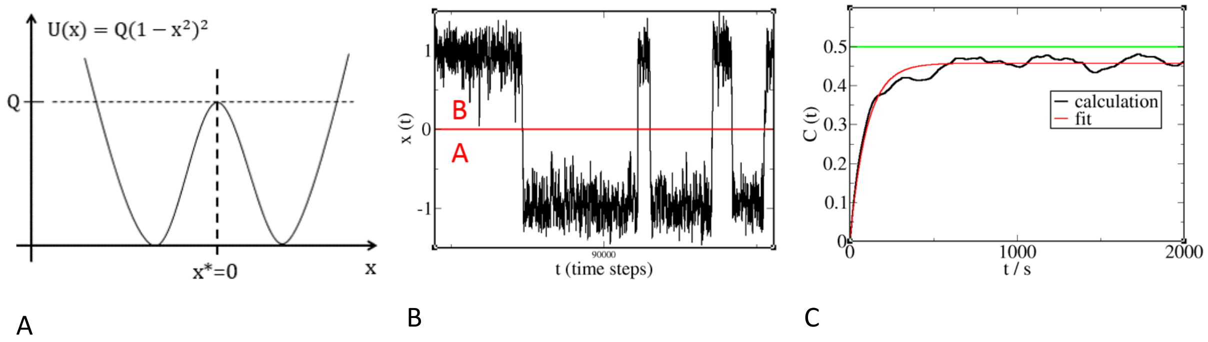

A B C

Figure 15. Barrier crossing over a generic double well potential of the form $U\,(x) = Q\,(1 - x^2)^2$ (A) where x is the reaction coordinate, and the associated long-time trajectory with transitions between the states. The time step for the Langevin dynamics integrator was $\Delta t = 0.01$. (B). The population correlation function calculated for the long equilibrium trajectory and the exponential fit of the form in Equation 66 yields the transition rate coefficient (C).

From the phenomenological rate equations of the form $\dot{c}_A\,(t) = -k_1 c_A(t) + k_2 c_B(t)$, the solution for the equilibrium concentrations of both states is obtained, $\Delta c_A(t) = \Delta c_A(0)\exp(-t/\tau_{rxn})$. The concentrations decay exponentially with a time constant being the reaction time $\tau_{rxn} = (k_1 + k_2)^{-1}$. For the system initially prepared in state A the concentration of the state B evolves in time as

$$c_B(t) = \langle c_B \rangle \left[1 - \exp(-\frac{t}{\tau_{rxn}})\right] \tag{66}$$

and asymptotically approaches the equilibrium value $\langle c_B \rangle$. The concentration can be expressed through the conditional probability to find a system in state B provided it was in the state A at time 0

$$C(t) = \frac{\langle h_A[x(0)]\; h_B[x(t)] \rangle}{\langle h_A \rangle}, \tag{67}$$

where the angular brackets $\langle \dots \rangle$ indicate the average over the equilibrium initial conditions. The correlation function $C(t)$ actually measures the correlation between state populations in time and characterizes the dynamics of transitions. Characteristic functions are used to define the stable states, where $h_B[x(t)]$ is a step function that is unity if the system is in state B and zero otherwise, and the characteristic function for the state A, $h_A[x(t)]$ is defined analogously.

$$h_B[x(t)] = \begin{matrix} 1 & \text{if} & x(t) \geq x^* \\ 0 & \text{if} & x(t) < x^* \end{matrix} \tag{68}$$

The concentrations in Equation 66 can be rewritten in terms of the conditional probability or the states' correlation function

$$C(t) = \langle h_B \rangle \, [1 - \exp(-\frac{t}{\tau_{rxn}})] \tag{69}$$

The correlation functions describes the dynamics of the transition in terms of microscopic degrees of freedom and is the link to the phenomenological description of reactions in terms of measurable rate constants or reaction times τ_{rxn}. For rare events involving transitions over large barriers the time scales are separated such that the reaction times are much longer than the actual duration of the transition, the so called molecular time τ_{mol}. For intermediate times, $\tau_{mol} < t \ll \tau_{rxn}$, there exists a regime where the correlation function grows linearly in time proportional to the forward rate k_1 and equivalently its derivative, the flux $\dot{C}(t)$, reaches a plateau.

$$C(t) \approx k_1 t\, ;\; \dot{C}(t) \approx k_1 \tag{70}$$

The height of this horizontal plateau for the flux is then defined as the forward reaction rate constant k_1.

For demonstration purposes and a later comparison with different methods for calculation of rate constants, we set up a simple symmetrical double-well model with Langevin dynamics [100]

$$m\ddot{x} = -\frac{dU(x)}{dx} - \gamma m\dot{x} + R(x) \tag{71}$$

with γ the friction constant, m the unit mass and $R(x)$ the random Gaussian force with zero mean and the variance proportional to the friction constant, $\langle R(t) \rangle = 0$, $\langle R(0)R(t) \rangle = 2kT\gamma\delta(t)$, respectively.

The states correlation function was calculated using Equation 66 for a long equilibrium trajectory, the black curve in Figure 15C. The exponential fit of the form of Equation 69 yielded the relaxation time for the process and therefore the reaction rate $k = k_1 + k_2 = \tau_{rxn}^{-1}$. The forward reaction rate constant for a symmetric double well potential where $k_1 = k_2$ was then simply given as $k_1 = 0.5\,k$.

For rare events involving transitions over large barriers and computationally demanding systems involving calculations of electronic energies which we employ for the $cis \rightarrow trans$ isomerization of azobenzene(s), the transition cannot be adequately sampled. Enhanced sampling methods have to be employed. In the so called reactive flux approach, the average flux of trajectories started at the dividing surface and end in the product state is calculated. For that one needs to predefine a reaction coordinate and the associated location of the dividing surface. The reactive flux rate constant is the dynamically corrected transition state theory (TST) rate constant and as such the true rate.

Another approach of calculating rate constants is based on the correlation function flux applied to the ensemble of transition paths, sampled by a TPS algorithm. The calculation is not as straightforward as simply employing the Equation 66 on the collected TPS paths to calculate the correlation function $C(t)$, as was feasible with the long equilibrium trajectory. Additionally, the work needed to confine the free ensemble of paths to an ensemble of a given length that connects the reactant and product regions has to be calculated.

In the end, the reactive flux and the correlation flux over the transition paths used to calculate the rate constant are equivalent and should yield the same value for the forward rate constant. For the double-well model system in which many transitions can be simulated, we calculated the population correlation function and the associated reaction times to compare the accuracy of the two enhanced sampling approaches. The calculation procedure is presented in the Results and Discussion Section 3.5.3.

2.7.1 Reactive flux formalism: the 'true rate'

Within the reactive flux formalism the rate constant is given as the average flux of trajectories initiated from a dividing surface that reach the product state [92, 99]. A reaction coordinate $\lambda(\mathrm{x})$ is defined as any function of the phase space points $\mathrm{x} \equiv \{\mathrm{r}, \mathrm{p}\}$ that separates the stable states. The location of the dividing surface $\lambda = \lambda^*$ along λ is determined as the point where its associated free energy $\mathrm{F}(\lambda) = -\mathrm{k_B T} \ln[\mathrm{P}(\lambda)]$ is maximal. The reactive flux rate is then given as the product of the probability of being at the barrier top relative to being in the reactant state, $\mathrm{P}(\lambda^*)$ and the dynamical factor $\mathrm{R(t)}$.

$$\mathrm{k_{RF}(t)} = \mathrm{P}(\lambda^*) \left\langle \dot{\lambda}(0)\theta(\lambda(\mathrm{t}))\right\rangle_{\lambda=\lambda^*} = \mathrm{P}(\lambda^*)\,\mathrm{R(t)} \tag{72}$$

In the above expression the $\langle \dots \rangle_{\lambda=\lambda^*}$ notation indicates an esemble average with λ constrained at λ^*. By convention, the system is defined to be in the state A or B if it is left, $\lambda < \lambda^*$ or right, $\lambda > \lambda^*$ of the dividing surface, respectively. The Heaviside step function is employed to count the occurences of being in the state B at time t, for which $\theta\left(\lambda(\mathrm{t})\right) = 1$. The relative probability can be expressed as

$$\mathrm{P}(\lambda^*) = \frac{\exp(-\beta\mathrm{F}(\lambda^*))}{\int_{-\infty}^{\lambda^*} \exp(-\beta\mathrm{F}(\lambda))\mathrm{d}\lambda} = \frac{\langle \delta\,(\lambda-\lambda^*)\rangle}{\langle \theta\,(\lambda^*-\lambda)\rangle}. \tag{73}$$

On the left hand side, the probability $\mathrm{P}(\lambda^*)$ is expressed with the Boltzmann weights for being in particular regions of phase space, while on the right hand side by directly counting the occurrences, with the use of delta functions $\delta(\lambda)$ to count occurrences of visiting the barrier top or the Heaviside functions $\theta(\lambda)$ to count when the system is in the reactant state A. The calculation then proceeds by initiating many fleeting trajectories from the dividing surface $\lambda\,(0) = \lambda^*$ and averaging the initial flux $\dot{\lambda}(0)$ of only those that reach the product state B at time t, $\theta\left(\lambda(\mathrm{t})\right) = 1$, which defines the dynamical factor $\mathrm{R(t)}$.

In this way possible recrossings or excursions back to the stable state A before settling into the product state B are accounted for. This is manifested by the initial oscillations for the times $\mathrm{t} < \tau_{\mathrm{mol}}$ or the molecular time, followed by setting to a plateau for the times intermediate between the molecular and the much longer reaction time $\tau_{\mathrm{mol}} < \mathrm{t} \ll \tau_{\mathrm{rxn}}$. Effectively, a correct choice of the reaction coordinate and the dividing surface is not relevant. Within Transition State Theory, on the other hand, it is assumed that all trajectories initiated at $\lambda = \lambda^*$ in the positive direction, the direction of the product state B actually reach the product state without recrossing back to the reactant. The expression for the TST rate can be written

$$\mathrm{k_{TST}} = \left\langle \dot{\lambda}(0)\theta\left(\dot{\lambda}(0)\right)\right\rangle_{\lambda=\lambda^*} \cdot \mathrm{P}(\lambda^*) = \frac{1}{2}\langle\, |\dot{\lambda}|\,\rangle_{\lambda=\lambda^*} \cdot \mathrm{P}(\lambda^*), \tag{74}$$

where the first term is rewritten as the average positive change in the reaction coordinate λ. The difference to the reactive flux calculation is in the factor R where only the positive initial flux for which $\theta(\dot{\lambda}(0)) = 1$ is averaged for all trajectories. In fact the factor $\mathrm{R(t)}$ is not time dependent and can be written $\mathrm{R(t)} \equiv \mathrm{R(0)}$. The TST rate thus is defined as the reactive flux rate at time $\mathrm{t} = 0$.

The dynamical correction to the TST rate can be expressed as the ratio of the two factors $\mathrm{R(t)}$ as

$$\kappa(\mathrm{t}) = \frac{\langle\dot{\lambda}(0)\theta(\lambda(\mathrm{t}))\rangle_{\lambda=\lambda^*}}{\langle\dot{\lambda}(0)\theta(\dot{\lambda}(0))\rangle_{\lambda=\lambda^*}} = \frac{\mathrm{k_{RF}(t)}}{\mathrm{k_{TST}}}, \tag{75}$$

and is termed the transmission coefficient $\kappa(\mathrm{t})$. It varies in the range $[0,1]$ and accounts for the deviation of the true rate from the TST rate.

For reactive flux calculations of the model double-well system the reaction coordinate is simply $\lambda \equiv \mathrm{x}$ with the dividing surface is placed at $\mathrm{x} = \mathrm{x}^* = 0$, and the definition of stable states as $\theta(\mathrm{x(t)}) = 0$ if the system is in state A and $\theta(\mathrm{x(t)}) = 1$ if it is in state B at time t. The relative probability of being at the dividing surface is simply calculated using the functional form of the potential for a given barrier height Q, where one can replace $\mathrm{F(x)} \equiv \mathrm{U(x)} = \mathrm{Q}\,(1 - \mathrm{x}^2)^2$ in Equation 73.

The calculation of the reactive flux rate for azobenzene(s) in vacuum and in DMSO consisted of two parts [101, 102]. First, the relative probability to be at the dividing surface $\mathrm{P(X^*)}$ expressed via free energies as a function of the coordinate X was calculated. Then, the dynamical factor $\mathrm{R(t)}$ was calculated with trajectories initiated from the dividing surface $\mathrm{X} = \mathrm{X}^*$. The free energy profile was constructed with respect to the coordinate X and the dividing surface located at the free energy maximum $\mathrm{X} = \mathrm{X}^*$. The configurations at the dividing surface were prepared in separate stochastic dynamics runs restrained at $\mathrm{X} = \mathrm{X}^*$. The actual configuration chosen as the initial for the dynamical factor calculation were chosen as the last ones of their respective time trajectories which still satisfied $\mathrm{X} = \mathrm{X}^*$. This ensured that we were using de-correlated configurations and sampled the dividing surface adequately. From these prepared configurations, 1000 fleeting trajectories were initiated with random momenta sampled from a Maxwell-Boltzmann distribution at temperature $333\ \mathrm{K}$ and evolved until they settled in a stable state. For vacuum 700 steps sufficed, while in solvent 1000 steps with the time step $\Delta\mathrm{t} = 0.5\ \mathrm{fs}$. The procedure of preparing the $\mathrm{X} = \mathrm{X}^*$ configurations in separate restrained runs and then initiating fleeting trajectories was repeated at least 5 times to obtain the error in the rate estimate.

2.7.2 Transition path flux and the correspondence with the reactive flux

The correlation function $\mathrm{C(t)}$ for the population of states in time defined in Equation 67 characterizes the transition between the two states and provides a way of obtaining the reaction rates from an exponential fit for time scales longer than the reaction time $\mathrm{t} > \tau_{\mathrm{rxn}}$. The correlation flux calculation can be set up for an ensemble of transition paths obtained by TPS sampling. The confinement of the free paths to the ensemble of constant length paths that connect the two stable states A, B has to be accounted for. If we consider the correlation function $\mathrm{C(t)}$ defined in Equation 67 as the ratio of partition functions of paths beginning in state A in time 0 and ending in state B at time t, one can calculate the associated free energy, or the reversible work to enforce such confinement of paths

$$\Delta \mathrm{F}(\mathrm{t}) = -\mathrm{k_B T} \ln \mathrm{C}(\mathrm{t}) \tag{76}$$

For a given time t, the free energy can be calculated by umbrella sampling with respect to an order parameter $\lambda(\mathrm{x})$, with the associated distribution of the order parameter $\mathrm{P}(\lambda\,;\mathrm{t})$. In the context of TPS, this means that a set of windows for the order parameter separating the two stable states are set up, such that they overlap. Then, in separate TPS runs for a given umbrella window the distribution $\mathrm{P}(\lambda\,;\mathrm{t}\,;\mathrm{i})$ is sampled for the i-th window $\lambda_{\mathrm{min}}[\mathrm{i}] < \lambda < \lambda_{\mathrm{max}}[\mathrm{i}]$. The distribution for the order parameter λ in the full range that is over all windows is calculated by histogram matching the distributions of the overlapping windows, since $\mathrm{P}(\lambda\,;\mathrm{t}\,) \sim \mathrm{P}(\lambda\,;\mathrm{t}\,;\mathrm{i})$, and normalizing the resulting $\mathrm{P}(\lambda\,;\mathrm{t}\,)$. The states correlation function can then be expressed as the integral over the distribution of the order parameter for a given path length, or path duration t'

$$\mathrm{C}(\mathrm{t}') = \frac{\langle \mathrm{h_A}[\mathrm{x}(0)]\,\mathrm{h_B}[\mathrm{x}(\mathrm{t}')]\rangle}{\langle \mathrm{h_A}\rangle} = \int_{\lambda_{\mathrm{B}}^{\mathrm{min}}}^{\lambda_{\mathrm{B}}^{\mathrm{max}}} \mathrm{P_A}(\lambda, \mathrm{t}')\,\mathrm{d}\lambda \tag{77}$$

By integrating this distribution over the region of the order parameter defining the state B, $\lambda_{\mathrm{B}}^{\mathrm{min}} < \lambda < \lambda_{\mathrm{B}}^{\mathrm{max}}$ one calculates the probability of reaching the state B at time t', given the trajectory started in the state A. This constitutes an alternative expression for the correlation function in terms of the reversible work of path confinement for a constant path duration, here denoted by t', and its associated distribution function $\mathrm{P}(\lambda\,;\mathrm{t}')$.

Based on this reformulation for the states correlation function $\mathrm{C}(\mathrm{t})$ in terms of the order parameter distribution for a constant path length $\mathrm{P}(\lambda\,;\mathrm{t})$, an efficient calculation based on the TPS ensemble was devised [91]. A convenient factorization of the correlation function yields

$$\mathrm{C}(\mathrm{t}) = \frac{\langle \mathrm{h_A}(\mathrm{x_0})\mathrm{h_B}(\mathrm{x_t})\rangle}{\langle \mathrm{h_A}(\mathrm{x_0})\mathrm{h_B}(\mathrm{x_{t'}})\rangle}\,\mathrm{C}(\mathrm{t}') \tag{78}$$

where $\mathrm{C}(\mathrm{t}')$ is the correlation function defined for an alternative path duration t'. The calculation of the rate for the transition path ensemble can then be broken down to first evaluating the $\langle \mathrm{h_B}(\mathrm{t})\rangle_{\mathrm{AB}}$ in the interval $[0, \mathrm{T}]$,

$$\langle \mathrm{h_B}(\mathrm{t})\rangle_{\mathrm{AB}} = \frac{\langle \mathrm{h_A}(\mathrm{x_0})\mathrm{h_B}(\mathrm{x_t})\rangle}{\langle \mathrm{h_A}(\mathrm{x_0})\rangle} \tag{79}$$

by performing the TPS sampling for the constant path length T that connect the stable states defined with respect to an order parameter $\lambda(\mathrm{x})$. If the time derivative of $\langle \mathrm{h_B}(\mathrm{t})\rangle_{\mathrm{AB}}$ displays a plateau, the intermediate time for the reaction where the flux settles has been reached for the given path length T, $\tau_{\mathrm{mol}} < \mathrm{t} \equiv \mathrm{T} \ll \tau_{\mathrm{rxn}}$. The correlation function at an alternative time point which comes out of the factorization in Equation 78 is then evaluated for a time $\mathrm{t}' < \mathrm{T}$, by umbrella sampling the TP ensembles of duration t' that begin in state A and end in the i-th window. The correlation function $\mathrm{C}(\mathrm{t}')$ is calculated by integrating the reconstructed distribution in the order parameter as in Equation 77. Finally the forward rate constant is expressed as plateau for the time derivative of the correlation function

$$k_{TPS}(t) = \frac{dC(t)}{dt} = \frac{\langle \dot{h}_B(t) \rangle_{AB}}{\langle h_B(t') \rangle_{AB}} \times C(t'). \tag{80}$$

This transition path formalism reduces to the reactive flux formalism when the stable states are defined as adjacent in the phase space, that is if $h_A(x) + h_B(x) = 1$. In other words, the dividing surface $\lambda(x) = \lambda^*(x)$ is placed at the boundary of the two states so that $h_A(\lambda) = \theta(\lambda - \lambda^*)$ and $h_B(\lambda) = \theta(\lambda^* - \lambda)$. Then, if both $C(t')$ and $\langle h_B(t') \rangle_{AB}$ are approximated for small t' as linear, the rate can be expressed as [103]

$$k(t) = \langle \dot{h}_B(t) \rangle_{AB} \times \frac{k(0)t'}{\langle \dot{h}_B(0) \rangle_{AB} t'} = \frac{\langle \dot{h}_B(t) \rangle_{AB}}{\langle \dot{h}_B(0) \rangle_{AB}} k^{TST} \tag{81}$$

It was previously defined that the reactive flux rate at zeroth time is equal to the transition state theory rate, that is $k(0) = k^{TST}$. Since $k(t) = \kappa(t) \cdot k^{TST}$, the dynamical correction in the form of the transmission coefficient $\kappa(t)$ is thus equal to the $\langle \dot{h}_B(t) \rangle_{AB}$ function normalized by its value at zeroth time $\langle \dot{h}_B(0) \rangle_{AB}$.

The double-well potential model system served as a demonstration of the equivalence of the two fluxes, the reactive flux and the flux of the correlation function calculated for the TPS ensemble. These results are presented in the Results Section 3.5.3. The model settings used for this example were the barrier height $Q = 4\ k_B T$ the time step the time step for the Langevin integrator $\Delta t = 0.01$s and the friction constant $\gamma = 1.0\ s^{-1}$. An ensemble of 10000 reactive pathways of constant length $T = 10$ s were generated with a shooting and shifting TPS algorithm for stochastic dynamics. The average $\langle h_B(t) \rangle_{AB}$ over the path ensemble was calculated using Equation 79, where indeed its derivative reached a plateau within the given path length. The probability factor of path confinement, $C(t')$ in Equations 77 was calculated for the time point $t' = 5$s, midway of the total path length. A set of 5 overlapping umbrella windows in the order parameter x, were defined up as $[-2, -0.4], [-0.7, 0], [-0.5, 0.5], [0, 0.7], [0.4, 2]$. What followed was sampling the associated distributions $P(x\,; t'\,; i)$ in separate TPS runs of pathways starting in the state A, left of the dividing surface $x < x^* \equiv 0$, and ending at time point t' in the state defined by the respective i-th umbrella window. The umbrella sampling TPS runs were thus normal TPS runs with variable definition for the end state, and the constant length of paths $T = t' = 5$s. The probability for the full range in the order parameter $P(x\,; t')$ was reconstructed by histogram matching [104], by rescaling the overlapping histograms $P_2'(\lambda) = P_2(\lambda) \cdot (P_1(\lambda_\alpha)/P_2(\lambda_\alpha))$ and normalizing the resulting histogram.

2.8 Activation entropy: Arrhenius and van’t Hoff analysis

The activation entropies and enthalpies can be obtained experimentally by measuring the reaction rate as the function of temperature [44]. By taking the natural logarithm of the expression for the transition state theory in Equation 23, assuming the transmission coefficient $\kappa = 1$ and decomposing the free energy to its enthalpic and entropic contributions, $\Delta G^{\#} = \Delta H^{\#} - T\Delta S^{\#}$, one obtains

$$\ln\left(\frac{k^{TST}}{T}\right) = \ln\left(\frac{k_B}{h}\right) + \frac{\Delta S^{\#}}{R} - \frac{\Delta H^{\#}}{RT}. \tag{82}$$

Assuming that the enthalpies and entropies depend only weakly on temperature, they are treated as constants for a given experimentally measured temperature range. One obtains the activation parameters from the plot of $\ln(k/T)$ against $1/T$, where k is the experimentally measured rate, which produces a straight line with the slope equal to $-\Delta H^{\#}/R$ from which the activation enthalpy is obtained. The activation entropy is extracted from the intercept defined for $1/T = 0$, where the temperature is $T = \infty$ and thus is poorly defined. More often, the resulting temperature dependence of the rate is interpreted using the empirical Arrhenius equation, written in the logarithmic form

$$\ln(k) = \ln A - \frac{E_a}{RT} \tag{83}$$

The Arrhenius parameters, the prefactor A and the activation energy E_a can be related back to the activation parameters as defined in the transition state theory from the definition for the activation energy

$$E_a = RT^2\left(\frac{d\ln k}{dT}\right)_V. \tag{84}$$

For a unimolecular reaction where there is no change in the number of molecules from the reactant to the TS, the relations between the Arrhenius and the activation parameters can be expressed as the Equation 85. The prefactor is essentially related to the entropic activation, while the activation energy is the enthalpic contribution.

$$\Delta H^{\#} = E_a - RT; \;\; \Delta S^{\#} = R\left(\ln A - \ln\frac{k_B T}{h} - 1\right) \tag{85}$$

To decompose the enthalpic and entropic contributions to the free energy, we employ an approach recently presented in the context of an enzymatic reaction modelled within the QM/MM framework [43]. Therein, the activation parameters were extracted from the temperature dependence of the free energies. Here we employ the same approach where given the coordinate X as the reaction coordinate we run simulations at different temperatures, $T = \{233, 283, 333, 383\}$ [K] to reconstruct the associated free energy profiles at the given temperatures, $F(X; T)$. Then from the functional dependence $(\Delta F^{\#}/T, 1/T)$ where $\Delta F^{\#}$ is the barrier height at a temperature T,

$$\frac{\Delta F^{\#}}{T} = \frac{\Delta H^{\#}}{T} - \Delta S^{\#}, \tag{86}$$

the activation entropy $\Delta S^{\#}$ is obtained as the negative intercept and the activation enthalpy $\Delta H^{\#}$ as the slope. The importance of the solvent is captured by direct sampling with molecular dynamics, unlike for the continuum solvent models which cannot account for the configurational entropy of the solvent.

3 Results and Discussion

The performance of various levels of theory in terms of the optimized geometries for the stable states and the transition structures as well as the activation energies were tested for the two compounds, the unsubstituted AB and the push-pull ppAB. The molecular schemes together with atoms and labels for the structural parameters are depicted in Figure 16.

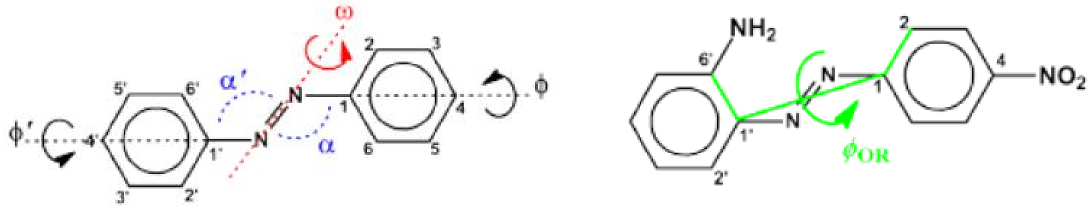

Figure 16. Molecular schemes of the compounds treated in this study with atom labels, azobenzene (left) and the push-pull substituted $4NO_2$-$6'NH_2$ AB referred to as ppAB (right). Also indicated are the labels for the geometric parameters.

3.1 Quantum Chemical Optimization – Benchmarking

In a seminal work concerning an ab-initio study for the isomerization of AB [21], a “perpendicular invertomer” was established as the lowest energy transition structure on the ground state potential energy surface. The structure is linear with respect to the bend angle $\alpha \sim 180°$ with its phenyl rings perpendicular, and the activation electronic energy calculated with CASSCF/6-31G* level of theory, $\Delta E^{\#} = 98.32 \text{ kJ mol}^{-1}$. The additional transition structures for the ground state PES considered were the “planar invertomer” with planar phenyl rings and the associated activation energy $\Delta E^{\#} = 135.56 \text{ kJ mol}^{-1}$, and the pure “rotamer”, with the dihedral $\omega = 90°$, the bend angle $\alpha \sim 125°$ and the activation electronic energy $\Delta E^{\#} = 164.43 \text{ kJ mol}^{-1}$. The transition structure with the largest electronic energy, the rotamer lied close to the conical intersection of the ground state S_0 and the excited state surface S_1. This result was confirmed for the lower level of theory B3LYP/6-31G* as well in a more recent study [4]. The electronic energy associated to the perpendicular invertomer was $\Delta E^{\#} = 106.1 \text{ kJ mol}^{-1}$, a slight overestimate compared to the CASSCF result. Furthermore, the transition structures for the push-pull substituted azobenzenes in gas phase were also found to be of an invertomer type. The structures were always linearized on the side of the phenyl ring carrying the electron acceptor group, for example a nitro group NO_2. In general, substitution with electron acceptors resulted in lowering of the activation energies compared to the pure azobenzene.

With these findings in mind, we compared the performance of semi-empirical methods, PM3 and DFTBA/DFTB3, with higher levels of theory. Our goal was to establish a computationally less demanding QM method to use in dynamical simulations that reproduced the geometric and energetic parameters for azobenzene in an adequate way. The higher levels of QM theory considered in benchmarking were the Hartree-Fock method (HF) and the density functionals, B3LYP, a very successful functional for a range of chemical applications [44] including the isomerization of azobenzene, and PBE, the density functional used to parametrize the semi-empirical DFTB functionals.

The resulting geometries of the transition structures and the activation parameters are given in Table 4 for the two compounds, AB and the push-pull ppAB (see Figure 16). For the unsubstituted AB, the electronic energy $\Delta E^{\#}$ was overestimated with HF compared to CASSCF, whereas with both density functionals B3LYP and PBE it was overestimated to a lesser extent and thus they performed better for pure azobenzene AB. The reaction energies ΔE_{ct} were underestimated by all methods considered (HF, B3LYP, PBE) when compared to the CASSCF result $\Delta E_{ct} = 84.10\ \mathrm{kJ\ mol^{-1}}$ [21]. The electronic activation and reaction energy for the push-pull derivative ppAB were previously evaluated at the B3LYP/6-31G* level of theory in [4] and amounted to $\Delta E^{\#} = 65.61\ \mathrm{kJ\ mol^{-1}}$ and $\Delta E_{ct} = 93.59\ \mathrm{kJ\ mol^{-1}}$, respectively. Our results substantially deviated from those, due to looser convergence criteria used in our optimization protocols. Both of the stated activation parameters were again overestimated with HF.

Table 4. Selected geometry and activation parameters for AB and ppAB at various levels of QM theory (Level of Theory) with the basis set 6-31G*. All energies are given in $\mathrm{kJ\ mol^{-1}}$, and angles in degrees. The energy parameters are: the electronic energy difference between cis and trans isomer i.e. the reaction energy, ΔE_{ct}, the electronic energy difference between the TS and the cis isomer i.e. the activation electronic energy, $\Delta E^{\#}$, and the activation Gibbs free energy at $T = 298.15\ \mathrm{K}$. The geometry parameters are dihedral angles and angles for the Transition Structure, labelling for which is indicated in Figure 16. The PCM model was used to represent solvent, PCM-dm DMSO and PCM-tol toluene, where the level of theory used was B3LYP/6-31G*. *DFTB3 energies were evaluated as Single Point Energies using cis, trans and TS structures optimized at DFTBA level, due to technical reasons (the TS search is not implemented for DFTB3 level of theory).

AB LoT	ΔE_{ct}	$\Delta E^{\#}$	$\Delta G^{\#}$	ω	α	α'	ϕ'	ϕ	ϕ_{OR}
HF	72.33	135.47	128.68	179.87	179.86	117.36	0.00	90.06	-102.11
B3LYP	63.58	105.97	96.97	179.10	179.43	117.00	0.49	93.92	106.03
PBE	56.75	96.97	90.65	-143.63	178.76	116.58	0.36	69.70	-85.1
PCM-dm	54.93	111.38	104.00	171.90	179.25	117.62	0.16	97.78	102.21
PCM-tol	59.54	108.34	99.85	172.07	179.36	117.27	0.31	98.36	-100.46
DFTBA	18.52	103.17	94.57	-107.64	179.95	114.96	5.77	17.85	-72.41
DFTB3*	6.55	93.51	-	-	-	-	-	-	-
PM3	9.22	113.45	111.50	-177.12	176.66	121.38	5.12	86.81	-103.12

ppAB LoT	ΔE_{ct}	$\Delta E^{\#}$	$\Delta G^{\#}$	ω	α	α'	ϕ'	Φ	ϕ_{OR}
HF	68.53	113.25	108.78	43.29	179.68	119.04	4.54	-132.94	103.84
B3LYP	59.29	80.22	74.51	-72.09	179.62	119.42	3.34	163.47	-96.92
PBE	51.75	70.91	63.85	102.56	179.42	119.34	3.33	-166.04	-97.45
PCM-dm	52.49	61.84	58.67	-89.24	134.43	121.10	5.53	-177.75	-144.18
PCM-tol	55.51	74.77	67.81	-52.27	179.13	119.99	2.46	143.66	104.17
DFTBA	21.86	74.03	66.95	94.68	179.70	116.37	2.10	174.97	122.81
DFTB3*	9.69	57.28	-	-	-	-	-	-	
PM3	8.58	101.75	97.22	-91.57	177.56	119.37	3.43	-176.03	114.12

Regarding the transition structure geometries for both AB and ppAB in vacuum, an invertomer with the nearly linear bend angle $\alpha \sim 180°$ and the phenyl rings close to perpendicular was predicted with all QM methods considered. An orientation dihedral parameter ϕ_{OR} was defined in the scheme in Figure 16 as the measure for the relative orientation of the phenyl rings, where $\phi_{\mathrm{OR}} \sim 90°$ for perpendicular and $\phi_{\mathrm{OR}} \sim 0, 180°$ for planar rings. One difference in the transition structure geometry across the QM levels of theory that stands out is in the central dihedral ω. For AB this parameter was close to the value it would attain in the trans state, $\omega \sim 180°$, while for the push pull it was closer to the value for the pure rotamer transition state, $\omega \sim 90°$. The push-pull transition stuctures were thus more rotamer-like where a combination of the central bend angle and dihedral, $\alpha \sim 180°$ and $\omega \sim 90°$, would indicate to a concerted motion along both degrees of freedom and thus some combination of inversion and rotation as the underlying mechanism. In this respect, the transition structure for the unsubstituted AB associated to the semiempirical DFTBA potential would indicate a greater concerted motion along the dihedral and angle degrees of freedom compared to the PM3 potential. On the other hand, for the push-pull ppAB this difference between the semiempirical methods considered was not evident where a similar concerted inverto-rotamer was predicted as the transition structure. In conclusion, the lowest energy transition structures associated to the ground states for both semiempirical methods DFTBA and PM3 was indeed the perpendicular invertomer, in agreements with the higher levels of theory.

Regarding the performance of the semiempirical methods with respect to the activation parameters compared to CASSCF as the highest level of theory [21], the same trends of overestimated activation energy and the underestimated reaction energy were obtained. Fortunately though, the DFTBA result deviated less than PM3 in this respect with the activation barriers $\Delta E^{\#}$ overestimated to a lesser extent. This fact justified our choice of the density functional tight-binding methods (DFTB) over the PM3 method. Unfortunately, due to technical difficulties concerning the implementation of a transition structure optimization algorithm with the extended DFTB3 method, the transition structure could not be obtained and the similar comparison with the PM3 method could not be performed. Nevertheless we consider the DFTB3 method to be an improvement over the DFTB(A) due to greater accuracy of the electronic density computation. Namely, the DFTB3 is an extension of the density-functional tight-binding method DFTB(A) insofar the total DFT energy is expanded up to the third-order around the reference density, instead of only up to the second, and with the charge redistribution calculated in a self-consistent manner [54, 55]. This is particularly valuable since we aim to explore the polarization effects of explicit solvents in the QM/MM electronic embedding scheme.

In conclusion, our choice of the semiemprical method to use in dynamical sampling was DFTB3 due to, firstly, the computational convenience as it has recently been implemented in Gromacs as the molecular dynamics engine of our choice [74]. Secondly, as established with benchmarking presented in this section, the transition structures and activation parameters predicted by the DFTB(A) were in good agreement with the results for the higher levels of QM theory.

Table 5. Structural parameters for the optimized cis and trans stable states for compounds: AB (cis), AB (trans), ppAB (cis), ppAB (trans). Compared for the B3LYP/6-31G* and PBE/6-31G* and its semi-empirical parametrizations, DFTBA and DFTB3. All angles are in degrees, and distances in Å

AB (cis)	ω	α	α'	ϕ'	ϕ	ϕ_{OR}	r_{CN}	r_{NN}	r_{NC}
B3LYP	9.78	124.12	124.12	50.09	49.88	-41.11	1.4357	1.2495	1.4358
PBE	11.99	123.98	123.98	47.42	47.37	-42.28	1.4343	1.262	1.4344
DFTBA	10.67	120.49	120.50	51.63	51.63	34.28	1.4203	1.2681	1.4202
DFTB3	9.99	121.41	121.35	54.21	54.15	-27.85	1.4397	1.2637	1.4397

****

AB (trans)	ω	α	α'	ϕ'	Φ	ϕ_{OR}	r_{CN}	r_{NN}	r_{NC}
B3LYP	180.00	114.81	114.81	0.01	0.01	-179.99	1.4186	1.2606	1.4186
PBE	-180.00	114.16	114.16	-0.02	-0.02	179.96	1.4184	1.2767	1.4184
DFTBA	180.00	113.86	113.86	0.02	0.00	-179.90	1.4128	1.2860	1.4128
DFTB3	-179.96	114.56	114.56	0.17	0.64	-179.26	1.4304	1.2935	1.4305

****

ppAB (cis)	ω	α	α'	ϕ'	ϕ	ϕ_{OR}	r_{CN}	r_{NN}	r_{NC}
B3LYP	12.50	126.14	124.79	32.34	57.60	86.00	1.4138	1.2545	1.4239
PBE	16.03	125.97	125.18	27.74	54.36	84.11	1.4087	1.2683	1.4178
DFTBA	-14.16	122.12	120.89	-37.95	-54.16	36.92	1.4086	1.2730	1.4096
DFTB3	14.13	123.71	121.39	39.74	58.12	97.03	1.4218	1.2678	1.4328

****

ppAB (trans)	ω	α	α'	ϕ'	Φ	ϕ_{OR}	r_{CN}	r_{NN}	r_{NC}
B3LYP	-178.17	114.83	115.99	5.88	7.04	-166.44	1.3956	1.2683	1.4127
PBE	-176.85	114.24	115.55	6.88	10.12	-162.36	1.3926	1.2862	1.4101
DFTBA	-177.04	114.62	113.70	5.19	15.48	-158.73	1.4058	1.2927	1.3959
DFTB3	-176.20	114.51	115.47	4.20	22.17	-152.61	1.4185	1.3019	1.4117

To complement the results for benchmarking the semiempirical DFTB against the higher levels of DFT theory, in this section we present the result for the optimized cis and trans stable states structures. Unlike the transition structures, the stable state structures optimization with DFTB3 was implemented in the ASE software [105]. Our main objective thus was to compare the performance of the DFTB3 functional against both the 'lower level' DFTB(A) as well as the higher level DFT methods, B3LYP and PBE, with respect to the stable states geometries. The structural parameters are listed in Table 5. We found that DFTB3 outperformed DFTBA where for a range of parameters, the bending angles α, α' and the side-dihedral angles ϕ, ϕ' were closer in value to the B3LYP result. The bond lengths r_{CN} seemed to be better reproduced by DFTB3, which is possibly due to an improved fitting procedure for the atom pairs repulsion potential [55, 56]. A difference in the phenyl ring orientation parameter ϕ_{OR} for the optimized cis ppAB structures, between methods DFTB3 where $\phi_{OR} = 97°$ and DFTBA where $\phi_{OR} =$

37°, was due to there being two different minima with respect to this parameter. The associated difference in electronic energy for the two structures was proved to be negligible.

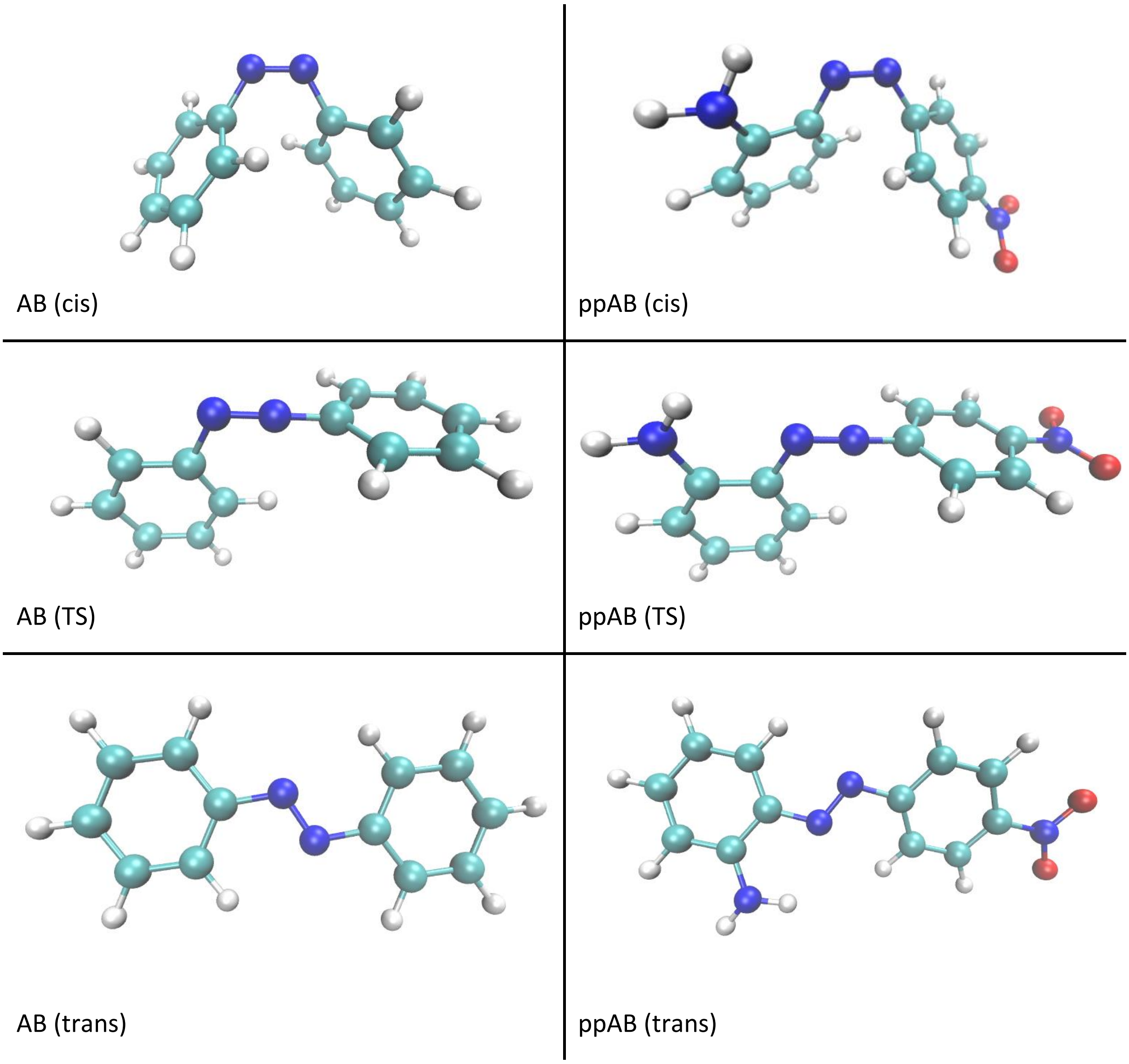
AB (cis)
ppAB (cis)
AB (TS)
ppAB (TS)
AB (trans)
ppAB (trans)

Figure 17. Optimized cis, trans and transition structures for AB (left column) and ppAB (right column) with the DFTBA method.

3.1.1 Polarizable Continuum treatment of solvent for the push-pull ppAB

The substitution of azobenzenes with electronically active residues that are either electron donors or acceptors to the phenyl rings, increases their polarity and in turn makes the cis → trans isomerization of the so called push-pull ABs particularly sensitive to solvent polarity. It has been speculated that the mechanism changes in polar solvents from inversion to rotation, where the bend angle does not linearize but stays close to the value it has in the cis state, $\alpha \sim 125°$. The transition state associated with the rotation mechanism, the "rotamer", has a formally broken N=N double bond which facilitates rotation. This allows for a formation of a transition structure with a "zwitterionic" character and a high dipole moment, which is further stabilized in highly polar solvents [4]. With solvent modelled as a polarizable continuum (PCM), the transition structures for the push-pull azobenzene ppAB in a highly polar DMSO, $\varepsilon = 46.7$, was in fact optimized into a bent structure with respect to the bend angle, $\alpha = 134°$. On the other hand, the transition structure in the low polarity toluene, $\varepsilon = 2.4$, remained linear, with the bend angle $\alpha = 179°$. The molecular structures for the optimized states are depicted in Figure 17, while the geometric as well as activation parameters are listed in Table 4 in the previous section. The activation energy $\Delta E^{\#}$ for the push-pull ppAB was lowered in DMSO compared to the gas phase or toluene due to a greater stabilization of the transition structure, in agreement with previous findings [4]. Due to stabilization of both the cis form and the transition structure, the reaction and the activation energies, ΔE_{ct} and $\Delta E^{\#}$ respectively, were lowered in DMSO. This would imply a greater stabilization of the more dipolar transition structure [4] compared to the cis isomer. For the unsubstituted AB the transition structure was insensitive to solvent polarity and was optimized into the same type of an invertomer as in the gas phase.

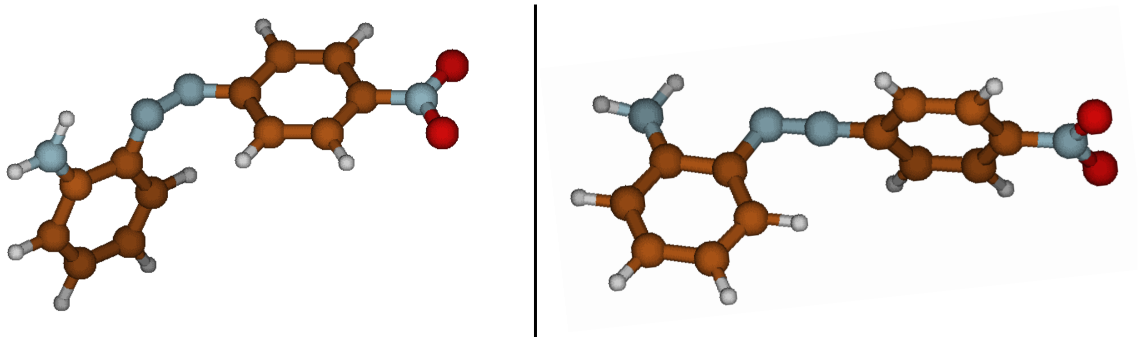

ppAB TS (DMSO)

ppAB TS (toluene)

Figure 18. Transition structures for ppAB optimized with the PCM model and the level of theory B3LYP/6-31G*. The transition structure in highly polar DMSO ($\varepsilon = 46.7$) is a rotamer, while for the low polarity toluene ($\varepsilon = 2.4$) is still an invertomer.

3.2 Potential of Mean Force: the $\omega, \alpha, X\ (\omega, \alpha)$ reactive coordinates

The main advantage of using the free energy surfaces (FES) over the potential energy surfaces is the explicit inclusion of entropic effects at a finite temperature. Consequently, the relative probabilities of being in a transition or a stable state are directly extractable from the FES. In this section we focus on the ppAB derivative in the gas phase described with *ab-initio* (QM: DFTB3) stochastic dynamics. Based on the QM optimized transition structures, the relevant reactive variables for the $\mathrm{cis} \rightarrow \mathrm{trans}$ isomerization are the central dihedral and the bend angle, ω, α, the collective variables with respect to which the free energy profile was reconstructed using metadynamics.

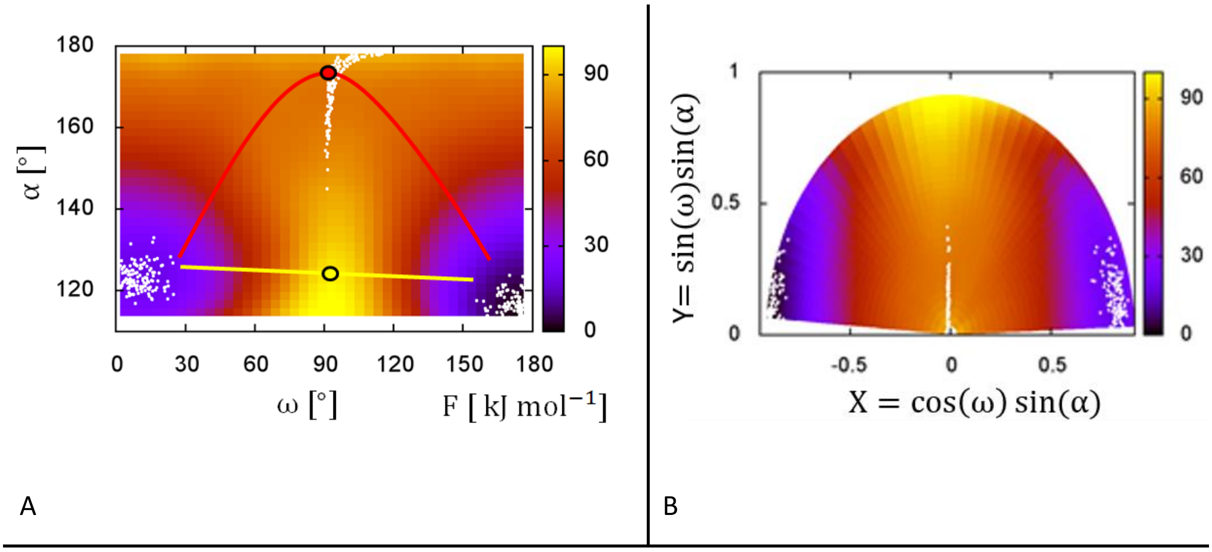

Figure 19. A: The free energy surface for ppAB as a function of (ω, α) coordinates reconstructed by meta-dynamics with the DFTB3 level of theory at temperature $\mathrm{T} = 333\ \mathrm{K}$. The red and the yellow curve illustrate the inversion and rotation pathway, respectively, with the location of the putative linear and the dihedral TS as spheres. Overlaid as white dots are the representative ensembles for the cis and trans stable states, $\mathrm{X}^{\mathrm{cis}} \sim 0.9$ and $\mathrm{X}^{\mathrm{trans}} \sim -0.9$, and the barrier top $\mathrm{X} = \mathrm{X}^{*} = -0.01$. B: The transformed FES as a function of the coordinates X and Y, where $\mathrm{X} = \sin\alpha \cos\omega$ and $\mathrm{Y} = \sin\alpha \sin\omega$. The stable states and the transition region are overlaid as white dots.

Upon inspection of the 2D free energy map in Figure 19A, the minimum energy path in the (ω, α) space for a finite temperature of $\mathrm{T} = 333\ \mathrm{K}$ seems to be of an inversion type via an extended bend angle $\alpha \sim 180°$, in accordance with the zero-temperature result represented by the optimized transition structure of the underlying potential energy surface. In fact at a finite temperature, the transition region connecting the two stable states, the cis $(\omega \sim 10°)$ and the trans isomer $(\omega \sim 180°)$, is rather broad for the values of the bend angle around $\alpha \sim 170°$. There are many potential pathways that proceed through transition states comparable in energy that are more bent with respect to the angle α and are thus more rotation-like. The pure rotational pathway though which would proceed without much change in the bend angle, $\alpha \sim 125°$ is much higher in free energy, by $\sim 30\ \mathrm{kJ\ mol}^{-1} \cong 11\ \mathrm{k_B T}$. The two extremal pathways, the inversion and rotation are depicted in Figure 19A with red and yellow solid lines and associated putative transition states as spheres, respectively.

A more intuitive picture of a reaction process is achieved through mapping the multidimensional problem to a free energy profile along a one-dimensional reaction coordinate. As a convenient coordinate we introduced a sine-cosine combination of the two central angles, $\mathrm{X} = \sin\alpha \cos\omega$. The coordinate X has a convenient property that the minimum energy path connecting the two stable states cis and trans on the potential energy surface associated to it is smooth and continuous, unlike for the coordinates ω, α. Starting from the saddle point, this path was obtained by the Internal Reaction Coordinate (IRC) following (described in Methods Section 2.2.1). The variation of the coordinates $\omega, \alpha, \mathrm{X}$ and ϕ_{OR} along the minimum energy path at the DFTBA level of theory is depicted in Figure 20. The minimum energy path with respect to the ω, α coordinates exhibited a singularity for the bend angle at $\alpha = 180°$, with an abrupt increase in the ω coordinate which is formally undefined at that value for the bend angle. The relative phenyl rings orientation parameter ϕ_{OR} is plotted to point out that the stable states reached by IRC following are not the global minima, as the phenyl rings in the optimized cis and trans isomers of ppAB at the DFTBA level of theory were not perpendicular as the end states of the IRC following path, but were $\phi_{\mathrm{OR}} = 37°$ in cis and $\phi_{\mathrm{OR}} = -159°$ in the trans isomer. The minimum energy path with respect to the $\omega, \alpha, \mathrm{X}$ and ϕ_{OR} coordinates was qualitatively similar for the unsubstituted AB which we do not show here.

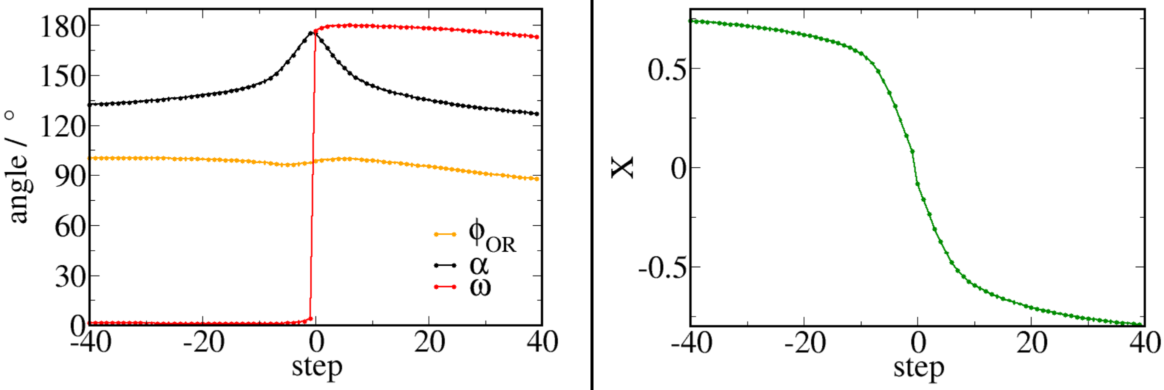

Figure 20. Internal Reaction Coordinate following: change in parameters $\alpha, \omega, \mathrm{X}$ and ϕ_{OR} along the minimum energy path for ppAB at the DFTBA level of theory. Starting from the 0-th step at the TS, with the step size $0.1\ \mathrm{Bohr} \equiv 0.053\ \mathrm{Å}$, in 40 steps in the negative direction towards the cis, and 40 steps in the positive direction towards the trans state.

The free energy profiles with respect to the coordinate X for compounds AB and ppAB in both vacuum and DMSO are depicted in Figure 21. They were reconstructed using umbrella sampling and WHAM reweighting as described in the Methods Section 2.4.2, whereat the simulations in explicit solvent were performed within the QM/MM framework with electronic embedding as described in the Methods Section 2.3. The one-dimensional coordinate X describes the cis → trans isomerization from the cis state, where $\mathrm{X}^{\mathrm{cis}} \sim 0.9$ via the transition region, where $\mathrm{X}^{\mathrm{TS}} \sim 0$, to the trans state $\mathrm{X}^{\mathrm{trans}} \sim -0.9$. Essentially, the coordinate X is a good order parameter insofar it distinguishes between the stable states.

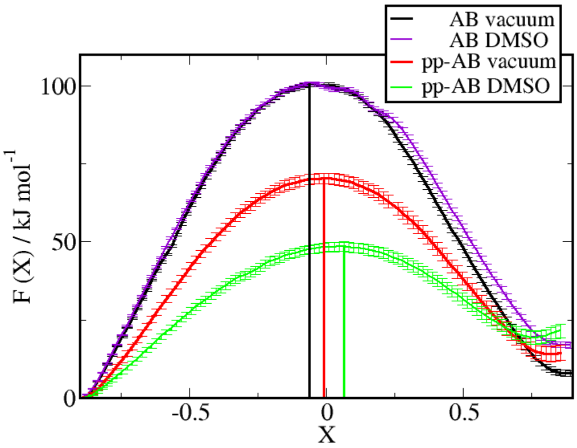

Figure 21. Potential of mean force (PMF) as a function of the coordinate $X = \sin\alpha\cos\omega$ for AB and ppAB in vacuum (black and red, respectively) and AB and ppAB in DMSO (violet and green, respectively). Calculated by WHAM reweighting the umbrella sampling distributions with 30 windows and the window size $\Delta X = 0.06$. The cis stable state is located at $X^{\mathrm{cis}} \sim 0.9$ and the trans at $X^{\mathrm{trans}} \sim -0.9$, with the transition region where the energy is maximal in the vicinity $X^{\mathrm{TS}} \sim 0$.

Notably, the position of the free energy maximum $X = X^*$ slightly shifted to more positive values in the following order AB in vacuum, ppAB in vacuum and ppAB in the highly polar DMSO, with the associated values $X^* = -0.06$, $X^* = -0.01$, $X^* = 0.06$ respectively. There was no shift in the position of the maximum going from AB in vacuum to DMSO where it remained at $X^* = -0.01$ for both cases. In terms of the (ω, α) parameters, this shift in X is mostly affected by the dihedral parameter ω and not the bend angle α, as reported in Table 6. This would imply that the shift was not due structures of the transition region being more bent with respect to the angle α, an effect expected at least in the case of ppAB in DMSO.

Some additional qualitative trends for the effect of solvent were reproduced with the potential of mean force approach. Firstly, the activation barrier heights, calculated as the difference in energies of the transition state and the cis state, $\Delta F^{\#} = F^{\mathrm{TS}} - F^{\mathrm{cis}} = F(X^*) - F(X^{\mathrm{cis}})$, were lowered in the same order as the QM optimized activation energies. In addition, the free energy barrier was reduced upon push-pull substitution that is going from AB to ppAB in vacuum, but also for the push-pull in highly polar DMSO where the free energy barrier was substantially lowered compared to the vacuum case.

Table 6. Activation and Geometry Parameters from the Free Energy Profiles $F(X)$ in Figure 21.

Compound	$\Delta F^{\#}/\mathrm{kJmol}^{-1}$	$\Delta F_{\mathrm{ct}}/\mathrm{kJmol}^{-1}$	X^*	$\omega/°$	$\alpha/°$
AB vacuum	92.46 +/- 1.56	7.92 +/- 0.94	-0.06	126.1 +/- 28.6	171.3 +/- 4.6
AB DMSO	83.78 +/- 1.42	16.95 +/- 0.89	-0.06	126.1 +/- 28.6	170.7 +/- 5.2
ppAB vacuum	56.25 +/- 4.06	14.11 +/- 2.47	-0.01	85.9 +/- 34.4	169.6 +/- 6.9
ppAB DMSO	29.20 +/- 3.64	19.34 +/- 2.20	0.06	68.8 +/- 22.9	166.7 +/- 9.2

3.2.1 Committor analysis for the coordinate X

The coordinate X describes the progress of a reaction between the stable states, from the cis isomer with $\mathrm{X}^{\mathrm{cis}} \sim 0.9$ via the transition state, with $\mathrm{X}^{*} \sim 0.0$, to the trans isomer, $\mathrm{X}^{\mathrm{trans}} \sim -0.9$. If the coordinate X is a good reaction coordinate, the transition region placed at its energy barrier that is the $\mathrm{X} = \mathrm{X}^{*}$ surface should coincide with "the separatrix". The separatrix is defined as a hypersurface containing transition states. Any trajectory that is relaxed from the transition state configurations, termed the transition state ensemble, has an equal probability of relaxing into either of the stable states. The so called committor probability $\mathrm{p_B}$ to commit into the state B should thus be 50 %. The distribution of the committor values for the transition state ensemble $\mathrm{P(p_B)}$ should thus be a Gaussian distribution centered at $\mathrm{p_B} \sim 0.5$.

The committor distributions for the configurations at the barrier top for the coordinate X were calculated by first restraining the system at the free energy maximum $\mathrm{X} \equiv \mathrm{X}^{*}$ (see Figure 21 and Table 6). Then, a total of 200 independent stochastic dynamics runs were produced from which single configurations for which $\mathrm{X} \equiv \mathrm{X}^{*}$ were selected randomly. In the second step, 100 fleeting trajectories per selected configuration were propagated until they relaxed into a stable state. The committor $\mathrm{p_B}$ was calculated as a fraction of those that reached the trans state as defined in Equation 58 of the Methods Section 2.5.4. The resulting committor distributions for AB and ppAB in, both, vacuum and in DMSO are plotted in Figure 22.

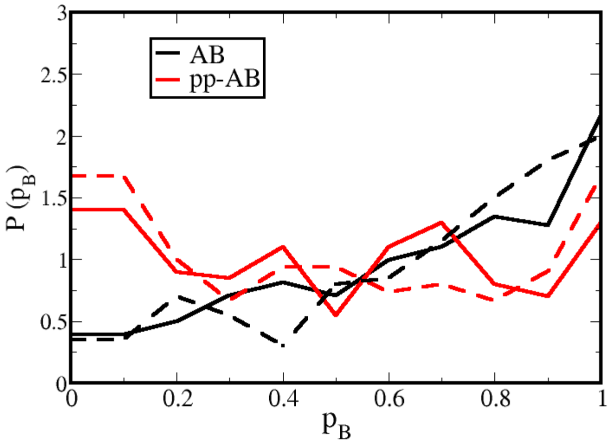

Figure 22. Committor distributions $\mathrm{P(p_B)}$ for ppAB (red) and AB (black) in gas phase (solid line) and in DMSO (dashed line) at $\mathrm{T} = 333\ \mathrm{K}$. They are uniform-like, with the ones for AB, in both vacuum and DMSO, are skewed to the trans state, $\mathrm{p_B} \sim 1$ (in red). Configurations restrained at the barrier top were used – 200 with $\mathrm{X} \equiv \mathrm{X}^{*} = -0.01$ for ppAB in vacuum, 200 with $\mathrm{X} \equiv \mathrm{X}^{*} = 0.06$ for ppAB in DMSO, 280 with $\mathrm{X} \equiv \mathrm{X}^{*} = -0.06$ for AB in vacuum and 200 with $\mathrm{X} \equiv \mathrm{X}^{*} = -0.06$ for AB in DMSO.

They were uniform-like for both ppAB and AB, with the latter being skewed to the trans state where the committor values are $\mathrm{p_B} \sim 1$. This skewing was reflected by a larger average committor value of $\bar{\mathrm{p}}_{\mathrm{B}} = 0.63 \pm 0.27$ for AB in vacuum, while for ppAB in vacuum it remained $\bar{\mathrm{p}}_{\mathrm{B}} = 0.50 \pm 0.30$. Notably, as a highly polar solvent, DMSO had no effect on the commitment probabilities for the ensembles restrained to the barrier top. The underlying cause for the uniform-like committor distribution could be the diffusive dynamics along the orthogonal directions, while skewing in either direction(s), to

$p_B \sim 1, 0$ is indicative of additional barrier(s) present along the orthogonal coordinates [34, 39]. In the latter scenario, the description of the reaction coordinate can be improved by introducing other order parameters relevant for the transition. In this respect, the skewing of the committor distributions for the $X = X^*$ ensemble of configurations for the AB derivative was thus indicative of the presence of additional barriers orthogonal to the surface $X = X^*$.

To resolve the underlying cause for the qualitative features of the committor distributions, we performed the committor analysis for the same restrained ensemble $X = X^*$ but at a very low temperature $T = 33$ K. For the conditions of a markedly reduced temperature, the diffusivity was essentially removed and the dynamics turned to almost entirely ballistic. In this case, the dynamics was governed solely by the potential gradient. For configurations both restrained $X = X^*$ and subsequently relaxed at the temperature $T = 33$ K, we observed a committor distribution skewed towards the trans state, $p_B \sim 1$, as shown in Figure 23 in magenta. The more pronounced skewing to $p_B \sim 1$ was observed for the unsubstituted AB in (B) than for the push-pull derivative ppAB in (A).

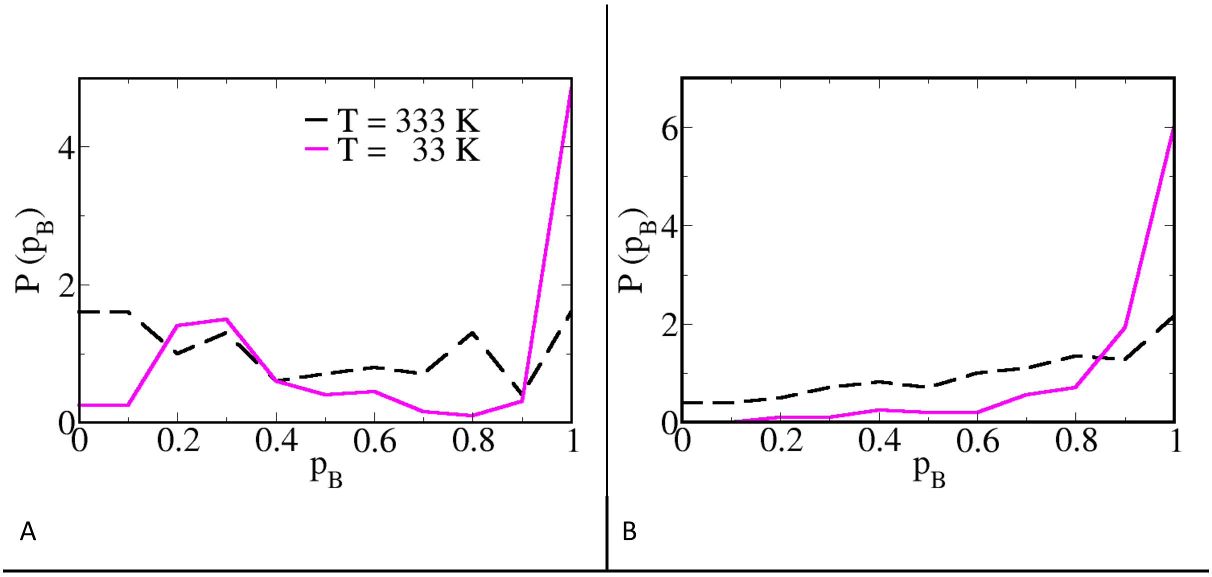

Figure 23. Committor distributions $P(p_B)$ compared at temperatures $T = 333$ K, $T = 33$ K for 200 independent configurations restrained at $X \equiv X^*$ in vacuum, for (A) ppAB, $X^* = -0.01$ and (B) AB, $X^* = -0.06$. The skewed distribution for more ballistic dynamics at $T = 33$ K is more pronounced for AB and indicates the presence of an additional barrier in order parameters orthogonal to X.

This finding indicated that $X \equiv X^*$ is a surface lying closer to the trans state basin of attraction and there exist additional barriers in variables orthogonal to it. Furthermore, the extremely pronounced skewing to only one stable state in the case of AB is indicative of there being a single dominant barrier along a single order parameter. For the push-pull ppAB, where the skewing was more complex and seemed to occur to the cis stable state, where $p_B \sim 0$, as well, there might be more parameters contributing to the reaction.

In conclusion, as the committor analysis for the ensemble of configurations restrained at the free energy barrier top $X \equiv X^*$ revealed, the coordinate X is not the ideal reaction coordinate. The committor analyses at a low temperature where the diffusivity was reduced revealed additional barriers orthogonal to the $X \equiv X^*$ surface to be present for both AB and ppAB. A single dominant barrier is most likely present for AB though, given the pronounced skewing of the committor distribution to the trans state only. In addition, the general broadening of the committor distributions can be attributed to the diffusive character for the underlying dynamics as expressed as the calculated χ coefficient measuring correlation of shooting outcomes as well as the transmission coefficients measuring the extent of trajectory recrossings, both of which will be discussed later in text. We revisit the reaction coordinate optimization and the identification of the other reactive coordinates beyond the coordinate X in Results Section 3.4.

3.3 Transition path sampling the **cis** → **trans** thermal isomerization

In this section we present the results of applying the transition path sampling algorithm for stochastic dynamics, as described in Section 2.5, to the cis → trans isomerization of AB and the push-pull ppAB derivatives. The main advantage over the potential of mean force approach presented in the previous section is that there is no need to predefine the reaction coordinate, but only parameters with respect to which the two stable states are well separated in the configuration space. We used the coordinate $\mathrm{X}\ (\omega, \alpha)$ to define the stable states.

The choice for a coordinate to define stable states is a possible source of bias. With a stringent definition in coordinate $\mathrm{X}\ (\omega, \alpha)$ the TPS stable states had comparable values for (ω, α) as in the equilibrated cis and trans states. Another source of bias was generating shooting points in the interface $\mathrm{X} = \langle -0.5, 0.5 \rangle$. Importantly, the interface should 'accommodate' both types of transition states, namely the inversion- and the rotation-like, allowing for possible switching to rotation-like paths during sampling. Fortunately, a rotation transition state is also located in the interface for the coordinate X, at $\mathrm{X}_{\mathrm{dih}}^{\mathrm{TS}} \sim 0$, since $\cos\ \left(\omega_{\mathrm{dih}}^{\mathrm{TS}} = 90°\right) \sim 0$ and $\mathrm{X} = \sin\alpha\cos\omega$. The inversion transition state attains the same value $\mathrm{X}_{\mathrm{lin}}^{\mathrm{TS}} \sim 0$ because of the bend angle coordinate and regardless of the dihedral, since $\alpha_{\mathrm{lin}}^{\mathrm{TS}} \sim 180°$ and $\sin\ (\alpha_{\mathrm{lin}}^{\mathrm{TS}} = 180°) \sim 0$. It is thus evident that the interface in coordinate X accommodates both the dihedral and linear transition states and allows for the possible divergence of pathways in the (ω, α) space.

The path statistics is collected in Table 7, such as the number of shooting points, the number of accepted path and the acceptance ratio. The latter was given by the ratio of the number of accepted paths and the total number of TPS iterations, and amounted to $\sim 40\%$ across the conditions. Since we performed 2-way shooting with stochastic dynamics, every newly accepted path was de-correlated from the previous. De-correlated paths did not share any configurations along the constant length paths apart from the configuration at the shooting point.

Table 7. Path Statistics for the collected TPS ensembles. The initial trajectory for all examples was of an inversion type. Path lengths were constant, $\mathrm{L} = 0.25$ ps for vacuum and $\mathrm{L} = 0.5$ ps for solvents.

	AB			**ppAB**		
	vacuum	toluene	DMSO	vacuum	toluene	DMSO
acceptance ratio	0.40	0.46	0.54	0.42	0.46	0.29
accepted paths	1196	457	542	2077	1100	865
shooting points	3000	1000	1000	5000	2415	3000

3.3.1 Time evolution of the reactive coordinates

The most straightforward way of analysing the sampled TPS trajectories is to inspect the time evolution for the relevant parameters. Most importantly, we monitor the central dihedral and the bend angle, ω, α, and the phenyl ring dihedrals ϕ, ϕ'. The phenyl ring dihedrals ϕ, ϕ' as well as the orientation dihedral parameter ϕ_{OR} as a measure for the relative orientation of the phenyl rings, are indicative of the so called "hula-twist" mechanism. For a hula-twist mechanism a simultaneous rotation around the N=N and twisting around one of the adjacent bonds, N-C occurs. This mechanism is known to be important for cis → trans isomerizations in general, even more so in restrained environments because of its volume preserving character.

To demonstrate the presence of hula-twisting, we plot the time evolution for the relevant parameters along the last accepted path of the TPS ensemble for AB in vacuum in Figure 24A, as well as the associated electronic energy in Figure 24B.

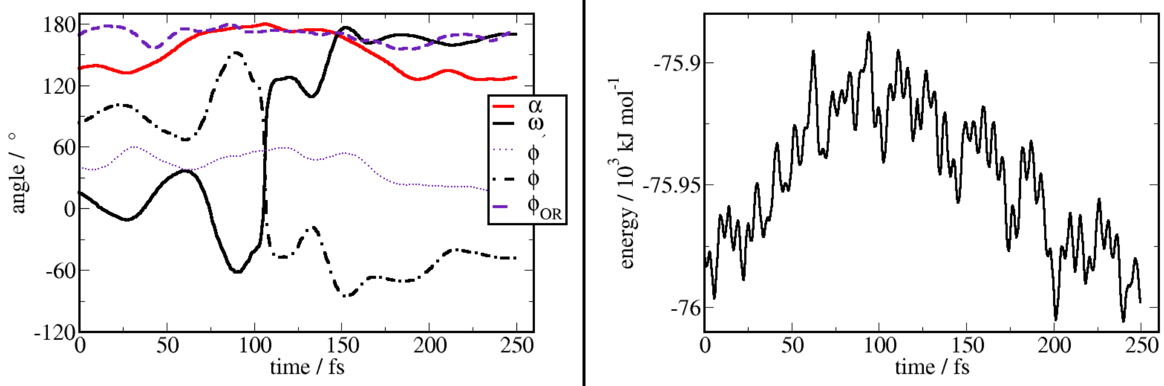

A

B

Figure 24. AB in vacuum. A: Time evolution of the structural parameters for cis → trans isomerization for the last accepted path of the TPS ensemble. B: Electronic energy along the same trajectory.

Based on the evolution of the central dihedral and the bend angle, $\omega, \alpha,$ the isomerization can be described as a mixture of inversion and rotation. The steady increase in the bend angle α is an uphill process and seems to initiate the rotation which proceeds downhill after the maximal angle has been achieved, $\alpha \sim 180^\circ$ at the middle of the path. Also, the side-dihedral adjacent to the side of the inverting nitrogen, the dihedral ϕ flipped by an amount $\sim 180^\circ$ following the flipping in the torsion coordinate ω. The simultaneous twisting around the adjacent N-C bond accompanied the rotation around the central N=N′ bond was observed and is indicative of the hula-twist mechanism. This feature was observed over all conditions where inversion was a dominant mechanism. We considered a TPS path for which the average bend angle $\alpha > 160^\circ$ to be of an inversion type, as defined later in text, in Section 3.3.3.

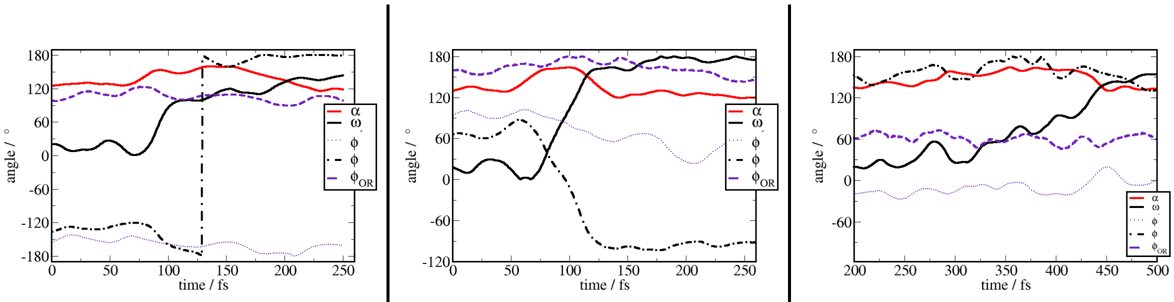

A

B

C

Figure 25. Time evolution of the structural parameters for cis → trans isomerization for the last accepted path of the TPS ensemble.

Both push-pull substitution and solvation in DMSO of the unsubstituted AB did not affect the observation that alongside inversion the hula-twist was also present. From the time evolution of the relevant parameters for ppAB in vacuum and AB in DMSO is plotted in Figure 25 A and B, respectively, it is apparent that the extension of the bend angle α occurred together with flipping in both of the central torsion ω and the twisting dihedral ϕ.

The one case where the hula-twist was not as pronounced was for ppAB in DMSO, where the underlying mechanism was more rotation-like and less inversion-like due to the less pronounced extension in the bend angle α, as depicted in Figure 22C. The orientation dihedral parameter ϕ_{OR} still remained close to constant during the transition.

To further corroborate the observation that the inversion and rotation occurred simultaneously, we calculated the duration of the two trajectory segments. The first segment was considered to be the "extension of the bend angle" from the value $\alpha = 140°$ to its maximal value, with the time duration $\tau_{\mathrm{inversion}}$. The second segment was considered to be the relaxation of the extended bend angle back to its initial value, $\alpha = 140°$, with the time duration τ_{rotation}. The statistics over the full TPS ensembles of paths is collected in Table 8. The inversion and rotation segments are on average equal in duration. In addition, the value for the dihedral ω at the midpoint of the segments or at the point where the bend angle α was maximal, amounted to an average of $\omega \sim 90°$. That is to say, half way through a cis → trans transition, the value for the rotation dihedral was midway between the values it assumes in the cis and trans stable states. All of this served to prove that indeed the isomerization progressed as a concerted motion along both degrees of freedom, the bend α and the torsion angle ω.

Table 8. Duration of the TPS paths segments leading up to the maximal extension of the bend angle to α_{max} and the associated value for the dihedral, $\omega_{\mathrm{for}\ \alpha_{\mathrm{max}}}$ ($\tau_{\mathrm{inversion}}$), and back relaxation to its initial value (τ_{rotation}). The statistics was calculated over the TPS ensembles.

compound	$\tau_{\mathrm{inversion}}$ [fs]	τ_{rotation} [fs]	α_{max} [°]	$\omega_{\mathrm{for}\ \alpha_{\mathrm{max}}}$ [°]
AB vacuum	46.4 +/- 19.2	43.8 +/- 19.5	174.9 +/- 3.8	90.2 +/- 40.2
AB DMSO	34.8 +/- 17.3	34.6 +/- 14.4	167.2 +/- 8.2	85.1 +/- 35.4
ppAB vacuum	51.3 +/- 28.3	56.8 +/- 27.3	172.9 +/- 6.0	85.5 +/- 40.1
ppAB DMSO	61.0 +/- 46.5	46.2 +/- 38.3	156.6 +/- 7.4	73.8 +/- 26.6

Based on the analysis of time evolutions for structural parameters, we observed the general mechanism for the cis → trans isomerization of azobenzene to be the 'rotation-assisted inversion with hula-twisting'. Interestingly, the push-pull derivative ppAB in the DMSO solvent experienced a pronounced shift to a more rotation-like mechanism with less pronounced hula-twisting. We extend this analysis to the full TPS ensemble of paths in the following sections.

3.3.2 Convergence test for the two alternative pathways: inversion vs rotation

A possible source of bias in the TPS sampling is the production of the initial reactive path. With the stable states defined with respect to the coordinate $\mathrm{X}\ (\omega, \alpha)$, the initial path connecting the cis and trans stable states was produced by steering the system along X. This resulted with an 'inversion-like' path in the (ω, α) space for all compounds and conditions considered. Even though the pure rotation path proceeding without the extension in the angle α is also plausible, it was shown to be much higher in energy and by $\sim 11\ \mathrm{k_B T}$ for ppAB in vacuum, see the free energy profile in Figure 21.

The convergence of TPS sampling given the alternative pure rotation path as the initial path was tested on the example of ppAB in vacuum. The initial rotation path was produced by steering along the dihedral coordinate ω only, without much change in the bend angle α. With the progression of TPS shooting and without biasing the sampling in any way, a switch to the energetically more favourable inversion was observed which we plot with the path density in the (ω, α) space in Figure 26.

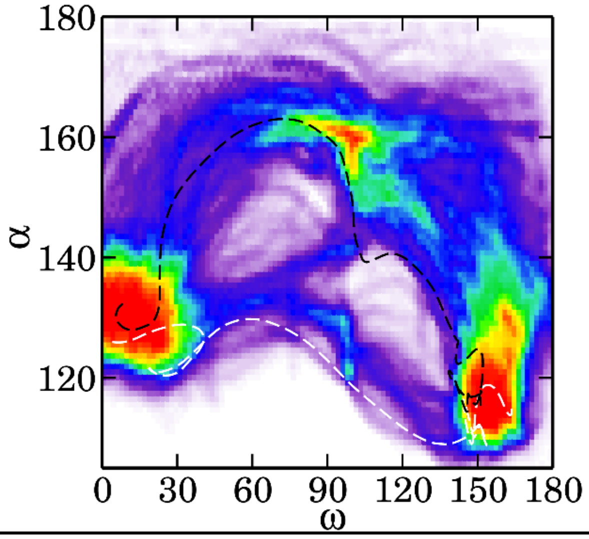

Figure 26. Convergence test of TPS sampling for ppAB in vacuum. Path density in (ω, α) space for an ensemble of 1473 paths where the initial path was of the rotation type, an example pathway depicted as white dashed line. An example initial path of an inversion character is depicted as a dashed black line. The path density ranges from white (no paths) to red via blue and green.

The back-switching to rotation-like pathways was not observed. This simple convergence test confirmed that starting from both an inversion like and rotation like pathway there was a tendency for the TPS sampling to converge to the same region in the (ω, α) space. The inversion-like pathway is indeed more natural for the system and that no bias was introduced by using it as an initial pathway.

3.3.3 Path densities and the most probable paths

One of our initial research questions was in how far does the push-pull substitution and polarity of the solvent affect the nature of the transition state. For that we inspect the path densities for the collected TPS path ensembles projected onto the central dihedral-angle (ω, α) space and the effect of increasing solvent polarity in the order vacuum, toluene, DMSO for both derivatives AB and ppAB.

The TPS path densities projected onto the two reactive coordinates (ω, α) across the conditions considered are plotted in Figure 27. Qualitatively described, the mechanism for both the push-pull substitution and the increased solvent polarity seemed to shift to a more rotation-like where the paths sample configurations with less extended bend angles α. This effect was more pronounced for the push-pull derivative ppAB than it is for the unsubstituted AB.

For a more quantitative analysis in terms of the mechanism, we defined the mechanism type by means of the maximal angle $\alpha_{\max}$ sampled in the interface of a TPS path. The three mechanism types are defined in the following way: inversion, $\alpha_{\max} > 150°$, mixed, $140° \leq \alpha_{\max} \leq 150°$ and rotation, $\alpha_{\max} < 140°$. It is worth emphasizing that we use the terms 'pathway' and 'mechanism' interchangeably. The mechanism statistics collected from the TPS path densities in (ω, α) is summarized in Table 9. The fraction of the pathway of a certain type ϕ_{TP} was calculated as a number of paths that sample a range in the bend angle $\alpha_{\max}$ defining a mechanism type divided by the total number of paths in an ensemble. This fraction is thus defined for the sub-ensembles of paths with rotation, mixed or inversion character.

Table 9. Statistics for the mechanism type for the TPS ensemble, expressed by the fraction of TPS paths out of the total TPS ensemble Φ_{TP} and the average angle associated with the interface for the most probable path $\alpha_{\mathrm{avg}}^{\mathrm{MP}}$.

	vacuum		toluene		DMSO	
mechanism type	AB	ppAB	AB	ppAB	AB	ppAB
Inversion	0.34	0.22	0.06	0.08	0.10	0.00
Mixed	0.63	0.70	0.80	0.76	0.75	0.00
Rotation	0.03	0.08	0.14	0.16	0.15	1.00
$\alpha_{\mathrm{avg}}^{\mathrm{MP}}$ [°]	169.6	164.4	161.6	163.9	157.0	141.5

We first note that there are rotation pathways detected for all cases, even for AB in vacuum (3 %) where we would expect for inversion to be prevalent the most. What is further striking for AB in vacuum is a high fraction of mixed pathways compared to the inversion, namely double as much. As expected, there is an increase in fraction of the mixed type for AB going from vacuum where $\phi_{\mathrm{TP}} \sim 60\ \%$ to solvent where $\phi_{\mathrm{TP}} \sim 80\ \%$, where the effect is the same for toluene and DMSO regardless of the solvent polarity. This effect can thus be ascribed to steric effects, where the extension of the bend angle is less pronounced due to the presence of explicit solvent. Upon push-pull substitution there was an increase in the mixed type of pathways as well which is demonstrated by an increased fraction of mixed type pathways for ppAB compared to AB in vacuum. The effect of solvent for the push-pull ppAB was strikingly different for different solvent polarity – the highly polar DMSO induced the switching to the rotation-like character for all the paths in the ensemble. The effect of toluene on ppAB was similar to its effect on AB insofar it induced sampling of more-mixed type pathways as a result of steric restrictions.

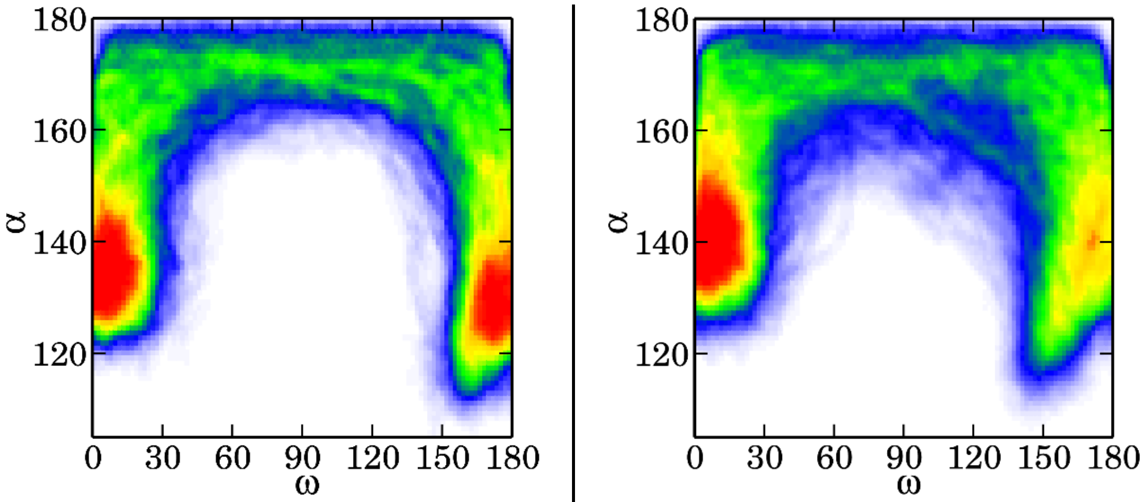

AB vacuum

ppAB vacuum

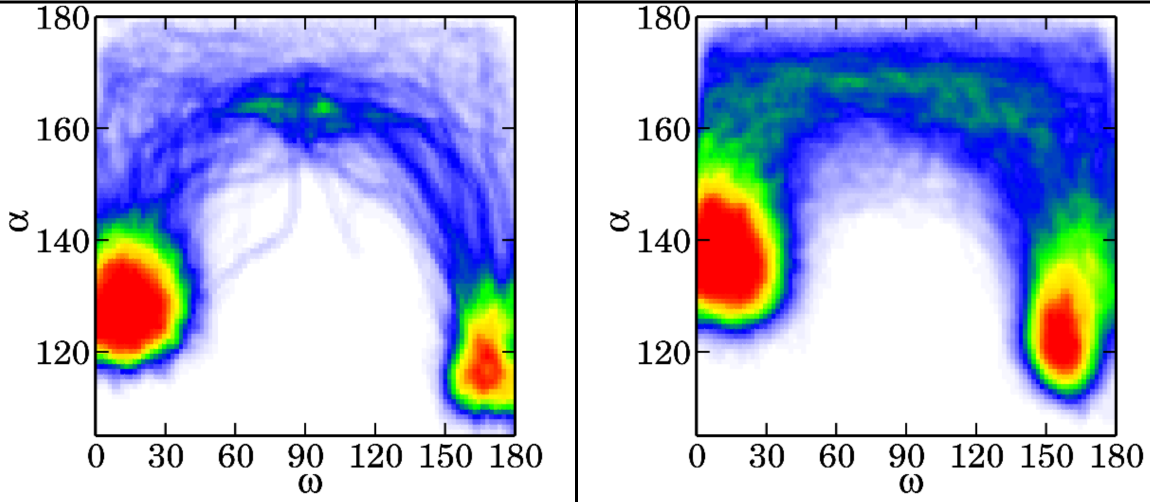

AB toluene

ppAB toluene

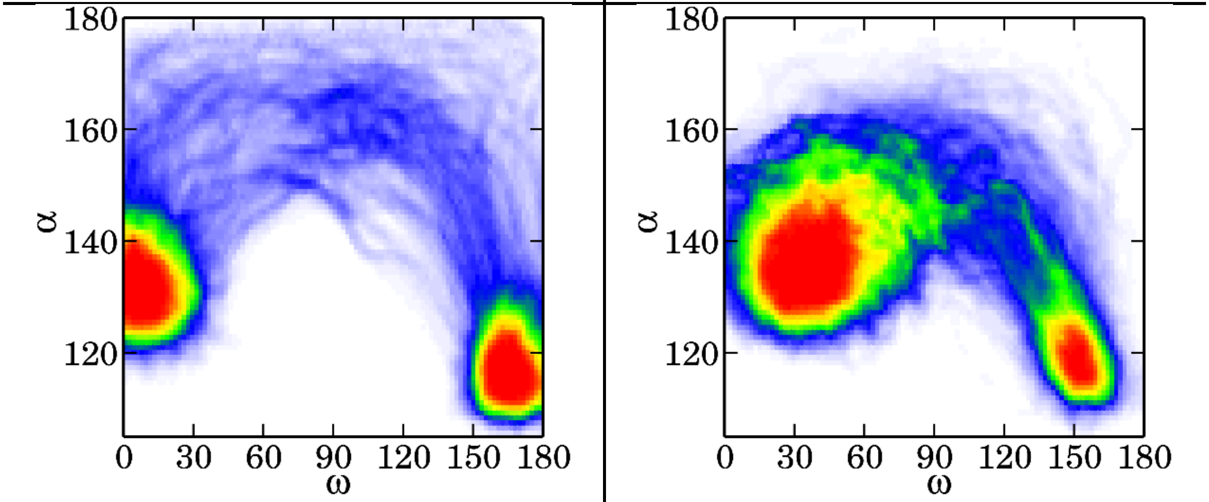

AB DMSO

ppAB DMSO

Figure 27. Path Densities projected onto the (ω, α) surface for compounds AB (left) and ppAB (right) in varying solvent conditions: in vacuum (topmost), in toluene (middle) and in DMSO (down most).

Another convenient measure for the presence of paths with rotation-like character within the inversion, mixed and rotation sub-ensembles are the average bend angles sampled in the interface, $\alpha_{\mathrm{avg}}^{\mathrm{MP}}$ associated with the sub-ensembles and the most probable paths for the full TPS ensemble of paths. The former are listed as the bottommost row in Table 9, while the most probable paths of the full TPS ensembles are depicted in Figure 28. The most probable paths were calculated as paths connecting the highest count bins in (ω, α) for the respective TPS configuration density. Comparing the most probable paths between vacuum, in black, and solvents, in red for toluene and in green for DMSO, the dramatic effect of DMSO on ppAB is evident as the most probable path is essentially a pure rotation path. It proceeds with minimal extension of the bend angle α with the average angle in the interface $\alpha_{\mathrm{avg}}^{\mathrm{MP}} = 141.5°$. Again, the effect of toluene is negligible for ppAB as the most probable path almost entirely coincides with the one for ppAB in vacuum. The effect of the solvents on the most probable path is apparent for the unsubstituted AB, whereat both DMSO and toluene have a similar effect of inducing a more rotation-like character, compared to the vacuum case.

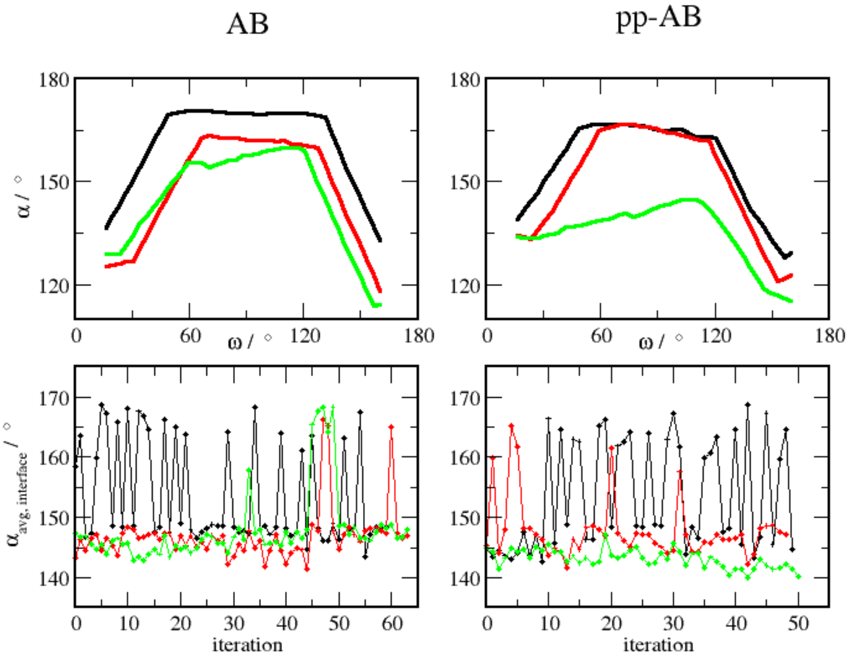

Figure 28. The most probable paths in the TPS ensemble projected onto the (ω, α) surface (up) for AB and ppAB in vacuum (black), toluene (red) and DMSO (green).The switching of the average angle for the interface, $\alpha_{\mathrm{avg,interface}}^{\mathrm{MP}}$ in the course of the TPS iterations (down), where the iteration steps are not given in absolute values. The average angles associated with the interface $\alpha_{\mathrm{avg}}^{\mathrm{MP}}$ are listed in the Table 9.

The switching between inversion and rotation is monitored by plotting the variation in value of the average angle sampled in the interface, $\alpha_{\mathrm{avg,interface}}^{\mathrm{MP}}$ with TPS iterations, depicted in the lower panel of Figure 28. As depicted with a black curve, the average bend angle in vacuum alternates between more extended $\sim 170°$ and less extended $\sim 150°$, while in solvents the switching to more extended states is less frequent. Remarkably, the switching to sampling more extended configurations with respect to the bend angle was completely absent for ppAB in DMSO.

We conclude this section by stating that the analysis of the TPS path densities projected onto the (ω, α) plane indeed confirmed our expectation that the high polarity solvent DMSO induced switching to rotation mechanism only for the push-pull derivative ppAB and not the unsubstituted azobenzene AB. The effect of toluene in inducing a more rotation-like character on the other hand was purely steric for both compounds.

3.3.4 The hula-twist component and the orientation dihedral parameter

For azobenzenes, the lowest energy path along a hula-twist coordinate was identified to be the lowest energy path for the non-radiative relaxation after photoisomerization [22]. Given that the non-radiative relaxation proceeds through a conical intersection between the excited state and ground state PES, it is plausible that the hula-twisting coordinate contributes to the thermal relaxation on the ground state potential surface as well.

Given the non-biased TPS paths for the $\mathrm{cis} \rightarrow \mathrm{trans}$ isomerization, it is possible to examine the relationship of the dihedral angles relevant to the hula-twist mechanism. Those are the central dihedral for the rotation around the N=N double bond and the two dihedrals for the rotation around the two adjacent C-N bonds, ω, ϕ, ϕ' respectively, defined in the molecular scheme in Figure 16. We confirmed the hula-twist to be present for both AB and ppAB in vacuum and DMSO already based on the time evolution of respective parameters in representative trajectories of the TPS ensembles, presented in Section 3.3.1. Here we extend the analysis to the whole TPS ensemble of paths.

The TPS configuration densities projected onto the (ω, ϕ) and (ω, ϕ') planes are plotted in Figure 29. For all conditions except ppAB in DMSO, the correlation between the two dihedral angles ω, ϕ is apparent as they change simultaneously by $\sim 180°$, while the other adjacent dihedral ϕ' stays close to constant during the transition. The adjacent single N'-C bond along which twisting occurs is in fact the one adjacent to the inverting nitrogen N', in the co-linear sequence of atoms N-N'-C. For the ppAB in DMSO where the mechanism is almost pure rotation with the co-linearity of the N-N'-C sequence of atoms minimal, the hula-twist is the least pronounced. There is still minimal change in the relative orientation of the phenyl rings during the transitions, as one can see from the molecular structures of representative trajectories, aligned with respect to the N-N'-C sequence of atoms in Figure 29. The phenyl rings stay close to parallel, with only the central moiety atoms C-N-N'-C moving out of the plane as the transition proceeds.

A convenient measure for the relative orientation of phenyl rings is the already introduced orientation dihedral angle ϕ_{OR}, which is $\phi_{\mathrm{OR}} = 90°$ if the rings are perpendicular and $\phi_{\mathrm{OR}} = 180°, 0°$ if they are parallel. The configuration densities of the TPS ensembles projected onto the $(\mathrm{X}, \phi_{\mathrm{OR}})$ plane serve to monitor the reorientation dynamics for the phenyl rings and are plotted in Figure 30. Overlaid in black dashed lines are the representative trajectories of the TPS ensembles which serve to further show that the orientation dihedral indeed stayed close to constant during the isomerization process. Also overlaid as black scatter dots are the transition state ensemble configurations projected onto the plane $(\mathrm{X}, \phi_{\mathrm{OR}})$. The TSE is spread out over the whole range of phenyl rings' orientations sampled which renders the phenyl ring orientation in fact irrelevant for the definition of the transition state.

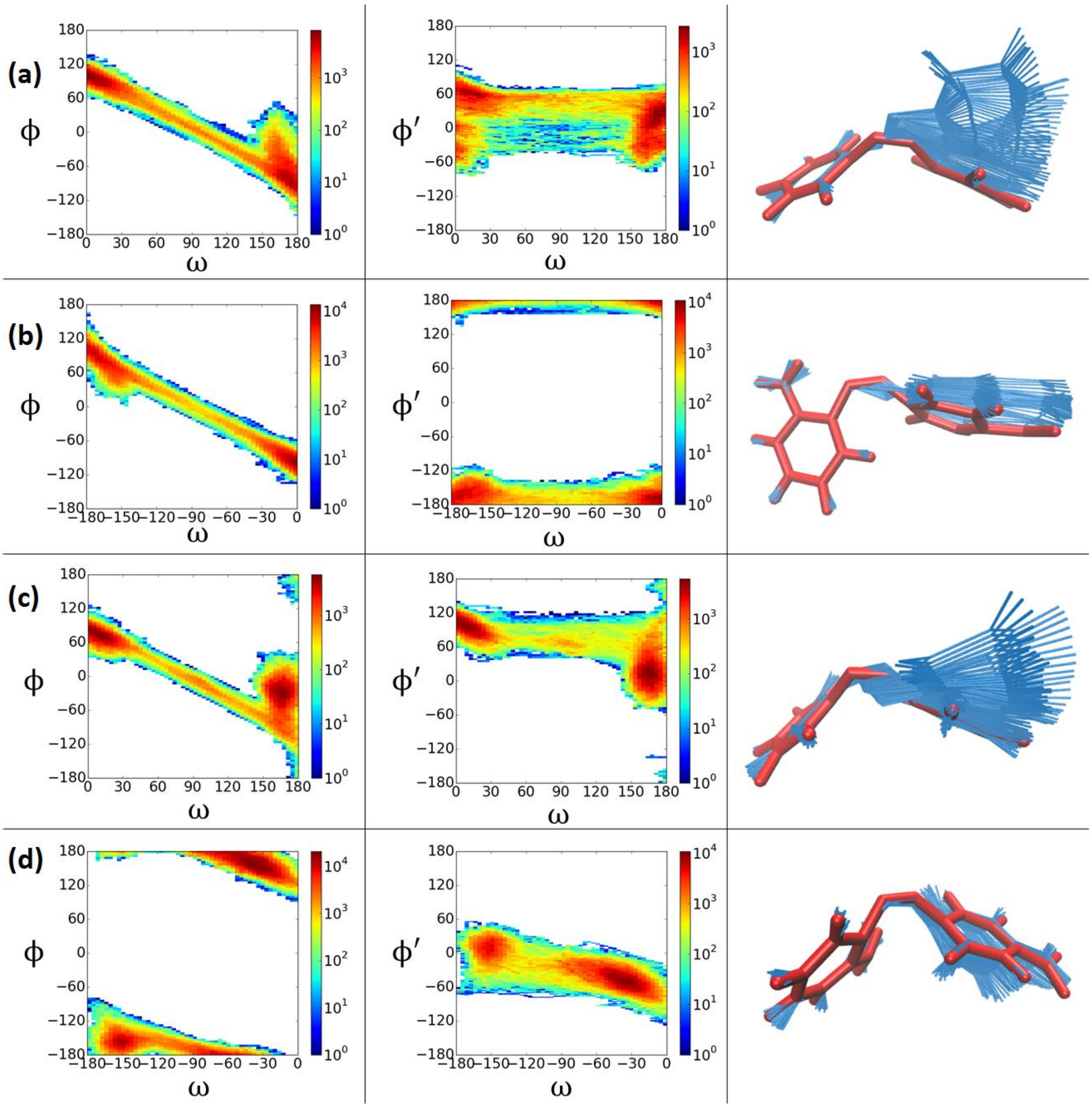

Figure 29. Hula-twist mechanism via the projections of TPS ensemble onto (ω, ϕ) and (ω, ϕ') planes for (a) AB in vacuum, (b) ppAB in vacuum, (c) AB in DMSO and (d) ppAB in DMSO. Configuration densities projected onto (ω, ϕ), leftmost, and (ω, ϕ') plane, middle. Rightmost are shown cartoons representing the last accepted transition paths from the TPS ensembles, colour coded with the initial cis state in red liquorice representation and the other structures from the trajectory overlaid as blue lines. The structures were aligned with respect to the C’ atoms of the phenyl rings (to keep one of them fixed in orientation) and the N atom of the central C’-N=N-C moiety

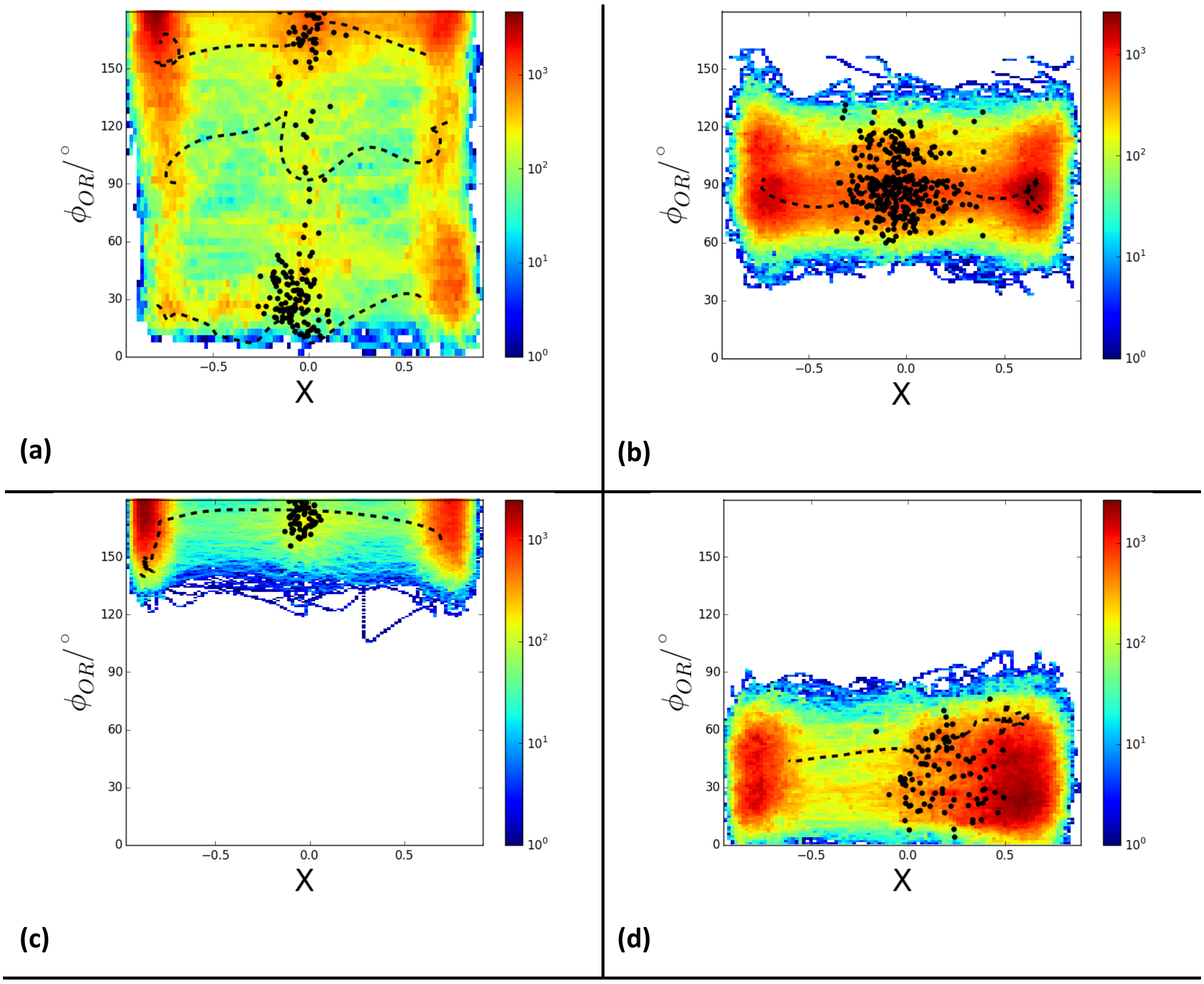

Figure 30. Hula-twist mechanism via the path densities projected onto the $(\phi_{\mathrm{OR}}, \mathrm{X})$ plane, for (a) AB in vacuum, (b) ppAB in vacuum, (c) AB in DMSO and (d) ppAB in DMSO. The representative paths from the TPS ensembles depicted in dashed black lines, and the transition state ensembles depicted as scatter plots. While the transition can occur through TSs with a wide range for the relative orientation for the phenyl rings (spread in ϕ_{OR} for the TSE), it remains nearly constant during a transition.

Admittedly, we note that there are sampling issues with respect to the orientation dihedral parameter ϕ_{OR}, as it is a slower degree of freedom. The sampling in ϕ_{OR} was ideally converged for AB in vacuum only, while for other conditions it covered a more limited range, as depicted by plotting the variation in the average value $\overline{\phi}_{\mathrm{OR}}$ with TPS iterations in Figure 31A. For the push-pull ppAB the phenyl rings remained close to perpendicular, $\phi_{\mathrm{OR}} \sim 90°$ while for both AB and ppAB in DMSO almost parallel with $\phi_{\mathrm{OR}} \sim 160°$ and $\phi_{\mathrm{OR}} \sim 30°$, respectively. The average value for the orientation dihedral $\overline{\phi}_{\mathrm{OR}}$ is clearly not efficiently sampled in the TPS paths as it does not drift too much from the values it assumes early in the iteration steps.

Regardless of the absolute value of ϕ_{OR} for a path, its standard deviation within a path is small across the TPS iterations. The standard deviation in ϕ_{OR} for a transition path, $\sigma(\phi_{\mathrm{OR}})$, is plotted as a function of the TPS iteration step in Figure 31B. It did remain small for all conditions considered, namely $\sigma(\phi_{\mathrm{OR}}) = 10.4° \pm 2.3°$ for AB in vacuum (black), $\sigma(\phi_{\mathrm{OR}}) = 7.1° \pm 0.6°$ for ppAB in vacuum (red), $\sigma(\phi_{\mathrm{OR}}) = 9.0° \pm 0.5°$ for AB in DMSO (violet) and $\sigma(\phi_{\mathrm{OR}}) = 8.5° \pm 0.6°$ for ppAB in DMSO (green).

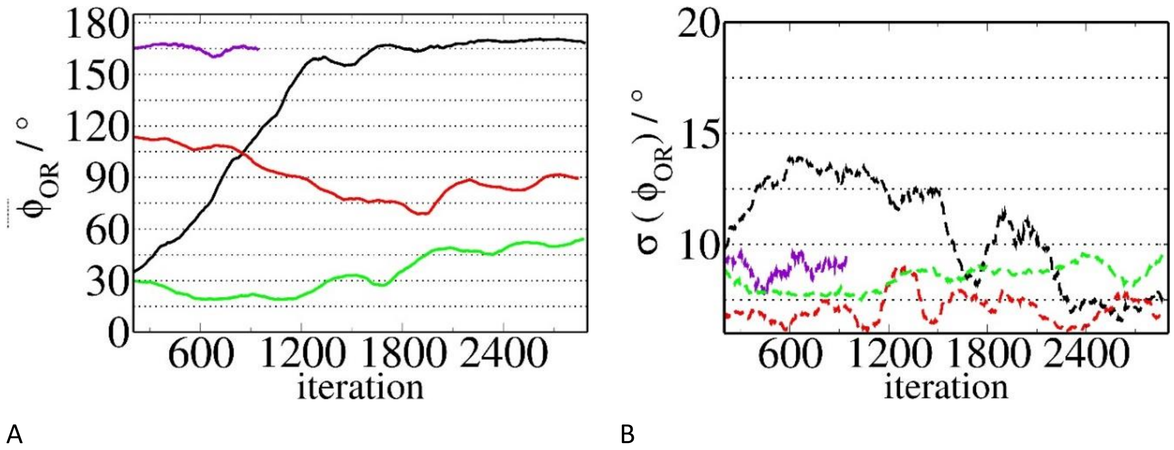

Figure 31. Variation of the orientation dihedral parameter with TPS iterations. (A) The average $\overline{\phi}_{OR}$ for AB in vacuum (black), ppAB in vacuum (red), AB in DMSO (violet) and ppAB in DMSO (green). At the bottom of the figure, the standard deviation $\sigma(\phi_{OR})$ in the same order. (F) Variation of the standard deviation of the orientation dihedral $\sigma(\phi_{OR})$ with TPS iterations. The relative orientation between the phenyl rings does not change considerably within the transition pathways, regardless of the average value for the angle $\overline{\phi}_{OR}$.

The convergence issues for the phenyl rings orientation parameter can be attributed to it being a slower degree of freedom not efficiently sampled within the short reactive paths, namely 0.25 ps in vacuum and 0.5 ps in solvents. The TPS path sampling settings such as the definition of stable states only with respect to the fast degrees of freedom and the path lengths would thus need to be revised in order to account for the full sampling of the slower degrees of freedom.

The clue into the energetics with respect to ϕ_{OR} is obtainable from long equilibrium runs in the cis and trans stable states, as well as the transition region with the system restrained to $X = X^*$. The resulting free energy profiles $F(\phi_{OR})$ are plotted in Figure 32. For AB in vacuum the orientation parameter is easily sampled in a full range with the associated barrier between sub-states thermally accessible and close to $\sim 1\ k_BT$. For ppAB in vacuum on the other hand the barrier is larger $\sim 1.5\ k_BT$ and there is additional structure for the cis isomer compared to pure AB, comparing the dashed red and solid red in Figure 32A, respectively. In addition to the minimum at $\phi_{OR} \sim 30°$ there is another minimum at $\phi_{OR} \sim 90°$ with the two states separated by $\Delta F \sim 1.5\ k_BT$. Furthermore, at the transition region $X = X^*$ for the push-pull ppAB, the phenyl rings are preferentially perpendicular with a large energy minimum at $\phi_{OR} \sim 80°$, unlike for the shallow minimum extended over the full range in ϕ_{OR} associated to the unsubstituted AB. It seems that the larger energetical barrier associated to the twisting of phenyl rings for the push-pull ppAB configurations at the transition regions is the reason that the TPS paths preferentially sampled are also those along which the phenyl rings remain perpendicular.

In conclusion, because of the slower equilibration time compared to the reaction times of TPS paths and larger barriers associated to the orientation dihedral parameter ϕ_{OR}, the TPS sampling is less efficient for the push-pull ppAB compared to the unsubstituted AB in vacuum. For the latter, the sampling is more efficient due to practically non-existent and thermally easily traversable barriers associated to this parameter.

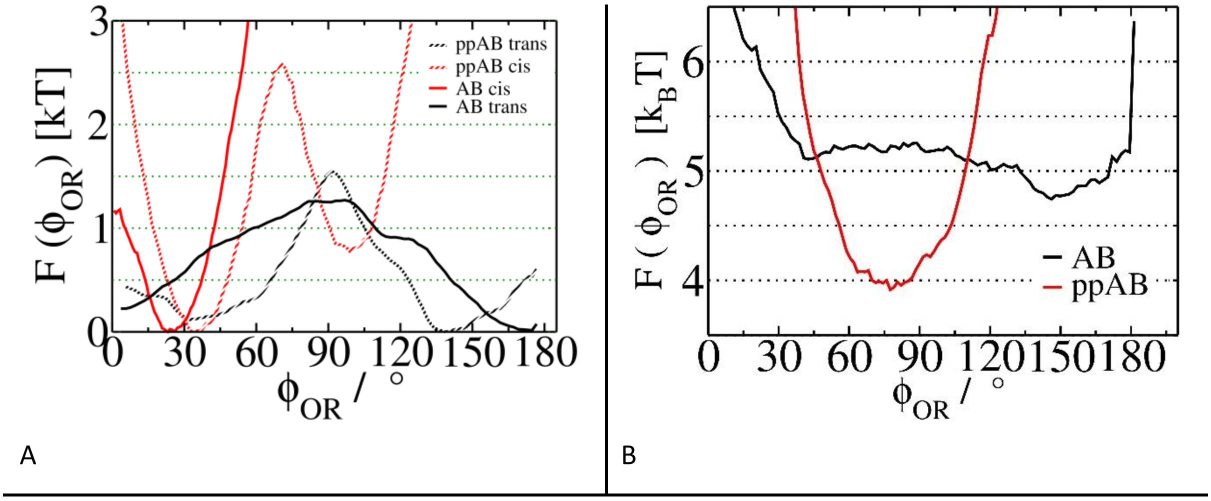

Figure 32. Free energy profiles for the orientation dihedral parameter, $F(\phi_{OR})$ in stable states (A) and transition region restrained to $X = X^*$ (B) for AB and ppAB in vacuum.

3.3.5 Transition state ensemble from the harvested transition paths

In this section, the observations regarding the mechanism for thermal cis → trans isomerization of azobenzenes in vacuum and DMSO are summed up by presenting the average structures associated to the transition state ensembles identified from the TPS paths. For the definition of configurations as transition states based on their committor probability refer to the Methods Section 2.5.4. Since a transition state structure is considered to be a fixed arrangement of atoms at the moment of a transition, an average structure is not necessarily a physically representative structure that is actually realized for a transition, but it is nevertheless informative in terms of the average geometrical parameters and their deviations within the TS ensemble. Also, it is worth noting that configurations chosen for the committor analysis were randomly picked out of the interface across the TPS path ensemble and might not be representative of the actual TS ensemble due to limitations of the TPS sampling. On the example of the orientation dihedral parameter ϕ_{OR}, we already witnessed the convergence issues for the slower degree of freedom.

Nevertheless, we consider the sampling to be representative for the fast degrees of freedom, namely the central dihedral and the bend angle, ω, α, as well as the X coordinate. The statistics for the relevant geometrical parameters are given in Table 10 and the average structures associated to the TS ensembles are plotted in Figure 33.

We first note that for AB in DMSO there is a marked reduction in the average bend angle $\alpha = 155°$, which might be surprising given the QM optimized transition structure using the polarizable continuum model for the solvent where it remained close to linear. The steric effect is presumably dominant over the polarization [4] in inducing the bending in angle α, as we observed a similar reduction in the bend angle for a much lower polarity toluene, where $\alpha = 164°$. The polarization effect in stabilizing a more bent transition structure is evident for ppAB in DMSO, where the average bend angle in the TS ensemble is as low as $\alpha = 148°$. The effect of toluene on the push-pull ppAB was comparable to the unsubstituted AB in toluene, where the bend angle associated to the average TS was $\alpha = 166°$.

The average dihedral angle ω across the TS ensembles in solvents for both AB and ppAB were close to $\omega \sim 90°$ indicative of the rotation assisted inversion as the mechanism. The TS ensemble for both AB and ppAB in vacuum is very spread out with respect to the rotation dihedral as quantified with the standard deviation $\sigma(\omega)$. This is indicative that inversion is more dominant in the mechanism, but also might also be a steric effect. Namely, for AB the standard deviation in the TS ensembles for both dihedrals ω, ϕ_{OR} was more pronounced in solvents than in vacuum.

Table 10. The averages and standard deviations for geometrical parameters in the Transition State Ensemble. The number of the configurations used to calculate the averages and standard deviations are listed in brackets. The angles are given in degrees.

		AB			**ppAB**	
	vacuum	toluene	DMSO	vacuum	toluene	DMSO
	(217)	(93)	(67)	(332)	(129)	(93)
α	170.2	164.3	155.3	166.2	165.8	148.4 +/-
$\sigma(\alpha)$	+/- 5.7	+/- 7.2	+/- 6.3	+/- 8.0	+/- 7.7	9.2
ω	-2.9	91.0	95.1	17.7	90.9	67.6 +/-
$\sigma(\omega)$	+/- 119.2	+/- 18.0	+/- 6.3	+/- 107.1	+/- 38.3	20.1
X	-0.06	0.05	-0.04	-0.04	0.10	0.18 +/-
$\sigma(X)$	+/- 0.18	+/- 0.05	+/- 0.05	+/- 0.14	+/- 0.08	0.15
ϕ_{OR}	33.8	28.0	170.2	90.0	72.3	36.7 +/-
$\sigma(\phi_{OR})$	+/- 89.4	+/- 12.3	+/- 5.7	+/- 14.9	+/- 11.2	15.5

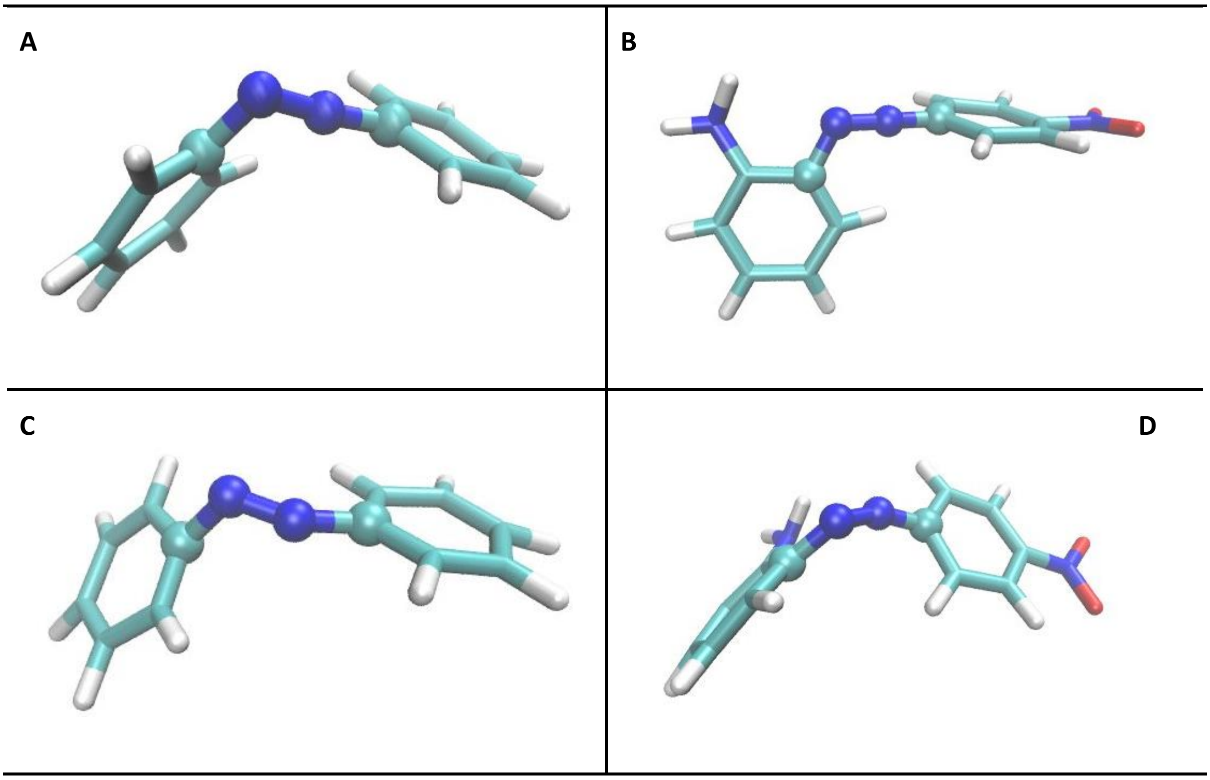

Figure 33. The average transition state from the Transition State Ensembles identified by committor analysis of the TPS pathways in the interface. (A) AB in vacuum, (B) ppAB in vacuum, (C) AB in DMSO, (D) ppAB in DMSO

Due to a possible uncomplete sampling with respect to the orientation dihedral parameter ϕ_{OR} as a slower degree of freedom, the TS ensembles and the associated average structures are not necessarily representative. To investigate this further, we employed an alternative method of generating trial configurations and identifying the transition states, namely from the ensembles restrained to the $\mathrm{X} = \mathrm{X}^*$ surface. Within this ensemble of configurations a broader range in the orientation dihedral parameter ϕ_{OR} is represented. In Figure 34 we compare the TS ensembles with respect to the parameter ϕ_{OR} identified with the two independent approaches, namely from the TPS paths and the ensembles restrained at $\mathrm{X} = \mathrm{X}^*$. The TS ensembles identified from the restrained ensembles of configurations $\mathrm{X} = \mathrm{X}^*$ are depicted as a horizontal scatter lines, while the TS ensemble identified from the TPS paths is plotted as a function of the TPS iteration step. Interestingly, the TS ensemble is more spread out with respect to ϕ_{OR}, than one would assume based on the TS ensembles identified solely from the TPS paths.

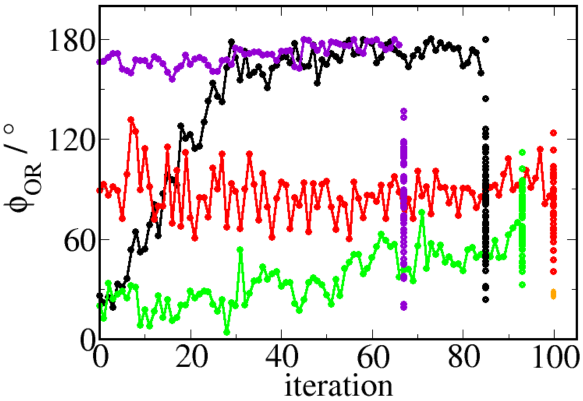

Figure 34. Variation in the orientation dihedral ϕ_{OR} in the TS ensembles identified from TPS paths – AB in vacuum (black), ppAB in vacuum (red), AB in DMSO (violet), ppAB in DMSO (green). The TPS iterations are not given in the absolute values. In horizontal scatter plots the TS ensemble identified from the $\mathrm{X} = \mathrm{X}^*$ restrained ensemble which samples a broader range in the parameter ϕ_{OR}. For ppAB in vacuum, extra configurations that were steered to $\phi_{\mathrm{OR}} \sim 30°$ are depicted in orange.

A curious result is obtained with ppAB in vacuum, where the equilibrium ensembles at $\mathrm{X} = \mathrm{X}^*$ naturally sample the $\phi_{\mathrm{OR}} \sim 90°$ region as was to be expected based on the free energy profiles $\mathrm{F}(\phi_{\mathrm{OR}})$ in Figure 32. A bias had to be introduced to force the system to sample the regions $\phi_{\mathrm{OR}} \sim 30°$ where the phenyl rings are close to planar. Strikingly, even those configurations with the phenyl rings close to planar were identified as transition states. The resulting TS ensemble clustered around $\phi_{\mathrm{OR}} \sim 30°$ is depicted as orange scatter alongside the scatter plot in red, the TS ensemble obtained by not imposing a bias on the orientation dihedral ϕ_{OR}.

For the push-pull ppAB in DMSO, the TS ensembles obtained from the TPS paths and the $\mathrm{X} = \mathrm{X}^*$ restrained ensembles were comparably spread out with respect to the orientation dihedral, $\phi_{\mathrm{OR}} \sim 70°$. This was not the case for the unsubstituted AB in DMSO, where the TPS sampling did not diverge much from the initial value $\phi_{\mathrm{OR}} \sim 170°$, while the restrained ensemble $\mathrm{X} = \mathrm{X}^*$ sampled essentially the full range in ϕ_{OR}, comparable to the AB in vacuum case. We assign this to a very poor performance of the TPS sampling for AB in DMSO, where the number of the performed TPS iterations was also the lowest compared to other cases.

Based on the TS analysis from both the TPS paths and the $\mathrm{X} = \mathrm{X}^*$ restrained ensembles, we conclude that the solvent did not affect the relative orientation of the phenyl rings as measured by the ϕ_{OR} parameter. TS ensembles assume a broad range of values for this parameter where for the push-pull ppAB the phenyl rings are preferentially perpendicular, and more so in vacuum than in DMSO.

3.4 Reaction Coordinate Analysis

In this section we refer back to characterization of the reaction coordinate in order to improve our understanding of the mechanism for $\mathrm{cis} \rightarrow \mathrm{trans}$ isomerization. For a good reaction coordinate, the committor distribution of configurations near its energy barrier is narrowly peaked around $p_B \sim 0.5$, while broadening or skewing of the committor distribution points to either diffusive dynamics or additional barriers present in orthogonal directions. The different scenarios for the free energy surfaces and the associated committors are represented in Figure 14 of the Methods Section 2.5.4.

In Figure 22 of the Results Section 3.2.1 we presented the result of the committor analysis for the coordinate X, where the resulting committor distributions for configurations restrained to $X = X^*$ were uniform like for both AB and ppAB in vacuum and in solvent, with a slight skewing to the trans state for the unsubstituted AB. We further characterize the quality of the coordinate X as the reaction coordinate with the Best-Hummer approach in the following Section 3.4.1.

The committor distributions at a low temperature resulted with further skewing to the trans state for both compounds AB and ppAB, plotted in Figure 23. It is thus most likely that additional order parameters contribute to the reaction coordinate. This was made clear from the committor distributions of the restrained ensemble $X = X^*$ at a low temperature $T = 33\ \mathrm{K}$ where barriers orthogonal to the $X = X^*$ surface could not be traversed thermally. For both AB and the push-pull ppAB this resulted with skewing of the committor distributions, while for AB the distribution was clearly unimodal towards the trans state. This served as an indication that a single orthogonal coordinate might in fact dominate, and even more so for AB than the push-pull ppAB.

In Section 3.4.3 we screen the sub-ensembles that commit to either of the stable states against the transition state ensemble in search of the order parameters that are correlated with the transition and might contribute to the reaction coordinate. In Section 3.4.4 we perform the likelihood maximization using TPS shooting points and their outcomes as input, where the reaction coordinate is modelled as a linear combination of many order parameters, as implemented by [97, 98].

3.4.1 Best-Hummer analysis for the coordinate X

The collected TPS ensemble of reactive paths provides the basis for the Best-Hummer analysis of reaction coordinates. For a good reaction coordinate the transition states are narrowly distributed around some characteristic value, $r = r^*$. This value in r is thus sampled only in reactive events or the dynamical bottlenecks for the system. It follows that the conditional probability of being on a transition path given a value of the reaction coordinate $P\,(\mathrm{TP} \mid r)$ should peak precisely in that region for the reaction coordinate that is at $r = r^*$. A Bayesian relation is used to express the conditional probability $P\,(\mathrm{TP} \mid r)$ as a ratio of distribution of the putative reaction coordinate in the TPS ensemble $p\,(r \mid \mathrm{TP})$ and the equilibrium distribution $p_{eq}(r)$, as defined in Equation 61 of the Methods Section 2.6.1. The quality of a reaction coordinate is thus quantified with the features for the conditional probability $P\,(\mathrm{TP} \mid r)$, namely its width and the intensity of its peak. For diffusive dynamics, the conditional probability attains a value $P\,(\mathrm{TP} \mid r) = 0.5$ on a stochastic separatrix, a hypersurface placed at $r = r^*$.

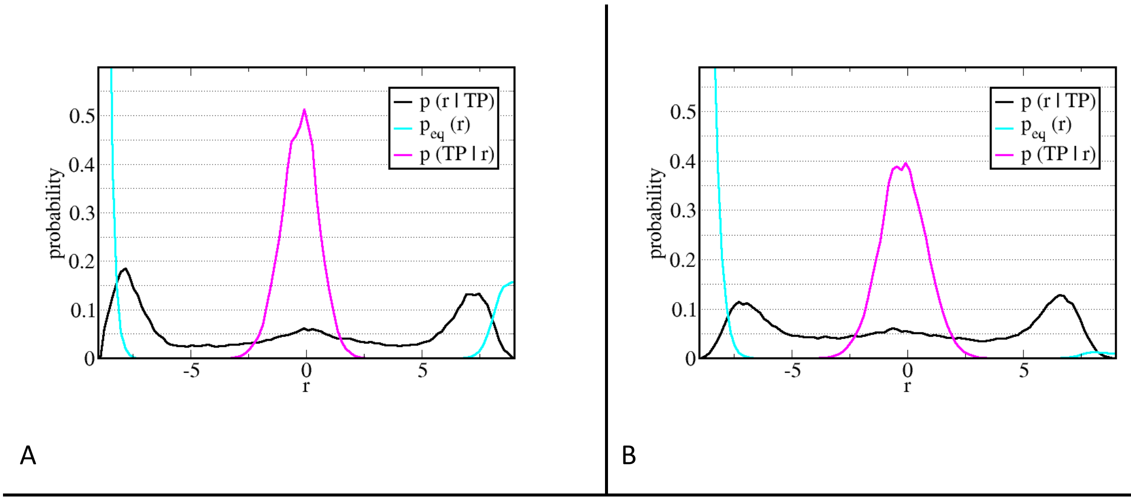

Figure 35. Best-Hummer analysis for the coordinate X as the reaction coordinate in vacuum $r \equiv 10 \cdot X$ for AB (A) and ppAB (B). The xy-axes were rescaled to yield the probability density that falls into the [0,1] range. The equilibrium distribution $p_{eq}(r)$ was calculated by WHAM reweighting [86] and the conditional distribution $p\ (r \mid TP)$ from the TPS ensemble.

The Best-Hummer analysis is first presented for the vacuum case for both compounds AB and ppAB in Figure 35. The conditional probability is more sharply peaked around the value characteristic for the transition state, $r = r^* \approx 0$ for AB, where the maximum and the standard deviation are $P\ (TP \mid r = 0) = 0.51 \pm 0.13$. For the push-pull ppAB, the maximum in the conditional probability was lowered, where $P\ (TP \mid r = 0) = 0.40 \pm 0.11$. Based on this simple analysis for the breadth and the intensity of the peak for the conditional probability $P\ (TP \mid r)$, it follows that the coordinate X is a better reaction coordinate for the unsubstituted azobenzene AB than for the push-pull derivative ppAB.

More importantly, the analysis served to further characterize the diffusivity of the underlying dynamics important for interpreting the committor distributions $P\ (p_B)$ and their spread. For purely diffusive dynamics the conditional probability can be expressed as $P\ (\ TP \mid r\ ) = 2p_B(1 - p_B)$, where p_B is the configuration committor probability for the ensemble of configurations restrained at the dynamical bottleneck for the reaction coordinate $r = r^*$, and in case of the coordinate X as the reaction coordinate, restrained at $r^* = X^*$. For diffusive dynamics, the average value for the expression $\langle\ 2p_B(1 - p_B)\ \rangle$ should be contained within the statistical error in the conditional distribution $P\ (TP \mid r)$. These values calculated for the committor distributions $P\ (p_B)$ associated to the restrained ensemble $r^* = X^*$, amounted to $\langle\ 2p_B(1 - p_B)\ \rangle = 0.34 \pm 0.15$ for the push-pull ppAB and 0.30 ± 0.16 for the unsubstituted AB in vacuum. The calculated average is thus not contained within the standard deviation of the peak in the conditional probabilities $P\ (TP \mid r)$ for the unsubstituted AB, unlike for the push-pull ppAB. This further showed that the dynamics for AB is less diffusive than for ppAB. Since the random noise and friction contributions to the total force for the stochastic dynamics were identical for both AB and ppAB in vacuum, it can be concluded that the trajectories for AB are more ballistic given the larger force due to the potential.

The Best-Hummer analysis was in DMSO solvent for both compounds AB and ppAB is presented in Figure 36. For AB, the introduction of the explicit DMSO solvent did not affect the quality of the reaction coordinate $r \equiv X$ from the one quantified with the conditional probability $P\ (TP \mid r)$ obtained in vacuum. The conditional probability of being on a transition path peaked at $P\ (TP \mid r) = 0.59 \pm 0.13$, and was not further spread out. On the other hand, there was a pronounced shift for the push-pull ppAB in the reaction coordinate $r \equiv X$ to more positive values. This effect was a result of the TS configurations being more rotamer-like with the reduction in the bend angle α, which in turn affected the values for the coordinate $X\,(\omega,\alpha)$. In addition, the maximum in the conditional probability was markedly reduced compared to the vacuum case, $P\,(TP\,|\,r) = 0.34 \pm 0.10$, while the spread around the maximum remained comparable.

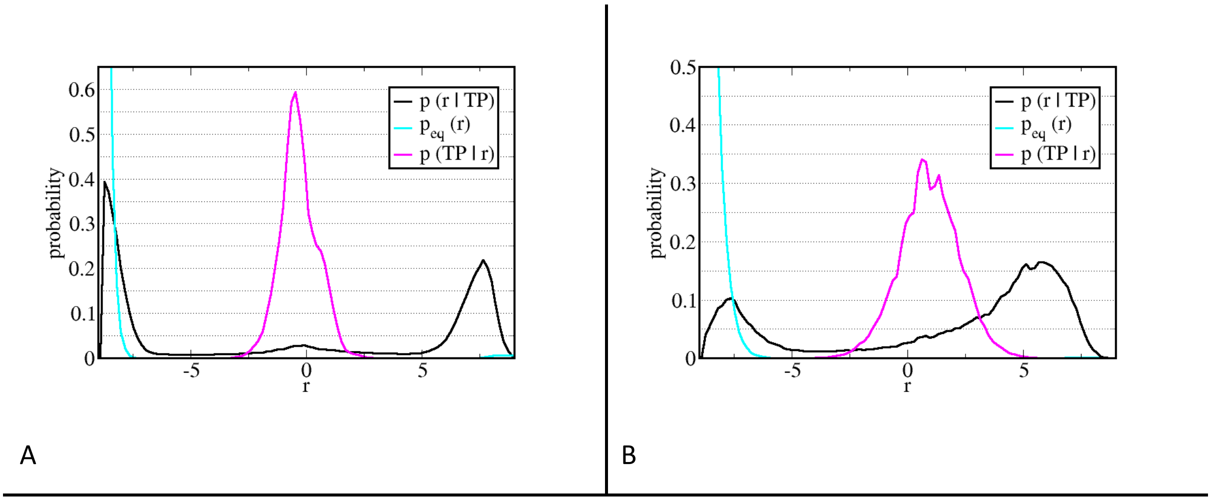

Figure 36. Best-Hummer analysis for the coordinate X as the reaction coordinate in DMSO $r \equiv 10 \cdot X$ for AB (A) and ppAB (B). The xy-axes were rescaled to yield the probability density that falls into the $[0,1]$ range.

The diffusive or ballistic nature for the underlying dynamics can be quantified by a coefficient [98]

$$\chi = -\langle [2\,h_B(x_k) - 1]\,[2\,h_B(x_{-k}) - 1] \rangle_{p_B=0.5}, \tag{87}$$

where $h_B(x_k) = 1$ if the fleeting trajectory ends in state B, and the trajectories initiated from a configuration x in the forward x_k or backward x_{-k} direction. The coefficient measures the decorrelation of trajectories outcomes and equals $\chi = 0$ for purely diffusive dynamics for which the outcomes are fully de-correlated. On the other hand, the forward and backward shooting for purely ballistic dynamics always result in opposite outcomes, where if the forward trajectory ends in A, $h_B(x_k) = 0$, then the backward necessarily ends in B, $h_B(x_{-k}) = 1$. The coefficient for fully correlated outcomes due to ballistic dynamics equals $\chi = 1$.

The calculated χ coefficient for ppAB in vacuum averaged over 38 transition states, as defined with the committor $p_B \sim 0.5$ in Methods Section 2.5.4, amounted to $\chi = 0.58$, a value characteristic of dynamics that is far from purely ballistic. Strikingly, the calculated χ coefficient for the unsubstituted AB, averaged over 39 transition states amounted to $\chi = 0.69$, a value associated to more ballistic dynamics than for the push-pull ppAB. The dynamics for the unsubstituted AB can be thus characterized as less diffusive and governed by the potential gradient in a greater extent.

In conclusion, as demonstrated with the Best-Hummer analysis of the transition paths the coordinate X was identified as a good reaction coordinates given that the conditional probability $P\,(TP\,|\,r)$ was unimodal around $r \equiv X = X^*$ the dynamical bottleneck for the coordinate X. Based on the width of the conditional distribution, the dynamics for the push-pull ppAB was shown to be more diffusive than for the unsubstituted AB. The effect of explicit DMSO solvent was apparent only for the case of the push-pull ppAB, where the conditional probability $\mathrm{P}\ (\mathrm{TP}\mid\mathrm{r})$ was shifted to more positive values and attained a lower maximum value.

3.4.2 Rate Constants from the Best-Hummer analysis

In this section we present the results of calculation of rate constants $\mathrm{cis}\xrightarrow{\mathrm{k}_1}\mathrm{trans}$ based on the Equation 62 of the Methods Section 2.6.1. The calculation for the rate constant given the collected TPS ensemble of paths should not in principle depend on the choice of the coordinate $\mathrm{r}\equiv\mathrm{X}$. Namely the determinative factor expressed as the ratio of the probability of being on a transition path and an average duration of the transition, $\mathrm{p}\ (\mathrm{TP})\ /\ \langle\mathrm{t}_{\mathrm{TP}}\rangle$, does not depend on the choice of r [95,96]. The evaluation of rates with different coordinates can be used as a test of convergence, which we do not conduct here due to computational demand of such calculations. The heavy parts of the calculation are the reconstruction of the equilibrium probabilities with umbrella sampling and WHAM reweighting, as well as the generations of the TPS ensembles in respective coordinates.

We present the estimated rate constants for compounds AB and ppAB in both vacuum and DMSO, calculated for the coordinate X as the reactive coordinate $\mathrm{r}\equiv\mathrm{X}$, in Table 11.

Table 11. Estimated rates for the cis → trans isomerization based on the Best-Hummer analysis.

compound	c_{A}	$\mathrm{p(TP)}$	$\langle\mathrm{t}_{\mathrm{TP}}\rangle\ [\mathrm{ps}]$	$\mathrm{k}_1[\ \mathrm{s}^{-1}]$
ppAB vacuum	0.018564	$1.387\cdot10^{-9}$	$0.111\ \pm0.036$	$3.39\cdot10^{5}\ \mathrm{s}^{-1}$
ppAB DMSO	0.0025904	$3.636\cdot10^{-6}$	$0.128\ \pm0.061$	$5.47\cdot10^{9}\ \mathrm{s}^{-1}$
AB vacuum	0.141991	$4.226\cdot10^{-14}$	$0.091\ \pm0.026$	$1.64\ \mathrm{s}^{-1}$
AB DMSO	0.0074237	$1.110\ \cdot10^{-13}$	$0.071\ \pm0.021$	$105\ \mathrm{s}^{-1}$

For AB, the estimated rate is 100 times faster in DMSO compared to vacuum, mostly due to the reduced molar fraction for the cis stable state c_{A} or alternatively, the decrease in the relative population of the cis state. From free energy profiles $\mathrm{F}\ (\mathrm{X})$ in Figure 21 of the Results Section 3.2, we observed this as an effect of relative destabilization of the cis isomer with respect to the trans in the highly polar DMSO. The effect is presumably entropic in origin and a result of greater ordering around the more dipolar TS compared to the cis isomer [26]. Due to the different strengths in solute-solvent interactions at the transition and stable states, the free energy barrier is reduced constituting a static effect of solvent on the rate constant [35]. The decrease of the energy barrier is also reflected through the fraction of time spent in a transition, $\mathrm{p(TP)}$ factor which is ~ 10 times larger for AB in DMSO than in vacuum. The dynamic effect of solvent on the rate constant should in principal be reflected by the average transition times $\langle\mathrm{t}_{\mathrm{TP}}\rangle$, where it might be expected for the explicit solvent to introduce friction and slow down the reaction. Surprisingly, going from vacuum to DMSO, the average transition time in fact is slightly reduced for AB.

The increase in the rate constant for the unsubstituted AB going from non-polar solvents to DMSO was reported in experimental studies. The measured acceleration in the rate going from vacuum-like conditions [25] to a highly polar acetonitrile [5] can be estimated as 10 fold. The ~ 100 fold increase in the rate constant for the unsubstituted AB going from vacuum to DMSO presented herein would thus be an overestimation of the effect.

For push-pull derivatives, a more dramatic increase in the rate for the cis → trans isomerization going from non-polar solvent to DMSO was measured experimentally. Namely, the measured rate constant reported in [31] was increased ~ 10000 times for some types of push-pull azobenzenes. Furthermore, in [26] only the lower limit for the rate was measurable, ~ 10 times the one measured in benzene.

Here, our estimate for the increase in the rate constant for the push-pull ppAB going from vacuum to DMSO was indeed comparable to the experimental findings, ~ 10000 times. The majority of the effect was static in origin, as the energy barrier reduced in DMSO due to stabilization of the highly dipolar TS solute. The relative probability of being in the cis state c_A was decreased ~ 10 fold while the fraction of time spent in the transition $p(TP)$ was increased ~ 1000 fold. The average transition times $\langle t_{TP} \rangle$ were comparable, implying that the introduction of explicit solvent did not result with further damping the system and affecting the barrier crossing dynamics.

In conclusion, the Best-Hummer estimates for the rates based on the TPS ensemble reproduced the experimental findings that the cis → trans isomerization rates are generally increased in polar solvents. The absolute rates are orders of magnitude off though which can be attributed to the many sources of errors in the rate constant computation.

3.4.3 Analysis of the transition state ensemble

In the previous section the coordinate X was proven to be a good reaction coordinate as prescribed by the Best-Hummer analysis of the transition path ensemble. Therein, the conditional probability of being on a transition path $P\ (TP \mid r)$ was maximized for values close to the dynamical bottleneck – the transition region for which $r^* \equiv X^* \approx 0$. Nevertheless, for an ideal reaction coordinate the transition states can be collapsed to a tight range around some characteristic value of the coordinate. The TS ensemble projected onto the reactive coordinate(s) should thus ideally be narrowly distributed.

For the main reactive coordinates describing the cis → trans isomerization, the central dihedral and the bend angle, ω, α, the TS ensemble was indeed broadly spread out for the both compounds AB and ppAB in vacuum and in DMSO solvent, which we plot in Figure 55 of the Appendix 6.1. In that respect, the projections of the TS ensembles of configurations onto the coordinate $X\,(\omega, \alpha)$ are as well substantially broad, as plotted in Figure 37. The TS ensemble assumes a broader range of values for the push-pull ppAB than the unsubstitued AB. There is also a distinct effect of the explicit solvent on the spread of the TS ensembles in the coordinate X, especially for the DMSO solvent on the push-pull ppAB.

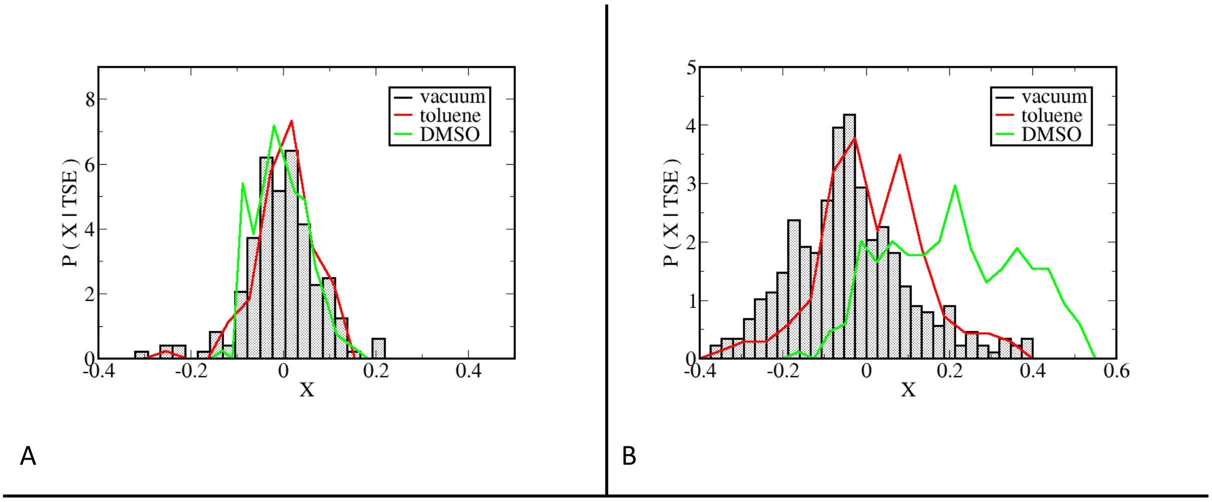

Figure 37. Distributions for the coordinate X in transition state ensembles for AB (A) and ppAB (B) in vacuum and solvents.

Even for the simplest case of the unsubstituted AB in vacuum, the projection of the TSE ensemble onto the coordinate X cannot be collapsed into a tight interval around a single value $\mathrm{X} \equiv \mathrm{X}^*$. In fact, the restrained ensemble of configurations was almost equally likely to commit to either of the stable states as it was to be a transition state, as demonstrated with an uniform-like committor at temperature $\mathrm{T} = 333\ \mathrm{K}$. Furthermore, for the low diffusivity conditions at $\mathrm{T} = 33\ \mathrm{K}$, the same restricted ensemble was more likely to commit to the trans stable state, indicative of additional barriers in coordinates orthogonal to the coordinate X that are crossed diffusively at higher temperatures.

The coordinates which are likely to contribute to the reaction coordinate are correlated with the transition. To identify them, we partitioned the full restrained ensembles at $\mathrm{X} \equiv \mathrm{X}^*$ with respect to their committor values into three sub-ensembles. Those were the sub-ensembles of configurations that committed to the cis and trans stable states, $\mathrm{p_B} \sim 0$ and $\mathrm{p_B} \sim 1$ respectively, and the TS ensemble, $\mathrm{p_B} \sim 0.5$. By comparing the committor sub-ensembles, variables that are narowly distributed in the TS ensemble about values distinct from those in stable states were identified. They later served as support for the reaction coordinate analysis performed in Results Section 3.4.4. Therein, many geometrical coordinates were screened as candidates for the reaction coordinate.

The distributions of coordinates in the sub-ensembles, identified as correlated with the $\mathrm{cis} \rightarrow \mathrm{trans}$ transition, are presented on the example of the push-pull derivative ppAB in vacuum. In solid blue line we plot the distributions in respective parameters for the sub-ensemble that committed to the cis state, defined by the committor value $\mathrm{p_B} < 0.2$, while the sub-ensemble that committed to the trans state, defined by the committor $\mathrm{p_B} > 0.8$, is plotted in solid green line. The configurations were assigned to the TS sub-ensemble based on their committor $\mathrm{p_B} \approx 0.5$ as described in Section 2.5.4, with their associated distributions of order parameters plotted in the red left-stairs representation.

The resulting distributions of order parameters for ppAB in vacuum, across the sub-ensembles that commit to either of the stable states and the TS states, are plotted in Figure 38.

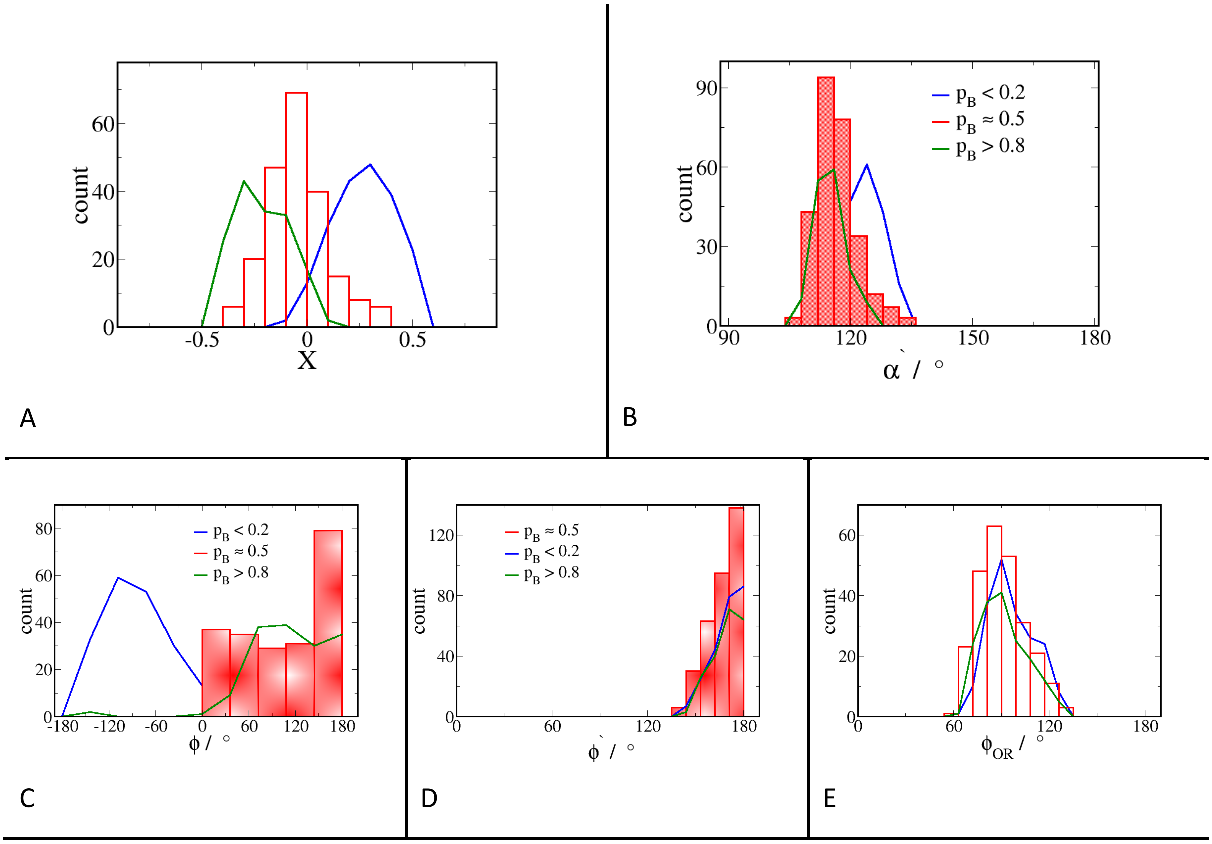

Figure 38. Transition state analysis Distributions of coordinates for ppAB in vacuum for the sub-ensembles of the restrained $\mathrm{X} = \mathrm{X}^{*}$ensemble: (A) in the coordinate X, (B) in the bend angle α', (C), (D), (E) in the adjacent dihedrals ϕ, ϕ' and the orientation dihedral parameter ϕ_{OR} respectively. The sub-ensembles were assigned based on their committor values as stated in the legends and in text.

Clearly the coordinate X is well separated between the sub-ensembles but with a substantial overlap between the TS and stable states' sub-ensembles (A). Both, the non-linear bend angle α' and one of the adjacent dihedrals ϕ change within the cis → trans transition, where the values adopted in the TS sub-ensemble overlap with those in the trans stable state (B and C, respectively). On the other hand, the ring orientation stays constant within the transition, as the corresponding distributions in ϕ_{OR} across the sub-ensembles overlap (E). Also, the bond lengths for the central moiety C-N=N'-C are expected to change during the inversion process, since the inverting nitrogen N' experiences a change in orbital hybridization from $\mathrm{sp}^2 \rightarrow \mathrm{sp}$. This is accompanied by the shortening of the N'-C and N=N' bonds, denoted r_{NC} and r_{NN} respectively. Upon re-hybridization of the inverting nitrogen N', more overlap with the neighbouring orbitals is induced. We found for the bond lengths r_{NC} and r_{NN} to be shorter in the TS sub-ensemble compared to the stable states and are plausible candidates as the reactive coordinates, which we do not shown here.

3.4.4 Likelihood maximization for the Reaction Coordinate

In this section we present the results of applying the likelihood maximization algorithm based on the TPS shooting history introduced in Methods Section 2.6.2. Combinations of many order parameters are considered in order to obtain a reaction coordinate as the one with the highest likelihood. Since the central C-N=N-C moiety experiences the most pronounced change within the $\mathrm{cis} \rightarrow \mathrm{trans}$ transition it is plausible that the order parameters such as angles, dihedrals and distances: α', ϕ, ϕ', r_{NC}, r_{NN}, defined for those atoms would be the most likely candidates for reactive coordinates, alongside the coordinate $X\ (\omega, \alpha)$.

The reaction coordinate was constructed as a linear combination of 2 and 3 order parameters and the likelihood calculated based on the shooting point configurations and the outcomes of their TPS shooting histories. Then, the reaction coordinate with the highest likelihood was kept as the best model. The total of set of 118 that is 136 geometrical parameters was considered for the optimization of pure AB and ppAB substituted derivative, the list of which is given in the Appendix 6.2. All the angles used as input were sine-transformed to produce a constant range for all order parameters including the coordinate X, namely $[-1, 1]$.

In the original implementation by Peters and Trout [97], an aimless shooting algorithm was employed to achieve decorrelated outcomes when shooting from the transition region. In the present setup for the TPS we employed a two-way shooting algorithm with stochastic dynamics for which decorrelated outcomes are ensured. Also, we shoot from the interface that accomodates the transition region. The input for the LM analysis was simply a set of shooting points and the outcomes of the forward segments for trajectories. In general, we found the LM algorithm was highly sensitive with respect to the input configurations used. It was primarily the range in X for the input configurations that made a difference, namely if configurations from a tight $X = [-0.15, 0.15]$, or a wider interface $X = [-0.5, 0.5]$, were used as well as the total number of input configurations. It is plausible to assume that configurations from a tighter interface contain variations of order parameters more relevant for the transition. On the other hand, configurations from a wider interface capture the variations along the slower degrees of freedom. It would therefore be needed to use the configurations from the full TS ensemble as input, especially for the ppAB derivative shown to be markedly spread out in the coordinate X. The resulting optimized RCs were composed of different structural parameters and to evaluate their relevance we used chemical intuition and the committor analysis as a more meaningful diagnostic.

In Tables 12 and 13 we present the result for the best reaction coordinates as optimized by the LM algorithm for the unsubstituted AB and the push-pull ppAB in vacuum, respectively.

For AB in vacuum, the input consisted of a total of 862 shooting point configurations from the tighter interface $X = [-0.15, 0.15]$ of which 553 ended in the state A, cis, and 309 ended in the state B, trans isomer. The log-likelihood $\ln L$ was maximized for all linear combinations of 2 and 3 parameters with the resulting optimized reaction coordinates for $n = 1, 2, 3$ order parameters in the expansion reported in Table 12. The change of the log-likelihood upon addition of the third order parameter did not significantly improve the reaction coordinate according to the Bayes Information Criterion, since it was smaller than $\delta L_{\min}$. The optimized reaction coordinate expanded up to $n = 2$ order parameters was thus sufficient to best describe the training data for the case of AB in vacuum. Firstly, we see that the coordinate X is the single order parameter with the highest log-likelihood that best describes the reaction coordinate. Among all combinations of two order parameters, the highest log-likelihood is achieved for the combination of the sine-bend angle $\sin\alpha'$, and with a significant improvement according to the BIC criterion. This bend angle which does not linearize in the isomerization process, was also shown to be correlated with the transition as it shortens going from cis → trans, see Figure 35B. The addition of the third order parameter to the expansion the increase of the log-likelihood was not significant according to BIC and we conclude that the optimized reaction coordinate $r = 2.00 - 1.56 \cdot X - 2.28 \cdot \sin\alpha'$ is the best one given the training data. It is interesting to indicate the additional parameters that contribute to the reaction coordinate, but do not increase its log-likelihood sufficiently. Those are namely the adjacent dihedral $\sin\phi'$ and a composite coordinate $\cos\omega\sin\phi'$ both relevant for the orientation of phenyl rings, and the bond length r_{NC} which was observed to shorten with the change in the electron distribution around the inverting nitrogen.

Table 12. Likelihood Maximization analysis of the TPS shooting points for AB in vacuum. The minimal improvement of likelihood to accept the additional order parameter in the reaction coordinate is indicated with δL_{min} (Bayes Information Criterion). The reaction coordinate as a combination of maximal 3, order parameters with the maximal log-likelihood $\ln L$ is given in the third column, with the optimized RC according to the BIC in red.

AB $\delta L_{min} = 3.4$ n	$\ln L$	Reaction coordinate
1	-573.1	$0.07 - 0.74 \cdot X$
2	-558.3	$2.00 - 1.56 \cdot X - 2.28 \cdot \sin\alpha'$
3	-556.8	$2.36 - 1.16 \cdot X - 2.37 \cdot \sin\alpha' - 1.05 \cdot \cos\omega\sin\phi'$
3 (2nd best)	-557.8	$2.14 - 1.49 \cdot X - 2.11 \cdot \sin\alpha' - 0.43 \cdot \sin\phi'$
3 (3rd best)	-557.9	$1.92 - 1.49 \cdot X - 1.93 \cdot \sin\alpha' - 0.70 \cdot r_{NC}$

For the push-pull ppAB in vacuum the input for the LM algorithm consisted from a total of 1028 shooting points of which 553 ended in the state A, cis, and 309 ended in the state B, trans isomer. The configurations from the wider interface $X = [-0.5, 0.5]$ were used as input though, since the LM algorithm yielded a more meaningful reaction coordinate than with the input from the tight interface, the result of which is shown in the Appendix 6.3. Interestingly, in case of the tight interface input the order parameters that emerged as relevant were combinations of the central and adjacent dihedrals ω, ϕ', with the coordinate X showing up only as the third most relevant with the lowest weight in the linear expansion. The optimized reaction coordinate is essentially the same as for the AB in vacuum with different expansion coefficients. The additional bend angle $\sin\alpha'$ significantly improves the log-likelihood of the coordinate X as the single order parameter RC, with the relative weight greater than was the case for pure AB. Again, the same order parameters for the phenyl ring orientation emerge as the best candidates in the expansion of the RC up to 3 order parameters, $n = 3$, but do not significantly improve its log-likelihood. We conclude that, for the training data used for both compounds, there is no difference in the LM-optimized reaction coordinate, found to be a function of the same coordinates $r\,(X, \sin\alpha')$.

Table 13. Likelihood Maximization analysis of the TPS shooting points for ppAB in vacuum. The minimal improvement of likelihood to accept the additional order parameter in the reaction coordinate is indicated with δL_{min} (Bayes Information Criterion). The reaction coordinate as a

combination of maximal 3, order parameters with the maximal log-likelihood $\ln L$ is given in the third column, with the optimized RC according to the BIC in red.

ppAB $\delta L_{\mathrm{min}} = 3.5$ n	$\ln L$	Reaction coordinate
1	-605.0	$0.09 - 1.19 \cdot X$
2	-588.4	$2.04 - 2.42 \cdot X - 2.47 \cdot \sin\alpha'$
3	-585.7	$1.46 - 2.34 \cdot X - 2.13 \cdot \sin\alpha' - 0.71 \cdot \sin\phi'$
3 (2^{nd} best)	-585.8	$1.58 - 2.09 \cdot X - 2.60 \cdot \sin\alpha' - 0.77 \cdot \cos\omega \sin\phi$

As a convenient representation for the quality of a reaction coordinate, the position of the dividing surface $r = r^*$ can be compared to the projections of the TS ensemble onto the reactive components, $r\,(X, \sin\alpha')$. The dividing surface in the reactive coordinates $X, \sin\alpha'$ was obtained by setting $r = 2.00 - 1.56 \cdot X - 2.28 \cdot \sin\alpha' = 0$. Namely, the committor function $p_B(r)$ was modelled as a tan function which crosses the value $p_B = 0.5$ at $r = 0$ where the transition region is thus positioned. The dividing surface placed at $r = 0$ and plotted in the $(X, \sin\alpha')$ space is a simple line, which for a good reaction coordinate should thus coincide with the TS ensemble projected onto the same components. The TS ensemble for AB and ppAB falls onto an approximately straight line, but cannot be perfectly approximated with the dividing surfaces associated with their respective LM optimized reaction coordinates, as shown in Figure 39A and 39B, respectively. The discrepancy between the dividing surface plotted in violet and the regression line to the TS ensemble plotted in red is more pronounced for the ppAB than the AB in vacuum. Equally, the TS ensemble is more spread out in both reactive coordinates $(X, \sin\alpha')$ for ppAB as well.

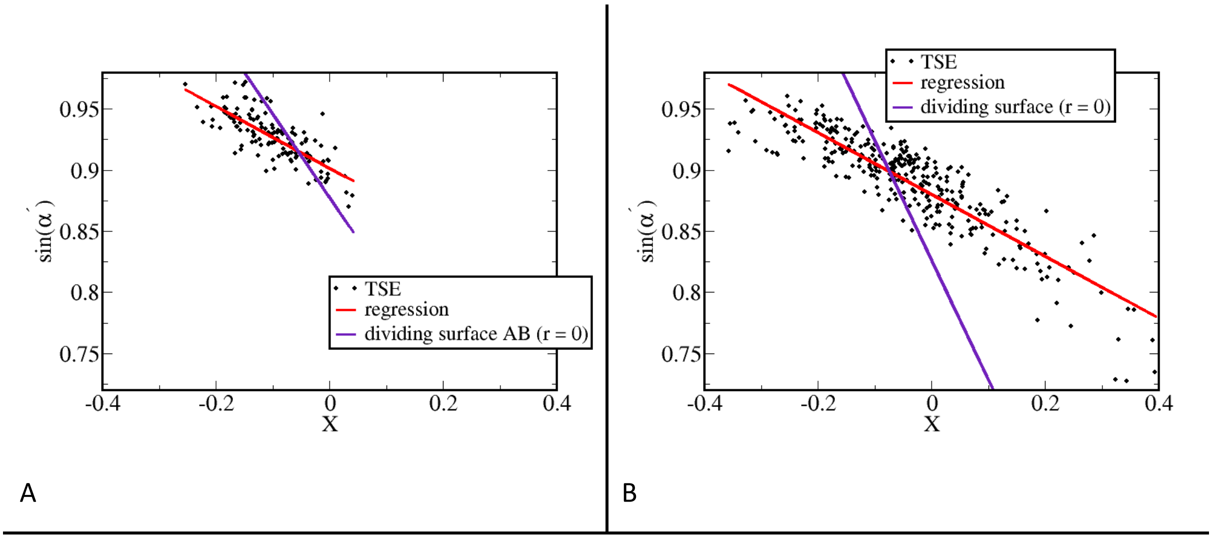

Figure 39. Transition state ensembles in the $(X, \sin\alpha')$ plane for (A) AB and (B) ppAB in vacuum. The dividing surface for the LM optimized coordinates $r\,(X, \sin\alpha') = 0$ are plotted in violet, while the regression line to the TSE projections in red.

The reaction coordinate $r\,(X, \sin\alpha')$ is indeed a better reaction coordinate for AB than ppAB. This is further demonstrated by comparing the distributions in the reaction coordinate for the sub-ensembles of stable states and the TS ensemble. The respective conditional distributions, $P\,(r \mid \rightarrow \mathrm{cis})$, $P\,(r \mid \rightarrow \mathrm{trans})$ and $P\,(r \mid \mathrm{TSE})$, are plotted in Figure 40 A and B for the unsubstituted AB and the push-pull ppAB, respectively. This also served as a confirmation that the optimized reaction coordinate r was in fact centered around $\mathrm{r} = 0$ in the transition state ensemble. A more substantial overlap in the conditional probabilities for the stable states and transition states sub-ensembles associated to the ppAB was observed. This would imply that configurations with a certain value of the reaction coordinate r from the overlap regions are equally likely to commit to a stable state as they are to be a transition state. The coordinate r is thus not an ideal descriptor for the reaction and there are additional variables not captured with the coordinate r with respect to which the respective states differ.

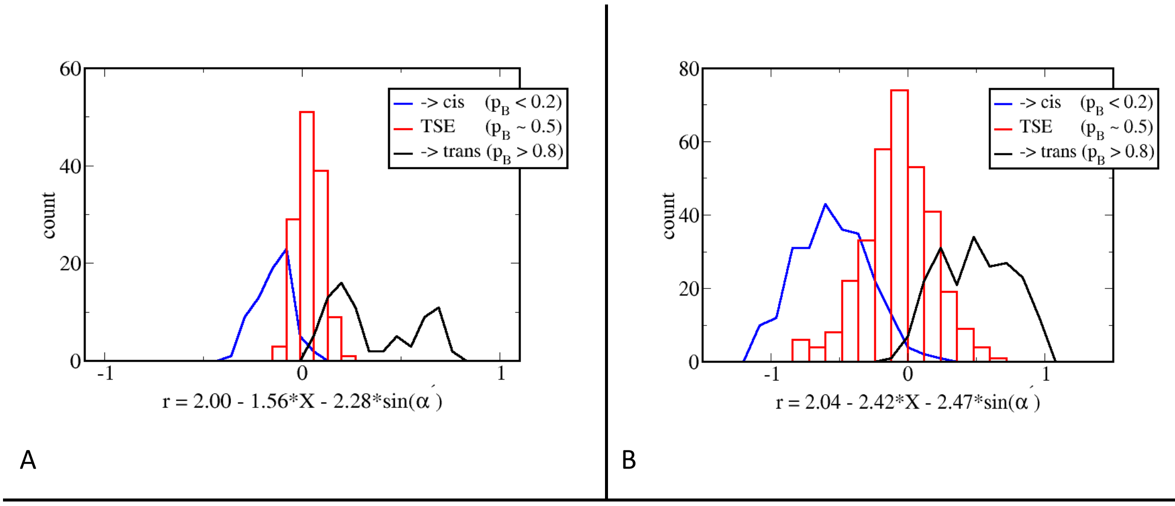

Figure 40. The probability distributions for AB and ppAB in vacuum as a function of the optimized reaction coordinate, r for the TSE $\mathrm{P}\ (\mathrm{r} \mid \mathrm{TSE})$ in red, and the configurations committed to cis $\mathrm{P}\ (\mathrm{r} \mid \rightarrow \mathrm{cis})$ in blue and trans stable states, $\mathrm{P}\ (\mathrm{r} \mid \rightarrow \mathrm{trans})$ in black.

3.4.5 Committor analysis for the optimized RCs

For a good reaction coordinate all its components are orthogonal to the separatrix that is the hypersurface which contains the transition states [34]. We expect for the optimized reaction coordinates $\mathrm{r}\ (\mathrm{X}, \sin\alpha')$ of the previous section to represent an improvement over the coordinate X in this respect. The ensemble of configurations restrained to the value $\mathrm{r} = 0$ as given by the model for the reaction coordinate and the committor function, should thus more completely accommodate the TS ensemble with the committor distribution a Gaussian centered around $\mathrm{p_B} \sim 0.5$.

The associated committor distributions for the ensembles restrained to the dividing surface $\mathrm{r}^* = 0$ of the reaction coordinate optimized for AB in vacuum, $\mathrm{r} = 2.00 - 1.56 \cdot \mathrm{X} - 2.28 \cdot \sin\alpha'$ is plotted in Figure 41A. It is indeed a Gaussian roughly centered around $\mathrm{p_B} = 0.5$. The alternative positions for the dividing surface with $\mathrm{r}^* = 0.05, 0.10$ are also plotted in black and red lines, respectively. By shifting the position of the dividing surface away from the transition region the skewing of the committor distributions is observed. We found this result to be a substantial improvement over the committor distribution for configurations restrained at $\mathrm{X} = \mathrm{X}^*$, uniform like and slightly skewed to the trans state (Figure 22). The single most dominant reactive barrier orthogonal to the coordinate X was thus identified as the other non-linear bend angle α'. The committor distribution for the ensemble $\mathrm{r}^* = 0$ is still quite broad with the average value $\langle 2\, \mathrm{p_B}(1 - \mathrm{p_B}) \rangle = 0.43 \pm 0.09$, smaller than the ideal 0.5. One possible interpretation of this broadening for the committor distributions is the diffusive dynamics [34, 39]. As a reminder, the calculated coefficient χ measuring the (de)correlation of trajectories' outcomes amounted to $\chi = 0.68$, a value far from the one it would attain for purely ballistic dynamics, $\chi = 1$. Nevertheless, the average committor value should ideally be 0.5 at the dividing surface. It is indeed possible that this simple 2 order parameters model for the reaction coordinate is not the ideal and there are other important reactive coordinates, which could not be identified given the training set of configurations. Given that the TS ensemble projections onto the reactive space $(\mathrm{X}, \sin\alpha')$ was still substantially spread out with its regression line not perfectly coinciding with the dividing surface $\mathrm{r}^* = 0$, it is likely the optimized coordinate $\mathrm{r}\ (\mathrm{X}, \sin\alpha')$ could still be improved by including more order parameters into the linear expansion for the reaction coordinate.

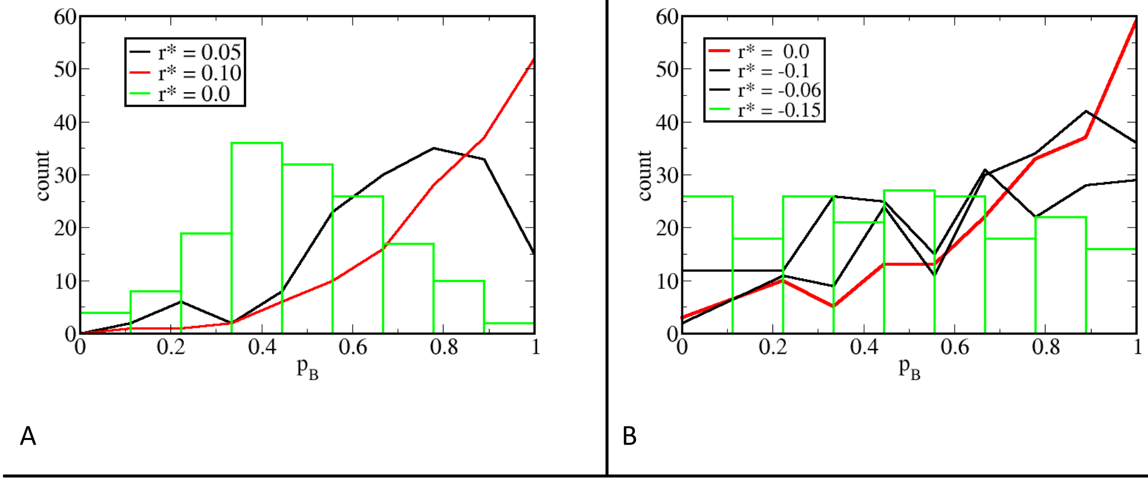

Figure 41. Committor analysis for AB and ppAB in vacuum for configurations restrained at the value(s) of the reaction coordinate r for the bin with the highest count in $\mathrm{P}\ (\mathrm{r} \mid \mathrm{TSE})$. (A) AB, $\mathrm{r}^* = \{0.00, 0.10, 0.15\}$ (B) ppAB, $\mathrm{r}^* = \{0.00, -0.06, -0.10, -0.15\}$. The committor distribution is Gaussian like for the $\mathrm{r}^* = 0.00$ restrained ensemble for AB in green, unlike the ensembles $\mathrm{r}^* = 0.00$ for ppAB in red, which is skewed to the trans state. Moving the position of the dividing surface to $\mathrm{r}^* = -0.15$ resulted in a uniform distribution (in green).

The committor analysis for the optimized reaction coordinate for push-pull ppAB in vacuum, $\mathrm{r} = 2.04 - 2.42 \cdot \mathrm{X} - 2.47 \cdot \sin\alpha'$, restrained at $\mathrm{r}^* = 0.0$ resulted with a committor distribution skewed to the trans state, plotted in red line in Figure 41B. We also tried moving the position of the dividing surface to account for possible miscalculations of the LME algorithm. This would correspond to changing the relative weights for the parameters $\mathrm{X}, \sin\alpha'$ in the expansion $\mathrm{r} = \mathrm{a}_0 + \mathrm{a}_1 \cdot \mathrm{X} + \mathrm{a}_2 \cdot \sin\alpha'$ and the corresponding slope in $(\mathrm{X}, \sin\alpha')$ space. By moving the position of the dividing surface in the negative direction the committor distribution indeed changed to a more uniform, until it reached the ideal uniform shape for the position $\mathrm{r}^* = -0.15$, plotted in green. Moving the position of the dividing surface to more negative values of r resulted with skewing to the opposite direction that is the cis stable state.

In conclusion, the optimized coordinate $\mathrm{r}\ (\mathrm{X}, \sin\alpha')$ for ppAB in vacuum is obviously a worse reaction coordinate compared to the unsubstituted AB. This was further corroborated by the comparison of its dividing surface at $\mathrm{r}^* = 0.0$ with the projections of the TS ensemble onto the reactive space $(\mathrm{X}, \sin\alpha')$ plotted in Figure 39B. Even though the dividing surface line crossed the most populated region of the TS ensemble, it was not parallel to the regression line. In fact, the TS ensemble was quite spread out along both $(\mathrm{X}, \sin\alpha')$ directions, more pronouncedly so than for AB in vacuum.

The highest likelihood coordinate involving the expansion in 3 order parameters for pp-AB as predicted with the LM analysis was a function of an additional adjacent dihedral defining the phenyl ring twisting, $\mathrm{r}\ (\mathrm{X}, \sin\alpha', \sin\phi')$, as reported in Table 13. We also tested the committor distribution for its associated dividing surface $\mathrm{r} = \mathrm{r}^*$ which did not show any improvement over the 2 parameter reaction coordinate as shown in the Appendix 6.4. We conclude that there are additional reactive coordinates that must be included which exceeds our current analysis. Another possibility is that the more appropriate reaction coordinate is modelled with interaction terms or as non-linear with respect to parameters $(\mathrm{X}, \sin\alpha')$. This is presented more clearly with the path densities in these reactive coordinates which we plot in the next section.

3.4.6 Solvent effect: TSE projections onto the $(\mathrm{X}, \sin\alpha')$ reactive coordinates

The likelihood maximization (LM) for the reaction coordinate presented in the previous section was successful for both compounds AB and ppAB in vacuum insofar an additional coordinate to the reaction coordinate X, the bend angle α' was correctly detected as reactive. In this section we explore the identified reactive space $(\mathrm{X}, \sin\alpha')$ in DMSO and toluene solvents and compare it to the vacuum case.

The LM algorithm applied to the solvated configurations of AB in both toluene and DMSO did not perform optimally. We tested the algorithm with various input configurations, either from the tight interface in the coordinate X, $\mathrm{X} = [-0.15, 0.15]$ or from the wide interface, $\mathrm{X} = [-0.5, 0.5]$. Given the fact that for the unsubstituted AB, the TS ensembles projected onto the coordinate X reported in Figure 37A were comparably spread out for both solvents toluene and DMSO as in vacuum, we expected for the tighter interface to be adequate to describe the reaction. The resulting optimized reaction coordinates are reported in the Appendix 6.3.

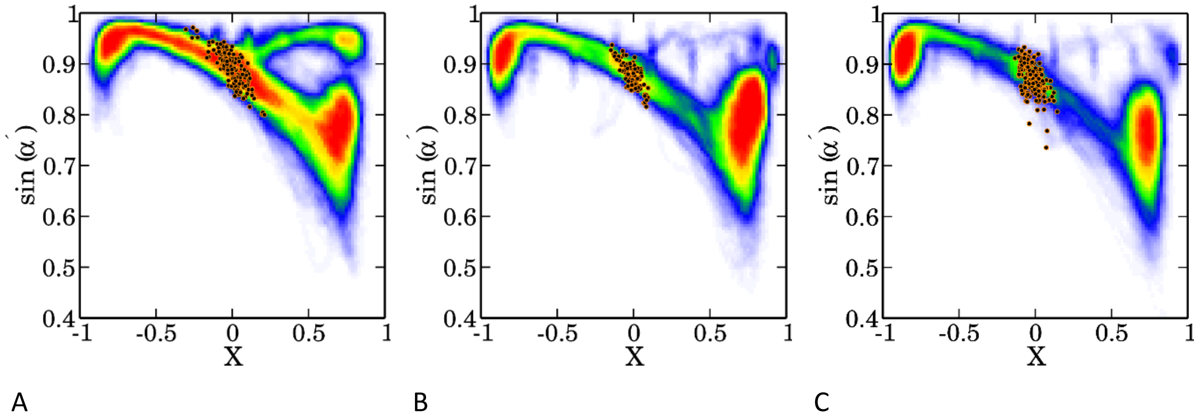

Figure 42. Path densities in the reactive space $\mathrm{X}, \sin\alpha'$ and the projected TS ensembles for AB in vacuum (A), in toluene (B) and in DMSO (C).

We inspect the form of the projected TS ensembles onto the two reactive parameters that make up the optimized reaction coordinate $\mathrm{r}\ (\mathrm{X}, \sin\alpha')$ with the TS ensemble projections superimposed on the path densities in the reactive space $(\mathrm{X}, \sin\alpha')$ for AB in vacuum and toluene and DMSO solvents in Figure 42. The features for the TS ensemble projections, depicted as black dots, seem to be comparable for all cases while in toluene (B) and DMSO (C) the TSE seems to be even more concentrated around the transition region than in vacuum. All TSE projections can roughly be placed on a straight line with similar slopes, which is indicative that the dividing surface does not deviate much from the one in vacuum. To evaluate in how far the dividing surface placed at $r = r^*$ for the reaction coordinate optimized for AB in vacuum is a good dividing surface in solvents as well, we performed the committor analysis for the ensembles restrained at $r = r^*$ in DMSO and toluene solvents. The reaction coordinate used was thus the one obtained for AB in vacuum, $r = 2.00 - 1.56 \cdot X - 2.28 \cdot \sin \alpha'$ and the configurations restrained to the dividing surface at $r = 0$. Strikingly, the resulting committor distributions for AB in toluene and in DMSO remained Gaussian like and centered around $p_B \sim 0.5$ and essentially overlap with the committor distribution obtained in vacuum, as shown in Figure 43.

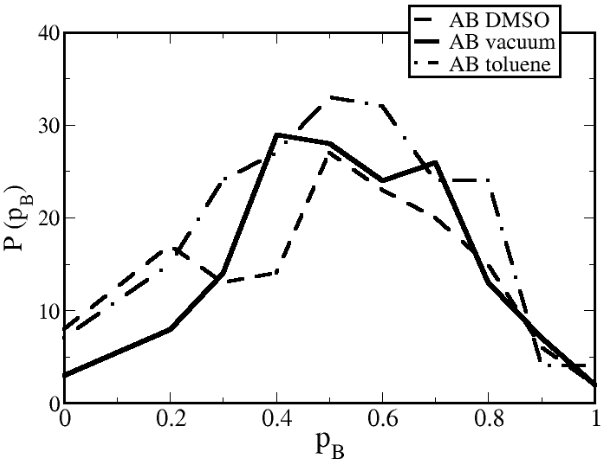

Figure 43. Committor analysis for the reaction coordinate optimized for AB in vacuum. It is a good reaction coordinate for AB in toluene and DMSO solvent as well (dashed lines), as the committor distribution for configurations restrained to the dividing surface $r = [-0.005, 0.005]$ essentially overlap, with some additional structure for AB in DMSO.

Admittedly, there is some additional structure for AB in DMSO, while both committor distributions have heavier tails in the regions where $p_B < 0.2$ and $p_B > 0.8$. This is to say that, there is a higher count of configurations that commit to cis and trans stable states, respectively. Overall, the reaction coordinate optimized for AB in vacuum performs as a good reaction coordinate in solvent as well.

As for the push-pull derivative ppAB we found the reaction coordinate $r\ (X, \sin \alpha')$ optimized using the configurations in vacuum, not to be ideal. The ensemble of configurations restrained at the dividing surface for the coordinate r yielded a uniform distribution of committors as depicted in Figure 41B, indicating they were equally likely to commit to either of the states. Thus, the kind of analysis we applied for the AB compounds in terms of characterizing solvent effects based on the features of committor distributions for the ensembles restrained at the dividing surface of r optimized in vacuum is not applicable. With the coordinate X as the reaction coordinate we observed the committor distributions of ensembles restrained at $X = X^*$ for the push-pull ppAB to be uniform in both vacuum and DMSO where they basically followed the same line within statistical error, as shown in Figure 22. In case of $r\ (X, \sin \alpha')$ as the reaction coordinate we would expect the same trends for the resulting committor distributions when going from vacuum to solvent.

The path densities and the projected TS ensembles in the reactive coordinates $(X, \sin \alpha')$ space for the push-pull derivative ppAB are plotted in Figure 44. The TS ensembles for ppAB are generally more spread out compared to the unsubstituted AB in vacuum. Moreover, the effect of solvent is reflected in the features for the TS ensemble projections more so in DMSO than in toluene, with pronounced uniform spreading in both reactive coordinates. This is in accordance with the pronounced shift in value of the coordinate $\mathrm{X}\ (\omega, \alpha)$ for transition states in DMSO due to pronounced bending in the bend angle α. The spread in the other bend angle, $\sin\alpha'$ is comparable across the TS ensembles, even though more pronounced compared to the TS ensembles for AB in vacuum and in solvents. The push-pull substitution effects the bend angle α' in the optimized transition structures as well, making it slightly greater than for the unsubstituted AB.

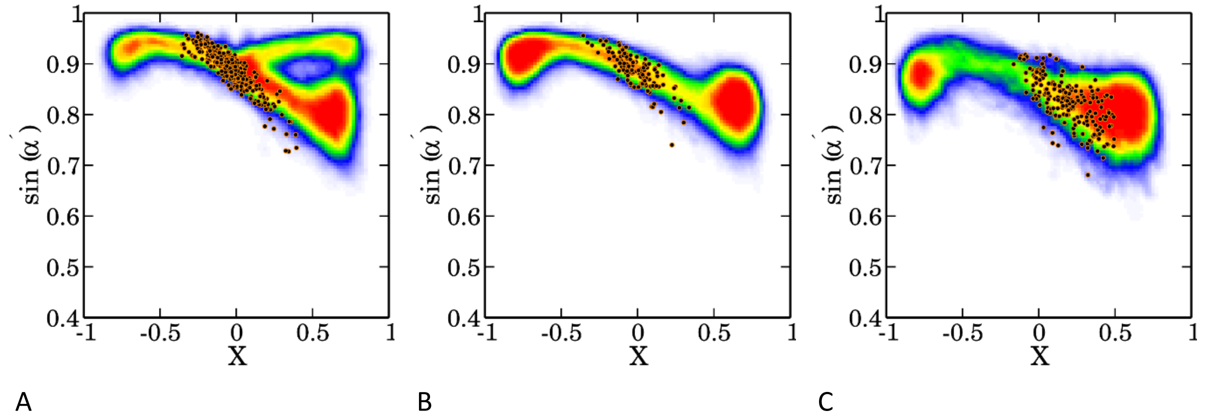

Figure 44. Path densities in the reactive space $\mathrm{X}, \sin\alpha'$ and the projected TS ensembles for ppAB in vacuum (A), in toluene (B) and in DMSO (C).

Another general feature of the path densities in the reactive space $(\mathrm{X}, \sin\alpha')$ for both AB and ppAB is the existence of an additional 'reactive channel' in vacuum that is not present in solvents. That is, a fraction of paths proceeds from the cis, $\mathrm{X}^{\mathrm{cis}} \sim 0.85$ to trans state, $\mathrm{X}^{\mathrm{trans}} \sim -0.85$ without much change in the bend angle α'. For this branch located in the upper region of $(\mathrm{X}, \sin\alpha')$ space, the bend angle α' assumes smaller values, that is greater values of its sine value, $\sin\alpha'$, characteristic for the trans state throughout the reaction. The main reactive channel proceeds from $\mathrm{cis} \rightarrow \mathrm{trans}$ with the reduction of the bend angle α' as predicted from the QM optimized cis and trans structures reported in Table 5 in Results Section 3.1. For the transition states, smaller values for the bend angle characteristic of the trans stable state are assumed, also in accordance with the geometry for the optimized transition structures.

3.4.7 Solvent effect for ppAB: LM analysis for the reaction coordinate

For the push-pull derivative ppAB in vacuum, a good reaction coordinate in terms of having a Gaussian-like committor associated with its dividing surface could not be optimized with likelihood maximization. This hindered the further inspection of the quality of the putative $\mathrm{r}\ (\mathrm{X}, \sin\alpha')$ identified in vacuum as the reaction coordinate for the push-pull ppAB in solvents. Interestingly, the LM optimization of the reaction coordinate using configurations of ppAB in solvents as input performed better than for AB in solvents. Therein, configurations from both a wide $\mathrm{X} = [-0.5, 0.5]$ and a tight interface in the coordinate X were used to test the performance of the LM algorithm. Here, we present the results for the tighter interface which encompassed the most of variation for the coordinate X in the TS ensemble, as can be seen in Figure 37B in Results Section 3.4.3.

For ppAB in toluene, a total of 1470 configurations from a tight interface $\mathrm{X} = [-0.15, 0.15]$ were used as input, of which 407 ended in state A and 1067 ended in state B. For ppAB in DMSO, a total of 838 configurations from a tight interface $\mathrm{X} = [0.0, 0.35]$ were used as input, of which 653 ended in state A and 185 ended in state B. The result of the LM optimization is presented in Table 14.

Table 14. LM analysis of the TPS shooting points for ppAB in solvents. The minimal improvement of likelihood to accept the additional order parameter in the reaction coordinate is indicated with $\delta\mathrm{L}_{\mathrm{min}}$ (Bayes Information Criterion). The reaction coordinate as a combination of maximal 3, order parameters with the maximal log-likelihood $\ln \mathrm{L}$ is given in the third column. The general labelling for distances, angles and dihedrals if not one of the angles and dihedrals indicated in the molecular schemes in Figure 16, are r for distances, α for angles and ϕ for dihedrals, with atom indices defining the parameter in the subscript. The atom indices can be read from molecular schemes in Figures 58 of the Appendix 6.2.

ppAB toluene $\delta\mathrm{L}_{\mathrm{min}} = 3.6$ n	$\ln \mathrm{L}$	Reaction coordinate
1	-923.6	$-0.27 + 1.48 \cdot \phi_{4,3,2,7}$
2	-903.6	$2.99 - 1.52 \cdot \mathrm{X} - 2.63 \cdot \sin\alpha'$
3	-876.1	$4.65 - 1.76 \cdot \mathrm{X} - 3.27 \cdot \sin\alpha' - 2.28 \cdot \sin\phi_{4,3,17,27}$
ppAB DMSO $\delta\mathrm{L}_{\mathrm{min}} = 3.4$ n	$\ln \mathrm{L}$	Reaction coordinate
1	-506.5	$-0.02 + 1.36 \cdot \sin\phi_{4,3,17,27}$
2	-496.2	$1.36 - 1.17 \cdot \mathrm{X} - 2.08 \cdot \sin\alpha'$
3	-484.4	$3.19 - 2.26 \cdot \sin\alpha' - 2.57 \cdot \sin\alpha - 1.87 \cdot \sin\phi$

First of all, a dihedral angle for the rotation of the amino group NH_2 attached to one of the phenyl rings $\phi_{4,3,17,27}$ emerges as the single order parameter with the greatest likelihood for ppAB and DMSO and as one of the order parameters for the highest likelihood 3-parameter coordinate for ppAB in toluene. The atom indices defining the dihedral are given in the molecular scheme in Figure 58 of the Appendix 6.2. This coordinate is obviously not crucial for the cis → trans isomerization, but there is apparently pronounced twisting of the amino group in DMSO solvent and the phenyl rings as given by the variation in the $\phi_{4,3,2,7}$ dihedral in toluene solvent. An increased variation in these dihedral parameters identified as significant by the LM algorithm, which was absent for configurations in vacuum, might have arisen upon interaction and the random kicks induced by the solvent molecules.

Interestingly, the highest likelihood coordinate for combination of 2 order parameters is a function of the same parameters as obtained for AB in vacuum, namely the $\mathrm{r}\ (\mathrm{X}, \sin\alpha')$ coordinate. What is more striking, the relative weights for the components in the reaction coordinate, $\mathrm{r} = \mathrm{a}_0 + \mathrm{a}_1 \cdot \mathrm{X} + \mathrm{a}_2 \cdot \sin\alpha'$, and therefore the slope $\mathrm{b} = -\mathrm{a}_1/\mathrm{a}_2$ for the dividing surface at $\mathrm{r} = 0$, are very similar for all cases. The slopes in the reactive space $(\mathrm{X}, \sin\alpha')$ amounted to $\mathrm{b} = -0.68, -0.58, -0.56$ for AB in vacuum, ppAB in toluene and ppAB in DMSO, respectively. The TS projections for ppAB in DMSO and toluene solvents onto the reactive space $(\mathrm{X}, \sin\alpha')$ and the optimized dividing surface $\mathrm{r}\ (\mathrm{X}, \sin\alpha') = 0$ for AB in vacuum are depicted in Figure 45. Remarkably, the dividing surface associated with the reaction coordinate optimized for the unsubstituted AB in vacuum crosses the high density regions of the TS ensemble projections and thus contains many of the transition states for the push-pull ppAB in solvents as well.

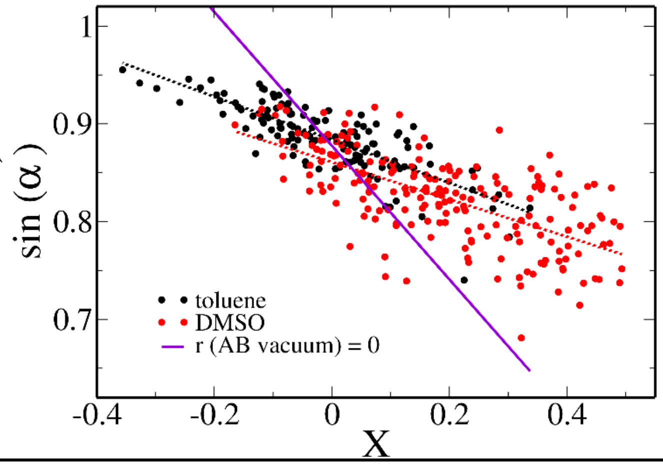

Figure 45. Transition state ensembles in the $(\mathrm{X}, \sin\alpha')$ plane for ppAB in solvents. The dividing surface for the LM optimized coordinate $\mathrm{r}\,(\mathrm{X}, \sin\alpha') = 0$ for AB in vacuum is plotted in violet, while the regression lines to the TSE projections in dashed black and red for ppAB in toluene and DMSO, respectively.

Another potentially meaningful reaction coordinate was obtained by using the configurations from a wider interface for ppAB in DMSO, reported in the Appendix 6.3.3. The coordinate X did not emerge as a reactive coordinate for any of the highest likelihood combinations of order parameters. The highest likelihood reaction coordinate with 2 parameters was $\mathrm{r} = 1.19 + 2.54 \cdot \sin\omega - 3.45 \cdot \sin\phi$, while the one for 3 order parameters was $5.01 - 3.19 \cdot \sin\alpha' - 2.37 \cdot \sin\alpha - 3.19 \cdot \sin\phi$. Obviously, the reaction coordinate on the level of 2 parameters is best described by a pure rotation and twisting around the adjacent C-N bond. On the level of 3 parameters, the best combination involves both of the bend angles and the twisting dihedral. Given that we found for the isomerization of ppAB in DMSO to proceed through an almost rotamer transition state (see the average transition state in Figure 33 in Section 3.3.5) the finding that the bend angle α nor the coordinate $\mathrm{X}\,(\omega, \alpha)$ did not emerge as the highest likelihood reaction coordinates is not surprising.

In conclusion, the solvents did not profoundly affect the quality of optimized reaction coordinate for the unsubstituted AB nor the structure of the transition state ensemble in the reactive coordinates $(\mathrm{X}, \sin\alpha')$ space. The committor distributions for the configurations restrained at its dividing surface $\mathrm{r}\,(\mathrm{X}, \sin\alpha') = 0$ remained Gaussian-like and centered around $\mathrm{p_B} \sim 0.5$ for both AB in toluene and DMSO, shown in Figure 43.

On the other hand, there was pronounced broadening of the TS projections onto the reactive space for the push-pull ppAB in vacuum, compared to the unsubstituted AB. This would indicate that the more adequate reaction coordinate is a more complex function of the reactive coordinates. Also, the reaction coordinate can be improved by including more reactive parameters in the linear expansion [97]. Nevertheless, the projections of the TSE associated with the push-pull ppAB in solvents roughly followed a straight line with the slope comparable to the dividing surface for the ideal reaction coordinate $\mathrm{r}\,(\mathrm{X}, \sin\alpha')$. The dividing surface in the optimized coordinate r was also shown to cross the most populated regions of the TS ensemble, in Figure 45. Furthermore, in the LM optimization using the configurations of ppAB in solvents, the same parameters emerged as the highest likelihood reaction coordinates with comparable relative weights, as reported in Table 14.

The solvent degrees of freedom seemed not to contribute to the reaction coordinate. It could be argued this is due to minimal coupling between the slower solvent and the fast solute degrees of freedom. The average $\mathrm{cis} \rightarrow \mathrm{trans}$ reaction times are approximately $\tau_\mathrm{r} \sim 0.1\ \mathrm{ps}$ which is 10 times slower than the typical relaxation times for the solvents in molecular simulations, expectedly $> 1\ \mathrm{ps}$ [106]. Nevertheless, a deeper analysis of the solvation shell is needed to further investigate the effect of solvent.

3.4.8 Charge rearrangement and the solvent effect

The $\mathrm{cis} \rightarrow \mathrm{trans}$ isomerization of azobenzene involves a pronounced increase in the dipole moment along the reactive trajectories between the two stable states [4]. The most of this change is induced by change in conformation, with for example the dipole moment of the planar trans conformer close to zero due to symmetry. At the transition state, the solvent might be expected to have a stabilizing effect on the electronic density as predicted by Marcus theory for true charge transfer reactions [108]. The transition structure with a linear NNC sequence of atoms is stabilized through resonance where the electrons move away from the inverting nitrogen and are accommodated by the π system of the phenyl ring. The effect is more pronounced for electron acceptor substituted azobenzenes at the para position of the phenyl ring [4]. Here, we analyse whether and how solvation induces shifts in the electronic density by monitoring the extent of rearrangement of partial charges on the QM atoms. In the QM/ MM scheme, the partial charges on the QM atoms are recalucated each time step during a reactive trajectory in response to the changing electronic embedding, represented by the solvent.

We evaluated the average partial charges associated to configurations along the reactive trajectory defined along the coordinate X. The atomic partial charges for the DFTB3 functional are calculated by integrating the electron densities represented by the orbitals belonging to a given QM atom. A series of restrained runs were set up in the range going from cis to the trans state with a step $\{\, \mathrm{X}_{\max},\ \Delta\mathrm{X},\ \mathrm{X}_{\min} \,\} = \{0.85, -0.05, 0.85\}$, with the total run time of $20\ \mathrm{ps}$.

The average partial charges along the coordinate X for the atoms that experience the most change along the reactive trajectory are plotted in Figure 46. Significant charge rearrangement occurs in the central moiety of atoms C-N-N'-C'-$(\mathrm{C_p}')_2$ and the surrounding phenyl rings carbons $\mathrm{C_p}'$, where N' is the inverting nitrogen. The electronic density shifts away from the inverting nitrogen N'. The most of the electronic density is accommodated by the associated phenyl ring where the two phenyl atoms $\mathrm{C_p}'$ attached directly to the central moiety experience the most decrease in the partial charges. Some of the electronic density is also transferred in the opposite direction of the central carbon C, as depicted with red arrowed lines in the scheme of Figure 46.

The general trend of shift for the electronic density away from the inverting nitrogen to the neighbouring phenyl rings is present for all cases considered. The polarizing solvent does not have a profound effect on the extent of charge rearrangement, demonstrated with the example of the unsubstituted AB going from vacuum, to toluene and to the high polarity DMSO.

Furthermore, the effect of push-pull substitution with electronically active species did not result with pronounced charge rearrangements to the atoms of the nitro and the amino functional groups, which we do not show here. That is, the partial charges for the nitro N,O atoms as well as the amino N,H atoms remained close to constant along the reactive trajectory and the redistribution of charges following the cis → trans isomerization was not transmitted all the way through the delocalized electronic system of the phenyl rings to the push-pull substituents. The atoms of the phenyl rings closest to the inverting nitrogen, -(C_p’)$_2$, again acted as recipients of the most negative partial charge. The general trend for the partial charges variation did not change pronouncedly in solvents.

A striking feature comparing the charge rearrangement for the unsubstituted AB and the push-pull ppAB in all conditions is the more continuous increase of the partial charges for the push-pull derivative. This can possibly be attributed to the azo-moiety being more susceptible to electronic rearrangements due to the presence of electronically active species as substituents.

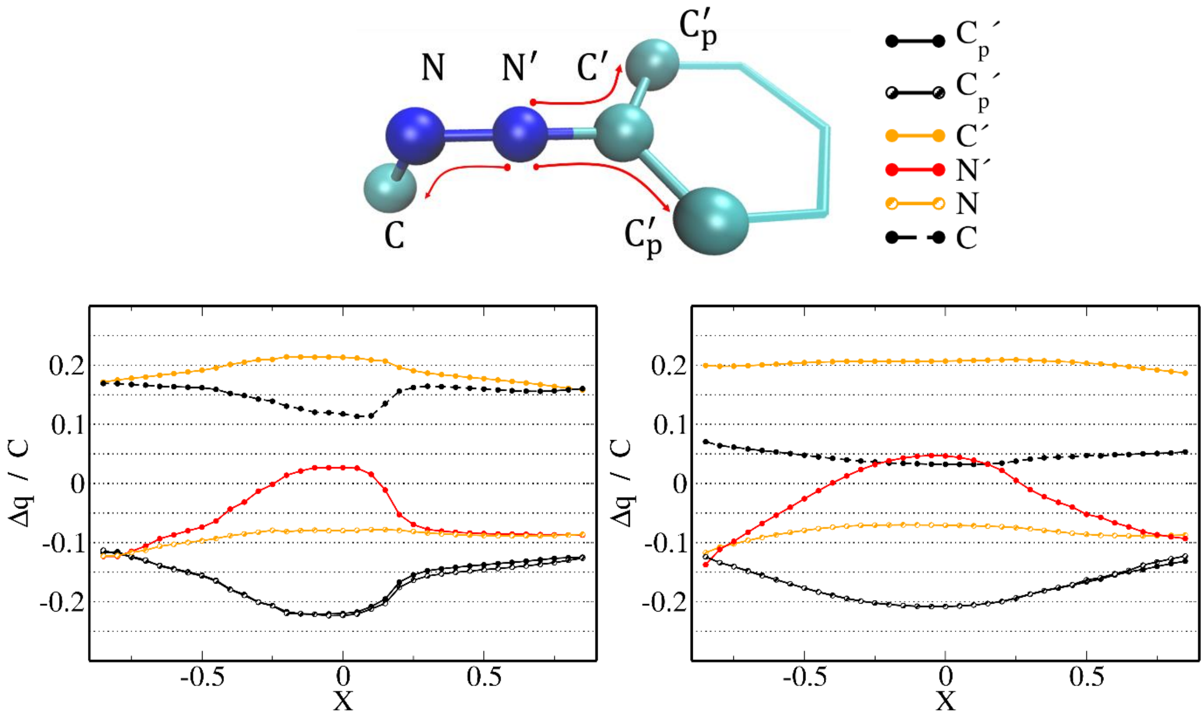

AB vacuum ppAB vacuum

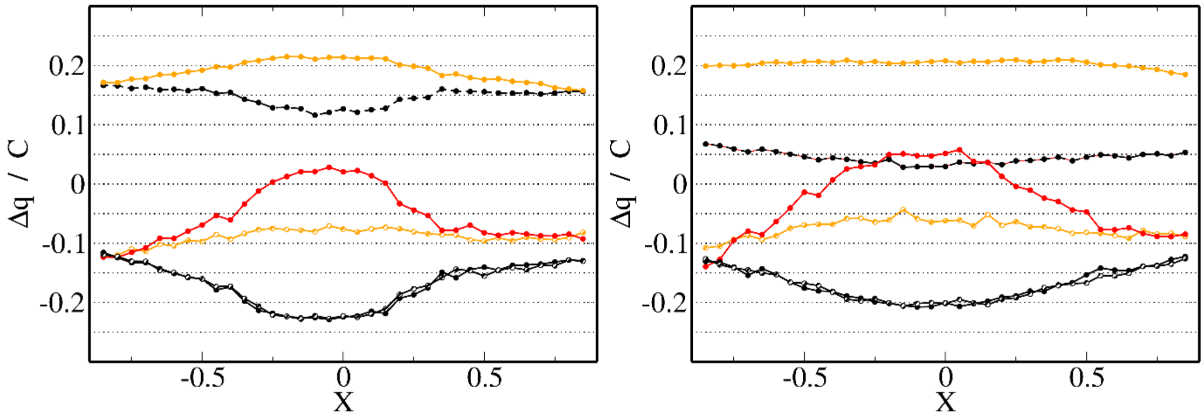

AB toluene ppAB toluene

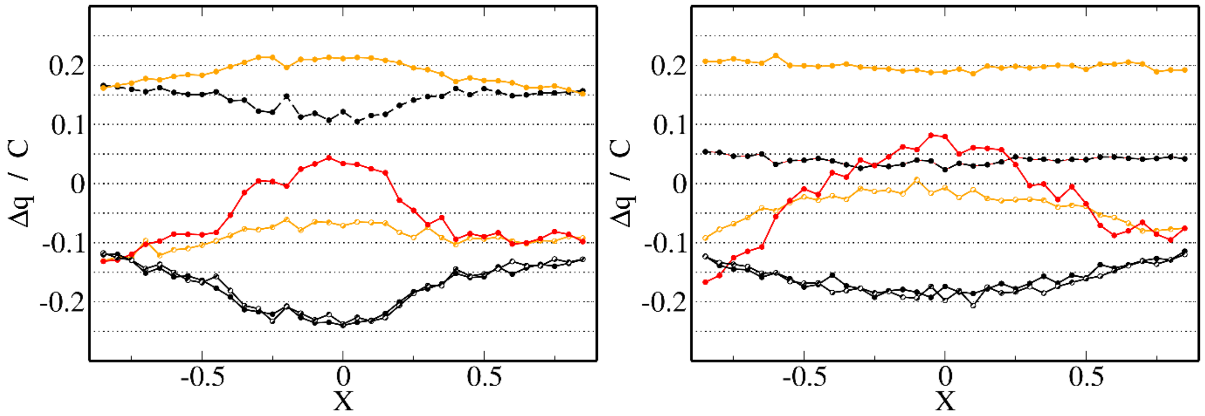

AB DMSO

ppAB DMSO

Figure 46. Charge rearrangement for the cis → trans isomerization: a schematic representation of the central moiety atoms C-N-N’-C’-(C_p’)$_2$, where N’ is the inverting nitrogen, and C_p’ phenyl ring carbons, with the legend for the partial charges trajectories plotted below. The movement of electrons is indicated with red arrows. Average partial charges for reactive trajectories in the coordinate X prepared in the range $\{\mathrm{X}_{\max},\ \Delta\mathrm{X},\ \mathrm{X}_{\min}\} = \{0.85, -0.05, 0.85\}$, where $\Delta\mathrm{X}$ is the step size. The configurations were restrained to the respective value in X with the harmonic potential strength $\kappa = 4000\ \mathrm{kJ\ mol^{-1}}$, with the total run of 20 ps.

A perhaps clearer effect of the polarizing solvent on the extent of charge rearrangement for the azo-moiety as a whole is represented by the dipole moment. The variation of the dipole moment along the reactive trajectory along the coordinate X is plotted in Figure 47. The dipole moment of the push-pull ppAB is an order of magnitude larger than for the unsubstituted AB. It shows a more abrupt increase in the transition region for the less polarizable AB, though, while it increases more continuously and to a lesser extent for the push-pull ppAB. The polarizing effect of solvent is clear for the both derivatives, AB and ppAB, where the dipole moments of the stable states are increased as well as the dipole moments of the transition states. The relative increase in the dipole moment going from the less polar toluene to the highly polar DMSO is more pronounced for the push-pull ppAB, compared to the unsubstituted AB.

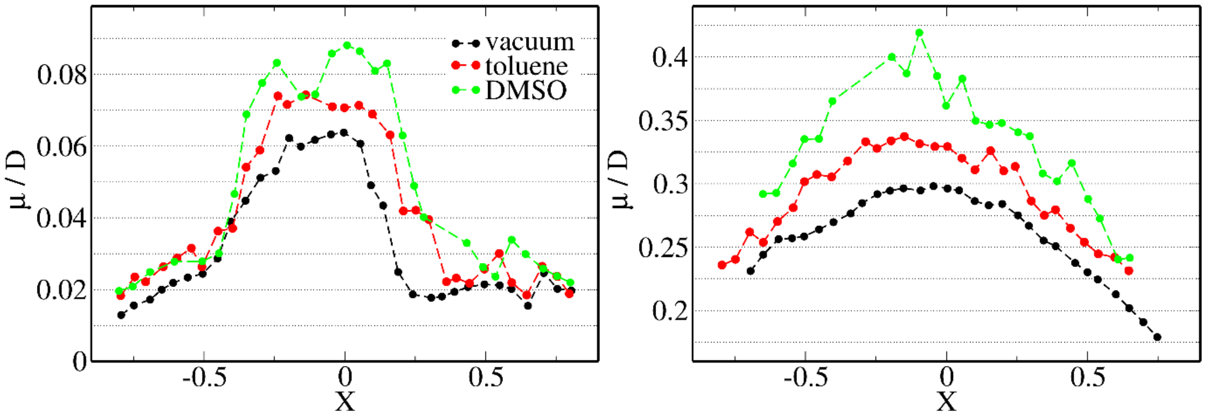

AB

ppAB

Figure 47. Dipole moments along the reactive trajectories with the increase in the solvent polarity, going from vacuum (black), toluene (red) to DMSO (green).

In conclusion, the polarizing solvent increases the dipole moment of the azo-moiety along the reactive trajectory for both derivatives AB and ppAB, with the most pronounced increase for the push-pull derivative in DMSO. This induced polarization at the transition state might result in increased solvent ordering due to stronger dipolar interactions. This could potentially justify the negative signs and magnitudes of activation entropies due to decreased solvent entropy at the transition state, which we discuss in Section 3.6.

3.5 Rate Constants – Reactive Flux

We introduced the reactive flux method of obtaining rate constant in Methods Section 2.7.1 as a method that provides a more direct measure for the real dynamically corrected rate. This correction arises due to some trajectories recrossing the dividing surface before definitely settling into one of the stable states. This treatment represents an improvement over the rate constant defined in transition state theory, where it is assumed that all trajectories initiated from the dividing surface in the direction of the product, by convention in the $\rightarrow +$ direction, actually reach the product state without excursions back to the reactant state. In the reactive flux calculation the velocity or the flux is averaged only for those trajectories that actually end in the product state. Due to this, the quality of the reaction coordinate and with it the position of the dividing surface is not crucial for obtaining the true rate, but it does affect the computational efficiency. The dynamical correction to the rate can be expressed by the transmission coefficient, which we defined in Equation 75.

In the next sections we present the results for first of all, transmission coefficients calculation for AB and ppAB in both vacuum and DMSO. The dynamical effect of solvent on top of the static effects due to solvent-solute interactions is discussed. Namely, the effect of solvent is twofold insofar it affects the height of the energy barrier due to (de)stabilizing solvent-solute interactions, but also affects the dynamics of the barrier crossings as some reactive trajectories (re)cross the barrier region before settling into a stable state. Finally, the reactive flux rate coefficients are compared with the rate coefficients calculated using the Best-Hummer approach from the TPS ensemble.

3.5.1 Transmission coefficients: Dynamic solvent effects

The effect of recrossing the dividing surface is captured by the transmission coefficient, a dynamical correction to the TST rate. In a similar study for isomerization of cyclohexane in a bath of explicit solvent, it was found for the transmission coefficient to increase with the solvent density [102]. The claim was that the non-chaotic trajectories that would recross the potential barrier many times and not dissipate energy as efficiently as the true TST trajectories, were quenched by the presence of solvent though which the rate was increased. In a further study of the same system [101] it was found that the transmission coefficient varied non-monotonically with the collision frequency of the solvent.

This turnover behaviour for the variation of the rate or equivalently the transmission coefficient was first described by Kramers [107]. For the general description of rate constants for barrier crossing with stochastic dynamics two regimes can be defined with respect to friction. For small frictions, or the underdamped regime, the system is inertial in the sense that there is little coupling between the reaction coordinate and the bath. In this regime the rate increases with the increasing friction or the collision frequency. For large frictions the system is in the overdamped regime where the rate decreases with friction due to ever increasing diffusivity.

We studied the turnover behaviour for the model double well potential introduced in Methods Section 2.7.1, the results of which are presented in Appendix 6.5. We also examined the effect of the barrier height on the position for the turnover, inspired by [100]. Therein, a reduced friction parameter was introduced that relates the imaginary frequency of the transition mode ω_B and the friction constant, $\gamma^* = \gamma/\omega_\mathrm{B}$. Our finding for the double-well potential crossing with stochastic dynamics was that for very large barriers, of the order of $\sim 100\ \mathrm{k_B T}$, the turnover occurred at lower values for the reduced friction γ^* and a higher values for the transmission coefficient κ. This would imply that first of all, the

TST result is more valid for high barriers, where $\kappa \sim 1$. The effect of the barrier height on rate constants was relevant to address in the context of the large barriers associated to the cis → trans isomerization of azobenzene(s). Upon fluorination, the barrier is increased even further compared to the unsubstituted AB. On the example of a fluorinated derivative 4F-azobenzene the activation free energy calculated with B3LYP/6-311G* level of theory by [5] was as high as $\Delta G^{\#} = 113.4\ \mathrm{kJ\ mol^{-1}}$. We in fact observed the transmission coefficients very close to unity for the 4F-AB, a result also presented in the Appendix 6.5.

The barrier height for the two compounds AB and ppAB is approximately $\sim 40\ \mathrm{k_B T}$. We performed an equivalent analysis with respect to turnover behaviour for the rate constant with increasing friction. Therein, the reduced friction parameter was determined as $\gamma^* = \gamma/\omega^{\#} = 1/(\tau_r\ \omega^{\#})$. The imaginary frequency associated to the transition mode was approximated by $\omega_B = \omega^{\#} \approx 1 \cdot 10^{13}\ \mathrm{s^{-1}}$ and the relaxation time τ_r was set as the decay time for the velocity autocorrelation function. A smaller relaxation time signifies that the motion is randomized faster and is thus more diffusive, so that the relaxation time reflects the strength of coupling to the heat bath. In order to observe the range for the bath coupling constants for which the turnover in rate occurred, the transmission coefficients were calculated at various time coupling constants $\tau_r = \{0.1, 0.2, 1.0, 5.0, 10.0\}\ [\mathrm{ps}]$ for the two compounds, AB and ppAB.

The resulting turnover behaviour was drastically different for the two compounds AB and ppAB, as plotted in Figure 48. In fact given the higher electronic energy barrier for AB than for ppAB, in the low coupling regime for small frictions the transmission coefficient was actually reduced. We conclude that higher energy attained when crossing the barrier was less effectively dissipated by the weakly coupled heat bath which increased the frequency of recrossings. This regime is also considered the energy activation regime, where the rate is proportional to the friction because the random kicks from the environment deposit energy into the reaction coordinate and increase the frequency of transitions. The energy activation regime was observed roughly in the same range of reduced frictions γ^* for both AB and ppAB, in red and black respectively.

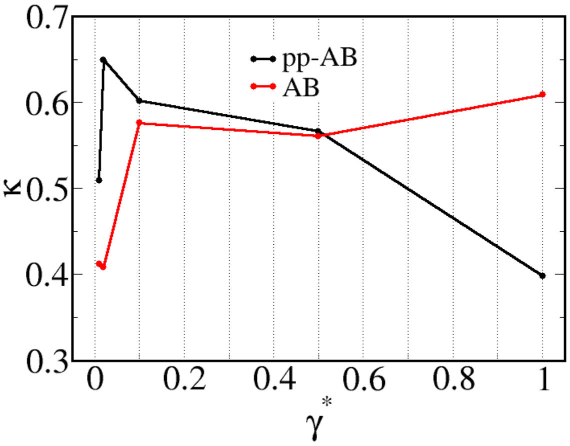

Figure 48. Kramers turnover for AB and ppAB in vacuum, where the coupling strength to the heat bath was varied by means of the relaxation time for the velocity autocorrelation function, τ_r. The reduced friction is then defined as $\gamma^* = 1/(\tau_r\ \omega^{\#})$, where $\omega^{\#}$ is the transition mode frequency, approximated as $\omega^{\#} \approx 10\ \mathrm{ps^{-1}}$.

The reduced friction associated with the relaxation time used throughout this work for simulations in vacuum, namely $\tau_{\mathrm{r}} = 0.1\ \mathrm{ps}$, was $\gamma^{*} = 1.0$ which would qualify as a strong coupling to the bath. In these conditions, the extent of recrossings was much larger for ppAB than for AB and the transmission coefficient κ lower. We conclude that in case of the larger barrier associated to AB, the energy dissipation is equally larger and more effective which results in the trajectories being trapped in the stable state more easily than in the case of a smaller barrier for ppAB where they recross more.

For the simulations in solvent, a weaker heat bath coupling time constants, namely $\tau_{\mathrm{r}} = 1.0\ \mathrm{ps}$, was chosen where we aimed for the explicit solvent molecules to primarily act as the heat bath. According to the corresponding value for the reduced friction, $\gamma^{*} = 0.1$, both AB and ppAB systems were in the energy-activation regime. The transmission coefficients for both AB and ppAB in vacuum were comparable, but still much lower that unity. This would imply that the energy dissipation was not efficient, with many high energy trajectories passing the transition region not relaxing efficiently in the product state. The weak coupling to the heat bath did not dissipate the excess energy as well.

Upon introduction of explicit solvent as the heat bath with the solvent density, the standard $\rho = 1.1\ \mathrm{g\ cm^{-3}}$ for both AB and ppAB in DMSO, we might expect an effect on the efficiency of energy dissipation. Therein, the coupling to the bath would be increased due to random kicks from the solvent molecules and therefore the excess energy dissipated more efficiently. This in turn should lead to an increase in the transmission coefficient, as the recrossing paths would be quenched in the presence of the explicit solvent. The effect described was in fact observed in the study of cyclohexane isomerization, as the transmission coefficient was increased with the increased solvent density [102]. The AB and ppAB systems in solvents were weakly coupled to the heat bath as defined with the reduced friction of $\gamma^{*} = 0.1$ and thus in the weak coupling regime. Alternatively, the effect of the thermal agitation by explicit solvent could thus increase the number of recrossings and therefore reduce the transmission coefficient.

The transmission coefficients calculated for AB and ppAB in vacuum and in DMSO using Equation 75 in Methods Section 2.7.1. are plotted in Figure 49, with the tabulated values given in Table 15 together with the resulting reactive flux rates.

First we note that there are considerable fraction of trajectories that re-cross the dividing surface $\mathrm{X} = \mathrm{X}^{*}$ and relax back into the reactant state, with the transmission coefficients dropping well below the transition state theory ideal $\kappa = 1$. This can be attributed to the friction constant used in the stochastic dynamics model for the solvent. There was a comparable reduction in the transmission coefficient observed for the double-well model system at this value of the reduced friction $\gamma^{*} = 1.0$ as well, see Appendix 6.5.

Upon introduction of explicit solvent, further recrossings are induced by the random kicks of solvent molecules and the transmission coefficient lowered. The effect is especially present for the push-pull derivative ppAB. The solvent induced reduction of the transmission coefficient is unlike the finding in [102] for cyclohexane isomerization, where it was actually increased due to quenching of the recrossing trajectories by the explicit solvent. The fact we made an opposite observation might be attributed to the low solvent density present in our systems, the lowest of the densities considered in the quoted study. Thus, we might expect for the quenching of recrossing trajectories and the associated increase in rate occur at greater solvent densities for our system as well.

The surprising increase of recrossings in DMSO was an even more so interesting finding, as this was observed for the push-pull derivative ppAB only and not for the unsubstituted AB. For ppAB, the average transmission coefficient dropped to $\kappa = 0.25$ in DMSO compared to $\kappa = 0.41$ for in vacuum, while it stayed unaffected for AB going from vacuum $\kappa = 0.55$ to DMSO $\kappa = 0.52$.

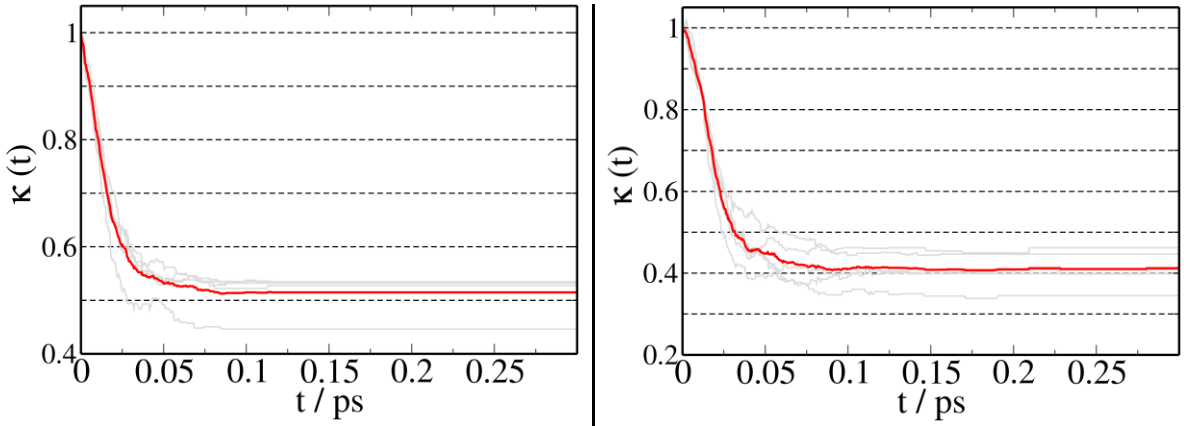

AB vacuum

ppAB vacuum

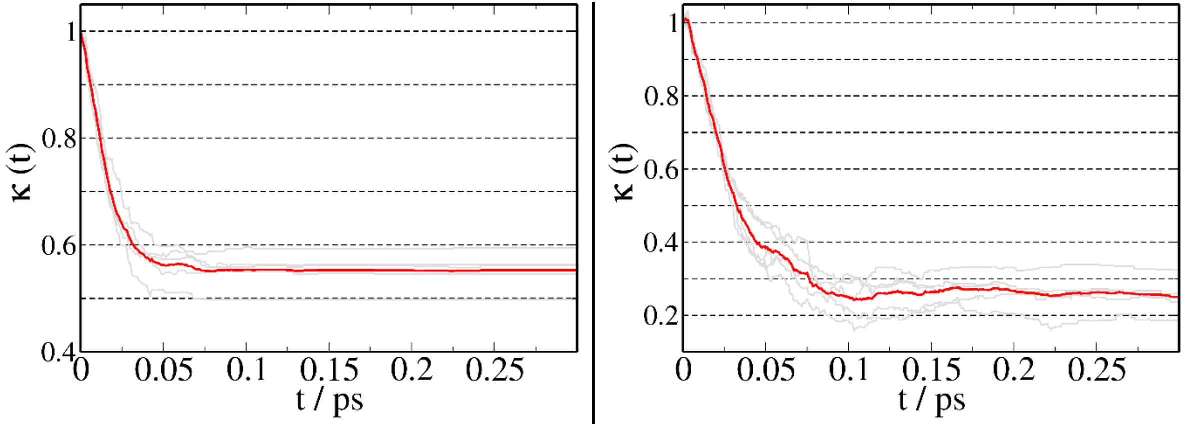

AB DMSO

ppAB DMSO

Figure 49. Transmission coefficients calculated using Equation 75 in Methods Section 2.7.1. for AB and ppAB in vacuum and DMSO. For solvent simulation, the density was $\rho = 1.1\ \mathrm{g\,cm^{-3}}$ while the relaxation time for the coupling with the heat bath $\tau_r = 1.0$ ps, while in vacuum $\tau_r = 0.1$ ps

The strength of the coupling to the bath as expressed with the relaxation time $\tau_r = 1.0$ ps and the reduced friction constant $\gamma^* = 0.1$ was weak for both AB and ppAB in the DMSO solvent. Formally, the reactions can be characterized as in the inertial regime, where the rate is proportional to friction. This makes us interpret the induction of recrossings in explicit DMSO solvent for ppAB only, and not AB, as due to stronger coupling with the solvent degrees of freedom for the former case. In the latter case the strength of coupling to the heat bath as determined by the relaxation time τ_r was still the only source of affecting the recrossing dynamics. The presence of explicit DMSO molecules had no effect in inducing more friction. As the push-pull ppAB has a larger dipole moment, both in the stable states and in the transition state, the dipolar interactions with the DMSO solvent are substantially larger than for the unsubstituted AB. The dissipation of energy from the transition mode or the reaction coordinate to the internal modes is thus slower in solvent where there are more of the non-TST type of trajectories that go towards the product trans state oscillate and return back to the reactant cis state.

The structure of the reactive flux correlation functions reflect the oscillatory nature of trajectories' barrier crossings. For the unsubstituted AB they seem to relax into either of the stable states without much oscillations, while the oscillatory nature of the barrier crossing dynamics is more apparent for the ppAB derivative.

3.5.2 Reactive Flux Rate Constants for AB and ppAB

We present the results of the reaction rate calculation using the reactive flux approach introduced in the Methods Section 2.7.1 for the two compounds AB and ppAB in both vacuum and DMSO. The true rate is reduced if the reactive trajectories recross the dividing surface and not relax in the product state. Here, we defined the dividing surface $X = X^*$ at the position of the free energy maxima in the coordinate X, with the stable states defined as adjacent in space: the cis state $X > X^*$ and the trans state $X < X^*$.

Table 15. Reactive flux rates for ABs calculated using Equation 70 in Methods Section 2.7.1. The relative probability to be at the dividing surface $P(X^*) = \exp\,[-\beta F(X^*)] \,/\, \int_{X^*}^{1} \exp\big(-\beta F(X)\big)dX = \exp\,[-\beta F(X^*)]\,/c_A$, where c_A is the probability to be in the reactant, cis state. The TST rate is given as the zeroth time reactive flux rate, $k^{TST} = k^{RF}(t=0)$, with the transmission coefficient as the ratio $\kappa = k^{RF}/k^{TST}$, evaluated at the plateau for the $k^{RF}(t)$ rate. The standard deviation $\sigma(\kappa)$ was estimated based on 5 re-evaluations of the reactive flux as described in the text.

compound	c_A	$\exp[-\beta F(X^*)]$	$P(X^*)$	$k^{TST}\ [s^{-1}]$	$k^{RF}\ [s^{-1}]$	$\kappa \pm \sigma(\kappa)$
AB vacuum	0.14	$1.76 \cdot 10^{-16}$	$1.24 \cdot 10^{-15}$	$8.65 \cdot 10^{-5}$	$4.46 \cdot 10^{-5}$	0.51 ± 0.04
AB DMSO	0.0074	$1.55 \cdot 10^{-16}$	$2.09 \cdot 10^{-14}$	$1.51 \cdot 10^{-3}$	$8.34 \cdot 10^{-4}$	0.55 ± 0.03
ppAB vacuum	0.019	$9.05 \cdot 10^{-12}$	$4.88 \cdot 10^{-10}$	35.71	24.58	0.41 ± 0.05
ppAB DMSO	0.0026	$2.41 \cdot 10^{-8}$	$9.30 \cdot 10^{-6}$	$3.21 \cdot 10^{5}$	$7.91 \cdot 10^{4}$	0.25 ± 0.05

First of all, we see the reactive flux rate k^{RF} in vacuum to be 6 orders of magnitude larger for the push-pull ppAB compared to AB, due to an exponential dependence on the barrier height which is lowered by push-pull substitution. There is a slight dynamical effect as well since the average transmission coefficient κ is lowered for the push-pull derivative ppAB. The transition state theory result for all cases considered is violated due to the transmission coefficient being much lower than unity, an assumed value for the TST theory. We observe that the TST result is violated even further for the push-pull ppAB compared to the AB, where the transmission coefficient is lowered due to the smaller barrier associated to ppAB. The relative probability $P(X^*)$ to be at the dividing surface was 5 orders of magnitude smaller for AB compared to ppAB.

As far as the effect of solvent polarity is concerned, the rate is increased for both compounds AB and ppAB in DMSO, with a dramatic increase for the push-pull ppAB. On the other hand, the rate is increased only 10 times for AB in DMSO which is an increase comparable to the experimental findings. The effect was entirely due to the $P(X^*)$ factor, and more specifically due to the relative probability of being in the cis state, c_A which was ~ 10 times smaller in DMSO than in vacuum for AB. The relative destabilization of the cis state going from vacuum to DMSO was observed with the free energy profiles $F(X)$ plotted in Figure 21, Section 3.2. This resulted in the reduction of the barrier and seemed to be the decisive factor for the increase in rate for AB going from vacuum to DMSO.

For the push-pull ppAB on the other hand, the relative probability to be at the transition state $P(X^*)$ was also increased by 4 orders of magnitude but due to stabilization of both, the cis state and the transition state. This resulted in the reduction of both factors, c_A and $\exp[-\beta F(X^*)]$, respectively. In addition, there was a slight dynamical effect insofar the rate was slightly reduced in DMSO compared to the vacuum and the transmission coefficient lowered.

We previously estimated the rate based on the collected TPS ensemble of paths, within the Best-Hummer framework as presented in Section 3.4.2 Table 11. The overall trend is reproduced by the reactive flux calculation, considering the predicted increase in the rate constant for both AB and ppAB going from vacuum to DMSO. The predicted increase in case of the rate calculated with reactive flux was approximately one order of magnitude smaller than the Best-Hummer result. Namely, the $\mathrm{cis} \rightarrow \mathrm{trans}$ isomerization rate was predicted to increase ~ 3000 fold versus ~ 10000 for ppAB and ~ 20 versus ~ 100 for AB going from vacuum to DMSO, for the two approaches, respectively. The discrepancy arose due to the $p(TP)$ factor of the Best-Hummer evaluation, which is the normalization factor of the conditional probability to be on the reaction path $p(TP \mid r)$, and is thus probably associated to the numerical errors introduced in the approach. When comparing to the experimental results for the rate the reactive flux estimates agree more, insofar the experimentally predicted increases in rates going from non-polar to polar solvents reported by [64, 65] were ~ 10 fold for the unsubstituted AB that is ~ 10000 for a push-pull derivative, not of the exact type used in this study though, namely the ppAB.

In conclusion, the solvent effects on the rate constants generally arise due to changes in the associated free energy barriers due to solute-solvent interactions. On the example of the push-pull derivative ppAB in the highly polar DMSO the free energy barrier for the $\mathrm{cis} \rightarrow \mathrm{trans}$ isomerization was reduced due to both stabilization of the transition state and the destabilization of the cis stable state. The stabilization can be attributed to the favourable enthalpic contribution to the free energy upon dipolar interactions between the more polar TS and DMSO solvent. The destabilization of the cis state on the other hand is apparently due to the unfavourable entropic factor outweighing the favourable enthalpic factor. Namely, the dipolar solute-solvent interactions increase the ordering of the solvent and thus reduce the entropy. The solvent can also affect the dynamics of the transitions by increasing the friction felt by the reaction coordinate and affect the frequency of recrossings. The latter effect is accounted for by the transmission coefficient. Importantly, for both compounds in vacuum for the given strong coupling to the heat bath, we found the transmission coefficient to be far lower than unity as predicted by the transition state theory. The introduction of explicit solvent DMSO had a marked effect for increasing the frequency of recrossings even further compared to the vacuum case only for the push-pull derivative, ppAB. We attribute this effect mostly to the markedly reduced free energy barrier in the presence of DMSO which was more easily recrossed and led to this further reduction of the transmission coefficient.

3.5.3 The transition path and the reactive flux for the model potential

We introduced the model system of barrier crossing for stochastic dynamics which we used to compare different approaches for rate constant calculation in Methods Section 2.7. A double-well potential modelled the isomerization between stable states with the dynamics governed by Langevin equation where the effect of the environment is represented by friction and friction dependent random force.

For this model system with the barrier height $\mathrm{Q} = 4\ \mathrm{k_B T}$ it was feasible to sample a sufficient number of $\mathrm{A} \leftrightarrow \mathrm{B}$ transitions and thus calculate the population correlation function. Subsequently, the reaction time or the rate constant $\tau_{\mathrm{rxn}} = \mathrm{k}^{-1}$ was obtained by fitting an exponential function of the form in Equation 66, and was plotted in Figure 15B and C of the Section 2.7. This served as a reference for the enhanced sampling methods, namely the reactive fluxes at the dividing surface or over the collected TPS ensemble of pathways.

Here we present the calculation of the rate constants with the reactive flux and the transition paths' flux approaches for the stochastic barrier crossing with settings described in Sections 2.7.1 and 2.7.2 respectively. The both approaches yielded equivalent rates. First, in Figure 50A we plot an example set of paths of the generated TPS ensemble for the double-well potential defined between stable states adjacent in space x. The border between the stable states was set exactly at the dividing surface $\mathrm{x} = \mathrm{x}^*$.

The resulting paths average $\langle \mathrm{h_B(t)} \rangle_{\mathrm{AB}}$ and its time derivative $\langle \dot{\mathrm{h}}_{\mathrm{B}}(\mathrm{t}) \rangle_{\mathrm{AB}}$ are plotted in Figure 50B. The plateau is clearly maintained throughout the path length. At zeroth time $\mathrm{t} = 0$, $\langle \dot{\mathrm{h}}_{\mathrm{B}}(0) \rangle_{\mathrm{AB}}$ attains a non-zero value since there is momentary population of state B given the adjacent definition of stable states. The probability factor of path confinement $\mathrm{C}\ (\mathrm{t}')$ which accounts for the reversible work to confine the reactive paths of constant length to begin in the reactant and end in the product state, was calculated for $\mathrm{t}' = 5\mathrm{s}$ and is plotted in Figure 51.

Finally, the resulting transition correlation flux calculated using the Equation 80 is plotted in Figure 52. For the case where the stable states are defined as separated in space, with the state A is $\mathrm{x} < -0.5$ and the state B $\mathrm{x} > 0.5$, the TPS rate $\mathrm{k^{TPS}(t)}$ plotted in orange increases in time only after a time lag, the time needed to make the transition $\mathrm{A} \rightarrow \mathrm{B}$. It then oscillates which is characteristic of trajectories that are recrossing the stable states boundaries before definitely relaxing into one of them. This time needed to actually make the transition is the molecular time τ_{mol}. When stable states were defined as adjacent in space so that the states' boundary was placed exactly at the dividing surface $x^* = 0$, the rate $\mathrm{k^{TPS}(t)}$ plotted in red settled into the same plateau as the rate calculated with separate stable states' definition, for times greater than the molecular time $\mathrm{t} > \tau_{\mathrm{mol}}$. As defined in Equation 51 for the correspondence between the TPS rate and the reactive flux rate, at zeroth time, the rate is equal to the TST rate $\mathrm{k}\ (0) = \mathrm{k^{TST}}$, which is also true for the reactive flux rate. In the present calculation it is clear that the two approaches evaluate different results for the TST rate at $\mathrm{t} = 0$.

For longer times though $\mathrm{t} > \tau_{\mathrm{mol}}$, both the reactive flux and the TPS flux plateau at very similar values at which the true rate is defined, $\mathrm{k_{RF}} = 8.712 \cdot 10^{-5}\ \mathrm{s}^{-1}$ and $\mathrm{k_{TPS}} = 8.503 \cdot 10^{-5}\ \mathrm{s}^{-1}$ respectively.

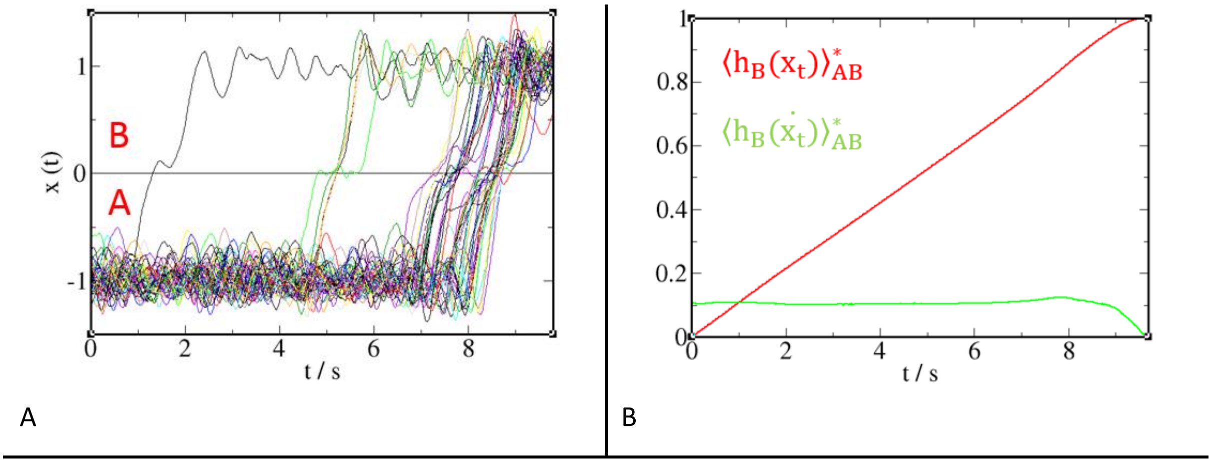

Figure 50. The TPS ensemble of pathways for the model double-well potential, described in Methods, Section 2.7. The constant path length was $T = 10$ s, for a unit mass, with the time step $\Delta t = 0.01$s and the friction constant $\gamma = 1.0\ s^{-1}$ for the underlying Langevin integrator (A). The associated path average $\langle h_B(t)\rangle_{AB}$ grows linearly in time as the state B is continuously populated, while its derivative $\langle \dot{h}_B(t)\rangle_{AB}$ maintains a plateau.

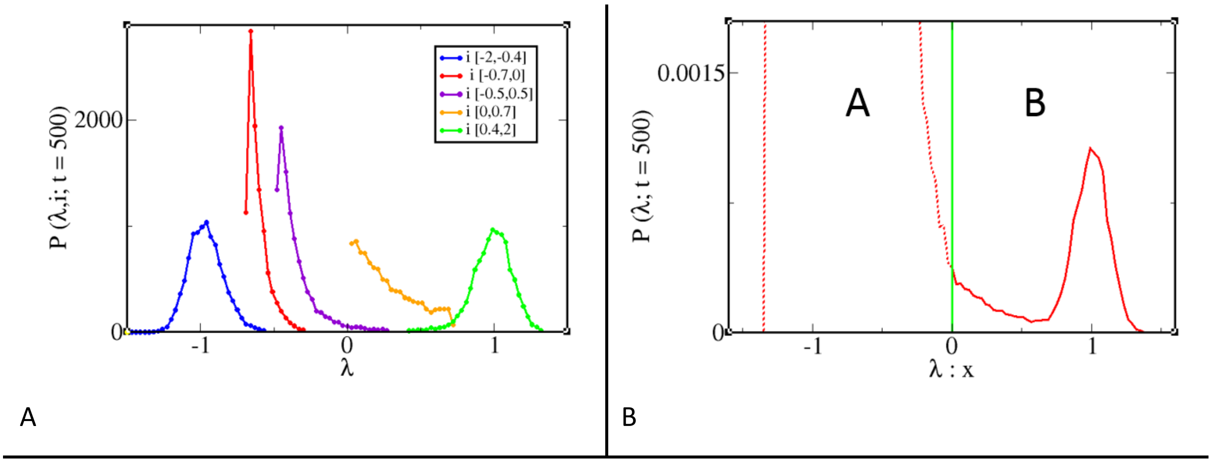

Figure 51. Calculation of the rate constant by the transition path flux method for the model potential. Distributions for the order parameter $\lambda \equiv x$ for overlapping umbrella windows (A) and the full range probability $P(\lambda \equiv x, t')$ reconstructed by histogram matching (B). The probability of path confinement factor is obtained by integration of the distribution over the range for the stable state B as indicated with the green vertical line.

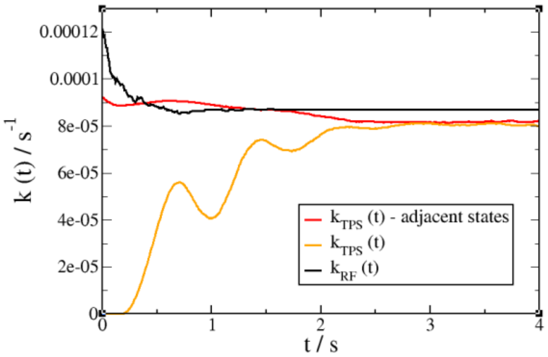

Figure 52. Comparison of the reactive flux rate and the transition rate calculated from TPS path ensemble for the double-well model potential. The states are either defined as adjacent, with the state $A, x < x^* \equiv 0$ and the state $B, x > x^* \equiv 0$ or separated in space; the state $A, x < -0.5$ and the state $B, x > 0.5$.

3.6 Activation Entropies from van't Hoff analysis

Activation entropies calculated with frequency analyses at the transition and cis stable states are evaluated as positive in sign for a range of azobenzene derivatives and do not agree with experimentally measured values which are usually negative [4, 5]. To improve upon these results, one could imply some adaption of the TST procedure such as Truhlar's variational transition state theory [109]; along the reaction (minimum energy-) pathway, the point at which $\Delta G^{\#}$is evaluated is varied away from the saddle point until the free energy of activation is eventually minimized. Another elegant possibility is to use the extended valence bond (EVB) approach to model the QM system, and to obtain the $\Delta G^{\#}$ through free energy perturbation [43].

With the present systems, we cannot apply these methods directly, because our order parameter is defined according to geometrical parameters that (at the saddle point of the BO surface) would not allow for a direct comparison of phase space weights obtained from TST, for instance. In principle, we would have to define an order parameter the hypersurface of which *at the saddle point coincides with the dividing plane* employed in the TST approach. Den Otter and Briels have actually constructed such a coordinate for the purpose of carrying out efficient reactive flux calculations [110]. It is only then when we could compare activation entropies according to the simple picture sketched in Figure 53 for a two-dimensional system. Technically, however, it is not feasible to introduce such a coordinate into the current numerical setup.

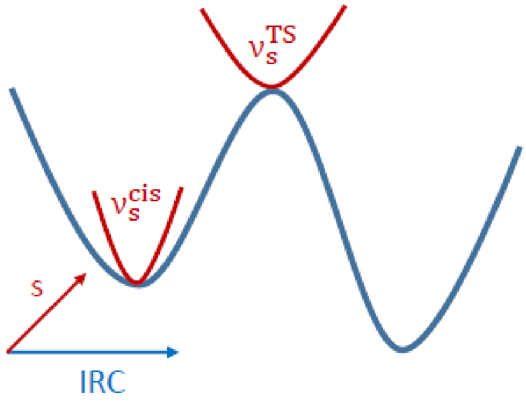

Figure 53. The schematic depiction of the normal modes' frequencies in directions s, orthogonal to the Internal Reaction Coordinate (IRC), that is the transition mode, at the transition state $\nu_s^{TS}$and the cis stable state ν_s^{cis}. In this simple picture, the change in entropy from the metastable state to the transition state may formally be described by the widening/narrowing parabola in s direction that cause the corresponding distribution of vibrational energies to change.

Nevertheless, for now we shall be content with tentatively using the computational van't Hoff approach outlined in the Methods Section 2.8 employing the coordinate X, in order to test the numerical feasibility of such an approach in general. The activation free energy was recorded at different temperatures and the activation entropy obtained from the intercept of the straight line fit.

As a reference, in Table 16 we shall first report and discuss the computed activation parameters using the classical (TST) approach for the higher level of theory B3LYP/6-31G* and the polarizable continuum solvent models (PCM) as well as the semiempirical DFTBA.

Table 16. Activation parameters from various theoretical treatments: entropy $\Delta S^{\#}[\mathrm{J\,K^{-1}\,mol^{-1}}]$, enthalpy $\Delta H^{\#}$ $[\mathrm{kJ\,mol^{-1}}]$ and the free energy, $\Delta G^{\#}$ $[\mathrm{kJ\,mol^{-1}}]$ for AB and ppAB calculated based on frequency calculations at stationary points (cis and TS) using partition functions and from van't Hoff analysis of the variation of free energy with temperature, with direct dynamical sampling. The Helmholtz free energies, $A = G - RT$, were obtained by simulations in NVT ensembles. The enthalpic contributions should thus not be compared directly. Also, the reported free energies from the computational van't Hoff analysis were evaluated as $\Delta G^{\#} = \Delta A^{\#} + RT$, where $\Delta A^{\#}$ were read off the regression line of the van't Hoff plot at the temperature $T = 298\ \mathrm{K}$.

	AB			**ppAB**		
Method	$\Delta S^{\#}$	$\Delta H^{\#}$	$\Delta G^{\#}$	$\Delta S^{\#}$	$\Delta H^{\#}$	$\Delta G^{\#}$
B3LYP/6-31G*	13.59	101.02	96.97	4.23	75.77	74.51
DFTBA	10.29	97.63	94.57	8.19	69.39	66.95
PCM (DMSO) B3LYP/6-31G*	7.27	106.17	104.00	-5.17	57.13	58.67
PCM (toluene) B3LYP/6-31G*	11.43	103.26	99.85	7.93	70.17	67.81
QM(DFTB3)-MD, vacuum	-9.45	89.89	94.55	-4.94	54.27	58.11
QM(DFTB3)/MM-MD, toluene	-1.92	86.70	89.75	-22.64	40.77	49.94
QM(DFTB3)/MM-MD, DMSO	21.15	91.98	88.12	-13.92	24.34	30.98

The enthalpies of activation are in good agreement with the experimentally observed ones [4, 25]. The general result for this computational approach in vacuum and PCM implicit solvent is a slightly positive activation entropy $\Delta S^{\#}$. Note that this phenomenon is not restricted to the solvent case: when included within the PCM model, the solvent is treated as a polarizable continuum. The entropic effect of the solute-solvent structure is thus included only indirectly, entropies are still evaluated from the normal mode frequencies of the transition structures only. As a matter of fact, the molecules at any of their transition states could well contribute to solvent ordering. In Table 17 we list the dipole moments of the cis- and transition (saddle point) states for the B3LYP level of theory. Obviously, at least for ppAB DMSO does have a pronounced effect on the dipole moment.

Table 17. Dipole moments for the optimized cis and TS structures using B3LYP/6-31G* level of theory for AB and ppAB in vacuum $\varepsilon = 0$, toluene, $\varepsilon = 2.4$ and DMSO, $\varepsilon = 46.7$.

Compound	$\mu_{cis}/\ \mathrm{D}$	$\mu_{TS}/\ \mathrm{D}$
AB vacuum	1.27	1.26
AB toluene	1.49	1.46
AB DMSO	1.78	1.70
ppAB vacuum	2.48	4.59
ppAB toluene	2.91	5.71
ppAB DMSO	3.43	9.05

Yet also the gas phase calculations result in positive activation entropies and are of the same magnitude. This points to a problem independent of solvent degrees of freedom, presumably from anharmonic effects (transition region is effectively a *seam* instead of an isolated point) or the fact that the saddle point of the BO surface does not correspond to the barrier top in *free* energy.

At least the latter problem can be resolved with the computational van’t Hoff plots obtained from umbrella sampling. The van’t Hoff plots, as defined in the Equation 86 of Methods Section 2.8, were obtained by collecting the free energy profiles for the temperature range, $\mathrm{T} = \{233, 283, 333, 383\}\,[\mathrm{K}]$ and calculating the associated free energy barriers $\Delta\mathrm{F}(\mathrm{T}) = \mathrm{F}^{\mathrm{TS}} - \mathrm{F}^{\mathrm{cis}}$ between the transition and the cis stable state, respectively (Figure 54). Admittedly, large errors in the resulting Helmholtz free energies associated to the sampled NVT ensembles were obtained by umbrella sampling and WHAM reweighting, as a result of limited simulation run times. The resulting van’t Hoff plots are remarkably well fitted to a straight line though, with the greater slope for AB compared to the push-pull ppAB reflecting the higher activation energy associated to the transition.

The activation parameters including the activation free energies $\Delta\mathrm{A}^{\#}$ as the Helmholtz free energies interpolated at the temperature $\mathrm{T} = 298\ \mathrm{K}$ are reported in Table 16. The activation enthalpies were evaluated from the sloped and the activation entropies $\Delta\mathrm{S}^{\#}$ are from the intercept at $1/\mathrm{T} = 0$ for the $\Delta\mathrm{F}/\mathrm{T}$ versus $1/\mathrm{T}$ plots.

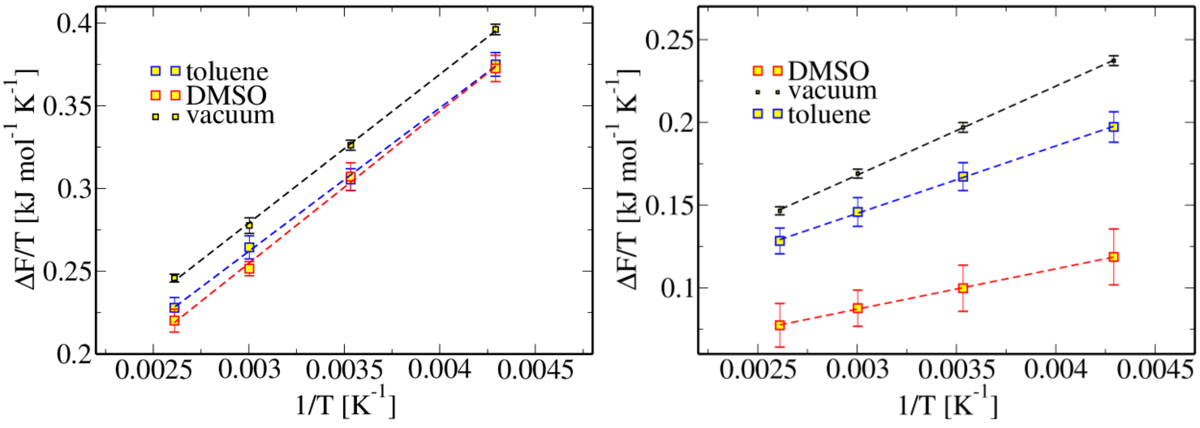

A

B

Figure 54. Van’t Hoff plots calculated for (A) AB and (B) ppAB in vacuum and in solvents: temperature dependence for the free energy barrier $\Delta\mathrm{F}(\mathrm{T})$ defined with respect to the coordinate X.

The standard errors of the intercept that is the activation entropy expressed in $\mathrm{J\,mol^{-1}\,K^{-1}}$ were $5.295, 7.105, 9.699$ for AB and $0.634, 2.405, 1.340$ for ppAB in vacuum, toluene and DMSO respectively. For the vacuum case, for both AB and ppAB the activation entropies were negative, within the error bars. Furthermore, the same negative sign for the activation entropy was obtained for the push-pull ppAB in solvents as well. On the other hand, for AB in DMSO the activation entropy was positive, while in toluene slightly negative with an error extending into the positive range. These results indicate that the computational van’t Hoof analysis is an approach that should be pursued further in the future.

4 Conclusion

In this thesis we performed a computational study of thermal $\mathrm{cis} \rightarrow \mathrm{trans}$ isomerization of azobenzene and a push-pull derivative in explicit solvents of varying polarity. The computational approach used was transition path sampling with stochastic dynamics and the QM/MM electronic embedding scheme. Within this scheme, the azo-moiety was described on a quantum level and the solvents with a classical force field, while the electronic density of the azo-subsystem was polarized by the solvent partial charges. To our knowledge this is the first time the direct sampling approach is used for this class of $\mathrm{cis} \rightarrow \mathrm{trans}$ reactions. We aimed to address the effect of push-pull substitution and solvents of different polarity, the low-polar toluene and the highly polar DMSO, on the reaction mechanism and dynamics with a more accurate approach. Namely, the isomerization of azobenzenes was previously tackled computationally by classical quantum chemical optimizations. Based on the optimized transition structure found to be an invertomer with the extended central bend angle and the perpendicular phenyl rings, the mechanism was proposed to be a 'rotation assisted inversion'.

In Section 3.1 we obtained essentially the same results using classical QM optimization for the two compounds treated within this study, namely the unsubstituted AB and a push pull derivative $4NO_2$-$6'NH_2$-AB, ppAB. The benchmarking with various quantum levels of theory was performed to justify the choice for the semiempirical method used for dynamical sampling, the density functional tight binding method DFTB3. This method was recently introduced as an integral part of the Gromacs simulation package and thus was computationally convenient and fast to use. In terms of the predicted transition structures and activation parameters, the DFTB3 method agreed well compared to the B3LYP functional established as the golden standard for this reaction. The polar solvent treated as a polarizable continuum yielded lowered activation energies for the push-pull derivative due to stabilization of a highly dipolar transition structure. In the highly polar DMSO, the transition structure was optimized into a rotamer with a much lower bend angle compared to the usual invertomer state. This was indicative of a change in mechanism for the push-pull derivatives in the polar medium, from inversion to rotation.

In Section 3.2 a potential of mean force approach was employed to map out the free energy in the reactive coordinates for the reaction, the central dihedral ω and the bend angle α. On the example of the push-pull ppAB in vacuum we observed for the inversion to be the energetically favoured route at a finite temperature as well. The transition region was shifted to values for the bend angle α lower than the strictly linear as predicted by the QM optimized transition structure though. With thermal energy present in the system, the paths deviated from the minimum energy path which proceeds via the strictly linear transition structure defined for the zero-temperature potential energy surface.

Furthermore, a one-dimensional coordinate $\mathrm{X} = \sin\alpha\cos\omega$ was introduced, which provided a foliation of hypersurfaces between the cis and trans stable states. The associated minimum energy path in the coordinate X was continuous and smooth. The potential of mean force with respect to the coordinate X was able to qualitatively capture the effect of lowered activation barrier upon both, the push-pull substitution and the introduction of the highly polar DMSO for the push-pull derivative ppAB. A subsequent committor analysis at the barrier top $\mathrm{X} = \mathrm{X}^*$ identified the coordinate X as not an ideal reaction coordinate due to many of the configurations committing to either of the two stable states. The committor distributions were found to be uniform for ppAB while slightly skewed to the trans state for the pure AB, in both, gas phase and in the DMSO solvent. The broadening of the committor distributions could partially be attributed to an underlying diffusivity in the dynamics, as expressed by the correlation coefficients χ measuring the correlation of trajectories' outcomes, but a more determinative factor in this respect was the existence of additional barriers in coordinates orthogonal to X. This was made clear by performing the committor analysis at very low temperatures and low diffusivity which were pronouncedly skewed to the trans isomer.

The main results were presented in Section 3.3 in the form of sampling real dynamical paths connecting the cis and trans stable states with the coordinate $\mathrm{X}\ (\omega, \alpha)$ used to define the stable states. As this particular choice for the coordinate and the initial reactive path were a possible source of bias, a convergence test was performed for the push-pull derivative ppAB in vacuum. A pure rotational path prepared by steering along the central dihedral ω only and proceeding without much change in the bend angle α was used as an alternative initial path. Strikingly, we found for the TPS sampling to spontaneously switch to the same region of (ω, α) space validating the inversion-like pathways as the more natural for the system. The main results were presented in the form of TPS paths' projections onto the reactive central dihedral-angle (ω, α) space. The effect of the push-pull substitution as well as the introduction of solvent was the shift to paths sampling lower bend angles α and being thus more rotational in character. The switch to the rotation mechanism was observed for the push-pull derivative in the highly dipolar DMSO. These findings were further substantiated with quantitative analysis for the mechanism types based on the maximal bend angle adopted in the transition as well as the calculation for the most probable paths in (ω, α) space.

The transition state ensemble was identified from the transition pathways as the configurations equally likely to commit to either of the stable states. The average TS structure associated to the push-pull ppAB in DMSO was evaluated as essentially a rotamer, based on its associated bend angle as low as $\alpha = 148.4°$. Addmitedly, due to sampling issues for the softer degrees of freedom, such as the dihedral defining the orientation of the phenyl rings ϕ_{OR}, we did not consider these ensembles to be representative of the full TS ensembles. Nevertheless, for the case of AB in vacuum where the sampling with respect to ϕ_{OR} was complete, the TS ensemble adopted a full range of relative phenyl rings' orientations, while for the push-pull ppAB the phenyl rings were found to be more restricted and close to perpendicular. The trend was also present in the DMSO solvent which thus had no effect on the relative orientation of the phenyl rings in the transition state ensemble(s). Finally, a hula-twist component to the mechanism was observed in all conditions considered, as there was a simultaneous rotation around the N=N' double bond as well as twisting around the N'-C bond adjacent to the inverting nitrogen N'. The relative orientation of the phenyl rings remained close to constant within the transition(s), again a consequence of them being a slower degree of freedom.

In Section 3.4 the quality of the coordinate X as the reaction coordinate was addressed. Firstly, based on the Best-Hummer analysis of the transition paths, it was found for the conditional distribution $\mathrm{p}\ (\mathrm{TP} \mid \mathrm{X})$ given the coordinate X, to peak at the transiton region $\mathrm{X} = \mathrm{X}^*$. The distribution was also broadened, presumably due to diffusive dynamics and the presence of barriers in directions orthogonal to X. As the most significant orthogonal coordinate contributing to the reaction coordinate the other bend angle α' was identified using the likelihood maximization method. The resulting reaction coordinate $\mathrm{r} = 2.00 - 1.56 \cdot \mathrm{X} - 2.28 \cdot \sin \alpha'$ was found to be a significant improvement over the coordinate X for the unsubstituted AB in vacuum as it yielded a Gaussian like committor distributions for the ensemble of configurations restrained at its dynamical bottleneck $\mathrm{r} = \mathrm{r}^*$. Furthermore, the same coordinate for AB in solvents, toluene and DMSO, yielded the same Gaussian structure for the committor distribution leading us to conclude that the solvent degrees of freedom did not contribute to the reaction in a decisive way. In case of the push-pull ppAB and the likelihood maximization analysis with configurations in both vacuum and solvents the same coordinates turned up as the most likely contributing to the reaction coordinate, $\mathrm{r}\,(\mathrm{X},\ \sin\alpha')$. The associated committor distributions though were still close to uniform. We concluded that the reaction coordinate for the push pull ppAB is more complex in a way that more reactive coordinates needed to be included in the expansion, or that the reactive coordinates have non-linear dependence or contain interaction terms, features not described by the reaction coordinate model at hand.

The dynamic effect of the solvent was examined by calculating the transmission coefficients in Section 3.5. The transmission coefficient is a measure for the extent of barrier recrossing from the transition state back to the reactant state. First of all, given the strength of the coupling to the heat bath used and the resulting friction present in the system, the transmission coefficients were much lower than unity reflecting the failure of the transition state theory for this friction regime. A turnover in the transmission coefficients for AB and ppAB going from weak to strong coupling to the heat bath was observed. Upon introduction of the DMSO solvent, only in the case of the push pull ppAB was the transmission coefficient further reduced. The dynamical effect of solvent induced recrossings at the transition region was thus absent for the unsubstituted AB. The true rate constants were calculated using the reactive flux formalism and the average initial flux in the coordinate X. They showed good agreement with the general trend measured in experiments, insofar the rate constants were increased in the high polarity DMSO solvent. The increase was 10-fold for AB that is 10000-fold for the push-pull ppAB going from vacuum to DMSO. The main cause for the pronounced increase in the rate for the push-pull ppAB was lowering of the activation barrier due to stabilization of the dipolar transition state in DMSO.

On the other hand, the milder increase in rate for the pure AB was not due to enthalpic stabilization in polar DMSO solvent but due to entropic favouring of the transition state and an associated positive activation entropy. The activation entropies were calculated from the computational van't Hoff analysis presented in Section 3.6. The positive activation entropy for the unsubstituted AB in DMSO was also measured experimentally. On the other hand, the calculated activation entropies for the push-pull ppAB in both DMSO and toluene solvent were negative due to the solvent electrostriction around the solute with an increasing dipole moment. The induced ordering around the more dipolar transition state was even more pronounced for the lower polarity toluene.

To finalize the Conclusion we briefly address the research questions and hypotheses posed in the Introduction Section 1.4. Regarding the effect of the push-pull substitution and the polarity of the solvent on the nature of the transition state, the assumption based on previous studies was confirmed insofar the effect was to increase the rotational character for the isomerization mechanism. The effect can be attributed mainly to stabilization of the more dipolar rotamer transition state. Regarding the dynamical effect of the solvent in terms of inducing more recrossings with the resulting true rate lowered compared to the transition state theory rate, it was found to be true even in the gas phase and for a range of coupling strengths to the heat bath. The introduction of explicit solvent resulted in further induction of recrossings only for the push-pull derivative ppAB in DMSO, and not for the unsubstituted AB. Regarding the activation entropies obtained from the computational van't Hoff analysis by directly sampling the solvent degrees of freedom, the entropic favouring of the transition state relative to the cis stable state and a positive activation entropy was evaluated only for the unsubstituted AB in DMSO. For all other cases considered, the evaluated activation entropy was negative, reflecting the induced ordering of solvent and reduction of its configurational entropy around a more dipolar transition state. The computational van’t Hoff analysis was thus proven to be a valuable tool of calculating activation entropies for this class of reactions, where there is significant charge rearrangement and a subsequent differential ordering of solvent around the reacting solute(s).

5 References

(1) G. S. Hartley. (1937). The cis form of azobenzene. *Nature, 140*, 281.

(2) J. Griffits. (1972). Photochemistry of Azobenzene and its Derivatives. *Chem. Soc. Rev., 1*, 481.

(3) A. A. Beharry and G. A. Woolley. (2011) Azobenzene photoswitches for biomolecules. *Chem. Soc. Rev., 40,* 4422

(4) J. Dokic, M. Gothe, J. Wirth, M. V. Peters, J. Schwarz, S. Hecht, P. Saalfrank. (2009) Quantum Chemical Investigation of Thermal cis to trans Isomerization of Azobenzene Derivatives. *Phys. Chem. A. 113,* 6763.

(5) C. Knie, M. Utecht, F. Zhao, H. Kulla, S. Kovalenko, A. M. Brouwer, P. Saalfrank, S. Hecht, and D. Bleger. (2014). ortho-Fluoroazobenzenes: Visible Light Switches with Very Long-Lived Z Isomers. *Chem. Eur. J., 20,* 1.

(6) W. R. Brode, J. H. Gould and G. M. Wyman. (1952) The Relation between the Absorption Spectra and the Chemical Constitution of Dyes. XXV. Phototropism and cis-trans Isomerism in Aromatic Azo Compounds. *J. Am. Chem. Soc., 74,* 4641.

(7) J. Bahrenburg, K. Röttger, R. Siewertsen, F. Renth and F. Temps. (2012). Sequential photoisomerisation dynamics of the push–pull azobenzene Disperse Red 1. *Photochem. Photobiol. Sci., 11,* 1210.

(8) H. Rau. (1973) Spectroscopic Properties of Organic Azo Compounds. *Angew. Chem. Int. Ed. Engl., 12,* 224.

(9) O. Sadovski, A. A. Beharry, F. Zhang and G. A. Woolley. (2009). Spectral Tuning of Azobenzene Photoswitches for Biological Applications. *Angew. Chem. Int. Ed., 48*, 1484.

(10) U. Kusebauch, S. A. Cadamuro, H. J. Musiol, M. O. Lenz, J. Wachtveitl, L. Moroder and C. Renner (2006) Photocontrolled Folding and Unfolding of a Collagen Triple Helix. *Angew. Chem. Int. Ed., 45,* 7015.

(11) U. Kusebauch, L. Lorenz, S. A. Cadamuro, H. J. Musiol, M. O. Lenz, C. Renner, J. Wachtveitl and L. Moroder. (2007) *Biopolymers, 88,* 532.

(12) S. L. Dong, M. Loweneck, T. E. Schrader, W. J. Schreier, W. Zinth, L. Moroder and C. Renner. (2006). A Photocontrolled β-Hairpin Peptide. *Chem. Eur. J., 12*, 1114.

(13) G. A. Woolley. (2005). Photocontrolling Peptide α Helices. *Acc. Chem. Res., 38*, 486.

(14) F. Zhang, A. Zarrine-Afsar, M. S. Al-Abdul-Wahid, R. S. Prosser, A. R. Davidson and G. A. Woolley. (2009). Structure-Based Approach to the Photocontrol of Protein Folding. *J. Am. Chem. Soc., 131*, 2283.

(15) E. Bartels, N. H. Wassermann and B. F. Erlanger. (1971). Photochromic Activators of the Acetylcholine Receptor. *PNAS, 68*, 1820.

(16) X. Liang, R. Wakuda, K. Fujioka and H. Asanuma. (2010). Photoregulation of DNA transcription by using photoresponsive T7 promoters and clarification of its mechanism. *FEBS J., 277*, 1551.

(17) M. Liu, H. Asanuma and M. Komiyama. (2006). Azobenzene-Tethered T7 Promoter for Efficient Photoregulation of Transcription. *J. Am. Chem. Soc., 128*, 1009.

(18) J. M. Kuiper and J. B. F. N. Engberts. (2004). H-Aggregation of Azobenzene-Substituted Amphiphiles in Vesicular Membranes. *Langmuir, 20*, 1152.

(19) K. Ishii, T. Hamada, M. Hatakeyama, R. Sugimoto, T. Nagasaki and M. Takagi. (2009). Reversible Control of *Exo*- and *Endo*-Budding Transitions in a Photosensitive Lipid Membrane, *Chem. Bio. Chem., 10,* 251.

(20) R. J. Mart and R. K. Allemann. (2016) Azobenzene photocontrol of peptides and proteins. *Chem. Commun., 52,* 12262.

(21) P. Cattaneo and M. Persico. (1999). An ab initio study of the photochemistry of azobenzene, *Phys. Chem. Chem. Phys., 1,* 4739.

(22) M. Quick, A. L. Dobryakov, M. Gerecke, C. Richter, F. Berndt, I. N. Ioffe, A. A. Granovsky, R. Mahrwald, N. P. Ernsting, and S. A. Kovalenko. (2014). Photoisomerization Dynamics and Pathways of trans and cis Azobenzene in Solution from Broadband Femtosecond Spectroscopies and Calculations. *J. Phys. Chem. B, 118*, 8756.

(23) S. Kucharski, R, Janik, H. Motschmann, C. Radge. (1999). *Trans-cis* isomerisation of azobenzene amphiphiles containing a sulfonyl group. *New J. Chem., 23,* 765.

(24) A. Cembran, F. Bernardi, M. Garavelli, L. Gagliardi, and G. Orlandi. (2004). On the Mechanism of the cis-trans Isomerization in the Lowest Electronic States of Azobenzene: S0, S1, and T1. *J. Am. Chem. Soc. 126,* 3234.

(25) X. Yu, Z. Wang, M. Buchholz, N. Fuellgrabe, S. Grosjean, F. Bebensee, S. Braese, C. Woell and L. Heinke. (2015). Cis-to-trans isomerization of azobenzene investigated by using thin films of metal–organic frameworks. *Phys. Chem. Chem. Phys., 17*, 22721.

(26) N. A. Wazzan, P. R. Richardson and A.C. Jones. (2010). *Cis-Trans* isomerisation of azobenzenes studied by laser-coupled NMR spectroscopy and DFT calculations. *Photochem. Photobiol. Sci., 9,* 968.

(27) M. Dong, A. Babalhavaeji, S. Samanta, A. A. Beharry, G. A. Woolley. (2015). Red-Shifting Azobenzene Photoswitches for in Vivo Use. *Acc. Chem. Res., 48,* 2662.

(28) T. Asano. (1980). Pressure effects on the thermal cis-trans isomerization of 4-dimethylamino-4'-nitroazobenzene. Evidence for a change of mechanism with solvent. *J. Am. Chem. Soc. 102*, 1205.

(29) T. Asano, T. Okada, S. Shinkai, K. Shigematsu, Y. Kusano, O. Manabe. (1981). Temperature and pressure dependences of thermal cis-to-trans isomerization of azobenzenes which evidence an inversion mechanism. *J. Am. Chem. Soc. 103*, 5161.

(30) T. Asano, T. Yano, T. Okada. (1982). Mechanistic study of thermal Z-E isomerization of azobenzenes by high-pressure kinetics. *J. Am. Chem. Soc., 104,* 4900.

(31) T. Asano, T. Okada. (1984). Thermal Z-E Isomerization of Azobenzenes. The pressure, solvent and substituent effects. *J. Org. Chem., 49,* 4387.

(32) D. M. Shin and D. G. Whitten. (1988). Solvent-Induced Mechanism Change in Charge-Transfer Molecules. Inversion versus Rotation Paths for the Z-E Isomerization of Donor-Acceptor Substituted Azobenzenes. *J. Am. Chem. Soc., 110,* 5206.

(33) K. Baba, H. Ono, E. Itoh, S. Itoh, K. Noda, T. Usui, K. Ishihara, M. Inamo, H. D. Takagi and T. Asano. (2006). Kinetic Study of Thermal *Z* to *E* Isomerization Reactions of Azobenzene and 4-Dimethylamino-4′-nitroazobenzene in Ionic Liquids [1-R-3-Methylimidazolium Bis(trifluoromethylsulfonyl)imide with R=Butyl, Pentyl, and Hexyl]. *Chem. Eur. J., 12,* 5328.

(34) C. Dellago, P. G. Bolhuis. (2008). Transition Path Sampling and Other Advanced Simulation Techniques for Rare Events*, Advances in Polymer Science, Springer*.

(35) D. Zahn. (2006). Exploring the Mechanisms of Reactions in Solution from Transition Path Sampling Molecular Dynamics Simulations. *J. Chem. Theory Comput., 2,* 107.

(36) P. Geissler, C. Dellago, D. Chandler. (1999). Kinetic Pathways of Ion Pair Dissociation in Water. *J. Phys. Chem. B, 103,* 3706.

(37) T. A. McCormick, D. Chandler. (2003). Grid−Flux Method for Learning the Solvent Contribution to the Mechanisms of Reactions. *J. Phys. Chem. B, 107,* 2796.

(38) J. Ramirez and M. Laso. (2001). Conformational kinetics in liquid *n*-butane by transition path sampling*. J. Chem. Phys., 115,* 7285.

(39) P. G. Bolhuis, C. Dellago, and D. Chandler. (2000). Reaction coordinates of biomolecular isomerization*. PNAS, 97,* 5877.

(40) A. Ma and A. R. Dinner. (2005). Automatic Method for Identifying Reaction Coordinates in Complex Systems*. J. Phys. Chem. B, 109,* 6769.

(41) R. J. Dimelow, R. A. Bryce, A. J. Masters, I. H. Hillier, and N.A. Burton. (2006). Exploring reaction pathways with transition path and umbrella sampling: Application to methyl maltoside. *J. Chem. Phys., 124*, 114113.

(42) L. L. Schaleger, and F. A. Long. (1960). Entropies of activation and mechanisms of reactions in solution. *Adv. Phys. Org. Chem. 1,* 1.

(43) M. Kazemi and J. Åqvist. (2015). Chemical reaction mechanisms in solution from brute force computational Arrhenius plots. *Nature Communications. 6,* 7293.

(44) F. Jensen. (2001). Introduction to computational chemistry. Wiley. New York.

(45) P. Atkins, J de Paula. (2006). Physical Chemistry. Eighth edition. WH Freeman and Company, New York.

(46) Gaussian 03, Revision A.1, M. J. Frisch, G. W. Trucks, H. B. Schlegel, G. E. Scuseria, M. A. Robb, J. R. Cheeseman, J. A. Montgomery, Jr., T. Vreven, K. N. Kudin, J. C. Burant, J. M. Millam, S. S. Iyengar, J. Tomasi, V. Barone, B. Mennucci, M. Cossi, G. Scalmani, N. Rega, G. A. Petersson, H. Nakatsuji, M. Hada, M. Ehara, K. Toyota, R. Fukuda, J. Hasegawa, M. Ishida, T. Nakajima, Y. Honda, O. Kitao, H. Nakai, M. Klene, X. Li, J. E. Knox, H. P. Hratchian, J. B. Cross, C. Adamo, J. Jaramillo, R. Gomperts, R. E. Stratmann, O. Yazyev, A. J. Austin, R. Cammi, C. Pomelli, J. W. Ochterski, P. Y. Ayala, K. Morokuma, G. A. Voth, P. Salvador, J. J. Dannenberg, V. G. Zakrzewski, S. Dapprich, A. D. Daniels, M. C. Strain, O. Farkas, D. K. Malick, A. D. Rabuck, K. Raghavachari, J. B. Foresman, J. V. Ortiz, Q. Cui, A. G. Baboul, S. Clifford, J. Cioslowski, B. B. Stefanov, G. Liu, A. Liashenko, P. Piskorz, I. Komaromi, R. L. Martin, D. J. Fox, T. Keith, M. A. Al-Laham, C. Y. Peng, A. Nanayakkara, M. Challacombe, P. M. W. Gill, B. Johnson, W. Chen, M. W. Wong, C. Gonzalez, and J. A. Pople, Gaussian, Inc., Pittsburgh PA, 2003.

(47) D. R. Yarkony, ed. Modern Electronic Structure Theory. Part I and II. (1995) World Scientific.

(48) W. Koch and M.C. Holthausen. (2001). A Chemist's guide to Density Functional Theory, WILEY-VCH.

(49) A. D. Becke. (1993). Density-functional thermochemistry. III. The role of exact exchange*, J. Chem. Phys., 98,* 5648.

(50) J. P. Perdew, K. Burke, and M. Ernzerhof. (1996). Generalized gradient approximation made simple. *Phys. Rev. Lett., 77*, 3865.

(51) C. Adamo and V. Barone. (1999). Toward reliable density functional methods without adjustable parameters: The PBE0 model. *J. Chem. Phys., 110,* 6158.

(52) J. J. P. Stewart. (1989). Optimization of parameters for semiempirical methods I. Method. II. Applications. *J. Comp. Chem., 10,* 209 and 221**.**

(53) G. Zheng, S. Irle, K. Morokuma. (2005). Performance of the DFTB method in comparison to DFT and semiempirical methods for geometries and energies of C_{20}–C_{86} fullerene isomers. *Chem. Phys. Lett., 412,* 210.

(54) M. Elstner, D. Porezag, G. Jungnickel, J. Elsner, M. Haugk, T. Frauenheim, S. Suhai, and G. Seifert. (1998). Self-consistent-charge density-functional tight-binding method for simulations of complex materials properties. *Phys. Rev. B, 58,* 7260.

(55) M. Gaus, Q. Cui and M. Elstner. DFTB3: Extension of the Self-Consistent-Charge Density-Functional Tight-Binding Method (SCC-DFTB). *J. Chem. Theory Comput., 4,* 931.

(56) M. Gaus, A. Goez, and M. Elstner. (2013). Parametrization and Benchmark of DFTB3 for Organic Molecules. *J. Chem. Theory Comput., 9,* 338.

(57) https://www.dftb.org/parameters/

(58) D. van der Spoel, E. Lindahl, B. Hess, G. Groenhof, A. E. Mark, H. J. Berendsen. (2005). GROMACS: Fast, flexible and free. *J. Comput. Chem., 26*, 1701.

(59) H. J. Berendsen, D. van der Spoel and R. van Drunen. (1995). GROMACS: A message-passing parallel molecular dynamics implementation. *Comp. Phys. Comm.**,** 91***,** 43.

(60) S. Miertus, E. Scrocco, and J. Tomasi. (1981). Electrostatic interaction of a solute with a continuum. A direct utilization of AB initio molecular potentials for the prevision of solvent effects. *Chem. Phys., 55,* 117.

(61) B. Mennucci and J.Tomasi. (1997). A new integral equation formalism for the polarizable continuum model: Theoretical background and applications to isotropic and anisotropic dielectrics. *J. Chem. Phys. 106,* 5151.

(62) M. Cossi, V. Barone, R. Cammi, J. Tomasi. (1996). Ab initio study of solvated molecules: a new implementation of the polarizable continuum model. *Chem. Phys. Lett., 255,* 327.

(63) J. L. Pascual-Ahuir, E. Silla and I. Tufion. (1994). GEPOL: An improved description of molecular surfaces. III. A new algorithm for the computation of a solvent-excluding surface. *J. Comput. Chem., 15,* 1127.

(64) H. Eyring. (1935). The activated complex and the absolute rate of chemical reactions. *Chem. Rev., 17,* 65.

(65) J. Baker. (1986). An algorithm for the location of transition states. *J. Comput. Chem*., *7,* 385.

(66) H. Eyring. (1935). The Activated Complex in Chemical Reactions. *J. Chem. Phys., 3,* 107.

(67) P. Atkins, R. Friedman. (2005). Molecular Quantum Mechanics. Fourth Edition. *Oxford University.*

(68) M. P. Allan, D. J. Tildesley. (1987). Computer Simulations of Liquids. *Clarendon Press*.

(69) T. D. Kuehne. (2013). Ab-initio Molecular Dynamics. *arXiv.*

(70) D. Marx and J. Hutter. (2009). Ab Initio Molecular Dynamics: Basic Theory and Advance Methods, *Cambridge University Press,* Cambridge.

(71) A. Warshel, M. Levitt. (1976). Theoretical studies of enzymatic reactions: dielectric, electrostatic and steric stabilization of carbonium ion in the reaction of lysozyme. *J. Mol. Biol., 103,* 227.

(72) H. M. Senn and W. Thiel. (2009). QM/MM Methods for Biomolecular Systems. *Angew. Chem. Int. Ed., 48,* 1198.

(73) L. Monticelli and E. Salonen, eds. (2013). Biomolecular Simulations: Methods and Protocols, Methods in Molecular Biology. Chapter 3 (Groenhof). Springer Science+Business Media, New York.

(74) T. Kubar, K. Welke, G. Groenhof. (2015). New QM/MM implementation of the DFTB3 method in the Gromacs package. *J Comput. Chem., 36,* 1978.

(75) T. Darden, D. York, L. Pedersen. (1993). Particle mesh Ewald: An N log(N) method for Ewald sums in large systems. *J. Chem. Phys. 98,* 10089.

(76) P. P. Ewald. (1921). Die Berechnung optischer und elektrostatischer Gitterpotentiale. *Ann. Phys. 64,* 253.

(77) F. Neese. (2012). The ORCA program system. *Comp. Mol. Sci., 2,* 73.

(78) J. Wang, R. M. Wolf, J. W. Caldwell, P. A. Kollman, D. A. Case. (2004). Development and testing of a general AMBER force field. *J. Comp. Chem., 25,* 1157.

(79) C. I. Bayly, P. Cieplak, W. D. Cornell, P. A. Kollman. (1993). A Well-Behaved Electrostatic Potential Based Method Using Charge Restraints for Deriving Atomic Charges: The RESP Model. *J. Phys. Chem., 97,* 10269.

(80) A. Laio and M. Parrinello. (2002). Escaping free-energy minima. *PNAS, 99,* 12562.

(81) B. Ensing, M. de Vivo, Z. Liu, P. Moore, M. L. Klein. (2006). Metadynamics as a Tool for Exploring Free Energy Landscapes of Chemical Reactions. *Acc. Chem. Res., 39,* 73.

(82) G. M. Torrie, J. P. Valleau. (1977). Nonphysical sampling distributions in Monte Carlo free energy estimation: umbrella sampling. *J. Comput. Phys., 23*, 187.

(83) G. M. Torrie, J. P. Valleau. (1974). Monte Carlo free energy estimates using non-Boltzmann sampling: Application to the sub-critical Lennard-Jones fluid. *Chem. Phys. Lett., 28,* 578.

(84) J. Kaestner. (2011). Umbrella sampling. *Comput Mol Sci*. Vol. 00.

(85) S. Kumar, D. Bouzida, R. H. Swendsen, P. A. Kollman, J. M. Rosenberg. (1992). The weighted histogram analysis method for free-energy calculations on biomolecules. 1. The method. *J. Comput. Chem. 13,* 1011.

(86) A. Grossfield. WHAM: an implementation of the weighted histogram analysis method, Version 2.0.9.

(87) J. R. Gullingsrud, R. Braun, K. Schulten. (1999). Reconstructing potentials of mean force through time series analysis of steered molecular dynamics simulations. *J. Comput. Phys., 151*, 190.

(88) C. Jarzynski. (1997). Nonequilibrium equality for free energy differences. *Phys. Rev. Lett., 78,* 2690.

(89) S. Izrailev, S. Stepaniants, B. Isralewitz, D. Kosztin, H. Lu, F. Molnar, W. Wriggers, and K. Schulten, (1998). Steered molecular dynamics, in Computational Molecular Dynamics: Challenges, Methods, Ideas, edited by P. Deuflhard, J. Hermans, B. Leimkuhler, A. E. Mark, S. Reich, and R. D. Skeel. Lecture Notes in Computational Science and Engineering, *Springer-Verlag, Berlin, 4,* 36.

(90) G.A. Tribello, M. Bonomi, D. Branduardi, C. Camilloni, G. Bussi. (2014). PLUMED2: New feathers for an old bird, *Comp. Phys. Comm., 185,* 604.

(91) C. Dellago, P. G. Bolhuis. (2001). Transition Path Sampling, *Adv. Chem. Phys., 123*, 1.

(92) C. Dellago, P. G. Bolhuis (2008). Transition Path Sampling and Other Advanced Simulation Techniques for Rare Events. *Adv. Polym. Sci., Springer*.

(93) J. Juraszek and P. G. Bolhuis. (2008). Rate constant and reaction coordinate of Trp-cage folding in explicit water. *Biophys. J. 95,* 4246.

(94) J. Vreede, J. Juraszek, and P. G. Bolhuis. (2010). Predicting the reaction coordinates of millisecond light-induced conformational changes in photoactive yellow protein. *PNAS, 107,* 2397.

(95) G. Hummer. (2004). From transition paths to transition states and rate coefficients, *J. Chem. Phys. 120,* 516.

(96) R. B. Best and G. Hummer. (2005). Reaction Coordinates and Rates from Transition Paths, *PNAS*, 102, 6732.

(97) B. Peters, B. L. Trout. (2006). Obtaining reaction coordinates by likelihood maximization. *J. Chem. Phys., 125,* 054108.

(98) B. Peters, G. T. Beckham, B. L. Trout. (2007). Extensions to the likelihood maximization approach for finding reaction coordinates. *J. Chem. Phys., 127*, 034109.

(99) T. S. van Erp, P.G. Bolhuis. (2008). Elaborating Transition Interface Sampling Methods. *Elsevier Sci*.

(100) H. X. Zhou. (1989). The exponential nature of barrier crossings studied by Langevin dynamics. *Chem. Phys. Lett., 164,* 285.

(101) J. M. Depapepe, J. P. Ryckaert and A. Bellemans (1993). Kinetics of the geometric isomerization of cyclohexane in a stochastic bath. *Mol. Phys., 78*, 1575.

(102) M.A. Wilson, D. Chandler. (1990). Molecular dynamics study of cyclohexane interconversion. *Chem. Phys., 149,* 11.

(103) C. Dellago, P. G. Bolhuis, and D. Chandler. (1999). On the calculation of reaction rate constants in the transition path ensemble, *J. Chem. Phys.,* 110, 6619.

(104) R. Pangaii, Berne. (1979). Monte Carlo simulation of hydrophobic interaction. *J. Chem. Phys., 71,* 2975. (105) https://wiki.fysik.dtu.dk/ase/about.html

(106) M. J. Bedard-Hearn, R. E. Larsen, and B. J. Schwartz. (2003). Understanding non-equilibrium solute and solvent Motions through molecular projections: computer simulations of solvation dynamics in liquid Tetrahydrofuran (THF). *J. Phys. Chem. B.*, 107, 14464.

(107) H. A. Kramers (1940). Brownian motion in a field of force and the diffusion model of chemical reactions. *Physica*, 7, 284.

(108) R. A. Marcus (1956*). On the theory of oxidation-reduction reactions involving electron transfer. I. J. Chem. Phys.* 24, 966.

(109) D. J. Truhlar (1984). Variational transition state theory. *Ann. Rev. Phys. Chem.* 1984. 35: 159.

(110) W. K. den Otter, W. J. Briels. (1997). The reactive flux method applied to complex isomerization reactions: Using the unstable normal mode as a reaction coordinate. *J. Chem. Phys.* 106: 5494.

6 Appendix

6.1 The transition state ensemble projected onto the (ω, α) plane.

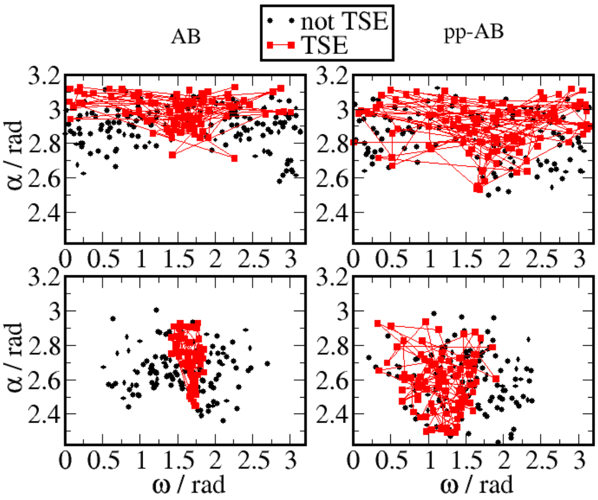

Figure 55. Comparison of the TSE ensembles and configurations not belonging to the TSE projected onto the (ω, α) plane (states that commit to cis and trans). Triangular shape for the TSE for AB and ppAB in vacuum (upper panel) is not reproduced in DMSO (lower panel).

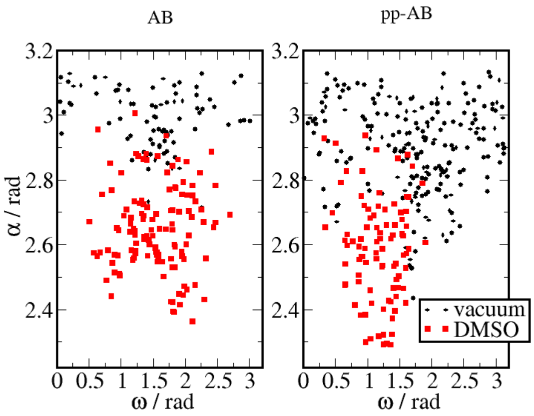

Figure 56. Transition State Ensembles projected onto the (ω, α) plane. The effect of push-pull substitution in gas phase (in black: left AB, right ppAB), as well as the effect of the polar solvent DMSO on both compounds (red dots). There is a pronounced shift to lower α for both, push-pull substitution and in DMSO, where the shift is even more pronounced for ppAB in DMSO.

6.2 List of all Order Parameters used as input for Likelihood Maximization Estimation

AB in vacuum

0 DISTANCE dist1 1,2
1 DISTANCE dist2 1,6
2 DISTANCE dist3 1,18
3 DISTANCE dist4 2,3
4 DISTANCE dist5 2,7
5 DISTANCE dist6 3,4
6 DISTANCE dist7 3,17
7 DISTANCE dist8 4,5
8 DISTANCE dist9 4,19
9 DISTANCE dist10 5,6
10 DISTANCE dist11 5,23
11 DISTANCE dist12 6,20
12 DISTANCE dist13 7,8
13 DISTANCE dist14 8,9
14 DISTANCE dist15 9,10
15 DISTANCE dist16 9,14
16 DISTANCE dist17 10,11
17 DISTANCE dist18 10,15
18 DISTANCE dist19 11,12
19 DISTANCE dist20 11,22
20 DISTANCE dist21 12,13
21 DISTANCE dist22 12,24
22 DISTANCE dist23 13,14
23 DISTANCE dist24 13,21
24 DISTANCE dist25 14,16
25 ANGLE ang1 2,1,6
26 ANGLE ang2 2,1,18
27 ANGLE ang3 6,1,18
28 ANGLE ang4 1,2,3
29 ANGLE ang5 1,2,7
30 ANGLE ang6 3,2,7
31 ANGLE ang7 2,3,4
32 ANGLE ang8 2,3,17
33 ANGLE ang9 4,3,17
34 ANGLE ang10 3,4,5
35 ANGLE ang11 3,4,19
36 ANGLE ang12 5,4,19
37 ANGLE ang13 4,5,6
38 ANGLE ang14 4,5,23
39 ANGLE ang15 6,5,23
40 ANGLE ang16 1,6,5
41 ANGLE ang17 1,6,20

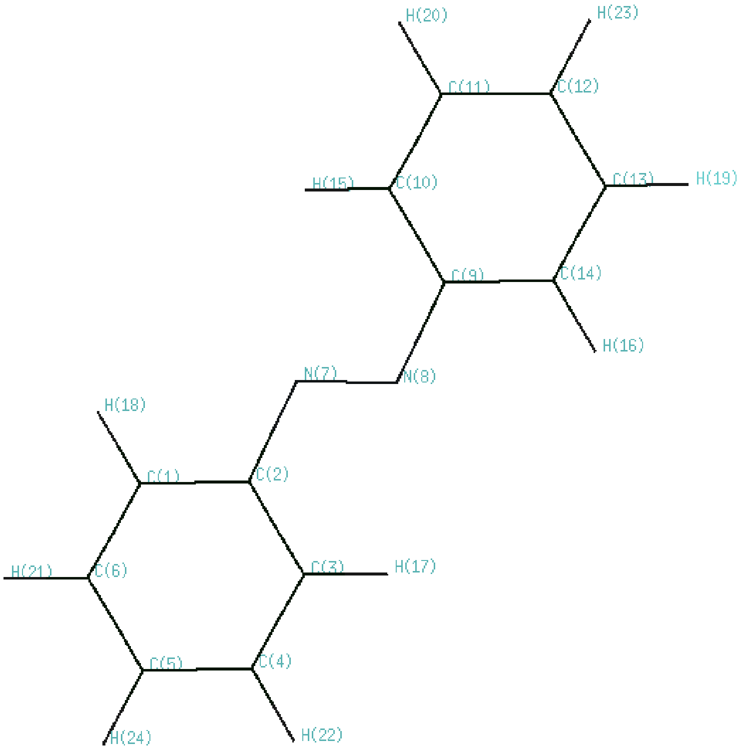

Figure 57. Molecular scheme of AB with atom indices

42 ANGLE ang18 5,6,20
43 ANGLE ang19 2,7,8
44 ANGLE ang20 7,8,9
45 ANGLE ang21 8,9,10
46 ANGLE ang22 8,9,14
47 ANGLE ang23 10,9,14
48 ANGLE ang24 9,10,11
49 ANGLE ang25 9,10,15
50 ANGLE ang26 11,10,15
51 ANGLE ang27 10,11,12
52 ANGLE ang28 10,11,22
53 ANGLE ang29 12,11,22
54 ANGLE ang30 11,12,13
55 ANGLE ang31 11,12,24
56 ANGLE ang32 13,12,24
57 ANGLE ang33 12,13,14
58 ANGLE ang34 12,13,21
59 ANGLE ang35 14,13,21
60 ANGLE ang36 9,14,13
61 ANGLE ang37 9,14,16
62 ANGLE ang38 13,14,16
63 TORSION dih1 6,1,2,3
64 TORSION dih2 6,1,2,7
65 TORSION dih3 18,1,2,3
66 TORSION dih4 18,1,2,7
67 TORSION dih5 2,1,6,5
68 TORSION dih6 2,1,6,20
69 TORSION dih7 18,1,6,5
70 TORSION dih8 18,1,6,20
71 TORSION dih9 1,2,3,4
72 TORSION dih10 1,2,3,17
73 TORSION dih11 7,2,3,4
74 TORSION dih12 7,2,3,17
75 TORSION dih13 1,2,7,8
76 TORSION dih14 3,2,7,8
77 TORSION dih15 2,3,4,5
78 TORSION dih16 2,3,4,19
79 TORSION dih17 17,3,4,5
80 TORSION dih18 17,3,4,19
81 TORSION dih19 3,4,5,6
82 TORSION dih20 3,4,5,23
83 TORSION dih21 19,4,5,6
84 TORSION dih22 19,4,5,23
85 TORSION dih23 4,5,6,1
86 TORSION dih24 4,5,6,20
87 TORSION dih25 23,5,6,1
88 TORSION dih26 23,5,6,20
89 TORSION dih27 2,7,8,9

90 TORSION dih28 7,8,9,10
91 TORSION dih29 7,8,9,14
92 TORSION dih30 8,9,10,11
93 TORSION dih31 8,9,10,15
94 TORSION dih32 14,9,10,11
95 TORSION dih33 14,9,10,15
96 TORSION dih34 8,9,14,13
97 TORSION dih35 8,9,14,16
98 TORSION dih36 10,9,14,13
99 TORSION dih37 10,9,14,16
100 TORSION dih38 9,10,11,12
101 TORSION dih39 9,10,11,22
102 TORSION dih40 5,10,11,12
103 TORSION dih41 5,10,11,22
104 TORSION dih42 0,11,12,13
105 TORSION dih43 0,11,12,24
106 TORSION dih44 2,11,12,13
107 TORSION dih45 2,11,12,24
108 TORSION dih46 1,12,13,14
109 TORSION dih47 1,12,13,21
110 TORSION dih48 4,12,13,14
111 TORSION dih49 4,12,13,21
112 TORSION dih50 12,13,14,9
113 TORSION dih51 2,13,14,16
114 TORSION dih52 21,13,14,9
115 TORSION dih53 1,13,14,16
116 TORSION dihOR 3,2,9,10
117 coordinate X

ppAB in vacuum

0 DISTANCE dist1 1,2
1 DISTANCE dist2 1,6
2 DISTANCE dist3 1,16
3 DISTANCE dist4 2,3
4 DISTANCE dist5 2,7
5 DISTANCE dist6 3,4
6 DISTANCE dist7 3,15
7 DISTANCE dist8 4,5
8 DISTANCE dist9 4,22
9 DISTANCE dist10 5,6
10 DISTANCE dist11 5,24
11 DISTANCE dist12 6,21
12 DISTANCE dist13 7,8
13 DISTANCE dist14 8,9
14 DISTANCE dist15 9,10
15 DISTANCE dist16 9,14
16 DISTANCE dist17 10,11
17 DISTANCE dist18 10,18
18 DISTANCE dist19 11,12
19 DISTANCE dist20 11,20
20 DISTANCE dist21 12,13
21 DISTANCE dist22 12,23
22 DISTANCE dist23 13,14
23 DISTANCE dist24 13,19
24 DISTANCE dist25 14,17
25 DISTANCE dist26 16,27
26 DISTANCE dist27 16,28
27 DISTANCE dist28 23,25
28 DISTANCE dist29 23,26
29 ANGLE ang1 2,1,6
30 ANGLE ang2 2,1,16
31 ANGLE ang3 6,1,16
32 ANGLE ang4 1,2,3
33 ANGLE ang5 1,2,7
34 ANGLE ang6 3,2,7
35 ANGLE ang7 2,3,4
36 ANGLE ang8 2,3,15
37 ANGLE ang9 4,3,15
38 ANGLE ang10 3,4,5
39 ANGLE ang11 3,4,22
40 ANGLE ang12 5,4,22

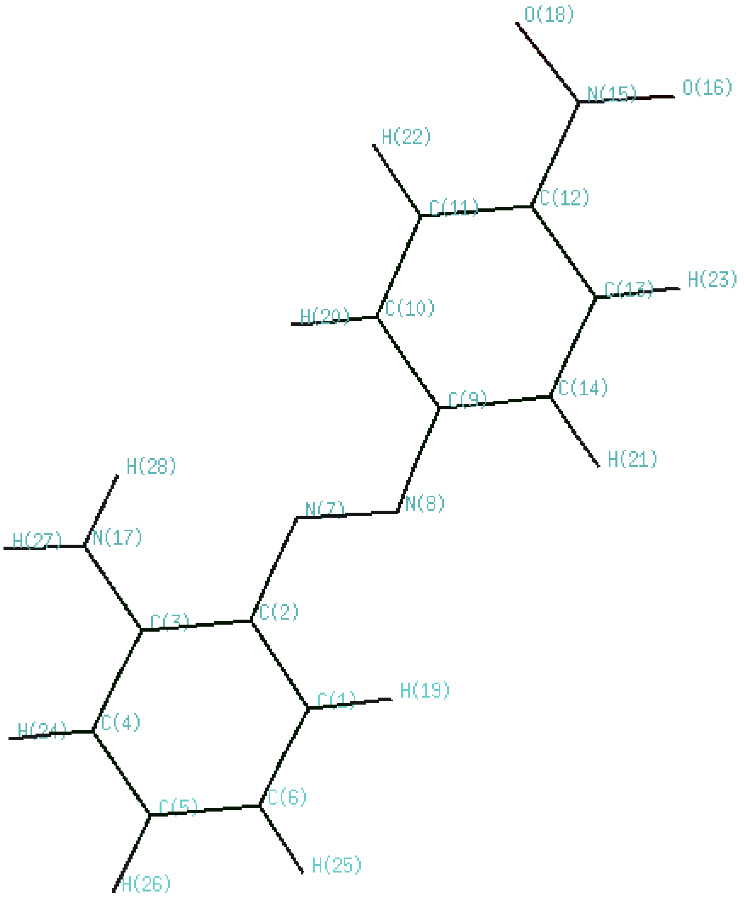

Figure 58. Molecular scheme of ppAB with atom indices

41 ANGLE ang13 4,5,6
42 ANGLE ang14 4,5,24
43 ANGLE ang15 6,5,24
44 ANGLE ang16 1,6,5
45 ANGLE ang17 1,6,21
46 ANGLE ang18 5,6,21
47 ANGLE ang19 2,7,8
48 ANGLE ang20 7,8,9
49 ANGLE ang21 8,9,10
50 ANGLE ang22 8,9,14
51 ANGLE ang23 10,9,14
52 ANGLE ang24 9,10,11
53 ANGLE ang25 9,10,18
54 ANGLE ang26 11,10,18
55 ANGLE ang27 10,11,12
56 ANGLE ang28 10,11,20
57 ANGLE ang29 12,11,20
58 ANGLE ang30 11,12,13
59 ANGLE ang31 11,12,23
60 ANGLE ang32 13,12,23
61 ANGLE ang33 12,13,14
62 ANGLE ang34 12,13,19
63 ANGLE ang35 14,13,19
64 ANGLE ang36 9,14,13
65 ANGLE ang37 9,14,17
66 ANGLE ang38 13,14,17
67 ANGLE ang39 1,16,27
68 ANGLE ang40 1,16,28
69 ANGLE ang41 27,16,28
70 ANGLE ang42 12,23,25
71 ANGLE ang43 12,23,26
72 ANGLE ang44 25,23,26
73 TORSION dih1 6,1,2,3
74 TORSION dih2 6,1,2,7
75 TORSION dih3 16,1,2,3
76 TORSION dih4 16,1,2,7
77 TORSION dih5 2,1,6,5
78 TORSION dih6 2,1,6,21
79 TORSION dih7 16,1,6,5
80 TORSION dih8 16,1,6,21
81 TORSION dih9 2,1,16,27
82 TORSION dih10 2,1,16,28

83 TORSION dih11 6,1,16,27
84 TORSION dih12 6,1,16,28
85 TORSION dih13 1,2,3,4
86 TORSION dih14 1,2,3,15
87 TORSION dih15 7,2,3,4
88 TORSION dih16 7,2,3,15
89 TORSION dih17 1,2,7,8
90 TORSION dih18 3,2,7,8
91 TORSION dih19 2,3,4,5
92 TORSION dih20 2,3,4,22
93 TORSION dih21 15,3,4,5
94 TORSION dih22 15,3,4,22
95 TORSION dih23 3,4,5,6
96 TORSION dih24 3,4,5,24
97 TORSION dih25 22,4,5,6
98 TORSION dih26 22,4,5,24
99 TORSION dih27 4,5,6,1
100 TORSION dih28 4,5,6,21
101 TORSION dih29 24,5,6,1
102 TORSION dih30 24,5,6,21
103 TORSION dih31 2,7,8,9
104 TORSION dih32 7,8,9,10
105 TORSION dih33 7,8,9,14
106 TORSION dih34 8,9,10,11
107 TORSION dih35 8,9,10,18
108 TORSION dih36 14,9,10,11
109 TORSION dih37 14,9,10,18
110 TORSION dih38 8,9,14,13
111 TORSION dih39 8,9,14,17
112 TORSION dih40 10,9,14,13
113 TORSION dih41 10,9,14,17
114 TORSION dih42 9,10,11,12
115 TORSION dih43 9,10,11,20
116 TORSION dih44 18,10,11,12
117 TORSION dih45 18,10,11,20
118 TORSION dih46 10,11,12,13
119 TORSION dih47 10,11,12,23
120 TORSION dih48 20,11,12,13
121 TORSION dih49 20,11,12,23
122 TORSION dih50 11,12,13,14
123 TORSION dih51 11,12,13,19
124 TORSION dih52 23,12,13,14

125 TORSION dih53 23,12,13,19
126 TORSION dih54 11,12,23,25
127 TORSION dih55 11,12,23,26
128 TORSION dih56 13,12,23,25
129 TORSION dih57 13,12,23,26
130 TORSION dih58 12,13,14,9
131 TORSION dih59 12,13,14,17
132 TORSION dih60 19,13,14,9
133 TORSION dih61 19,13,14,17
134 TORSION dihOR 3,2,9,10
135 coordinate X

6.3 Likelihood Maximization Estimated Reaction Coordinates

The general labelling for distances, angles and dihedrals if not one of the angles and dihedrals indicated in the molecular schemes in Figure 16, are r for distances, α for angles and ϕ for dihedrals, with atom indices defining the parameter in the subscript. The atom indices can be read from molecular schemes in Figures 57 and 58, of The Appendix 6.2.

6.3.1 ppAB in vacuum with input configurations from the tight interface, $X\,[-0.15, 0.15]$

*a total of 1937 input configurations, with 922 trajectory outcomes in state A and 1015 in state B

ppAB $\delta L_{\min} = 3.8$ n	$\ln L$	Reaction coordinate
1	-1178.8	$1.37 - 1.82 \cdot \sin\omega$
2	-1142.2	$0.38 - 1.88 \cdot \sin(\phi') - 1.75 \cdot \sin\omega$
3	-1119.2	$0.89 - 2.14 \cdot \sin(\phi') - 1.83 \cdot \sin\omega - 1.06 \cdot X$
3 (2nd best)	-1125.1	$0.53 - 2.06 \cdot \sin(\phi') - 1.44 \cdot \sin\omega - 1.34 \cdot \sin\alpha$

6.3.2 AB in DMSO and toluene with input configurations from the tight interface, $X\,[-0.15, 0.15]$

*a total of 589 input configurations, with 204 trajectory outcomes in state A and 385 in state B

AB toluene $\delta L_{\min} = 3.2$ n	$\ln L$	Reaction coordinate
1	-364.3	$1.64 - 2.13 \cdot X$
2	-353.7	$2.73 - 1.95 \cdot \sin\alpha_{6,1,2} - 2.40 \cdot X$
3	-348.0	$0.34 + 4.12 \cdot \sin\phi_{7,2,3,17} - 3.46 \cdot \sin\phi_{1,2,3,17} - 3.74 \cdot \sin\phi_{21,6,1,2}$

*a total of 994 input configurations, with 494 trajectory outcomes in state A and 500 in state B

AB DMSO $\delta L_{\min} = 3.5$ n	$\ln L$	Reaction coordinate
1	-612.8	$1.46 - 3.70 \cdot \sin\alpha_{3,4,21}$
2	-588.0	$2.79 - 4.27 \cdot \sin\alpha_{3,4,21} - 1.74 \cdot X$
3	-564.3	$-2.98 + 4.44 \cdot r_{11,20} + 2.62 \cdot \sin\phi_{23,12,13,19} - 2.18 \cdot X$

6.3.3 ppAB in DMSO and toluene with input configurations from the wide interface, $X\ [-0.5, 0.5]$

*a total of 502 input configurations, with 238 trajectory outcomes in state A and 264 in state B

ppAB toluene $\delta L_{min} = 3.1$ n	$\ln L$	Reaction coordinate
1	-316.1	$1.86 - 2.75 \cdot X$
2	-307.4	$0.51 - 2.85 \cdot X + 1.72 \cdot \sin \phi_{OR}$
3	-302.0	$2.83 - 4.86 \cdot X + 2.06 \cdot \sin \phi_{OR} - 2.23 \cdot \sin \alpha'$

*a total of 1057 input configurations, with 714 trajectory outcomes in state A and 343 in state B

ppAB DMSO $\delta L_{min} = 3.5$ n	$\ln L$	Reaction coordinate
1	-674.4	$-1.39 + 1.78 \cdot \sin \phi_{OR}$
2	-660.1	$1.19 + 2.54 \cdot \sin \omega - 3.45 \cdot \sin \phi$
3	-640.5	$5.01 - 3.19 \cdot \sin \alpha' - 2.37 \cdot \sin \alpha - 3.19 \cdot \sin \phi$

6.4 Distributions of the stable states' and the TS sub-ensembles

The distributions of the the optimized reaction coordinate for ppAB in vacuum, $\mathrm{r}\ (\mathrm{X}, \sin\alpha', \sin\phi')$ in the sub-ensembles that commit to cis, trans stable states and the TS ensemble as well as the associated committor distribution at $\mathrm{r} = \mathrm{r}^*$ are presented in Figure 59.

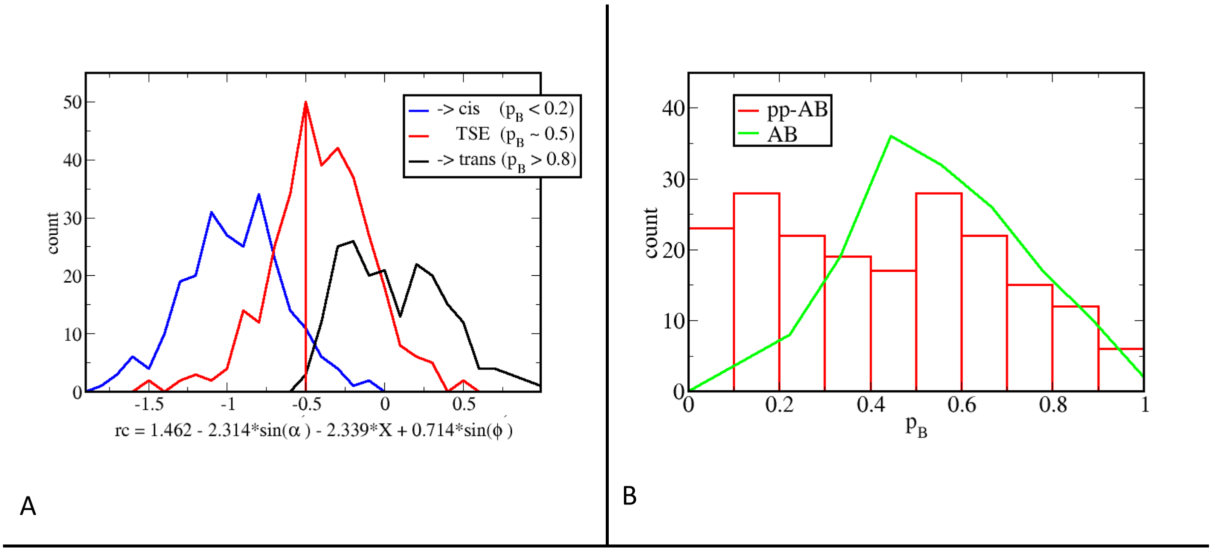

Figure 59. The probability distributions $\mathrm{P}\ (\mathrm{r} \mid \mathrm{TSE})$ for ppAB in vacuum as a function of the optimized reaction coordinate, r for the TSE $\mathrm{P}\ (\mathrm{r} \mid \mathrm{TSE})$ in red, and the configurations committed to cis $\mathrm{P}\ (\mathrm{r} \mid \to \mathrm{cis})$ in blue and trans stable states, $\mathrm{P}\ (\mathrm{r} \mid \to \mathrm{trans})$ in black. (A) Committor distributions $\mathrm{P}\ (\mathrm{p_B})$ for the LM optimized reaction coordinates, rc^* for ppAB in red and AB in green The configurations for which the committor was calculated were restrained at the value where $\mathrm{P}\ (\mathrm{rc} \mid \mathrm{TSE})$ attained its maximum, $\mathrm{rc}^* = -0.55$ and $\mathrm{rc}^* = 0.00$ for ppAB and AB, respectively.

6.5 Kramers turnover for the transmission coefficient

Here we present the results for the double well model potential defined in the Methods Section 2.7.as well as for the 4F-azobenzene studied with QM:PM3 stochastic dynamics. The two regimes for the transmission coefficient (and the rate constant) are defined for low and high friction, in terms of the reduced friction parameter $\gamma^* = \gamma/\omega_\mathrm{B}$, where γ is the friction constant in the Langevin dynamics and ω_B the angular frequency at the barrier top, evaluated for the model double well potential and a unit mass $\mathrm{m} = 1$, as $\omega_\mathrm{B} = \sqrt{\mathrm{k}} = \sqrt{\mathrm{U}''} = \sqrt{-4\mathrm{Q}}\mathrm{i}$, where Q is the barrier height and i the imaginary number. For the 4F-azobenzene, 2,2'-6,6'-tetrafluoroazobenzene (Figure 61), described on the PM3 semiempirical level of theory, it was evaluated as the real part of the imaginary frequency associated to the transition normal mode, $\omega_\mathrm{B} = \omega^\# \approx 1 \cdot 10^{13}\ \mathrm{s}^{-1} = 10\ \ \mathrm{ps}^{-1}$. The time constants used for the propagation of stochastic trajectories for the reactive flux calculation were thus $\tau_\mathrm{r} = 1/\gamma = \{0.1,\ 0.05,\ \ 0.01,\ 0.001\}$ [ps] and the reduced frictions $\gamma^* = 1/(\tau_\mathrm{r}\omega_\mathrm{B}) = \{1, 2, 10, 100\}$.

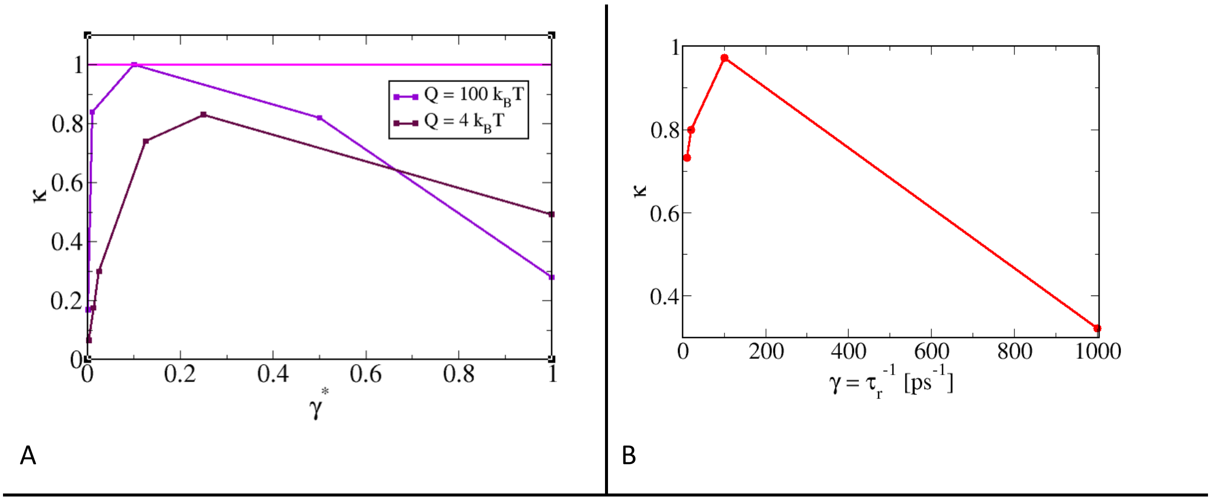

Figure 60. Kramers turnover for the transmission coefficient over a small and a large barrier (A), where $\mathrm{Q} = 4\ \mathrm{k_B T}$ and $\mathrm{Q} = 100\ \mathrm{k_B T}$, respectively. The maximum shifts towards the lower γ^* and higher κ – the inertial regime is reduced and the dissipation of energy along the reaction coordinate very fast (large potential gradient). In (B), the fast dissipation of energy into internal degrees of freedom is dominant for the multi-dimensional phase space of 4F-azobenzene.

The turnover was observed for the value of strong coupling with the heat bath, $\tau_r = 1/\gamma = 0.01\ \mathrm{ps}$, at which point the transmission coefficient was maximal. Due to strong coupling to the heat bath and the multidimensionality of the phase-space the dissipation of energy is fast and the trajectories relax into a stable states basins without returning to the transition region and recrossing back to the reactant state. The transition state theory in which no recrossings are assumed, is valid for this regime, $\kappa \sim 1$. For the highest value of the friction constant $\gamma = 1000\ \mathrm{ps}^{-1}$ the system was in the diffusive regime where the transmission coefficient is again low.

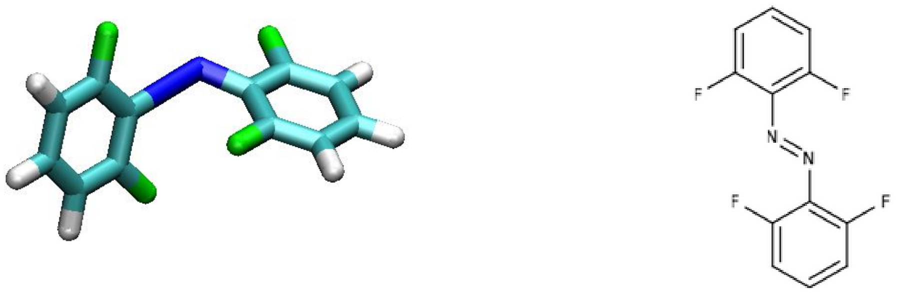

Figure 61. 4F-azobenzene: optimized transition structure at B3LYP/6-31G* level of theory (left) and the molecular scheme (right)

7 Erklärung

Hiermit versichere ich, dass die vorliegende Arbeit an keiner anderen Hochschule eingereicht sowie selbständig und ausschließlich mit den angegebenen Mitteln angefertigt worden ist.

Potsdam, Mai 2017